UNIVERSIDAD COMPLUTENSE DE MADRID
FACULTAD DE CIENCIAS FÍSICAS
Departamento de Estructura de la Materia, Física Térmica y Electrónica

TESIS DOCTORAL

Measurement of the $\sin^2(2\theta_{13})$ neutrino mixing angle with the two detectors of the Double Chooz experiment

Medida de ángulo de mezcla de neutrinos $\sin^2(2\theta_{13})$ con los dos detectores del experimento Double Chooz

MEMORIA PARA OPTAR AL GRADO DE DOCTOR

PRESENTADA POR

Diana Navas Nicolás

Directora

Inés Gil Botella

Madrid
Ed. electrónica 2019

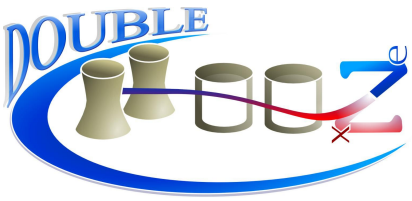

Measurement of the θ_{13} neutrino mixing angle with the two detectors of the Double Chooz experiment

Medida de ángulo de mezcla de neutrinos θ_{13} con los dos detectores del experimento Double Chooz

Memoria de investigación presentada por

Diana Navas Nicolás

para optar al grado de Doctor

Dirigida por

Dra. Inés Gil Botella

Facultad de Ciencias Físicas
Departamento de Estructura de la Materia, Física Térmica y Electrónica

En Madrid, mayo de 2019

Contents

List of Figures

List of Tables

Abstract

Neutrinos are the most abundant massive particles in our Universe but its existence was only predicted 90 years ago. In fact they were not experimentally observed until 60 years ago due to their extraordinarily low cross-section and even nowadays many questions concerning these subatomic particles remain open, as their mass magnitude and ordering, their Dirac or Majorana nature or the possibility of CP-violation.

The Standard Model of Particle Physics establishes that neutrinos are massless particles. Nevertheless in 2015, Takaaki Kajita and Arthur McDonald were awarded with the Nobel prize in Physics for the discovery of the phenomenon of neutrino flavour oscillations, only possible if neutrinos are massive, demonstrating that a neutrino of one particular flavour has non-zero probability to be detected with a different flavour. These oscillations are governed by six independent parameters: 3 mixing angles θ_{12}, θ_{23} and θ_{13}, two mass squared differences and a δ_{CP} phase responsible for the CP-violation in the leptonic sector, being this last parameter still unknown as well as the neutrino mass ordering.

Thus both observables become targets of current and future neutrino experiments. One promising way to measure them is through the asymmetry of the oscillation probabilities between $\nu_\mu \to \nu_e$ and $\bar{\nu}_\mu \to \bar{\nu}_e$ appearance in long baseline accelerator experiments. These two probabilities are proportional to the neutrino mixing angle θ_{13}, being therefore not only a fundamental parameter to complete the knowledge about the neutrino mixing but also a milestone towards observing CP violation.

The information on the θ_{13} can be obtained from accelerator and nuclear reactor neutrino experiments. However the measurement of θ_{13} with accelerators is limited by matter effects or the θ_{23} octant degeneracy. On the other hand nuclear reactors are a very intense and pure source of electron antineutrinos suitable to study the properties of these evasive particles. A new generation of nuclear reactor experiments, Double Chooz (DC), Daya Bay and RENO has been able to provide an unambiguous determination of θ_{13}. The key of these experiments falls on the $\bar{\nu}_e$ disappearance, comparing the observed flux between identical near and far detectors, reducing the systematic uncertainties of the reactor $\bar{\nu}_e$ flux prediction and detection. The Double Chooz near detector (ND), operational since December 2014, is located around 400 meters far from the reactors and measures the $\bar{\nu}_e$ rate before the oscillation takes place. The far detector (FD), around 1050 meters away from reactors and operating since April 2011, is placed closed to the oscillation maximum and is able to detect the $\bar{\nu}_e$ disappearance.

The main objective of this thesis is to present the most precise measurement of θ_{13} by the Double Chooz experiment using 865 days of data taken, for the first time,

with the two DC detectors, thanks to an increase of statistics and a major reduction of systematic errors. The improvement of this value falls on the effective iso-flux site geometry and on a novel detection technique, called Total neutron Capture (TnC).

This new $\bar{\nu}_e$ detection method integrates simultaneously over Gadolinium and Hydrogen neutron captures coming from the $\bar{\nu}_e$ interaction in the full scintillation detector volume. The TnC technique provides remarkable advantages over any single isotope dependant detection. It increases the detection efficiency volume, yielding higher statistics, and causes a significant reduction of the detection systematics, since there is no need to consider any distinction among neutron captures on the isotopes of the detector scintillator and the complex neutron spill in/out currents among the detector volumes. The determination of the detection systematic uncertainties is one of the specific objectives of this thesis.

One of the challenges of this new analysis falls is the control of the large accidental background, dominant in the H channel, thanks to a multi-variable Artificial Neural Network, which takes advantage on the fact that the distributions of the delayed energy as well as the time and spatial signal coincidence are different between the accidental and the antineutrino sample. With this tool, the signal to background ratio is around 10 in the FD and 22 in the ND while keeping $\bar{\nu}_e$ selection efficiency around 85%.

Thus, after the $\bar{\nu}_e$ selection is complete, a deficit in the neutrino candidates is observed with respect to the prediction and this is interpreted as an oscillation.

In the framework of the oscillation analysis, the measurement of the θ_{13} mixing angle is carried out via two different methods. The first one, called Reactor Rate Modulation is based on the classification of the neutrino interactions rate according to different reactor power configurations. Moreover this analysis allows for a direct measurement of the background in a model independent way. The performance of a global fit to both the oscillation amplitude and the background rate by analysing the neutrino candidates rate for different reactor powers consists of the second specific objective of this report.

The second method allows for a measurement obtained by comparing the observed IBD rate+shape spectrum against the neutrino non-oscillation model prediction (data to MC fit) or by comparing directly the far detector data to the near detector data (data to data fit). This analysis is based on the fact that the disappearance probability introduced by a non-zero value of θ_{13} depends on the neutrino energy.

The data to MC Rate+Shape fit, adopted as the nominal θ_{13} Double Chooz measurement, provides a value of $\sin^2(2\theta_{13}) = 0.105 \pm 0.014$. There is a difference between the prediction and the data around 5 MeV that can not be explain by the θ_{13} oscillation and is not covered by the model uncertainties. Therefore the MC prediction is questioned since this distortion has been observed by all reactor neutrino experiments. However the DC θ_{13} measurement and the considered errors are immune to this discrepancy. Prove of this is the data to data fit, performed by the comparison of the observed FD spectra to the prediction extracted from the ND spectrum. The value obtained $\sin^2(2\theta_{13})=0.103\pm0.017$ is in excellent agreement with the main result.

The Reactor Rate Modulation best fit value is found at $\sin^2(2\theta_{13}) = 0.095 \pm 0.016$, a competitive measurement and consistent within 1σ with the results obtained using

the Rate+Shape fit.

In conclusion, the results shown in this thesis correspond to the most precise θ_{13} measurement by the Double Chooz experiment, exploiting for the first time its FD and ND configuration, achieving a major reduction of reactor and detection systematics thanks to the iso-flux configuration and a novel detection technique.

Resumen

Los neutrinos son las partículas más abundantes en nuestro Universo y sin embargo su existencia fue predicha hace apenas 90 años. De hecho, no fueron observadas de forma experimental hasta hace 60 años debido a su sección eficaz extraordinariamente pequeña e incluso hoy, permanecen sin respuesta muchas cuestiones relativas a estas partículas subatómicas, como por ejemplo, la magnitud y el ordenamiento de sus masas, su naturaleza de Dirac o de Majorana o la posibilidad de que violen la simetría CP.

El Modelo Estándar de la Física de Partículas establece que los neutrinos son partículas sin masa. A pesar de ello en 2015, Takaaki Kajita y Arthur McDonald fueron galardonados con el Premio Nobel de Física por el descubrimiento del fenómeno de las oscilaciones de los neutrinos. Este proceso, que solo puede tener lugar si los neutrinos son masivos, hace posible que un neutrino pueda ser detectado en cierto momento con otro sabor diferente al que tenía en el momento de su origen. Estas oscilaciones están gobernadas por seis parámetros independientes: 3 ángulos de mezcla θ_{12}, θ_{23} y θ_{13}, dos diferencias cuadráticas de masa y una fase δ_{CP} responsable de la violación CP en el sector leptónico. Este último parámetro, junto con el ordenamiento de las masas de los neutrinos, es aún una incógnita.

Debido a esto, ambos observables se han convertido en los objetivos de los experimentos de neutrinos actuales y futuros. Un modo prometedor para medirlos es a través de la asimetría que surge en las probabilidades de oscilación entre los canales $\nu_\mu \to \nu_e$ y $\bar{\nu}_\mu \to \bar{\nu}_e$ en experimentos de aceleradores. Estas dos probabilidades son propocionales al ángulo de mezcla de neutrinos θ_{13}, parámetro fundamental no solo para completar el conocimiento de la matriz de mezcla de neutrinos, sino también para observar la violación de CP.

La medida de θ_{13} puede realizarse tanto con experimentos de neutrinos que usan aceleradores como con los que usan reactores nucleares. Sin embargo, la medida con aceleradores se ve muy limitada por los efectos de materia o por la degeneración del octante de θ_{23}. Por otra parte, los reactores nucleares son una fuente muy intensa y pura de antineutrinos electrónicos, lo que los hace convenientes para el estudio de las propiedades de estas esquivas partículas. Una nueva generación de experimentos que usan reactores nucleares, Double Chooz (DC), Daya Bay y RENO, ha sido capaz de proporcionar una determinación inequívoca de θ_{13}. La clave de estos experimentos recae en la desaparición de los $\bar{\nu}_e$ al cabo de cierta distancia y en la comparación del flujo observado entre los detectores cercano y lejano, idénticos entre sí, lo que permite reducir las incertidumbres sistemáticas asociadas al flujo de $\bar{\nu}_e$ de los reactores y a la detección de dicho flujo. El detector cercano de Double Chooz

(ND), en funcionamiento desde diciembre de 2014, se encuentra a una distancia de 400 metros de los reactores y es capaz de medir la tasa de $\bar{\nu}_e$ antes de que tenga lugar la oscilación. Por su parte el detector lejano (FD), a 1050 metros de los reactores y en funcionamiento desde abril de 2011, está situado cerca del máximo de oscilación y detecta la desaparición de estos neutrinos.

El objetivo principal de esta tesis se centra en mostrar la medida de θ_{13} más precisa del experimento Double Chooz usando 865 días de datos tomados, por primera vez, con los dos detectores, gracias a un aumento de la estadística y a una reducción considerable de los errores sistemáticos. La mejora de este valor se basa en la geometría del experimento (distribución de los detectores con respecto a los reactores), que facilita que los detectores vean la misma proporción de flujo de los reactores, y en una nueva técnica de detección, llamada Captura Total de neutrones o Total neutron Capture (TnC).

Este nuevo método de detección de $\bar{\nu}_e$ integra simultáneamente sobre las capturas de neutrones en núcleos de Gadolinio e Hidrógeno, procedentes de la interacción de los neutrinos en todo el volumen centellador del detector. La técnica TnC proporciona grandes ventajas sobre cualquier otro método de detección que dependa únicamente de la captura en un solo isótopo. En primer lugar aumenta el volumen efectivo de detección con el consiguiente aumento de la estadística, y provoca una disminución de la incertidumbre sistemática asociada a la detección, puesto que no hay necesidad de hacer una distinción entre los posibles isótopos que pueden capturar los neutrones ni tampoco hay que considerar las complejas corrientes de neutrones entre los diferentes volúmenes de los detectores. La determinación de los errores sistemáticos de detección es uno de los objetivos específicos de esta tesis.

Uno de los desafíos que surgen en este nuevo análisis es el control del elevado número de coincidencias accidentales, dominantes en el canal de H, el cual se lleva a cabo gracias a una Red Neuronal Artificial. Esta variable se aprovecha del hecho de que la distribución de la energía así como la coincidencia espacial y temporal de las señales de la interacción de neutrinos son diferentes entre la muestra de fondo accidental y la muestra de antineutrinos. Con esta herramienta, la proporción de señal sobre fondo está en torno a 10 en el FD y a 22 en el ND, al mismo tiempo que la eficiencia de selección de $\bar{\nu}_e$ se mantiene alrededor del 85%.

Una vez que se ha realizado la selección de $\bar{\nu}_e$, se observa un déficit en el número de candidatos de neutrinos con respecto al que se había predicho. De esta forma, se interpreta que dicho déficit surge debido a la oscilación de los neutrinos.

En el marco del análisis de las oscilaciones de neutrinos, la medida del ángulo de mezcla θ_{13} se realiza por medio de dos métodos diferentes. El primero, llamado Modulación de la Tasa del Reactor o Reactor Rate Modulation, se basa en la clasificación de las interacciones de neutrinos en función de las distintas configuraciones de la potencia de los reactores. Además, este análisis permite realizar una medida directa del fondo de manera independiente. El segundo objetivo específico de este documento consiste, pues, en la realización de un ajuste global tanto a la amplitud de oscilación como a la tasa de fondo por medio del análisis de los candidatos seleccionados para diferentes potencias de los reactores.

El segundo método de análisis permite una medida del ángulo a partir de la comparación de los neutrinos observados con los esperados en caso de no oscilación, considerando para ello tanto la forma del espectro como la tasa de candidatos (ajuste

Rate+Shape de los datos sobre el Monte Carlo (MC)) o a partir de la comparación directa de los datos del detector lejano con el cercano (ajuste de los datos del FD sobre los datos del ND). Este análisis se basa en que la probabilidad de oscilación, causada por un valor distinto de cero de θ_{13}, depende de la energía del neutrino incidente.

El ajuste Rate+Shape de los datos sobre la predicción del MC, medida de θ_{13} de referencia en Double Chooz, proporciona un valor de $\text{sen}^2(2\theta_{13}) = 0.105 \pm 0.014$. Existe una diferencia visible entre la predicción y los datos en torno a la región de energía de 5 MeV que no se explica por medio de la oscilación y que las incertidumbres del modelo no son capaces de cubrir. Debido a esto, la predicción de MC ha sido puesta en entredicho, ya que la discrepancia ha sido observada por todos los experimentos de reactores. Sin embargo, tanto la medida de DC de θ_{13} como sus errores son inmunes a esta distorsión del espectro. Prueba de ello es el ajuste de datos sobre datos, llevado a cabo a partir de la comparación del espectro observado por el FD con la predicción extraída a partir del espectro del ND. El valor que se obtiene de esta forma, $\text{sen}^2(2\theta_{13})=0.103\pm0.017$, está en perfecto acuerdo con el resultado principal.

El mejor valor extraído con el ajuste del Reactor Rate Modulation es $\text{sen}^2(2\theta_{13}) = 0.095 \pm 0.016$, resultado competitivo y consistente dentro de 1σ con los obtenidos usando el ajuste Rate+Shape.

Para concluir, los resultados mostrados en esta tesis se corresponden con la medida más precisa de θ_{13} llevada a cabo por el experimento Double Chooz hasta la fecha. Se ha explotado por primera vez la configuración FD y ND, consiguiendo una gran reducción de los errores sistemáticos asociados a la predicción del flujo del reactor y a la detección de antineutrinos, gracias a la configuración geométrica del experimento y a una nueva técnica de detección.

Chapter 1

Neutrino Physics

1.1 Introduction

This chapter is focused on the discussion about the neutrally charged particles called neutrinos, introducing its discovery and the long journey made to understand these particles and the main purpose of this thesis, the oscillation phenomena, both in a theoretical and experimental way.

Section 1.2 describes the neutrino particle discovery. The properties of the neutrinos in the context of the Standard Model of Particle Physics are discussed in section 1.3 and the problem concerning the nature of the neutrino and the absolute neutrino mass determination in section 1.4. The current state of the art regarding the measurement of the oscillation parameters and the leading experiments involved in the field are detailed in sections 1.5 and 1.6. Finally section 1.7 lists the open questions related to neutrino properties, for instance the CP violation in the neutrino sector, the mass ordering or the existence of sterile neutrinos, and the future efforts that will be carried through by the neutrino community to answer them.

1.2 Neutrino Discovery

Neutrino history dates back to 1914, starting with the study of the nuclear beta decay by James Chadwick [1], process in which a radioactive nucleus decays into a lighter nucleus and a electron. In principle the kinetic energy of the two-body product should be fixed but the observations showed a continuous electron energy spectrum, violating the energy conservation law. Fortunately a new interpretation emerged, assuming that an additional particle was participating in the decay, carrying part of the electron energy. This school of thought was favored by Wolfgang Pauli, who postulated in 1930 a new particle, called "neutron", with spin-1/2 to conserve angular momentum, neutrally charged to ensure charge conservation and much lighter than a proton, that would restore the energy conservation [2].

As Pauli wrote in his letter "I have done something very bad today by proposing

a particle that cannot be detected; it is something no theorist should ever do", it seemed impossible to find a way to test his theory and the proposal had very little support, even less when Chadwick discovered in 1932 a second constituent of the atomic nucleus, which he named neutron due to its neutral electric charge [3]. However two years latter, Enrico Fermi developed a theory for the β-decay, in which he considered a third particle that was also liberated in the process (eq. 1.1) and he called it neutrino remarking that should be tiny [4].

$$\begin{aligned} \beta^+ \text{ decay: } & p \rightarrow n + e^+ + \nu \\ \beta^- \text{ decay: } & n \rightarrow p + e^- + \bar{\nu} \end{aligned} \tag{1.1}$$

The great success of Fermi's theory fell on the explanation of the inverse beta decay process (IBD), in which an antineutrino collides with a proton, producing a positron and a neutron ($\bar{\nu} + p \rightarrow n + e^+$). This way Fermi's theory provided, at least in paper, a manner to detect neutrinos and verify their existence.

Shortly after Fermi proposed his theory, Hans Bethe and Rudolf Peierls calculated the neutrino interaction probability with the matter through the inverse beta decay. Their study concluded that a target made of lead with a thickness about one light year was necessary to get only one neutrino interaction, i.e. an interaction cross-section of less than 10^{-44} cm^2, so the detection of neutrinos was long thought impossible [5]. But as Peierls commented 50 years later, they were not aware for "the existence of nuclear reactors (or particle accelerators) producing neutrinos in vast quantities".

In their first attempt to detect neutrinos in 1953, under the experiment Poltergeist, Clyde Cowan and Fred Reines used a new detection technology, a liquid scintillator counter, to detect the products of the inverse β-decay. The detector was placed near a plutonium reactor in Hanford, Washington, and looked for the characteristic pulses of the positron annihilation and the neutron capture on hydrogen nuclei of the liquid scintillator. The experiment found an excess of events that was consistent with the prediction of neutrino interactions but it only had a signal-to-background ratio of $\sim$0.2 [6]. After this experience, Cowan and Reines modified the detector including a cadmium-water target to increase the neutron capture cross-section, allowing to distinguish in a better way the real signal from the possible background contamination. Located in the Savannah River Plant, South Carolina, the detector worked during 900 hours with the reactor on and 250 hours being the reactor off, achieveing an estimation of the background rate. Finally in 1956, the experiment observed a neutrino signal in $\sim$5% agreement with the neutrino cross-section prediction and with a signal-to-background ratio of 3/1 [7]. The neutrino had been finally detected.

1.3 Neutrinos in the Standard Model

The Standard Model of Particle Physics (SM) is a set of theories that describes the three fundamental interactions (strong, electromagnetic and weak forces) and their effects on the elementary particles. The SM is based on the local gauge group $SU(3) \times SU(2) \times U(1)$, where color $SU(3)$ corresponds to quantum chromodynamics (QCD), $SU(2)$ belongs to weak isospin and $U(1)$ to the hypercharge group.

The SM describes the physics of the elementary particle with high precision. Elementary particles are described as localized wave functions propagating through space-time that interact each other through four types of fundamental interactions (forces), i.e. gravitational, weak, electromagnetic and strong forces, ordered from the weakest to the strongest force. The magnitude of these forces in this order is approximately $10^{-39} : 10^{-6} : 10^{-2} : 1$, although it depends on the energy scale.

In figure 1.1 all the particles included in the SM are shown, classified into three main categories: matter particles, gauge particles and the particle associated to the mechanism of matter generation, the Higgs Boson. The matter particles, known as fermions, are divided into two categories: quarks and leptons. Leptons only interact through the electromagnetic or the weak force, while quarks are also sensitive to the strong force. These fermions are grouped into 3 generations of 2 particles each one, with similar properties like identical way of interaction but different masses and flavour quantum numbers. Moreover each particle of the fermion group has associated an antiparticle, i.e. a particle with same characteristics but opposite electric charge. If the particle has neutral charge, then there is the possibility that the particle coincides with its antiparticle. This is called Majorana particle. On the contrary, if the particle differs from its antiparticle, it is known as Dirac particle.

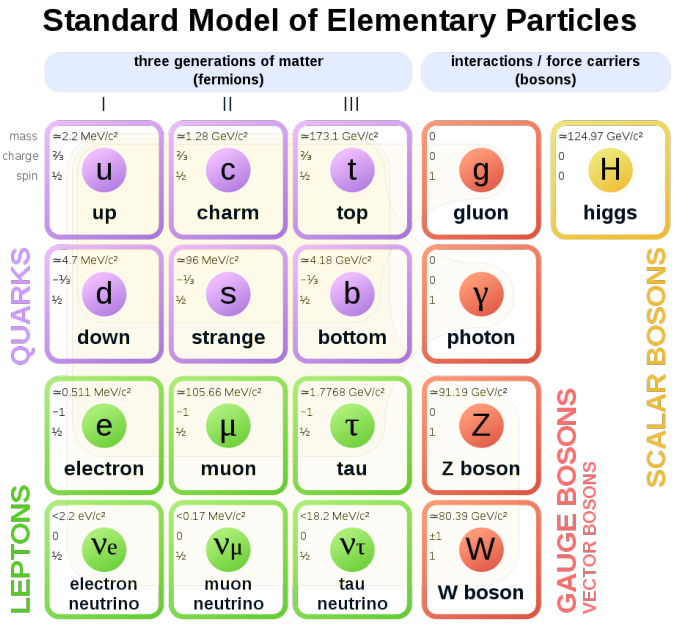

Figure 1.1: Elementary particles in the Standard Model. From [8].

Fermions are also grouped in weak isospin doublets, corresponding to left-handed fields (ψ_L) and weak isospin singlets if they are particles with right-handed chirality states (ψ_R).

The next group of figure 1.1 contains the gauge bosons, in charge of transmitting the interactions across the matter particles. Gluons are the mediator particle of the strong interaction, the electromagnetic interaction is carried out by photons and the weak interaction by the W and Z bosons.

Last but not least there is the Higgs boson, which generates the particle mass.

Fermions are allowed to acquire mass through the so called Higgs mechanism [9]. This mechanism is known as spontaneous symmetry breaking and couples the right-handed singlets with the left-handed doublets via the Yukawa interaction with the Higgs field:

$$\mathcal{L}_{\text{mass}} = -M_D \left(\bar{\psi}_R \psi_L + \bar{\psi}_L \psi_R\right) \tag{1.2}$$

being the Dirac mass of the ψ fermion $M_D = \frac{1}{\sqrt{2}} y^{\psi} v$, where y^{ψ} is the Yukawa coupling constant and v is the vacuum expectation value of the Higgs field (246 GeV).

In the Standard Model, neutrinos and their corresponding antineutrinos are fermions, specifically leptons of spin $1/2$, electrically neutrals, so they only interact via weak interactions. There are three neutrino generations, each serving as the partner of one of the three charged leptons:

$$\begin{pmatrix} e \\ \nu_e \end{pmatrix} \begin{pmatrix} \mu \\ \nu_\mu \end{pmatrix} \begin{pmatrix} \tau \\ \nu_\tau \end{pmatrix} \tag{1.3}$$

Since the observed neutrinos are only left-handed (or the antineutrinos only right-handed), they are not allowed to acquire mass through the Higgs mechanism and they are considered as massless particles. Moreover to conserve the lepton number in the SM, neutrinos cannot change their flavours during their propagation. However, due to the phenomenon of neutrino flavor oscillations observed by several neutrino experiments, neutrinos can turn into another flavour and thus must have mass. This way neutrinos are the first hint for new physics beyond the Standard Model and their study could lead to an extension of this theory.

1.4 Neutrino Mass

As seen in previous section, the SM requires an extension to accommodate massive neutrinos. Three possible mechanisms of mass generation are described.

1.4.1 Dirac mass

The addition of neutrino fields with right-handed chirality ν_R allows the formulation of a Dirac mass term for neutrinos following equation 1.2:

$$\mathcal{L}_{Dirac} = -m_D \bar{\nu}\nu = -\frac{y^{\nu} v}{2} \left(\bar{\nu}_L \nu_R + \bar{\nu}_R \nu_L\right) \tag{1.4}$$

Taking into account that the upper limit for the neutrino mass is roughly 2 eV, the neutrino Yukawa coupling constant needs to be of the order of 10^{-11}, which is too small compared with the Yukawa coupling constant for the electron, the next lightest fermion, five orders of magnitude larger. This suggests that a different mechanism controls the neutrino mass generation.

1.4.2 Majorana mass

From the fact that the neutrinos do not have electromagnetic charge and considering no lepton number conservation, a Majorana mass term can be constructed:

$$\mathcal{L}_{Majorana} = -\frac{m_M}{2}\left(\bar{\nu}_R(\nu_R)^C + (\bar{\nu}_R)^C\nu_R\right) \tag{1.5}$$

where $(\nu_R)^C = C\bar{\nu}_R^T$ is the charge-conjugated field and is left-handed and m_M is the Majorana mass.

This process violates lepton number conservation by two units, being not contemplated in the SM, and it is independent of the symmetry breaking, offering a possible explanation of the smallness neutrino mass.

1.4.3 See-saw mechanism

One of the most popular models for the neutrino mass generation is the so-called see-saw mechanism, postulated by H. Fritzsch, M. Gell-Mann and P.Minkowski [10],[11]. In this mechanism, the most general neutrino mass is written as a mix of Dirac and Majorana terms:

$$\begin{aligned}\mathcal{L}_{D+M} &= -m_D\left(\bar{\nu}_L\nu_R + \bar{\nu}_R\nu_L\right) - \frac{m_M}{2}\left(\bar{\nu}_R(\nu_R)^C + (\bar{\nu}_R)^C\nu_R\right) \\ &= -\frac{1}{2}\begin{pmatrix}(\bar{\nu}_L)^C & \bar{\nu}_R\end{pmatrix}\begin{pmatrix}0 & m_D\\ m_D & m_M\end{pmatrix}\begin{pmatrix}\bar{\nu}_L\\ (\nu_R)^C\end{pmatrix} + h.c.\end{aligned} \tag{1.6}$$

When the mass matrix $\begin{pmatrix}0 & m_D\\ m_D & m_M\end{pmatrix}$ is diagonalized, the eigenvalues can be extracted as $\frac{1}{2}\left(m_M \pm \sqrt{m_M^2 + 4m_D^2}\right)$. Since m_D derives from the electroweak symmetry breaking, it should be closer to the energy scale of this process, that is ∼100 GeV. On the contrary, m_M is not linked to the EW symmetry breaking scale, being able to acquire any value, in particular $m_M >> m_D$. This way the two eigenvalues can be approximated by:

$$m_{\text{light}} \approx \frac{m_D^2}{m_M} \tag{1.7}$$

$$m_{\text{heavy}} \approx m_M \tag{1.8}$$

This mechanism is beyond the SM because it involves the observed light left-handed neutrino but also a very heavy right-handed neutrino, not allowed in the SM. This process starts with a left-handed neutrino colliding with the Higgs boson and acquiring a mass m, comparable to the mass of other quarks and leptons. Then the neutrino turns into a right-handed neutrino, much heavier than the neutrino allowed by the energy conservation law. However, the Heisenberg uncertainty principle admits this circumstance for a short time interval and once this interval passed, the particle transforms back into a left-handed neutrino with mass $m_{\text{light}} << M_D^{\text{fermion}}$ by colliding with the Higgs boson again.

The Dirac or Majorana nature of the neutrino is not yet known. Experimentally this can be tested through process that violate the total lepton number by two units, like the neutrinoless-double beta decay, described in section 1.4.4.2. On the other

hand the absolute mass of the neutrinos can be deduced from the conservation of momentum and energy in weak interactions, a direct process summarized in section 1.4.4.1.

1.4.4 Experimental seaches for neutrino mass

Neutrino oscillations physics is only sensitive to the squared mass differences ($\Delta m^2_{ij} = m^2_i - m^2_j$). It is crucial that these experiments are able to distinguish very small energy differences to be sensitive to the tiny value of the neutrino mass (see fig. 1.2). However oscillation experiments are unfortunately insensitive to the absolute scale of neutrino masses, they can only provide a lower limit. Thus other type of projects are needed.

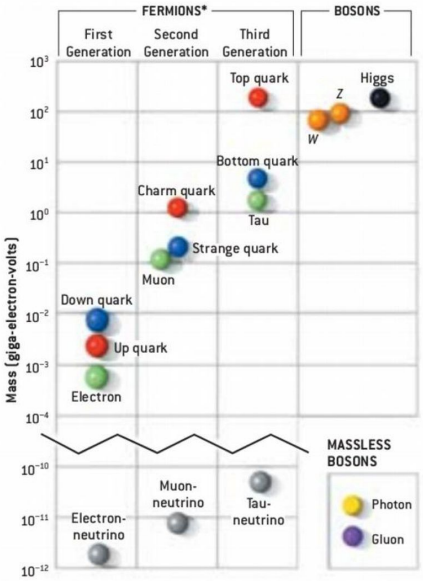

Figure 1.2: Masses of known elementary particles, assuming a normal ordering for neutrino masses. Image from [12].

1.4.4.1 Beta-decay experiments

Up to now, the most direct method to determine the absolute neutrino mass is through the β-decay process. This method consists of the measurement of the energy spectrum of the β-decay near the endpoint of the electron spectrum. If the neutrino is massive, then the endpoint energy would be lower than expected and the difference will become the neutrino mass, as remarked in figure 1.3. Unfortunately this is extremely challenge and due to the electron energy resolution of nowadays experiments, it is only possible to estimate an upper limit.

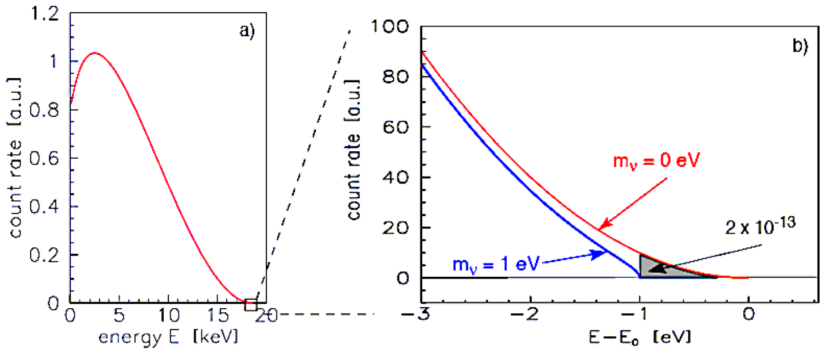

Figure 1.3: Left: Electron energy spectrum in β-decay. Right: Endpoint of the spectrum assuming a non-zero neutrino mass (in blue) opposite to the massless neutrino (in red). Image from [13].

The element chosen in the past for this purpose is the gaseous tritium, which decays as $^3\mathrm{H} \rightarrow ^3\mathrm{He} + e^- + \bar{\nu}_e$, due to the unusually low energy released in the decay and the simplicity of the final state elements. The Mainz experiment (in Germany) and Troitsk (in Russia), which used a Magnetic Adiabatic Collimation with an Electrostatic Filter (MAC-E) as spectrometer, provided an upper limit on the mass of the electron neutrino of $m_{\nu_e} < 2.3$ eV in the case of Mainz [14] and $m_{\nu_e} < 2.05$ eV from the Troitsk experiment with a 95% confidence level [15].

Currently there are several projects that aim to decrease the limit on the neutrino mass in the near future. The KATRIN experiment has recently started operations using molecular tritium T_2 and expects to reach a sensitivity of 0.2 eV after 3 beam years [16]. Another experiment is Project-8, which will use the Cyclotron Radiation Emission Spectroscopy (CRES) and tritium in its atomic phase, that expects to achieve a sensitivity of $m_{\nu_e} \lesssim 40$ meV with an exposure of $10 - 100$ m^3 years [17].

Using a different element, the decay of ^{163}Ho ($^{163}\mathrm{Ho} + e^- \rightarrow ^{163}\mathrm{Dy}^* + \nu_e$), two collaborations HOLMES and ECHo [18] will try to determine the value of m_{ν_e} also through observations of the endpoint of the electron capture decay. They expect to reach a sensitivity of $m_{\nu_e} \lesssim 1$ eV and $m_{\nu_e} \lesssim 1.5$ eV respectively. Taking into account that the current upper limit using this isotope is 225 eV [19], there will be a high improvement if these results are achieved.

1.4.4.2 Neutrinoless Double Beta-decay

The neutrinoless double beta decay is a hypothetical very rare nuclear event, forbidden in the Standard Model, in which two neutrons suffer β-decay simultaneously and contrary to what happens in the equation 1.1, there is no emission of neutrinos. This process is only allowed if neutrinos are Majorana particles [20], i.e the neutrino is its own antiparticle, since lepton number is not conserved through the decay (in the initial state $l = 0$ and in the final state $l = 2$). This neutrinoless mode ($0\nu\beta\beta$) was first proposed by Wendell H. Furry in 1939 [21] as a method to test Majorana's theory applied to neutrinos.

However this transition is energetically possible only for 35 nuclei, of which only a few are experimentally relevant: ^{82}Se, ^{76}Ge, ^{100}Mo, ^{130}Te and ^{136}Xe. The experiments looking for the $0\nu\beta\beta$ aim to measure the half-life time $T^{0\nu}_{1/2}$ of the decay, which

is related to the effective Majorana mass $m_{\beta\beta}$ through:

$$\frac{1}{T^{0\nu}_{1/2}} = G^{0\nu}|M^{0\nu}|^2 \left(\frac{|m_{\beta\beta}|}{m_e}\right)^2 \tag{1.9}$$

where $G^{0\nu}$ is the phase space factor, $M^{0\nu}$ is the nuclear matrix element of the 0ν process and m_e is the electron mass.

The strongest constraints until date on the half-life for different isotopes are listed in table 1.1.

Table 1.1: Half-live $T^{0\nu}_{1/2}$ for different isotopes obtained recently by $0\nu\beta\beta$ experiments.

Experiment	Isotope	$T^{0\nu}_{1/2}$ (yr.)	$m_{\beta\beta}$ (meV)
Gerda [22]	^{76}Ge	$> 8 \times 10^{25}$	120-260
CUPID-0 [23]	^{82}Se	$> 2.4 \times 10^{24}$	376-770
CUORE [24]	^{130}Te	$> 1.5 \times 10^{25}$	110-520
KamLAND-Zen [25]	^{136}Xe	$> 1.07 \times 10^{26}$	45-160

The Majorana effective mass can be also represented as a function of the lightest neutrino mass, taking into account the current values of mixing parameters assuming only the 3 neutrino flavours shown in eq. 1.3. Looking at figure 1.4, it can be seen that the value of $m_{\beta\beta}$ depends on the mass ordering only if $m_{lightest} < 40$ meV. Considering the values of $m_{\beta\beta}$ from table 1.1, it can be deduced that current neutrinoless double beta decay experiments cannot determine the neutrino mass ordering. But if future generation of experiments are able to test a smaller limit of $m_{\beta\beta}$, they will be able to determine the mass ordering if this is normal and $m_{lightest} < 10$ meV.

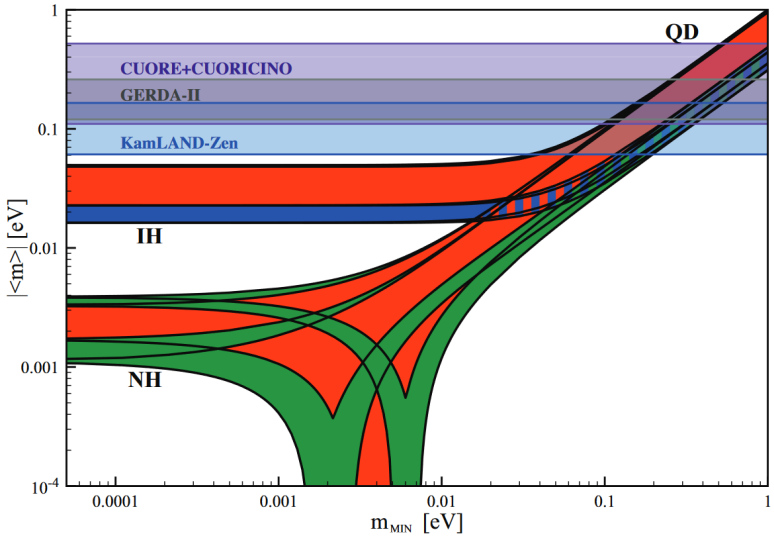

Figure 1.4: Effective Majorana neutrino mass as a function of the lightest neutrino mass in the two cases of normal and inverted ordering. The shaded areas correspond to the 2σ regions due to error propagation of the uncertainties on the oscillation parameters. Image from [46].

This scenario changes if neutrinos are Dirac particles, since there is not this kind of restrictions then for an inverted ordering scheme. In the same way, if there are sterile neutrinos (m_{ν_s} ~1 eV), explained in more detail in section 1.7.4, the allowed bands are located at higher $m_{\beta\beta}$ [26].

1.4.4.3 Cosmology

The cosmological mass is defined as the sum of the three active neutrino masses $\sum m_\nu = m_{\nu_1} + m_{\nu_2} + m_{\nu_3}$, since there is a close connection between the neutrino masses measurements obtained in the laboratory and those probed by cosmological observations. The most constraining cosmological upper bound come from the Planck satellite, which combine the Cosmic Microwave Background (CMB) observations including lensing, temperature and polarization constraints with measurements of the Barionic Acustic Oscillation (BAO) scale, achieving $\sum m_\nu$<0.12 eV (95%, Planck TT,TE,EE+lowE+lensing+BAO) [27].

1.5 Neutrino Oscillations

Neutrino oscillations are a quantum effect predicted by Bruno Pontecorvo in 1957 [28] that arises from the fact that the neutrino weak interaction eigenstates could differ from the mass eigenstates due to the neutrino non-zero mass. This way one neutrino created with a specific lepton flavour (electron, muon or tau) can be measured with a different flavour after traveling some distance. In a mathematical mode each neutrino flavour eigenstate $|\nu_\alpha\rangle$ is the coherent superposition of the mass eigenstates $|\nu_i\rangle$:

$$|\nu_\alpha\rangle = \sum_i^n U^*_{\alpha i}|\nu_i\rangle \tag{1.10}$$

where α denotes the three neutrino flavours (e, μ, τ). Assuming that there are only these three flavours participating in the mixing, the conversion between the bases is expressed by the 3x3 unitary matrix U_{PMNS}, called like this for Pontecorvo, Maki, Nakagawa, and Sakata [29]:

$$\begin{aligned} U_{\text{PMNS}} &= \begin{pmatrix} U_{e1} & U_{e2} & U_{e3} \\ U_{\mu 1} & U_{\mu 2} & U_{\mu 3} \\ U_{\tau 1} & U_{\tau 2} & U_{\tau 3} \end{pmatrix} \\ &= \begin{pmatrix} 1 & 0 & 0 \\ 0 & c_{23} & s_{23} \\ 0 & -s_{23} & c_{23} \end{pmatrix} \begin{pmatrix} c_{13} & 0 & s_{13}e^{-i\delta_{CP}} \\ 0 & 1 & 0 \\ -s_{13}e^{i\delta_{CP}} & 0 & c_{13} \end{pmatrix} \begin{pmatrix} c_{12} & s_{12} & 0 \\ -s_{12} & c_{12} & 0 \\ 0 & 0 & 1 \end{pmatrix} \end{aligned} \tag{1.11}$$

where $c_{ij} = \cos\theta_{ij}$, $s_{ij} = \sin\theta_{ij}$ and δ_{CP} is a phase that could lead to a CP non conservation in the neutrino mixing.

1.5.1 2 flavour case

In the 2 flavour case, the rotation between flavour and mass states reduces to:

$$\begin{pmatrix}\nu_\alpha\\ \nu_\beta\end{pmatrix} = \begin{pmatrix}\cos\theta & \sin\theta\\ -\sin\theta & \cos\theta\end{pmatrix}\begin{pmatrix}\nu_1\\ \nu_2\end{pmatrix} \tag{1.12}$$

and

$$\begin{aligned}\nu_\alpha(t) &= \cos\theta\nu_1(t) + \sin\theta\nu_2(t)\\ \nu_\beta(t) &= -\sin\theta\nu_1(t) + \cos\theta\nu_2(t)\end{aligned} \tag{1.13}$$

Following Schroedinger equation:

$$i\frac{\partial\nu_k(t)}{\partial t} = E_k\nu_k \Rightarrow \nu_k(t) = \nu_k(0)e^{-iE_kt/\hbar} \tag{1.14}$$

Having into account that at time $t = 0$, $\nu_\alpha = 1$ and $\nu_\beta = 0$ and inverting equation 1.13, this leads to:

$$\begin{aligned}\nu_1(0) &= \cos\theta\\ \nu_2(0) &= \sin\theta\end{aligned} \tag{1.15}$$

$$\tag{1.16}$$

So equation 1.14 can be rewritten as:

$$\begin{aligned}\nu_1(t) &= \cos\theta e^{-iE_1t/\hbar}\\ \nu_2(t) &= \sin\theta e^{-iE_2t/\hbar}\end{aligned} \tag{1.17}$$

From this last equation and also equation 1.13, the transition amplitude $A(\nu_\alpha \to \nu_\alpha)$ is defined as:

$$A(\nu_\alpha \to \nu_\alpha) = \cos^2\theta e^{-iE_1t/\hbar} + \sin^2\theta e^{-iE_2t/\hbar} \tag{1.18}$$

And the survival probability, defined as $|A(\nu_\alpha \to \nu_\alpha)|^2$:

$$\begin{aligned}P(\nu_\alpha \to \nu_\alpha) &= \left(\cos^2\theta e^{-iE_1t/\hbar} + \sin^2\theta e^{-iE_2t/\hbar}\right)\left(\cos^2\theta e^{+iE_1t/\hbar} + \sin^2\theta e^{+iE_2t/\hbar}\right)\\ &= 1 + \sin^2\theta\cos^2\theta\left[-2 + 2\cos\left(\frac{E_2 - E_1}{\hbar}t\right)\right]\\ &= 1 + \frac{\sin^2 2\theta}{2}\left[-1 + \cos\left(\frac{E_2 - E_1}{\hbar}t\right)\right]\\ &= 1 - \frac{\sin^2 2\theta}{2}\left[1 - \cos^2\left(\frac{E_2 - E_1}{2\hbar}t\right) + \sin^2\left(\frac{E_2 - E_1}{2\hbar}t\right)\right]\\ &= 1 - \sin^2 2\theta\sin^2\left(\frac{E_2 - E_1}{2\hbar}t\right)\end{aligned} \tag{1.19}$$

Considering that neutrinos involved in oscillation experiments are ultrarelativistic and they propagate with the same momentum p ($E \simeq p \gg m$), the following approximation can be made:

$$E_i = \sqrt{(p_ic)^2 + (m_ic^2)^2} \simeq pc + \frac{m_i^2c^4}{2p} \simeq E + \frac{m_i^2c^4}{2E} \tag{1.20}$$

And equation 1.19, substituting that during a time t the neutrino travels a distance $L = ct$, can be expressed as:

$$P(\nu_\alpha \to \nu_\alpha) = 1 - \sin^2 2\theta \sin^2 \left(\frac{\Delta m^2 c^4 L}{4\hbar c E} \right) \tag{1.21}$$

Finally if the neutrino energy E units are MeV, the term $\Delta m^2 c^4$ is expressed in eV, the distance L in meters and $\hbar c = 197$ fm×MeV, equation 1.21 is rewritten as:

$$P(\nu_\alpha \to \nu_\alpha) = 1 - \sin^2 2\theta \sin^2 \left(\frac{1.27 \Delta m^2 L}{E} \right) \tag{1.22}$$

If neutrinos were massless or had exactly the same mass without regard flavours, $P(\nu_\alpha \to \nu_\alpha)$=1 (i.e. no oscillation). Then, neutrino oscillations take place only if neutrinos have mass.

On the other hand, the transition probability can be simply deduced from equation 1.21 as:

$$P(\nu_\alpha \to \nu_\beta) = 1 - P(\nu_\alpha \to \nu_\alpha) \tag{1.23}$$

1.5.2 3 flavour case

Considering now the 3 neutrino flavours (e, μ and τ), the time evolution of an initial pure α-flavoured neutrino travelling in the vacuum is expressed as:

$$|\nu_\alpha(t)\rangle = \sum_j^3 U^*_{\alpha,j} e^{-i(E_j t - p_j L)} |\nu_j\rangle \tag{1.24}$$

Using equation 1.20, the mass eigenstante $|\nu_j\rangle$ can be written also as a function of the flavour eigenstate $|\nu_\beta\rangle$:

$$|\nu_\alpha(t)\rangle = \sum_{\beta=e,\mu,\tau} \left(\sum_j^3 U^*_{\alpha,j} e^{-i\frac{m_j^2}{2E}L} U_{\beta,j} |\nu_\beta\rangle \right) \tag{1.25}$$

The probability to observe a neutrino created with a specific flavour α with a difference favour after a distance L, can be written as:

$$\begin{aligned}
P(\nu_\alpha \to \nu_\beta) &= |\langle \nu_\beta | \nu_\alpha(L) \rangle|^2 = \left| \sum_j U^*_{\alpha,j} U_{\beta,j} e^{-i\frac{m_j^2}{2E}L} \right|^2 \\
&= \sum_{j,k} U^*_{\alpha,j} U_{\beta,j} U_{\alpha,k} U^*_{\beta,k} e^{-i(E_j - E_k)t} \\
&= \sum_{j,k} U^*_{\alpha,j} U_{\beta,j} U_{\alpha,k} U^*_{\beta,k} e^{-i\frac{\Delta m^2_{jk}}{2E}L} \\
&= \delta_{\alpha\beta} - 4 \sum_{j>k} \mathrm{Re}\left(U^*_{\alpha,j} U_{\beta,j} U_{\alpha,k} U^*_{\beta,k} \right) \sin^2 \left(\frac{\Delta m^2_{jk} L}{4E} \right) \\
&\pm 2 \sum_{j>k} \mathrm{Im}\left(U^*_{\alpha,j} U_{\beta,j} U_{\alpha,k} U^*_{\beta,k} \right) \sin \left(\frac{\Delta m^2_{jk} L}{2E} \right)
\end{aligned} \tag{1.26}$$

where the sign (+) in the imaginary part corresponds to the neutrinos case and the (-) to the antineutrinos case. If $\alpha = \beta$, this neutrino oscillation is known as survival probability, while if $\alpha \neq \beta$ is called transition probability. The oscillation frequency is proportional to the squared mass difference $\Delta m^2_{jk} = m^2_k - m^2_j$ and the oscillation amplitude is proportional to the PMNS matrix elements, $U_{\alpha,j}$.

Comparing equation 1.23 with equation 1.26, it can be appreciated that the general formulation for the oscillation probability in the three neutrino flavour scenario becomes more complex than the two flavour case, since it depends on imaginary part of $U_{\alpha,j}$.

The difference between the neutrino and antineutrino oscillation probability indicates CP violation which is expressed by:

$$\text{CP} = P(\nu_\alpha \to \nu_\beta) - P(\bar{\nu}_\alpha \to \bar{\nu}_\beta) = 4 \sum_{j>k} \text{Im}\left(U^*_{\alpha,j} U_{\beta,j} U_{\alpha,k} U^*_{\beta,k}\right) sin\left(\frac{\Delta m^2_{jk} L}{2E}\right) \tag{1.27}$$

Looking at the disappearance probability, one can see that the CP symmetry always holds:

$$P(\nu_\alpha \to \nu_\alpha) = 1 - 4 \sum_{j>k} |U_{\alpha,j}|^2 |U_{\alpha,k}|^2 \sin^2\left(\frac{\Delta m^2_{jk} L}{4E}\right) = P(\bar{\nu}_\alpha \to \bar{\nu}_\alpha) \tag{1.28}$$

Therefore, the CP violation effect should be searched for only in appearance measurements.

1.5.3 Matter effects

The oscillation probability shown in sections 1.5.1 and 1.5.2 corresponds to oscillations through vacuum. However when neutrinos pass through matter it is needed to take under consideration matter effects. During propagation, electron neutrinos ν_e in the Sun and in the Earth can interact via Neutral Current (NC) in which a Z^0 boson is exchanged or via Charge Current (CC), in which a $W^\pm$ is exchanged, while only NC reactions are possible for ν_τ and ν_μ.

In the case of electron neutrinos and antineutrinos, the CC interaction with the electrons in the surrounding matter medium induces a potential given by:

$$V_{CC} = \pm\sqrt{2} G_F N_e \tag{1.29}$$

where the sign (+) is for neutrinos and (-) for antineutrinos. G_F is the Fermi coupling constant and N_e is the electron density. In the case of the three flavours, the NC interactions with protons, neutrons and electrons induce the potential:

$$V_{NC} = \pm\frac{1}{2} G_F N_n \tag{1.30}$$

being again the sign (+) for neutrinos and (-) for antineutrinos. In this case the potential only depends on the neutron density, since the proton and electron density cancels each other. Due to these potentials, the mass eigenstates differ from the ones in vacuum, in the same way as the mixing angles.

In the two flavour case, the mixing angle involved in the ($\nu_e \rightarrow \nu_\mu$ transition is given by:

$$\tan 2\theta_m = \frac{\tan 2\theta}{1 \mp \frac{2\sqrt{2}EG_F N_e}{\Delta m^2 \cos 2\theta}} \tag{1.31}$$

where the sign (-) stands for neutrinos and the (+) for antineutrinos. Neutral current scattering contributes as a term which is equal for both flavours, thus disappearing. The squared mass difference is given by:

$$\Delta m^2_m = \sqrt{(\Delta m^2 \cos 2\theta \mp 2\sqrt{2}EG_F N_e)^2 + (\Delta m^2 \sin 2\theta)^2} \tag{1.32}$$

where again the sign (-) stands for neutrinos and the (+) for antineutrinos.

From equation 1.31, it can be observed that independently of how small could be θ, θ_m can give a maximal mixing angle ($\theta_m = \pi/4$) if the resonance condition is satisfied:

$$\cos 2\theta = \pm \frac{2\sqrt{2}EG_F N_e^{\text{res}}}{\Delta m^2} \tag{1.33}$$

This resonance constitutes the Mikheev-Smirnov-Wolfenstein (MSW) effect [30]. Thus, at a certain electron density N_e, ν_e ($\bar{\nu}_e$) could suffer an increased (decreased) transition to other flavours like ν_μ, leading to a suppressed (increased) electron neutrino flux with respect to the other two flavours.

1.6 Measurements of neutrino oscillations

Following the mathematical formalism of the oscillation effects in equations 1.10 and 1.11, neutrino oscillations are described by six parameters: three mixing angles, two mass squared differences and a CP violation phase factor. Thanks to past, nowadays and future neutrino experiments, these observables have been or will be measured. These experiments use neutrinos or antineutrinos produced by the Sun, by cosmic-ray interactions in the atmosphere, by accelerators and by nuclear reactors, being called solar, atmospheric, accelerator and reactor (anti)neutrinos respectively. The following section describes the state of the art of neutrino oscillations.

1.6.1 Measurement of θ_{12} and Δm^2_{21}

Oscillations in this sector were first observed by solar neutrino experiments. Neutrinos are produced in the Sun via fusion reactions, being the most frequency the *pp* chain whose net result is: $4\text{p}+2\text{e}^- \rightarrow {}^4\text{He}+2\nu_e+26.731$ MeV. The four processes involved in neutrino production are:

$$\begin{aligned}
\mathbf{pp} &: \text{p}+\text{p} \rightarrow \text{d} + e^+ + \nu_e \\
\mathbf{pep} &: \text{p} + e^- + \text{p} \rightarrow \text{d} + \nu_e \\
\mathbf{^7Be} &: {}^7\text{Be} + e^- \rightarrow {}^7\text{Li} + \nu_e \\
\mathbf{^8B} &: {}^8\text{B} \rightarrow 2({}^4\text{He}) + e^+ + \nu_e
\end{aligned} \tag{1.34}$$

The predicted spectra of the emitted neutrinos following the BS05(OP) model [31] are shown in figure 1.5. Taking this into consideration, Raymond Davis and John Bahcall designed in 1964 the first underground neutrino experiment, located in the Homestake mine at Lead (South Dakota), with the purpose of detecting neutrinos from the Sun. The detector consisted of 400000 litres of C_2Cl_4 and fell on the radiochemical production of ^{37}Ar from the following reaction:

$$\nu_e + {}^{37}\mathrm{Cl} \rightarrow e^- + {}^{37}\mathrm{Ar} \quad (\mathrm{E_{th}} = 814 \text{ keV}) \tag{1.35}$$

The number of detected neutrinos was deduced by counting the number of ^{37}Ar atoms present in the detector. After almost 30 years of data taking, the achieved result gave room to what was known as the "solar neutrino problem": the number of detected solar neutrinos were only one third of what the Standard Solar Model predicted.

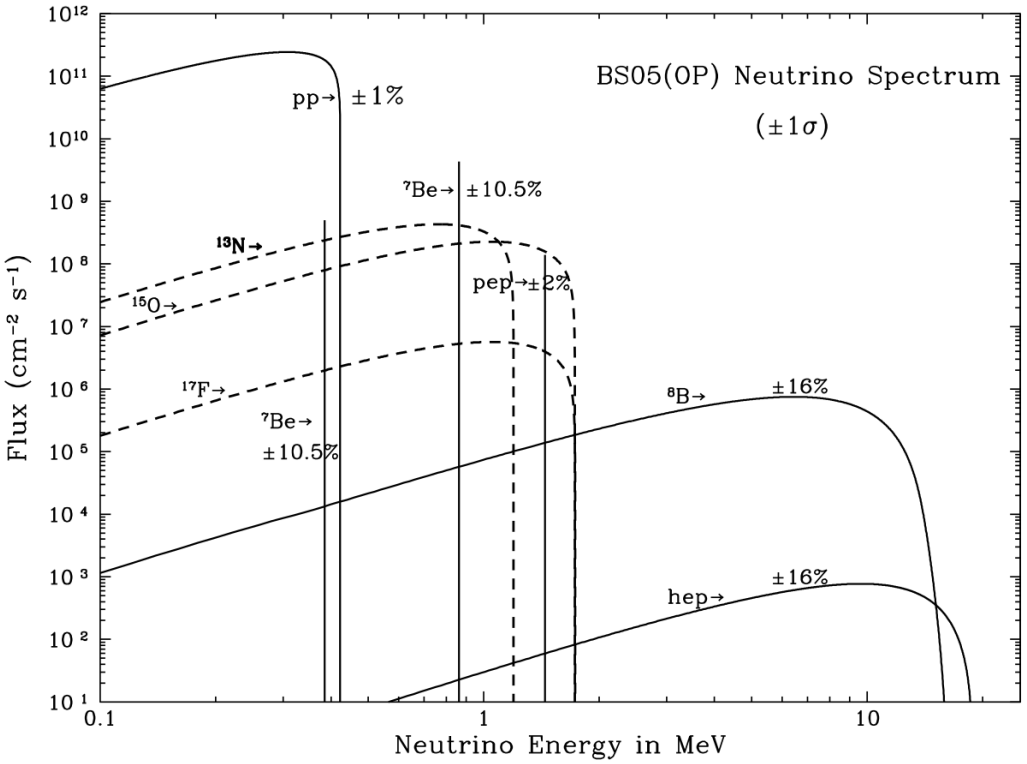

Figure 1.5: Predicted neutrino energy spectra for the neutrino fluxes emitted by the Sun according to the solar model BS05(OP). Percentages show the theoretical uncertainty. Image from [32].

Other experiments as GALLEX in the Gran Sasso Laboratory (Italy) or SAGE in the Baksan Neutrino Observatory (Russia), also measured a deficit of around 1/2 with respect to the prediction [33], [34]. They used ^{71}Ga as target (ν_e+^{71}Ga→ e^-+^{71}Ge) and, unlike Homestake experiment, they were able to measure neutrinos coming from the *pp* reaction due to its lower energy threshold.

In 1987 a new window was opened with the Kamiokande water-Cherenkov detector that allowed to measure neutrinos in time. Initially this experiment was designed to study the proton decay but it was later realized that it could be also used to detect solar neutrinos. Neutrinos coming from the Sun can elastically scatter on electron and the recoiled electron produces Cherenkov radiation that could be observed:

$$\nu_x + e^- \rightarrow \nu_x + e^- \tag{1.36}$$

This technique has two main advantages: the process is sensitive to the three neutrino flavours and it provides information about the neutrino incident direction thanks to the recoil electron direction. Nevertheless as Kamiokande [35] as its successor Super-Kamiokande (SK) [36] detected just 0.4 times what was predicted by the Solar Standard Model.

Finally the answer to the solar neutrino problem came from the SNO experiment (Sudbury Neutrino Observatory, Canada) in 2002. This experiment is based also in the Cherenkov technique but the difference with respect to SK falls on the use of heavy water (D_2O) instead of regular water (H_2O). Therefore the detector is able to detect not only the elastic scattering but also the charge current reaction (CC), equation 1.37, and the interactions with the deuterium D nucleus through the neutral current reaction (NC) that involves any neutrino flavour, following equation 1.38:

$$\nu_e + D \rightarrow e^- + p + p \text{ (CC)} \tag{1.37}$$
$$\nu_x + D \rightarrow \nu_x + p + n \text{ (NC)} \tag{1.38}$$

Therefore if SNO detected a non-zero muon and tau neutrino, this would imply a strong evidence of the process of neutrino oscillations since only electron neutrinos are generated in the Sun (eq. 1.34). The measured fluxes by the SNO collaboration are:

$$\phi^{\text{ES}}_{\text{SNO}} = (2.35 \pm 0.22 \text{ (stat)} \pm 0.15 \text{ (syst)}) \times 10^6 \text{cm}^{-2}\text{s}^{-1} \tag{1.39}$$
$$\phi^{\text{CC}}_{\text{SNO}} = (1.68 \pm 0.06 \text{ (stat)} \, ^{+0.08}_{-0.09} \text{ (syst)}) \times 10^6 \text{cm}^{-2}\text{s}^{-1} \tag{1.40}$$
$$\phi^{\text{NC}}_{\text{SNO}} = (4.94 \pm 0.21 \text{ (stat)} \, ^{+0.38}_{-0.34} \text{ (syst)}) \times 10^6 \text{cm}^{-2}\text{s}^{-1} \tag{1.41}$$

Moreover the individual flavour fluxes (e, μ, τ) can be extracted using the following system of equations:

$$\phi^{CC}_{\text{SNO}} = \phi^{\nu_e}_{\text{SNO}} \tag{1.42}$$
$$\phi^{NC}_{\text{SNO}} = \phi^{\nu_e}_{\text{SNO}} + \phi^{\nu_{\mu,\tau}}_{\text{SNO}} \tag{1.43}$$
$$\phi^{ES}_{\text{SNO}} = \phi^{\nu_e}_{\text{SNO}} + 0.1553 \times \phi^{\nu_{\mu,\tau}}_{\text{SNO}} \tag{1.44}$$

where 0.1553 is the ratio of the elastic scattering cross sections for the $\mu+\tau$ and electron flavours. These relations are illustrated in figure 1.6, where it can be appreciated that $\phi^{\nu_{\mu,\tau}}_{\text{SNO}} = (3.26 \pm 0.25 \text{ (stat)} \, ^{+0.40}_{-0.35} \text{ (syst)}) \times 10^6 \text{cm}^{-2}\text{s}^{-1}$.

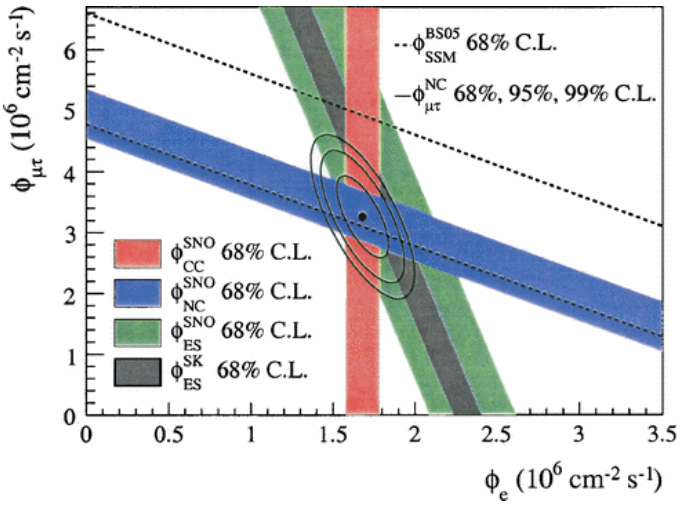

Figure 1.6: $\nu_\mu + \nu_\tau$ flux versus ν_e flux. CC (red), NC (blue), and ES (green) flux measurements are indicated by the filled bands. The elastic scattering from Super-Kamiokande result is shown as a dark band [37]. The point represents $\phi^{\nu_e}_{\rm SNO}$ from the CC flux and $\phi^{\nu_{\mu,\tau}}_{\rm SNO}$ from the NC-CC difference with 68, 95, and 99% C.L. contours included. From [38].

Results from SNO and the rest of solar neutrino experiments brought into the interpretation of the observed ν_e deficit as a consequence of neutrino oscillations and they are consistent with the LMA (large mixing angle) solution in which the squared mass difference is $\Delta m^2_{21} \sim 7.5 \times 10^{-5}$ eV^2 and $\sin^2 2\theta_{12} \sim 0.85$. However the SNO experiment alone could not restrict the LMA region, since there were other solutions like the SMA (small mixing angle) also compatible with the conclusion of solar experiments.

Later in 2008, the Borexino experiment, a 300-tons of ultra pure liquid scintillator detector, measured ^{7}Be solar ν_e and the pep ν_e, with energies of 862 keV and 1.4 MeV, respectively, by using neutrino-electron elastic scattering (eq. 1.36). This way the collaboration was able to measure the solar neutrino deficit around the low energy region $\sim$ 1 MeV (see figure 1.7), region where the oscillation probability is suppose to change due to matter effects and tested the MSW-LMA solution [39].

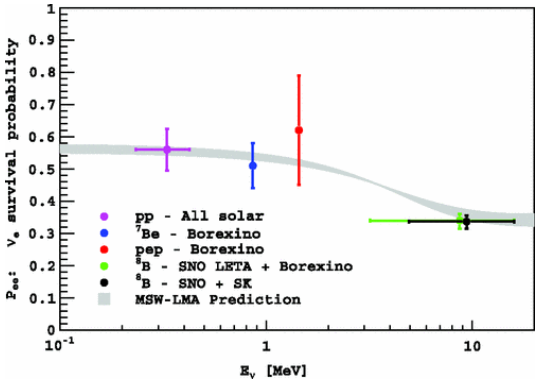

Figure 1.7: Electron neutrino survival probability as a function of energy. Grey band represents the 1σ MSW-LMA prediction. From [39].

Consequently in order to confirm the LMA region, a new experiment was designed in Japan. KamLAND is a 1 kton ultra-pure liquid scintillator detector located at the old Kamiokande's site and it is able to detect electron antineutrinos coming from the Japan nuclear reactors located at an average distance of 180 km. Due to the low energy of the emitted neutrinos ($\sim$ 4 MeV), this experiment is sensitive to a Δm^2_{21} range down to $\sim 10^{-5}$ eV^2. This way, a combined global analysis of the previous solar data and KamLAND results shows that the LMA is the unique solution to the solar neutrino problem with a confidence level greater than 5σ [40]. The best values are $\tan^2\theta_{12} = 0.436^{+0.029}_{-0.025}$ and $\Delta m_{21} = (7.53 \pm 0.18) \times 10^{-5}$ eV^2 (see fig. 1.8a). KamLAND observed not only the ν_e deficit, but also for the first time its periodic dependence with the neutrino energy expected from neutrino oscillations (see fig. 1.8b).

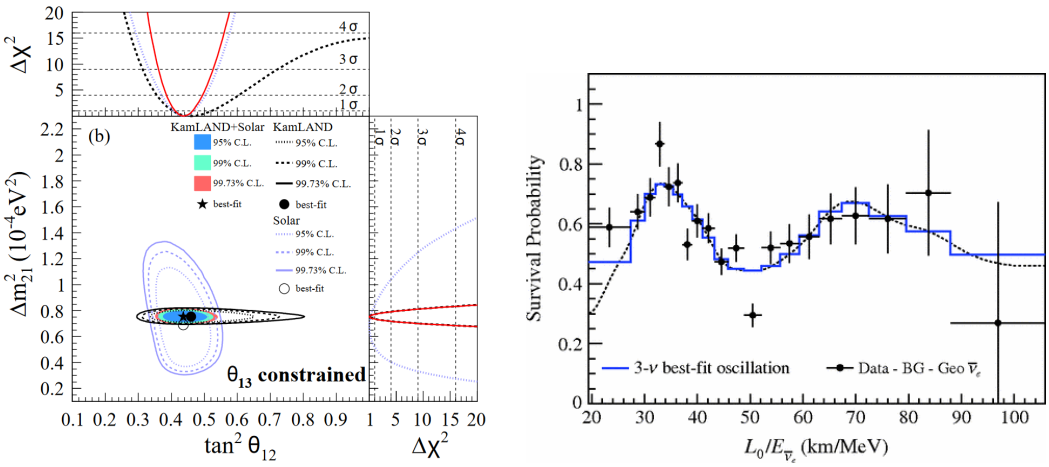

(a) (b)

Figure 1.8: (a) Allowed regions projected in the $(\tan^2\theta_{12}, \Delta m^2_{21})$ plane, for solar and KamLAND data from the three-flavour oscillations analysis. The shaded regions are from the combined analysis of the solar and KamLAND data. The side panels show the $\Delta\chi^2$ profiles projected into the $\tan^2\theta_{12}$ and Δm^2_{21} axes. (b) Ratio of the observed $\bar{\nu}_e$ spectrum to the expectation for no-oscillation versus L/E for the KamLAND data. Figure from [41].

It can be noted that there is a $\sim 2\sigma$ tension between the best-fit value of Δm^2_{21} given by the KamLAND experiment and the value obtained using global solar neutrino data [42], since solar experiments prefer lower value of Δm^2_{21}. On the other hand in terms of θ_{12}, there is consistency between KamLAND and global solar best-fit value.

1.6.2 Measurement of θ_{23} and Δm^2_{32}

The first measurement of Δm^2_{32} and θ_{23} has been performed mainly by using atmospheric neutrinos. These are produced by the decay of pions π and kaons K, caused by the interaction of cosmic rays in the high atmosphere:

$$\pi^{\pm} \rightarrow \mu^{\pm} + \nu_{\mu}(\bar{\nu}_{\mu}) \tag{1.45}$$

The resultant muons subsequently decay as:

$$\mu^{\pm} \rightarrow e^{\pm} + \bar{\nu}_{\mu}(\nu_{\mu}) + \nu_{e}(\bar{\nu}_{e}) \tag{1.46}$$

It is expected that the ratio between muon and electron neutrinos be 2:1. Since they come from the decay of heavier particles than the electron, the atmospheric neutrinos energy is higher than in the case of solar or reactor neutrinos, covering a range from a few MeV to several GeV.

As explained in previous section, Kamiokande had become a experiment to detect solar neutrinos using the Cherenkov technique. Atmospheric neutrinos constituted the irreducible background that did not allow to improve the limits of the proton half-life, so Kamiokande was also good at measuring them. Atmosferic neutrinos were detected as well by the IMB (Irvine-Michigan-Brookhaven) experiment, installed in a salt mine in Ohio. Both experiments reported an indication of atmospheric $\nu_{\mu} + \bar{\nu}_{\mu}$ deficit [43],[44]. It was not until 1998 that Super-Kamiokande had the first evidence of neutrino oscillations following the atmospheric neutrino disappearance [45].

The main goal of SK was not the quantity of atmospheric neutrinos detected, but the ratio between events due to muon and electron neutrinos. Since SK also use the Cherenkov method, the flavour of the produced lepton is identified by the sharpness and intensity of the Cherenkov ring and the position of this ring allows to determine the lepton direction, which is correlated to the neutrino direction. Therefore they observed that this ratio was 2:1 as they expected only when the neutrinos fell upon the vertical direction but there was a significant zenith-angle dependent deficit of μ-like events. Latest results of SK are shown in figure 1.9. There are twice more μ-like events going downward than upward, while in the case of the e-like events, the zenith-angle distribution is consistent with the expectation.

The hypothesis that neutrinos had interacted crossing the earth was discarded since the earth is almost transparent for neutrinos with energy of about few GeV and moreover the same pattern should have been found for the case of electrons. So this behaviour is interpreted as neutrino oscillation in the way that muon neutrinos coming from the opposite side of the Earth's atmosphere ($\sim$ 10000 km away) oscillate into other neutrino flavour and disappear, while oscillations do not take place for muon neutrinos coming from above the detector, since they have travelled only a few kilometres and do not have time to change their flavour. The oscillation is attributed to a two-flavour $\nu_{\mu} \leftrightarrow \nu_{\tau}$ transition. Furthermore Super-Kamiokande showed that the ratio between data and prediction at large L/E followed the characteristic sinusoidal behaviour of the ν_{μ} survival probability (see fig. 1.10).

The muon neutrino disappearance has been confirmed by other atmospheric neutrino experiments like MACRO [47] and Soudan2 [48] or by neutrino telescope experiments, like ANTARES [49] and IceCube - DeepCore [50].

Long baseline accelerator experiments are also involved in the observation of the muon neutrino deficit. The beam of muon neutrinos is produced mainly from the collision of protons of a few GeV with a fixed target A that create charged pions which decay through the reaction:

$$\begin{aligned} p + A &\rightarrow \pi^{\pm} + X \\ \pi^{\pm} &\rightarrow \mu^{\pm} + \nu_{\mu}(\bar{\nu}_{\mu}) \end{aligned} \tag{1.47}$$

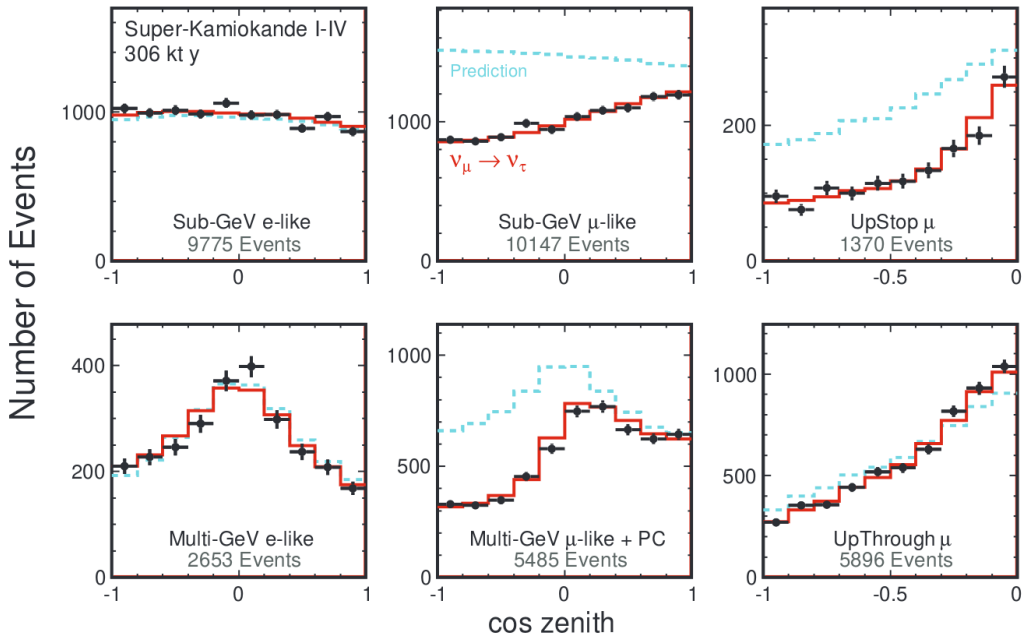

Figure 1.9: Zenith angle distributions for fully contained 1-ring e-like and μ-like events with visible energy <1.33 GeV (sub-GeV) and >1.33 GeV (multi-GeV). The dotted histograms show the non-oscillated Monte Carlo events, and the solid histograms show the best-fit expectations for $\nu_\mu \leftrightarrow \nu_\tau$ oscillations. From [46].

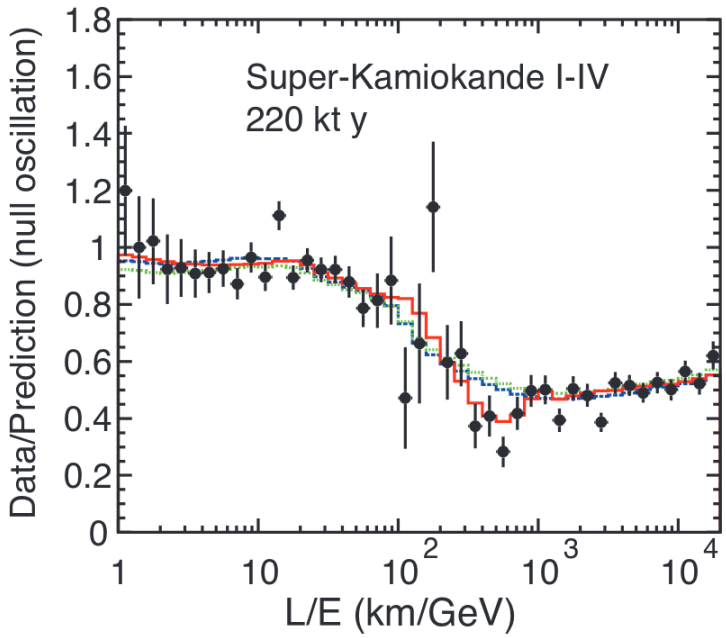

Figure 1.10: Black points show the ratio between data and MC prediction with no oscillation, as a function of the reconstructed L/E. The error bars are statistical. The solid line shows the best fit with 2-flavour $\nu_\mu \leftrightarrow \nu_\tau$ oscillations. From [46].

The K2K (KEK To Kamioka) [51] experiment was the first long-baseline accelerator experiment (250 km between the KEK proton synchrotron and the SK detector) which measured a clear neutrino oscillation signal from the $\nu_\mu \to \nu_\mu$ disappearance.

MINOS (Main Injector Neutrino Oscillation Search) [52] in Fermilab measured the oscillation parameters of $\nu_\mu \to \nu_\mu$ and $\bar{\nu}_\mu \to \bar{\nu}_\mu$ separately using both the π^+ and π^- beams.

The T2K (Tokai to Kamioka) experiment [53], sucessor of K2K with 295 km of distance between the production of the neutrino beam in the J-PARC and the SK detector, has the peculiarity that the direction of the neutrino beam is 2.5° deflected from the direction to the SK detector, allowing this way a narrower energy distribution peaking at ∼0.6 MeV. The T2K experiment has measured the $\nu_\mu \to \nu_\mu$ disappearance and confirmed the large deficit with significantly higher statistics than K2K. This high statistics allows T2K to observe also the $\nu_\mu \to \nu_e$ and $\bar{\nu}_\mu \to \bar{\nu}_e$ appearance signals.

Latest experiment explained here is NOνA [54], which uses Fermilab's NuMI beamline as its neutrino source. The NOνA detectors are situated 14 mrad off the NuMI beam axis, so they are exposed to a relatively narrow band of neutrino energies centered at 2 GeV [55]. The far detector is located in Minnesota, 810 km away from the near detector in Fermilab. NoνA, as T2K, also studies four oscillation channels: $\nu_\mu \to \nu_\mu$, $\bar{\nu}_\mu \to \bar{\nu}_\mu$, $\nu_\mu \to \nu_e$ and $\bar{\nu}_\mu \to \bar{\nu}_e$.

Combining several of these experiments results well using atmospheric or accelerator neutrinos, figure 1.11 shows the 90% CL allowed regions in the $\sin^2(2\theta_{23}) - \Delta m^2_{32}$ plane, for the case of normal mass ordering.

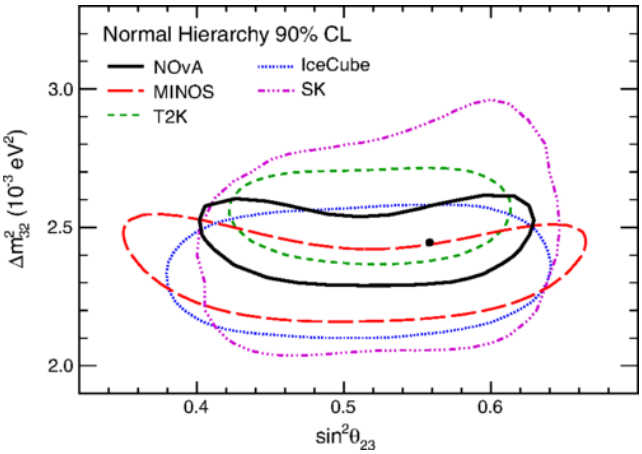

Figure 1.11: The 90% confidence regions for the $\sin^2(2\theta_{23}) - \Delta m^2_{32}$ plane assuming normal mass ordering derived from the T2K [56], NOνA [57], MINOS [58], Super-Kamiokande [59], and IceCube [60] experiments. From [57].

1.6.3 Measurement of θ_{13}

The mixing angle θ_{13} has been the last angle to be measured due to the extra difficulties for the observation of the related oscillations since θ_{13} is the smallest mixing angle of the PMNS matrix. The discovery of a non-zero θ_{13} leads to a opportunity to determine the neutrino mass ordering and the search for the CP

violation process.

The first direct indication of a non-zero value came from long baseline accelerator experiments and the study of $\nu_\mu \rightarrow \nu_e$ oscillations. In 2011 the experiment T2K observed six ν_e candidate events, while the expectation for no oscillation was 1.5±0.3 events. This result implied a non-zero θ_{13} with statistical significance of 2.5σ [61]. In the same way MINOS also performed $\nu_\mu \rightarrow \nu_e$ appearance, disfavoring the $\theta_{13} = 0$ hypothesis by the data at the 89% CL [62].

However current accelerator experiments cannot measure θ_{13} independently of other oscillation parameters like Δm^2_{32}, θ_{23} or the CP-violating phase δ_{CP}. Fortunately a most direct and precise measurement of θ_{13} is possible using neutrinos coming from nuclear reactors. The products of the fissions in the nuclear cores produce an intense, isotropic and pure $\bar{\nu}_e$ flux. From equation 1.22 and assuming short baselines, the survival probability of the reactor electron antineutrino with energy E_ν in vacuum can be written as:

$$P(\bar{\nu}_e \rightarrow \bar{\nu}_e) = 1 - \sin^2 2\theta_{13} \sin^2 \left(\frac{1.27 \Delta m^2_{31}(eV^2) L(m)}{E_\nu(MeV)} \right) \tag{1.48}$$

Then the value of θ_{13} can be measured directly from oscillations. The probability is plotted in fig. 1.12. Since reactor experiments work at short distances (∼1 km), then matter effects can be neglected.

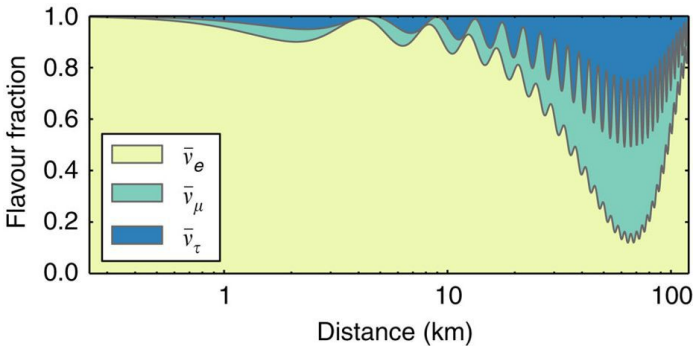

Figure 1.12: Expected flavour composition of the reactor antineutrino flux, for antineutrinos of 4 MeV energy used as an example, as a function of distance to the reactor cores. From [63].

In the late 1990s, the Palo Verde and CHOOZ reactor experiments began to observe electron antineutrinos at distances of the order of the kilometer. Both experiments used Cowan and Reines' approach, i.e. a tank filled with liquid scintillator doped, in this case, with Gadolinium to increase the neutron capture cross-section. In the case of CHOOZ, the detector was located around 1050 m away from the twin core of the Chooz-B power plant in France, while in the case of Palo Verde the detector was 750, 890 and 890 m away from the 3 reactor cores of the Palo Verde Nuclear Generating Station in Arizona. Having collected 2991 $\bar{\nu}_e$ candidates, CHOOZ estimated a observed-to-predicted ratio of R = 1.01 ± 2.8%(stat) ± 2.7%(syst). Using a value of $|\Delta m^2_{13}| = 2.5 \times 10^{-3}\text{eV}^2$, CHOOZ established an upper limit of $\sin^2(2\theta_{13}) < 0.19$ [64]. In the case of Palo Verde, the ratio was R=1.01 ± 2.4%(stat) ± 5.3%(syst) which agreed with CHOOZ results but it was less restrictive due to larger systematic uncertainties [65].

With the purpose of improving this limit, a new generation of reactor experiments has been taking data for the past few years. Double Chooz [66] gave the first indication of a non-vanishing value of θ_{13} in 2011 (using only the Far Detector), ruling out the no-oscillation hypothesis at the 94.6% CL, followed by the 5σ observation from Daya Bay in 2012 [67]. RENO confirmed non-zero θ_{13} soon after [68]. These three experiments identify reactor neutrinos via the inverse beta decay, but unlike CHOOZ, these collaborations rely on a near detector located at baselines of a few hundred meters, causing the most significant improvement over the previous generation. The uncertainty in the predicted antineutrino flux is largely suppressed by the relative measurement between near and far detectors, as well as common uncertainties in both detectors related to detection methods. With larger detector and better shielding, together with better chemical recipes of the Gd-loaded liquid scintillator, the new generation gets larger signal statistics and improves the detector performance and stability. The detectors configuration with respect to the nuclear reactor cores for each experiment is shown in figure 1.13. Double Chooz relies on two reactors and two detectors, RENO counts on six reactors and two detectors, while Daya Bay has six reactors and three detector halls (8 detectors in total). The main features of each detector are listed in table 1.2.

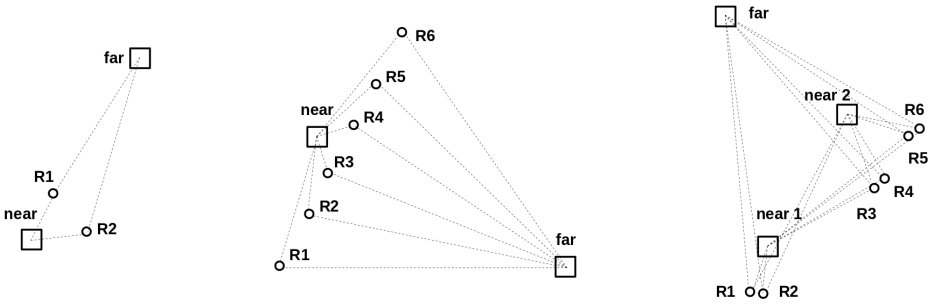

Figure 1.13: 2D geometry of the experimental setups of Double Chooz (left), RENO (middle) and Daya Bay (right) experiments. The squares indicate the detectors and the circles indicate the reactor cores. The dotted lines depict the baselines between detectors and reactors, while distances are summarized in table 1.2. From [69].

Table 1.2: Key parameters of the present reactor θ_{13} experiments, including the reactor power, average distance between detectors and reactors, depth of the detectors and target mass.

Experiment	Reactor power (GW_{th})	Distance (m) Near/Far	Depth (mwe) Near/Far	Target mass (ton)×detector
Double Chooz	8.5	400/1050	120/300	8×2
Daya Bay	17.4	470.576/1648	260/860	20×8
RENO	16.5	294/1383	120/450	16×2

The combined value from the three experiments results can be appreciated in fig. 1.14 from [70]. This analysis does not include the latest results of Double Chooz that are presented in this thesis. Most updated results from Daya Bay and RENO

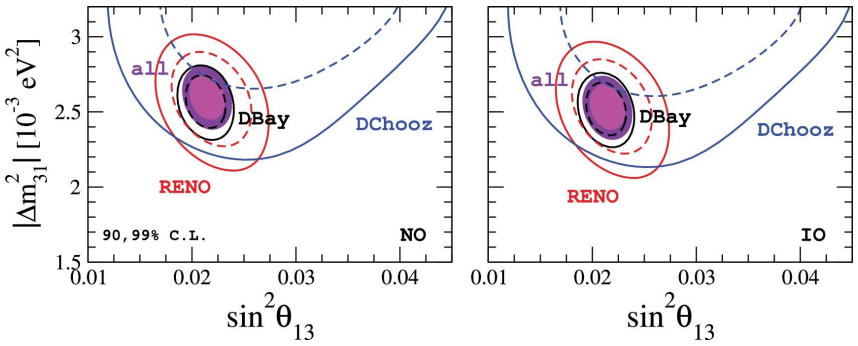

Figure 1.14: 90 and 99% C.L. allowed regions at the $\sin^2(\theta_{13})$˘Δm^2_{31} plane from each reactor neutrino experiment (dashed, solid lines) and from the combination of the three experiments (colored regions). The left (right) panels correspond to normal (inverted) mass ordering. From [70].

are listed in Chapter 7. Concerning accelerator results, T2K most updated θ_{13} result with marginalization over δ_{CP} and θ_{23} is $\sin^2(2\theta_{13}) = 0.1055^{+0.0266}_{-0.0236}$ for NO and $\sin^2(2\theta_{13}) = 0.1160^{+0.0302}_{-0.0254}$ [56].

1.6.4 Overview of oscillation parameters

Best-fit values of neutrino oscillation parameters from a global fit to experimental data available in November 2018 [71] are listed in fig. 1.15 and the two dimensional plots from this global 3ν oscillation analysis are compiled in fig. 1.16.

NuFIT 4.0 (2018)

	Normal Ordering (best fit)		Inverted Ordering ($\Delta\chi^2 = 4.7$)	
	bfp $\pm 1\sigma$	3σ range	bfp $\pm 1\sigma$	3σ range
$\sin^2\theta_{12}$	$0.310^{+0.013}_{-0.012}$	$0.275 \to 0.350$	$0.310^{+0.013}_{-0.012}$	$0.275 \to 0.350$
$\theta_{12}/^\circ$	$33.82^{+0.78}_{-0.76}$	$31.61 \to 36.27$	$33.82^{+0.78}_{-0.76}$	$31.61 \to 36.27$
$\sin^2\theta_{23}$	$0.580^{+0.017}_{-0.021}$	$0.418 \to 0.627$	$0.584^{+0.016}_{-0.020}$	$0.423 \to 0.629$
$\theta_{23}/^\circ$	$49.6^{+1.0}_{-1.2}$	$40.3 \to 52.4$	$49.8^{+1.0}_{-1.1}$	$40.6 \to 52.5$
$\sin^2\theta_{13}$	$0.02241^{+0.00065}_{-0.00065}$	$0.02045 \to 0.02439$	$0.02264^{+0.00066}_{-0.00066}$	$0.02068 \to 0.02463$
$\theta_{13}/^\circ$	$8.61^{+0.13}_{-0.13}$	$8.22 \to 8.99$	$8.65^{+0.13}_{-0.13}$	$8.27 \to 9.03$
$\delta_{\mathrm{CP}}/^\circ$	215^{+40}_{-29}	$125 \to 392$	284^{+27}_{-29}	$196 \to 360$
$\frac{\Delta m^2_{21}}{10^{-5}\ \mathrm{eV}^2}$	$7.39^{+0.21}_{-0.20}$	$6.79 \to 8.01$	$7.39^{+0.21}_{-0.20}$	$6.79 \to 8.01$
$\frac{\Delta m^2_{3\ell}}{10^{-3}\ \mathrm{eV}^2}$	$+2.525^{+0.033}_{-0.032}$	$+2.427 \to +2.625$	$-2.512^{+0.034}_{-0.032}$	$-2.611 \to -2.412$

Figure 1.15: Three-flavour oscillation parameters from the fit to global data in January 2018. The numbers in the 1st (2nd) column are obtained assuming normal ordering NO (inverse ordering IO), whereas in the 3rd column results are minimized with respect to the ordering. Note that $\Delta m^2_{3l} = \Delta m^2_{31} > 0$ for NO and $\Delta m^2_{3l} = \Delta m^2_{32} < 0$ for IO. From [71].

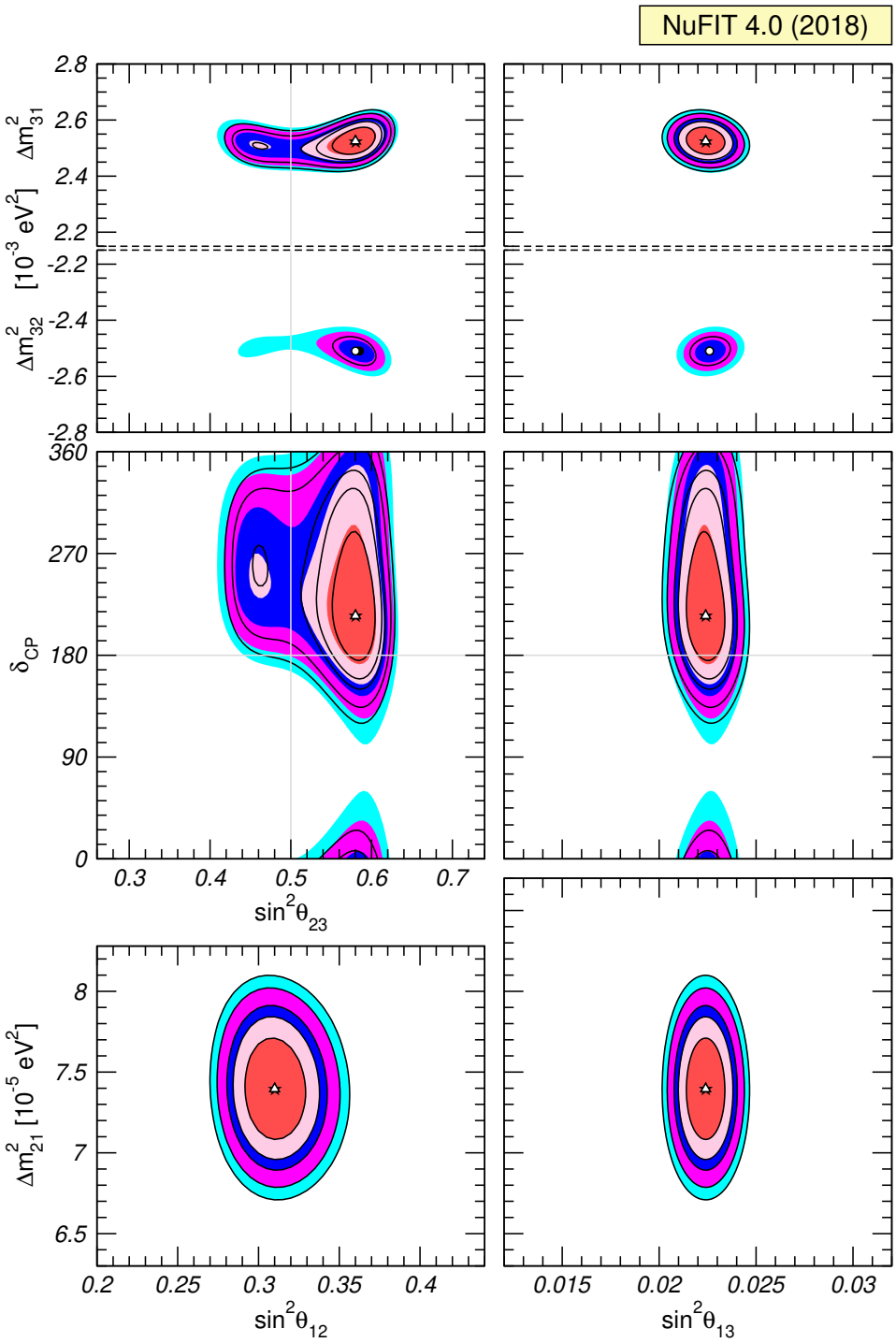

Figure 1.16: Global 3ν oscillation analysis. Each panel shows the two-dimensional projection of the allowed six-dimensional region after marginalization with respect to the undisplayed parameters. The different contours correspond to the two-dimensional allowed regions at 1σ, 90%, 2σ, 99%, 3σ CL. The atmospheric mass-squared splitting Δm^2_{31} is the one for NO and Δm^2_{32} is the one for IO. The regions in the lower 4 panels are based on a $\Delta\chi^2$ minimized with respect to the mass ordering. From [71].

Concerning the solar neutrino data sample, the results of θ_{12} and Δm^2_{21} have been measured with a precision of 2.3% and 2.8% respectively. In the atmospheric sector, the precision for θ_{23} and $\left|\Delta m^2_{3l}\right|$ is 8.3% and 1.3%. Finally the value of θ_{13} has been obtained with a precision of 1.8%.

However not all the parameters that govern the neutrino oscillations have been determined, being the main open challenges of the three-neutrino picture: the CP violation phase, the neutrino mass ordering and the θ_{23} octant problem, that are detailed in the following section.

In the future, medium baseline ($\sim$50 km) reactor neutrino oscillation experiments with neutrino target mass of $\sim$20 kton and very good energy resolution of $3\%/\sqrt{E_\nu}$(MeV) will be focused on the determination of the neutrino mass ordering. This is the case of the Jiangmen Underground Neutrino Observatory (JUNO) experiment [72] in Kaiping, Jiangmen (China), whose construction started in January 2015 and expects a $\Delta\chi^2{>}9$ with $\sim$6 years of data taking.

Thanks to the measurement of θ_{13} by the already explained new generation of reactor experiments, future long baseline accelerator neutrino experiments such as the DUNE experiment [73] under construction at Fermilab (USA) or Hyper-Kamiokande [80] in Japan, starting construction in 2020, will perform precision measurements of neutrino oscillations, including the possible CP violation phase in the lepton sector as well as the neutrino mass ordering.

1.7 Open Questions

During the last decades, the precision of the best-known oscillation parameters has been improved thanks to new generation of neutrino experiments that have allowed the compilation of new data from long-baseline accelerators or nuclear reactors. However, as said before, there are still open challenges in the three-neutrino picture.

1.7.1 CP violation

As could be seen in the PMNS mixing matrix (equation 1.11), the mixing angle θ_{13} is coupled to the CP violating phase δ_{CP}. Using the last data from reactor neutrinos, $\sin^2(2\theta_{13})$ has been measured to be non zero and since it is relatively large, the measure of δ_{CP} becomes accessible.

If $\delta_{\mathrm{CP}} \neq 0$ or $\delta_{\mathrm{CP}} \neq \pi$) it would imply that charge and parity are not conserved in the neutrino sector and in this case neutrinos would interact in a different manner than antineutrinos. Long-baseline accelerator experiments could help to determine the exact value through the study of the appearance of electron (anti)neutrino from a muon (anti)neutrino beam, where the transition probability, assuming matter effects, can be approximated up to second order in $\alpha = \Delta m^2_{21}/\Delta m^2_{32}$ as [74]:

$$
\begin{aligned}
P(\nu_e \to \nu_\mu) &\approx P_0 + P_{\sin\delta} + P_{\cos\delta} + P_3 \qquad (1.49)\\
P_0 &= \frac{1}{(A-1)^2}\sin^2\theta_{23}\sin^2 2\theta_{13}\sin^2[(A-1)\Delta]\\
P_3 &= \frac{\alpha^2}{A^2}\cos^2\theta_{23}\sin^2 2\theta_{12}\sin^2(A\Delta)\\
P_{\sin\delta} &= -\alpha\frac{8J_{CP}}{A(1-A)}\sin\Delta\sin A\Delta\sin[(1-A)\Delta]\\
P_{\cos\delta} &= \alpha\frac{8J_{CP}\cot\delta}{A(1-A)}\cos\Delta\cos A\Delta\sin[(1-A)\Delta] \qquad (1.50)
\end{aligned}
$$

where

$$\Delta = \frac{\Delta m^2_{31} L}{4E},\ A = \sqrt{2} G_F N_e \frac{2E}{\Delta m^2_{31}} \qquad (1.51)$$

being G_F the weak coupling constant, N_e the number density of electrons in the propagation medium and

$$8J_{CP} = \sin\delta\cos\theta_{13}\sin 2\theta_{12}\sin 2\theta_{13}\sin 2\theta_{23} \qquad (1.52)$$

Current long baseline oscillation experiments, like T2K and NOνA or the atmospheric experiment SK, are able to excluded $\delta_{CP} = \pi/2$ at $>3\sigma$. The latest results from T2K (not included in the previous results of the global fit analysis) reinforce that the conserving values of CP lie outside the 2σ region [75] (see figure 1.17). In the case of NOνA, data prefers normal ordering at 1.8σ and excludes $\delta_{CP} = \pi/2$ at $>3\sigma$ [77]. Finally Super-Kamiokande found that the best fit value of δ_{CP} is 4.18 (3.84) radians in the normal (inverted) fit. These results are enhanced by the combination with the published binned T2K data on ν_μ disappearance and ν_e appearance [59].

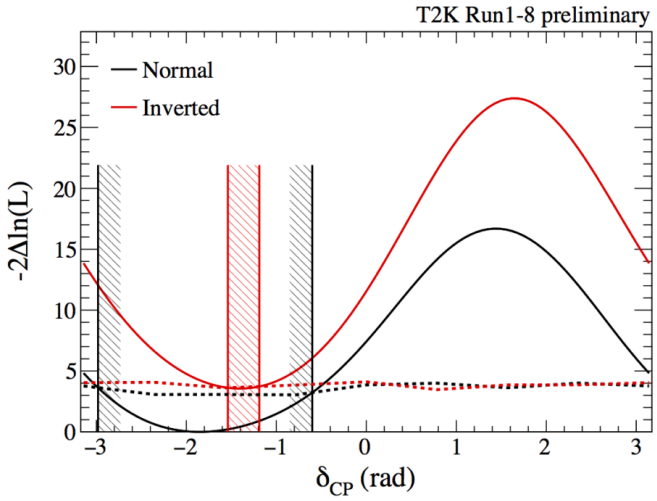

Figure 1.17: $-2\Delta\ln L$ (equivalent of $\Delta\chi^2$) as a function of δ_{CP} for the normal (black) and inverted (red) mass ordering. The vertical lines show the corresponding allowed 95% confidence interval, calculated using the Feldman-Cousins method. From [75].

From the global fit [70] that includes also the global oscillation data sample, it can be extracted that the global sensitivity is dominated by the T2K experiment. From this global analysis, $\delta_{CP} = \pi/2$ is disfavored with 4.8σ assuming normal ordering or 6.1σ for inverted ordering (see figure 1.18). The best fit values for the CP violating phase are located at $\delta_{CP} = 1.21\pi$ (NO) and $\delta_{CP} = 1.56\pi$ (IO).

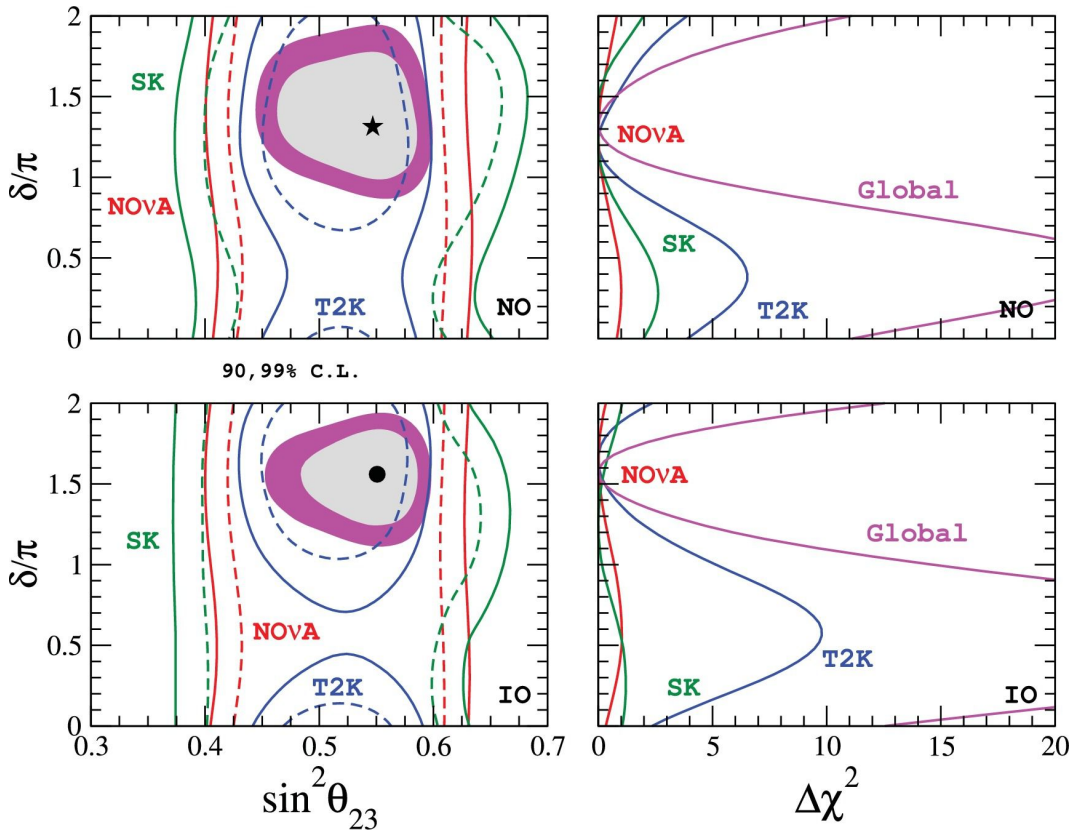

Figure 1.18: Left: 90 and 99% allowed regions from T2K (blue lines) and NOνA (red) data, from the atmospheric Super-K results (green) and from the global fit of all the oscillation experiments (coloured regions). The star indicates the best fit point from the global analysis, found for normal mass ordering, while the black dot indicates the local minimum for inverted mass ordering. Right: $\Delta\chi^2$-profile as a function of the CP phase δ from T2K, NOνA and Super-K atmospheric (with the same color code as in the left panel) and from the global fit (magenta). In both cases, the upper (lower) panels correspond to normal (inverted) mass ordering. From [70].

In the near future DUNE will search for CP violation using the ν_μ to ν_e and $\bar{\nu}_\mu$ to $\bar{\nu}_e$ oscillation channels of the LBNF beam neutrinos in a wide range of neutrino energies over the 1300 km baseline. The expected sensitivity to CP violation as well as the expected 1σ resolution as a function of exposure in years is shown in figure 1.19.

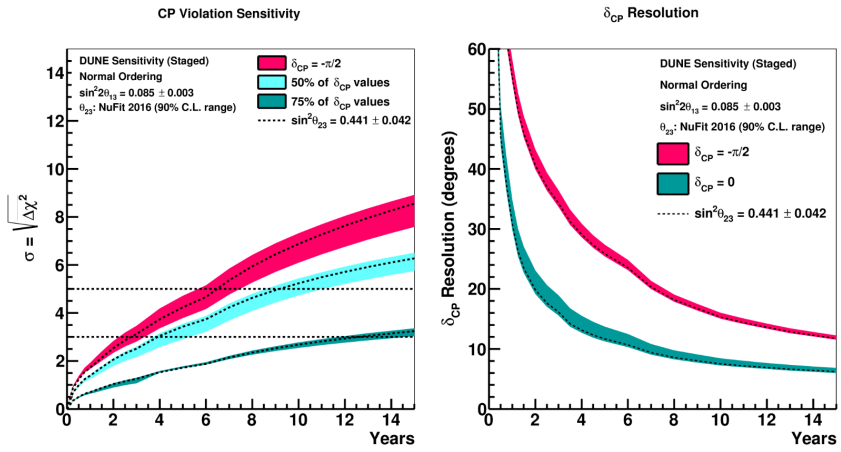

Figure 1.19: Left: significance with which CP violation can be determined for 75% and 50% of δ_{CP} values and for δ_{CP}=-$\pi/2$. Right: expected 1σ resolution as a function of exposure in years. Width of band indicates variation in sensitivity for θ_{23} values in the NuFit2016 90% C.L. From [76].

1.7.2 Mass ordering

In the same way as for the CP violation phase, the relatively large measured value of θ_{13} has opened up the possibility of determining the neutrino mass ordering through earth matter effects. In the current status, the absolute squared mass differences $|\Delta m^2_{ij}|$ have been well determined thanks to the study of neutrino oscillations, as well as the order of m_1 and m_2. However the sign of Δm^2_{13} is yet unknown and this is the so-called neutrino mass ordering problem. The case in which $m_1 < m_2 < m_3$ or $\Delta m^2_{13} > 0$ is called normal ordering (NO) while the case in which $m_3 < m_1 < m_2$ or $\Delta m^2_{13} < 0$ is called inverted ordering (IO) (see fig. 1.20).

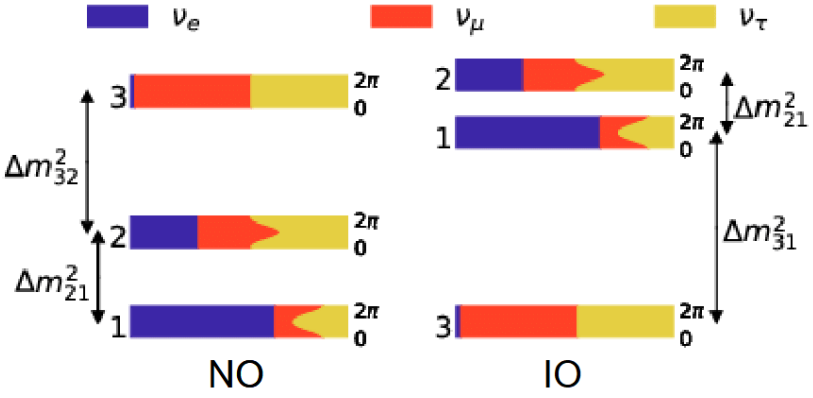

Figure 1.20: The two possible neutrino mass orderings (left: normal ordering, right: inverted ordering). The range of probability of finding the α-flavour in the i-th mass eigenstate as indicated as the CP-violating phase δ_{CP} is varied. The bottom of the bars is for the value of δ_{CP}=0 and the top of the bars is $\delta_{CP} = 2\pi$. From [78].

When neutrinos travels through the Earth, in the NO scenario the neutrino oscillation probability will be enhanced while in the IO scenario will be suppressed. In the case of antineutrinos, the effect is the opposite one. This effect is the MSW effect explained in section 1.5.3. Then the study of the matter-induced asymmetry in the oscillations of neutrinos and antineutrinos could provide a determination of the mass ordering.

It is also possible to determine the mass ordering with experiments studying atmospheric neutrinos but their sensitivity depends strongly on the chosen value of $\sin^2\theta_{23}$ and the fact that if this angle is maximal (minimal) the sensitivity will be also maximal (minimal), so it relies on the next described open question: the θ_{23} octant problem.

Latest results of NOνA and T2K show only a slight preference for normal mass ordering at the level of 1.8σ in the case of NOνA and with a bayesian factor NO/IO=7.9 for T2K data [75], [77]. On the other hand, a global fit done using also solar data, short-baseline reactor neutrino data, atmospheric experiments results and the already mentioned T2K and NOνA, besides K2K and MINOS, obtains a global preference of 3.4σ ($\Delta\chi^2 = 11.7$) in favor of normal ordering [70].

Furthermore the 95% limit of $\sum m_\nu < 0.12$ eV from Planck satellite (section 1.4.4.3), puts pressure on the inverted mass ordering (which requires $\sum m_\nu \gtrsim 0.1$ eV).

Concerning future prospects, the DUNE experiment, with the longest baseline ever for an accelerator neutrino experiment (1300 km), will be able to measure the neutrino mass ordering with a significance above 5σ for any set of the oscillation parameters (θ_{23}, δ_{CP}) after 7 years of analysis over the oscillation probability of $\nu_\mu \to \nu_e$ and $\bar{\nu}_\mu \to \bar{\nu}_e$ [79]. Also Hyper-Kamiokande, 25 times larger than Super-Kamiokande will be able to determine the neutrino mass ordering through the study of atmospheric neutrinos. After 10 years Hyper-K is expected to resolve the mass hierarchy at $\sqrt{\Delta\chi^2} > 3$ for both ordering assumptions and when $\sin^2\theta_{23}$>0.53 [80].

1.7.3 θ_{23} octant

Identifying the true value of θ_{23} is an important goal for future experiments, given its importance for understanding the mechanism behind neutrino masses and mixing, since the quantity $\tan^2\theta_{23}$ gives the ratio of the coupling of the third neutrino mass state to ν_μ and ν_τ.

The mixing angle θ_{23} can be extracted from the ν_μ survival probability in vacuum:

$$P(\nu_\mu \to \nu_\mu) = 1 - \sin^2(2\theta_{23}) \left(\sin^2 \frac{\Delta m^2_{31} L}{4E} \right) \tag{1.53}$$

However this probability is insensitive to the octant of θ_{23}, that is, if it lies in the first octant ($\theta_{23} < \pi/4$) or in the second octant ($\theta_{23} > \pi/4$). Therefore a precise determination requires combined measurements of the ν_μ disappearance and $\nu_\mu \to \nu_e$ appearance with neutrinos and antineutrinos.

Looking at figure 1.21 from the global fit [70], it can be extracted that long–baseline experiments (NOνA, T2K and MINOS) indicated by black lines, have a preference for values of θ_{23} close to maximal mixing, with a value of $\sin^2\theta_{23} = 0.508$ for NO and IO. Once the atmospheric data is added, there is an increase of this angle and a small

discrepancy between mass orderings appears: $\sin^2\theta_{23} = 0.54$ for NO and $\sin^2\theta_{23} = 0.53$ for IO. Lastly if the constraint in θ_{13} from reactor experiments is added, the angle moves to larger values for both mass orderings, achieving $\sin^2\theta_{23} = 0.55$

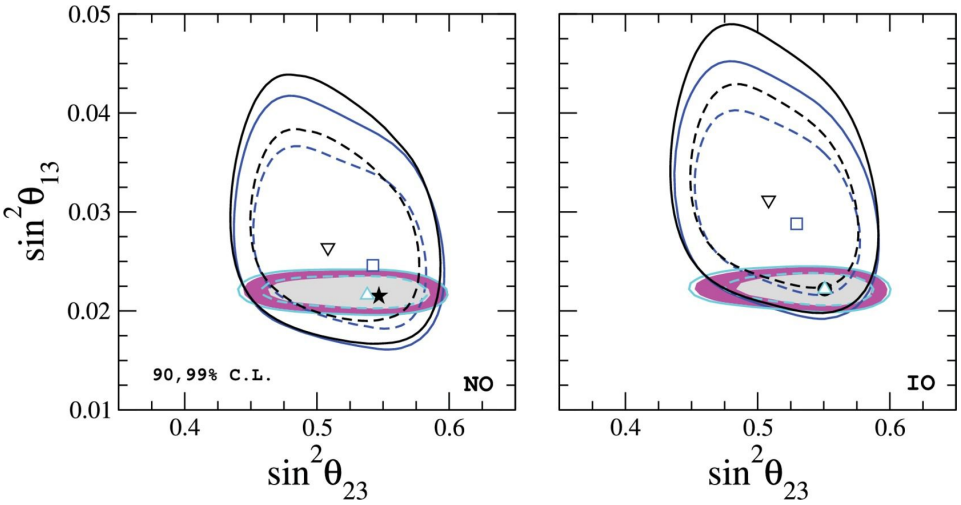

Figure 1.21: 90 and 99% C.L. (2 d.o.f.) allowed regions for $\sin^2\theta_{13}$ and $\sin^2\theta_{23}$ from the combination of different neutrino data samples: long-baseline data only (black lines), long-baseline plus atmospheric (blue), long-baseline plus reactors (cyan) and from the global fit of all experiments (colored regions). Left (right) panel corresponds to normal (inverted) mass ordering. The best fit points are indicated by black down-triangles (long-baseline data), blue squares (long-baseline plus atmospheric), cyan up-triangles (long-baseline plus reactors), and a black star for the global fit in the case of NO and a black dot in the case of IO. From [70].

The latest results shown in the XXVIII International Conference on Neutrino Physics and Astrophysics in June 2018 from T2K consists of a mixing angle $\sin^2\theta_{23} = 0.536^{+0.031}_{-0.046}$ for NO and $\sin^2\theta_{23} = 0.536^{+0.031}_{-0.041}$ for IO [75]. NOνA results for its part are consistent with maximal mixing [57]. SK prefers a value of $\sin^2\theta_{23} = 0.550^{+0.039}_{-0.057}$ for NO and $\sin^2\theta_{23} = 0.550^{+0.035}_{-0.051}$ for IO [59]. MINOS excludes maximal mixing at 1.1σ and has a preference of 0.8σ for the lower octant [81].

Thus the octant degeneracy remains a problem in the current generation of neutrino oscillation experiments. The octant discrimination is a task in current and future long-baseline experiments.

1.7.4 Sterile neutrinos

The standard three-neutrino oscillation scenario has been well described from the experiments discussed through this chapter. Furthermore collider experiments can determine the number of neutrinos coupled to the Z boson through the measurement of its decay width, concluding that the number of active neutrinos is 2.9840±0.0082, consistent with the three active neutrino model [82]. From cosmological measurements of the observation of the Cosmic Microwave Background (CMB) it can be extracted that the number of neutrinos is $N_{eff} \approx 3.046$, slightly larger than 3 since

the three standard model neutrinos were not completely decoupled at the electron-positron annihilation era [83]. In particular, the data on CMB anisotropies from the Planck satellite, in combination with baryon acoustic oscillations (BAO) measurements, lead to an allowed range of $N_{eff} = 3.11^{+0.44}_{-0.43}$ (at 95% CL, data from Planck TT+lowE+lensing+BAO), that is restricted to $N_{eff} = 2.99^{+0.34}_{-0.33}$ if the complete polarization likelihood from Planck is used [27].

However there have been some anomalous experimental results that do not fit in the 3 neutrino flavour scenario, suggesting the possibility of one or more additional neutrino states with masses at the eV scale. On one hand there is the Gallium neutrino anomaly measured in the GALLEX and SAGE experiments, already explained in section 1.6.1. For calibration purposes they measured the flux of ν_e produced by radioactive sources introduced inside the detectors. They found a observed to expected ratio smaller than unity: $R_{\mathrm{Ga}} = 0.86 \pm 0.06$ and interpreted this result as a consequence of ν_e disappearance due to an oscillation of $\sin^2(2\theta) > 0.07$ and $\Delta m^2 > 0.35$ eV^2 at 99% CL [84].

On the other hand the Liquid Scintillator Neutrino Detector (LSND) experiment [85], at Los Alamos National Laboratory in New Mexico, observed an excess of $\bar{\nu}_e$ events in a beam of $\bar{\nu}_\mu$. Since the distance travelled by the muon neutrinos was just 30 meters, the collaboration concluded that the number of electron neutrinos detected was too high to be produced over the short distance by the usual oscillation mechanism and interpreted this results as an oscillation occurred in the Δm^2=(0.2–10) eV^2 range, indicating a neutrino mass greater than 0.4 eV. It must be noticed that KARMEN [86], a very similar experiment with a distance L$\sim$18 m did not measured any excess of electron neutrinos. Most recently the MiniBooNE experiment, using the Fermilab accelerator with a distance up to detector of 540 m and looking at both channels of appearance $\bar{\nu}_\mu \to \bar{\nu}_e$ and $\nu_\mu \to \nu_e$, has confirmed the LSND excess at 4.8σ and combining both experiments the total significance increases at 6.1σ [87]. Additionally, recent re-evaluation of the expected reactor antineutrino flux has led to the suggestion that there may be an additional neutrino mass-splitting at the eV scale [88].

The possible explanation points to a fourth neutrino, a lepton insensitive to the weak interaction named as sterile. There is a strong effort from the neutrino community trying to find an answer for this open question, with new short-baseline (SBL) detectors like STEREO in the ILL nuclear reactor in Lyon [89], DANSS [90] or NEOS [91], besides current experiments with a program of sterile research like IceCube [92], NOνA [93] or Daya Bay [94].

A global fit has been performed within the 3+1 scheme in [95], using reactor neutrino data, driven by DANSS and NEOS $\bar{\nu}_e \to \bar{\nu}_e$ data. This fit drives to a $\gtrsim 3\sigma$ preference for sterile neutrino oscillations with $\Delta m^2_{41} \approx 1.3$ eV^2 and $|U_{e4}| \approx 0.1$, where $|U_{e4}|$ comes from:

$$P^{\mathrm{SBL}}_{\alpha\alpha} = 1 - 4\,|U_{\alpha 4}|^2 \left(1 - |U_{\alpha 4}|^2\right) \sin^2\left(\frac{\Delta m^2_{41} L}{4E}\right) \tag{1.54}$$

Considering also the Gallium anomaly, as well as Karmen and LSND data, atmospheric neutrino data and solar neutrino data, the fit results show a small tension (2.2σ) between gallium and reactor data, but again a global best-fit is obtained at $\Delta m^2_{41} = 1.3$ eV^2 (see figure 1.22).

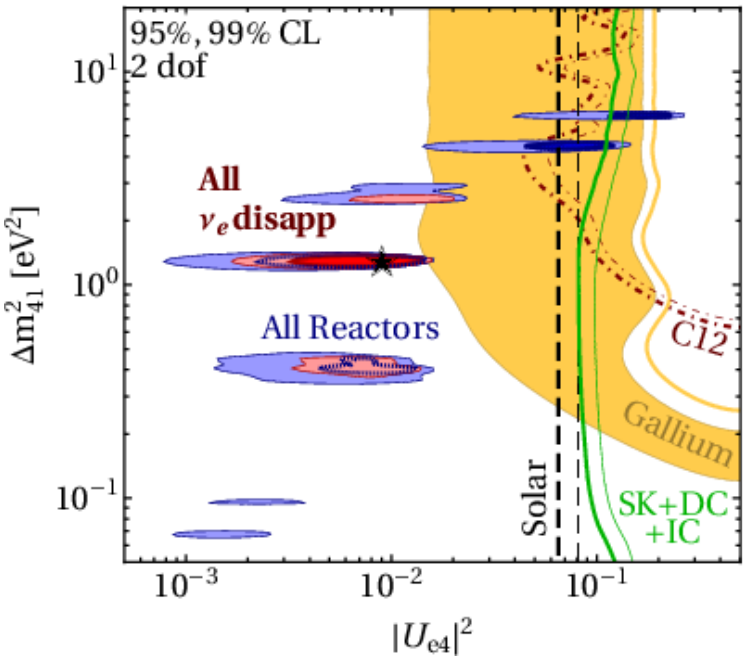

Figure 1.22: Constraints on $\nu_e/\bar{\nu}_e$ disappearance in the 3+1 scenario. Preferred parameter regions at 95% and 99% CL, projected onto the plane spanned by the mixing matrix element $|U_{e4}|^2$ and the mass squared difference Δm^2_{41}. The parameter space inside the shaded areas and to the left of the exclusion curves is allowed. From [95].

In summary, current neutrino experiments have improved the precision in the determination of the best-known oscillation parameters. The program of experimental research in neutrino physics extends beyond 2030, so in the upcoming years the new data collected by current and future experiments is expected to solve fundamental aspects of neutrino mixing that remain unknown, like the nature of massive neutrinos, the presence of sterile neutrinos, the status of the CP violation in the lepton sector or the neutrino mass ordering.

Chapter 2

The Double Chooz Experiment

2.1 Introduction

Double Chooz is one of the three current neutrino experiments aiming to provide the measurement of the θ_{13} mixing angle through the electron antineutrinos dissapearance coming from nuclear reactors.

This chapter is devoted to explain the Double Chooz experiment concept, the reactor neutrino detection and the delayed coincidence method, as well as the description of the two liquid scintillator detectors used to tag the products of the inverse beta decay reaction. The calibration systems involved in the understanding and tuning of the detectors response are also detailed in the following sections.

2.2 Experimental setup

The Double Chooz experiment is set up within the Chooz Nuclear Power Plant, situated near the village of Chooz, in the north of France, close to the Belgian border. This power plant has two running pressurized water reactor cores B1 and B2, which emit around 10^{21} $\bar{\nu}_e$/s. The Far detector (FD), ∼1050 meters away from the reactor cores and the Near detector (ND), close to them ∼ 400 m, measure the antineutrino flux (view of the Double Chooz site in figure 2.1).

The choice of the two detector positions falls on two main reasons. Looking at the figure 1.12, the first θ_{13} oscillation maximum is roughly at 2km distance from reactors for a mean antineutrino energy of 4 MeV. However, since the CHOOZ experiment laboratory was already located at 1.05 km from the Chooz cores, Double Chooz decided to take advantage of the existence and availability of this laboratory to build the FD. On the other hand, the location of the ND was determined in order to cancel the systematic errors relative to the nuclear reactors uncertainties (lack of knowledge of the $\bar{\nu}_e$ flux and spectrum). This scenario is known as isoflux condition, which imposes that the two detectors observe the same ratio of flux from the two reactors. As the flux is anti-proportional to the distance square $D_{d,R}$, where d labels

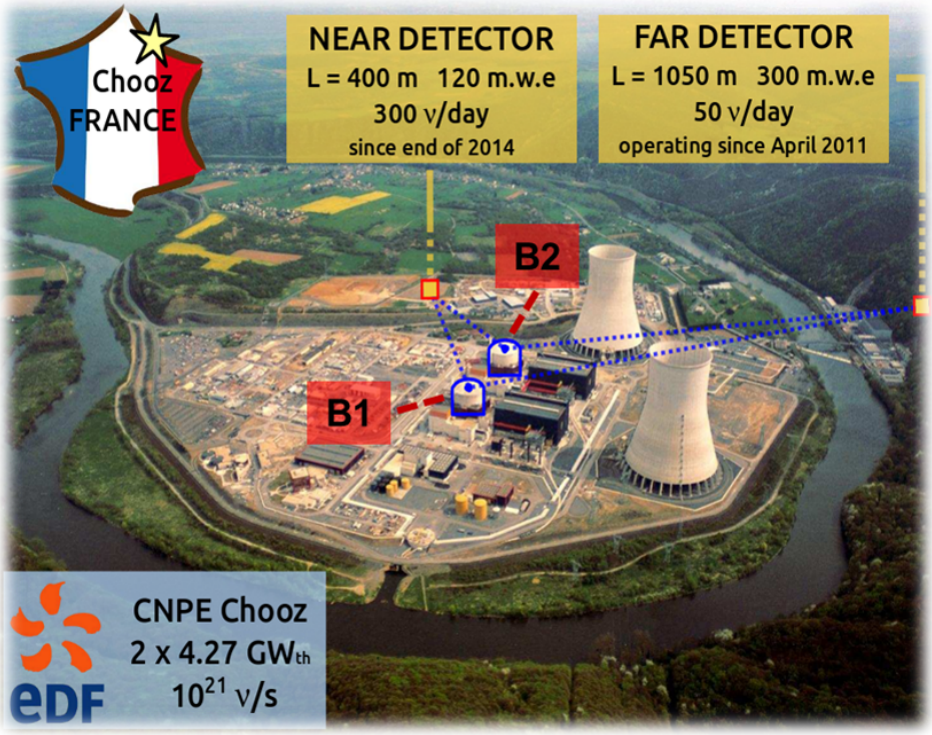

Figure 2.1: Double Chooz experimental site.

detector and R reactor (more details in Chapter 3), the isoflux condition can be rewriten as a function of this last variable:

$$\frac{\phi_{ND,B1}}{\phi_{ND,B2}} = \frac{\phi_{FD,B1}}{\phi_{FD,B2}} \implies \frac{D_{ND,B1}}{D_{ND,B2}} = \frac{D_{FD,B1}}{D_{FD,B2}} \tag{2.1}$$

Nevertheless, following a study completed by the French electric power company EDF to determine the best combination of location and overburden, as well as the preliminary cost of the needed civil construction, it was decided that the feasibility of excavating a ≈40 m deep shaft was only possible at a 250–300 m distance from the nuclear reactor cores. The final distances from the detectors to each reactor core and the overburden in meters of water equivalent are summarized in table 2.1 [96].

Table 2.1: Distance between detectors and reactor cores in meters and detectors overburden in meters of water equivalent.

Detector	Distance to B1 (m)	Distance to B2 (m)	Overburden (m.w.e.)
ND	468.761 ± 0.015	355.388 ± 0.015	120
FD	1114.656 ± 0.015	997.839 ± 0.015	300

Computing equation 2.1 including the distances of table 2.1, it can be seen that the Double Chooz detectors are not perfectly isoflux. Despite this, these detector positions allow that a large part of the correlated flux uncertainties cancels in the two detectors analysis, as will be explained in section 3.2.4.

The Double Chooz detectors were designed to perform functionally identical to reduce the set of systematic errors related to the detector and to the event selection procedure. Even though the Double Chooz experiment goal was to obtain a θ_{13} measurement with a multi-detector (MD) configuration using the two detectors, two phases can be clearly distinguished. In the first period, from April 2011 to December 2014, only the FD was functioning taking data. Notwithstanding, Double Chooz was the first reactor experiment in providing an indication of a non-zero θ_{13} [66]. Due to some internal delays, the ND finally started taking data in December 2014, simultaneously with the FD. The far detector working as single detector will be denoted in the thesis as FD-I, while in the second period, will be written as FD-II.

2.3 Electron antineutrino production

The source of electron antineutrinos for the Double Chooz experiment are two N4 PWRs (presurized water reactors), named B1 and B2, of the Chooz power plant in the Ardennes region in France, with a nominal thermal power of 4.25GWth per core. N4-PWRs are light water reactors among the most powerful reactors in the world.

Their initial fuel consists of enriched uranium dioxide (UO_2) pellets composed of ^{238}U enriched with some percent of ^{235}U. In a fresh fuel assembly, as soon as the reactor is operating, reactions of neutron capture on ^{238}U produce ^{239}Pu and ^{241}Pu (eq. 2.2), contributing also to the energy production.

$$^{238}_{98}\mathrm{U} \xrightarrow{(n,\gamma)} {}^{239}_{92}\mathrm{U} \xrightarrow[23.45\ \mathrm{min}]{\beta^-} {}^{239}_{93}\mathrm{Np} \xrightarrow[2.35\ \mathrm{day}]{\beta^-} {}^{239}_{94}\mathrm{Pu} \xrightarrow{(n,\gamma)} {}^{241}_{94}\mathrm{Pu} \tag{2.2}$$

As the energies released per fission of each isotope are very similar among them (200 MeV/fission), the contribution of each isotope to the total thermal power is very close to its contribution to the total number of fissions. In burnt fuel, the main contributions come from the two fissile isotopes ^{235}U and ^{239}Pu.

2.4 Electron antineutrino detection

Reactor antineutrinos are detected through their interaction via the inverse beta decay (IBD) with a proton in a volume filled with liquid scintillator:

$$\bar{\nu}_e + p \rightarrow e^+ + n \tag{2.3}$$

The energy threshold for this reaction in the laboratory frame (proton at rest) can be deduced from:

$$\begin{aligned}
(E_{\bar{\nu}_e,th} + M_p)^2 &= (E_{e^+} + E_n)^2 \rightarrow M_p^2 + E_{\bar{\nu}_e,th}^2 + 2M_p E_{\bar{\nu}_e,th} = M_n^2 + E_{e^+}^2 + 2M_n E_{e^+} \\
E_{\bar{\nu}_e,th} &\sim \frac{M_n^2 + 2M_n E_{e^+} - M_p^2}{2M_p} = \frac{(M_n - M_p)(M_n + M_p) + 2M_n E_{e^+}}{2M_p} \\
E_{\bar{\nu}_e,th} &\sim M_n - M_p + E_{e^+} = M_n - M_p + M_{e^+} = 1.806\ \mathrm{MeV}
\end{aligned} \tag{2.4}$$

where the following three assumptions have been adopted: at the energy threshold, no neutron recoil is considered, the positron is at rest so p_{e^+}=0 and natural units are used (c=1).

Below this energy threshold, the antineutrino energy is not able to generate the mass of the positron (M_{e^+} = 511 keV) and the additional mass of the neutron with respect to the proton $M_n - M_p$ = 1.293 MeV. Since the antineutrinos emitted by the reactors have an energy of a few MeV, there is no enough energy to produce a μ or τ in this neutrino-proton reaction, so this detection channel is only exclusive to electron flavor. As a consequence, the Double Chooz experiment is only sensitive to the deficit of the electron antineutrinos in the reactor flux as a result of the neutrino oscillations.

On the other hand, the cross-section of the IBD reaction is analytically known and it is estimated from the neutron lifetime and expressed in terms of the electron antineutrino energy [97]:

$$\sigma_{\text{IBD}}\left(E_{\bar{\nu}_e}\right) = K\left(E_{\bar{\nu}_e} - \Delta\right)\sqrt{\left(E_{\bar{\nu}_e} - \Delta\right)^2 - m_e^2} \tag{2.5}$$

with $\Delta = M_n - M_p$ and

$$K = \frac{2\pi^2}{m_e^5 f^R \tau_n} = 0.961 \times 10^{-43}\ \text{cm}^2/\text{MeV}^2 \tag{2.6}$$

being f^R the phase space factor of the free neutron decay [98] and τ_n the measured neutron lifetime from the MAMBO-II experiment [99].

Although the neutrino energy spectrum cannot be directly measured, it can be extracted from the measured positron spectrum. As said before, the neutron recoil energy is negligible due to the fact that the neutron is much heavier than the positron, so the antineutrino kinetic energy is mostly transferred to the positron. This positron slows down loosing its kinetic energy within picoseconds by scattering with the scintillator molecules and subsequently annihilates with an electron, being then the total energy detected from the prompt signal:

$$E_{\text{vis}} = E_{e^+} + M_e \simeq E_{\bar{\nu}_e} - M_n + M_p + M_e = E_{\bar{\nu}_e} - 0.782\ \text{MeV} \tag{2.7}$$

where the same approximation as in equation 2.4 has been used, i.e., $E_{\bar{\nu}_e} \simeq M_n - M_p + M_{e^+}$.

The observed positron spectrum has the same energy resolution as the electron antineutrino energy distribution (figure 2.2) but shifted by 0.8 MeV. It is formed by the convolution of the emitted $\bar{\nu}_e$ spectrum from the reactor cores and the IBD cross section. This spectrum begins at 1.806 MeV, since this is the energy threshold for an IBD reaction as was derived in equation 2.4.

2.4.1 Coincidence Method

Reactor neutrino experiments use the IBD interaction (eq. 2.3) to detect $\bar{\nu}_e$ due to two mayor reasons: the charged current interaction has a larger interaction cross section for $\bar{\nu}_e$ with energy of a few MeV than any other processes, and the final state particles (positron and neutron) can be detected in coincidence, which largely suppresses backgrounds compared with the single signal detection.

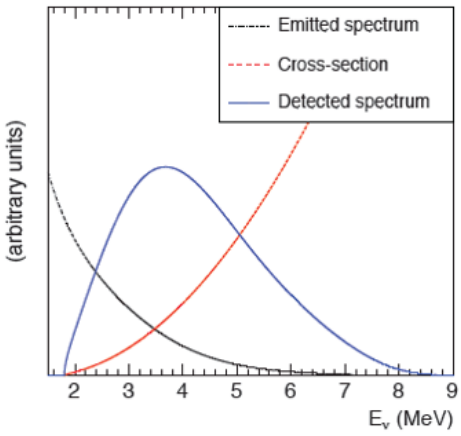

Figure 2.2: Detectable antineutrino spectrum (blue solid line) obtained by folding the emitted reactor antineutrino spectrum (black dash-dotted line) with the IBD cross-section (red dashed line).

As described above, once the antineutrino enters in the detector, it could hit a proton found in the detector liquid scintillator and converts into a positron and a neutron (a schematic view of the reaction is represented in fig. 2.3).

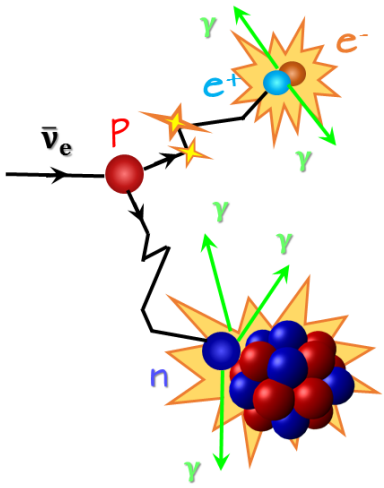

Figure 2.3: Inverse beta decay reaction scheme.

First, the positron suffers multiple scattering losing its energy and it annihilates promptly with an electron of the scintillator. The scintillation light produced by the energy absorbed by the scintillator and the pair annihilation (2×0.511 MeV) is collected by photomultiplier tubes, defining the prompt signal. Secondly, the neutron slowly thermalizes by successive scatterings on Hydrogen atoms until it is captured by a nucleus, predominantly one that is abundant in the liquid scintillator, like H or Carbon, having the first one the larger capture cross-section. Then the nucleus that was in a short-lived excited state, quickly decays releasing γ rays of around 2.2 MeV in the H case and this process produces also scintillation light, causing this

way the delayed signal. Nonetheless, as a result of its large neutron capture cross-section, reactor experiments also use scintillators loaded with Gadolinium (^{64}Gd), being roughly 8×10^9 times larger than Hydrogen. Another advantage of the use of Gd falls on the fact that the energy of the delayed signal due to the neutron capture in Gd peaks at 8 MeV, beyond natural radioactivity that makes harder a H capture analysis. Consequently, the Gd channel has been the main analysis in the single-detector phase of Double Chooz, as well as for Daya Bay and RENO experiments.

Despite this, another IBD detection approach has been devised with the Total neutron Capture technique (TnC), a novel analysis presented for the first time by the Double Chooz collaboration. This approach relies on a maximally opened delayed energy range that allows to integrate over the γ-peaks of all possible isotopes (Gd, H and C) in the full detector volume, thus combing past Gd-only and H-only selections knowledge. This technique will be detailed in Chapter 5.

2.5 The Double Chooz Near and Far detectors

The Double Chooz experiment counts on two identical detectors. Each one consists of a main detector, an outer veto and several calibration devices. The detector is made of four concentric cylindrical volumes with a chimney in the top center that allows to fill in and calibrate these volumes, and a satellite muon detector in the top part. From inside out, the main detector, labeled Inner Detector (ID), is subdivided into three optically coupled tanks: the Neutrino Target (NT), the Gamma-Catcher (GC) and the Buffer tank (BF). Then the Inner Veto (IV) volume surrounds these three regions and finally, both ID and IV, are topped by the Outer Veto (OV) muon detector. Each of this vessels has an opening at the top for a chimney to allow for radioactive source deployment. A schematic view of the detectors is printed in figure 2.4. Furthermore in the case of the FD, a 15 cm thick steel shield surrounds the IV, while in the case of the ND, there is a 1 m thick volume filled with pure water.

2.5.1 Inner Detector

The Inner Detector goal is the measurement of the signals produced by the IBD interaction. A picture taken before the ID top lid closure is shown in figure 2.5. It is possible to distinguish the three volumes (NT, GC and BF) and the photomultiplier tubes (PMTs) in charge of collecting the light signals.

2.5.1.1 Neutrino Target

The Neutrino Target (NT) is the innermost volume of the detectors. Its vessel is an acrylic cylinder of 2.46 m height, 2.30 m diameter and 8 mm thickness filled with 10.3 m^3 of organic liquid scintillator, almost twice more than the liquid present in the original CHOOZ experiment. The acrylic vessel is transparent to ultraviolet and visible photons with wavelengths above 300 nm. The liquid scintillator in the target is composed of 20% ortho-phenylxylylethane (o-PXE), $C_{16}H_{18}$ and of 80% n-dodecane ($C_{12}H_{26}$), thus the ratio of C:H is approximately 1:2. The admixture of

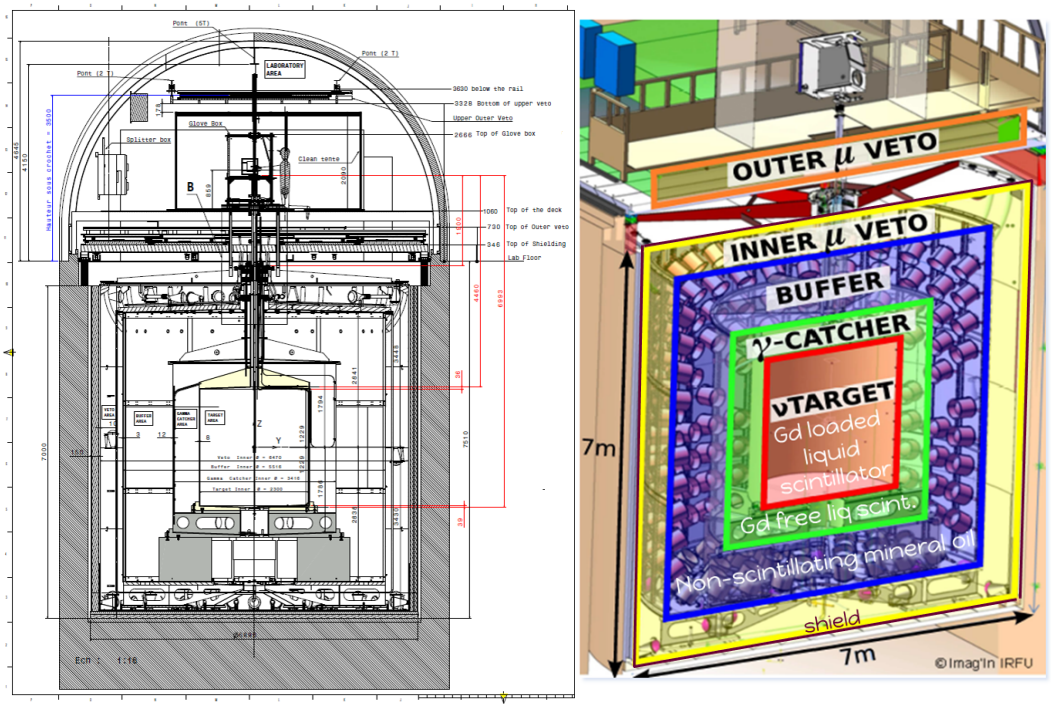

Figure 2.4: Blueprint of the Double Chooz detectors.

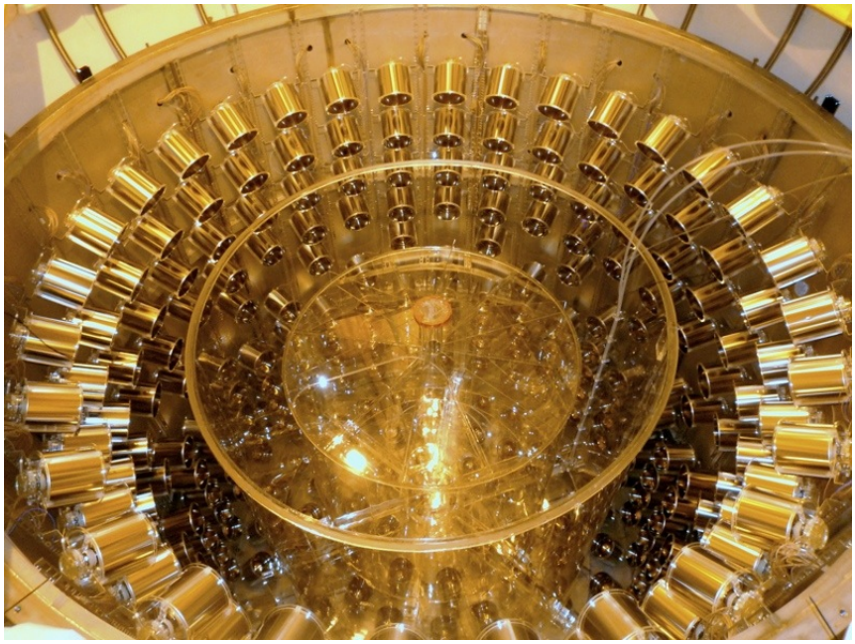

Figure 2.5: Real view of the FD Inner Detector.

the dodecane lowers the light yield, but improves the chemical compatibility with the acrylic vessel and also increases the number of free protons in the neutrino target. The fluors PPO (2,5-diphenyloxazole) and BisMSB (4-bis-(2-methylstyryl)benzene), are added as wavelength shifters to prevent the re-absorption of the scintillation light and to shift the wavelength of the emitted photons to the visible spectrum to match the PMT quantum efficiency range.

The target scintillator is doped with Gadolinium due to its large capture cross-section. With the used concentration of 1 g/l (0.123%) roughly 80% of the neutrons in the target will be captured on Gd. To ensure time stability of the Gd-doped liquid, the Gd atoms are encapsulated in Gd(III)-tris-(2,2,6,6-tetramethyl-heptane-3,5-dionate) molecules [100]. The optical stability of the liquid scintillator is granted by the stability of Gd-fraction in the center of the detector, that is, the relative abundance of neutron captures on the Gd-nuclei in the center of the NT, which has been found to be stable on $<0.1\%$ level over 7 years of data taking, as can be appreciated in figure 2.6. This is one of the main improvements with respect to the CHOOZ experiment, which was limited in sensitivity by the optical instability of its Gd-loaded liquid scintillator.

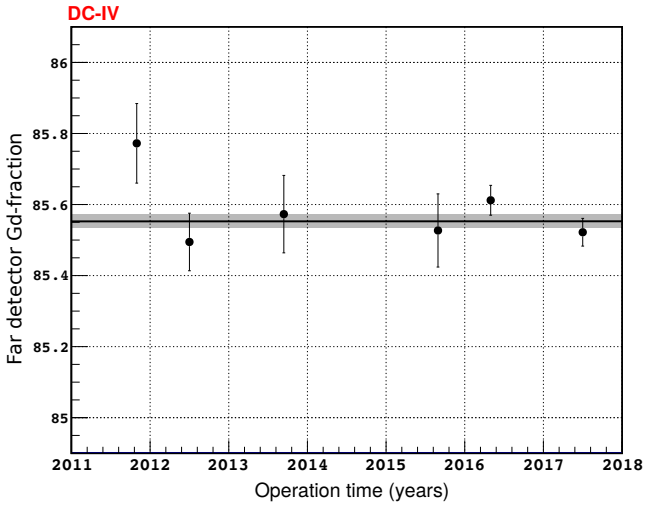

Figure 2.6: Gd fraction for the different calibration campaigns in the Double Chooz FD. The grey line corresponds to the weighted mean value.

2.5.1.2 Gamma Catcher

The Gamma Catcher (GC) volume surrounds the NT and it is made by an acrylic vessel with a thickness of 12 mm and a total volume of 22.4 m^3, that is filled with liquid scintillator (not doped with Gd). This time, since there is no Gd, a commercial mineral oil (Ondina909) is added in addition to the PXE and dodecane to increase the detector response uniformity, matching so the CG with the NT scitillator in light yield and density. The final composition consists of 30% dodecane, 66% mineral oil, 4% PXE, 2 g/l of PPO and 20 mg/l of Bis-MSB.

The main purpose of the GC is to ensure that the energy of the γ's from the IBD reactions produced in the NT is fully absorbed in the scintillating volumes, thus enhancing the efficiency for detecting neutron captures at the edges of the NT,

and improving the uniformity of the detector response. Furthermore the GC is also suitable for detection of IBD reaction products with neutron captures on H, providing a statistical independent analysis from the Gd sample that can be used as validation of the θ_{13} measurement ([101] and [102]). As the GC volume is 2.2 times larger than the NT, this allows to have captures on H almost twice as large as Gd captures, reducing the statistical uncertainty of θ_{13}. On the other hand, the GC also acts as a buffer to fast neutrons entering the detector from outside.

2.5.1.3 Buffer

The Buffer vessel is the outermost volume of the Inner Detector, made from a low background stainless steel and it is filled with a mixture of mineral oil (54%) and n-alkanes. This vessel optically isolates the ID from the IV and serves as support for the 390 10" ID photomultiplier tubes. It has a 105 cm thick layer of non scintillating mineral oil, resulting in a volume of 114 m^3, that shields the NT and GC scintillating liquids from natural radioactivity present in the PMTs, the steel vessel and the surrounding rock. Including the Buffer as additional sub-volume constituted one of the improvements overt the CHOOZ detector design.

2.5.2 Inner Veto

The Inner Veto (IV) is an active liquid scintillator detector surrounding the ID, whose main purpose consists of tagging incoming muons and muon-induced backgrounds, such as fast neutrons, and shielding the ID against low energy radioactive background. The IV is optically isolated from the ID and filled with 90 m^3 of liquid scintillator which is monitored by 78 8" PMTs arranged around the sides (12 PMTs), bottom (48 PMTs), and top (24 PMTs) of the cylinder, with different orientations, maximizing the uniformity of light collection. The IV liquid scintillator composition is a mixture of LAB (Linear Alkyl Benzene) and n-alkanes (CobersolC70) with 2 g/L of PPO and 20 mg/L of bis-MSB. The walls of this vessel are made from steel and are painted in white to increase reflectivity. The outside of the Buffer vessel is coated with a thin polymer film (VM2000), a material highly reflective in the wavelength range 300 - 700 nm, that approximately doubles the light collection.

2.5.3 Shielding

The ID and IV are encased to shield the detector against external gamma rays and neutrons from natural radioactivity. In the case of the FD, the shield consists of 15 cm of low activity demagnetized stainless steel while in the case of the ND a 1 meter-thick water shield surrounds the detector.

2.5.4 Outer Veto

Not only the IV supposes a mayor improvement with respect to the CHOOZ experiment, but also the Outer Veto (OV) does. It is an array of overlapping plastic scintillator strips installed above the stainless steel shield (fig. 2.7). The purpose of the OV is to tag and veto cosmic muons and related background events. The dimensions of the FD OV are 12.8 m×6.4 m centered on the detector chimney, while

in the ND the covered area is larger (11.0×12.8 m^2) due to the higher rate of cosmic muons. With two layers of strips in orthogonal directions, both muon timing and position informations are available. The OV consists of 64 plastic scintillator strips of 5×1×320 cm coupled to 1.5 mm wavelength shifting optic fibers that are connected to the 64 channel multi-anode PMT (Hamamatsu H8804).

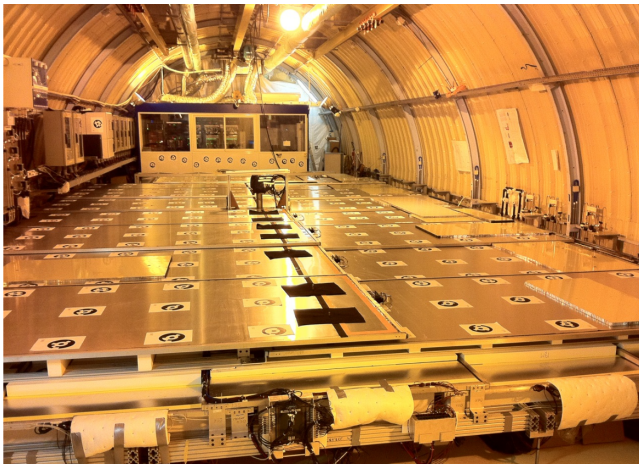

Figure 2.7: Photo of the lower OV in the Double Chooz far hall.

2.6 Photomultiplier tubes

To detect the scintillation light produced in the ID, the experiment relies on a set of 390 10-inch diameter low-background PMTs (R7081MOD-ASSY) produced by Hamamatsu Photonics [103], which are characterized by good photoelectron separation and timing resolution [104],[105]. 270 of these 390 PMTs are held on the buffer tank side walls and the rest are equally divided in the buffer tank bottom and top lid as can be seen in the simulation of fig. 2.8. The PMT glass is made with platinum coating to reduce possible contamination of radioactive isotopes, like ^{238}U. The base circuit part is enclosed in epoxy resin to protect the PMT electronics from the buffer oil.

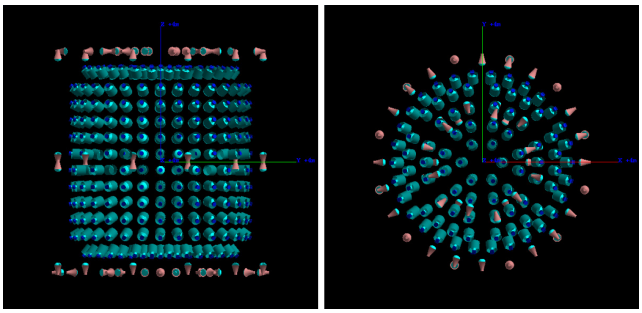

Figure 2.8: Simulated images of the positions of the ID (blue) and IV (brown) PMTs. Left: side view. Right: top view.

The PMT system not only consists of the PMT, but also of a magnetic shield (0.5 mm thick, 275 mm height and 300 mm inner diameter) made with a mu-metal cylinder to suppress effects from magnetic fields [106], a support structure, the High Voltage (HV) supply, the HV/signal splitter to separate the generated signal in the PMT ($\sim$ 10mVpp) from the HV supply ($\sim$1500V) and also to filter the noise induced by the HV supply and the HV cables ($\sim$300 mVpp) and finally, the cable down to the front-end electronics (FEE) (see fig. 2.9).

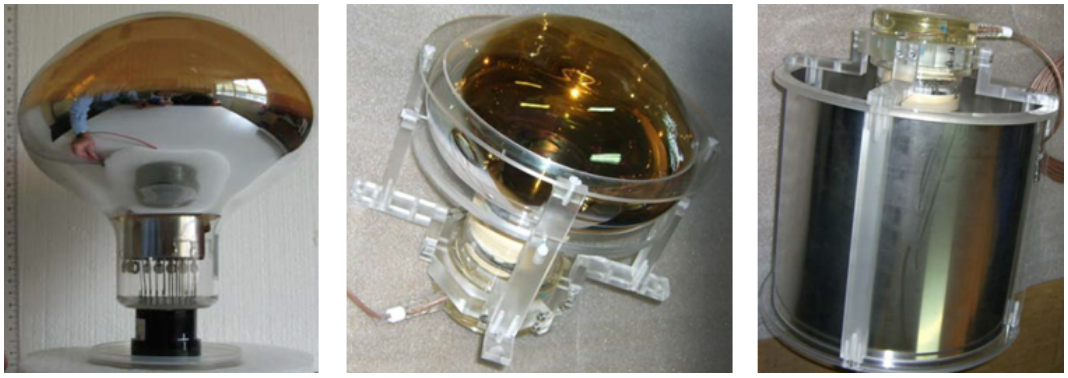

Figure 2.9: Left: Hamamatsu R7081 PMT. Center: one PMT with its base circuit encapsulated in epoxy and the signal cable attached in the acrylic support. Right: one PMT in the mu-metal shield.

In the case of the IV, there are 78 8-inch Hamamatsu R1048 PMTs, recycled from the SuperKamiokande experiment and, originally, the Irvine-Michigan-Brookhaven (IMB) experiment [107]. They are located strategically within the IV to maximize muon detection efficiency, with 24 PMTs on the top wall, 42 on the bottom and 12 circling the middle of the side wall (fig. 2.8). These PMTs and their bases are enclosed within a conical mu-metal structure to shield also from magnetic field, as is illustrated in figure 2.10.

Figure 2.10: Hamamatsu R1408 8" PMT in the IV, encapsulated in stainless steel.

2.7 Acquisition Systems

The search of the IBD neutrino events is possible thanks to a high precision data acquisition system (DAQ). This system is in charge of collecting the scintillation light and its conversion into an electronic signal that is written in readable data for the off line analysis. The Double Chooz experiment has two independent sub-systems, refereed as neutrino DAQ (NuDAQ) and outer veto DAQ (OVDAQ). The NuDAQ is responsible for the ID and IV signals, while the OVDAQ makes the same but for the outer veto system.

2.7.1 NuDAQ

The NuDAQ is a readout system (fig. 2.11) which reads out signals from the 390 ID and the 78 IV PMTs. The photomultiplier detects light at the photocathode which emits electrons by photoelectric effect. The photoelectrons are accelerated by a high voltage potential until they hit a dynode plate, liberating more electrons which will be also accelerated and hit another dynode, knocking out more electrons. This process occurs across 10 dynodes covering a span of about 1.5 kV, producing a gain output on the last dynode (anode) of $\sim 10^7$.

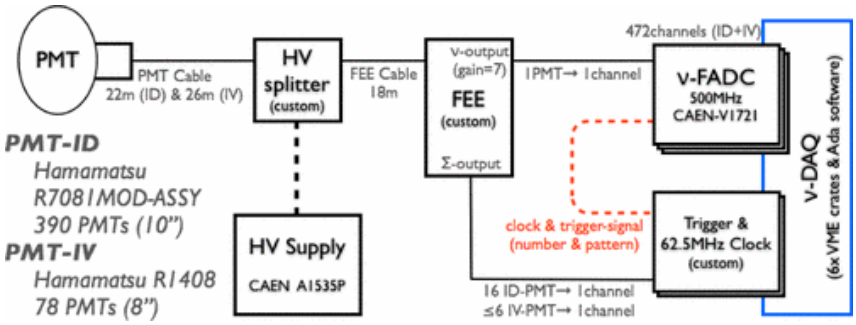

Figure 2.11: Block diagram of the Double Chooz readout and DAQ system [108].

Each PMT is connected via one single cable to the readout system, carrying both the HV and the PMT signal. This is solved using HV splitter boxes, decoupling both components and supplying the PMTs with a HV of 1.3 kV by CAEN-A1533P modules [109]. From the splitter boxes, the signal is sent to the front-end electronic (FEE) modules which amplifies the signals by a factor of 7.8 and filters the electronic noise. The amplified analog signal is afterwards digitized by a ν-FADC system which relies on 64 modules CAEN Vx1721. Each card has 8 channels with 8-bit flash-ADC (FADC) resolution that are sampled at 500 MHz. Each channel is connected to a single PMT, holding up to 1024 4 μs waveforms.

The FEE also delivers the sums of the ID and IV PMT analog signals by groups of 16 ID-PMTs or 5 IV-PMTs, which are send to a custom trigger system [110]. The trigger logic depends on the total charge collected on each board and multiplicity among the group, resulting in charge equivalent to about 0.3 MeV in the ID or 10 MeV in the IV, corresponding to an 8 cm minimum-ionizing muon track. The trigger is designed to be virtually deadtime free and the trigger efficiency is 100.0% above all analysis thresholds. Finally upon discrimination, a trigger signal is simultaneously

sent to all Flash-ADC and the digitalized waveforms are stored by the DAQ.

To read and store the data from the NuDAQ FADC, the Double Chooz experiment makes use of six Read Out Processors (ROP) and Event Building Processors (EBP). The 256 ns signal read from the FADCs is saved as binary file and converted to ROOT format [111] and finally the new data is transferred to off site computers.

2.7.2 OVDAQ

The data acquisition system for the OV is independent from the ID and IV readout. Each multi-anode PMT of the plastic scintillator plane is connected to a readout module with a MAROC2 ASIC [112] which allows an adjustment of the electronic gain of the 64 PMTs analogue signals. When two overlapping scintillator strips record hits, the signals are converted into digitized charge and hit time via FADC and are recorded in a FPGA (Altera EP1C6Q240) [113].

A global clock (32 ns per clock) is provided by the trigger system of the NUDAQ to the OVDAQ in order to share the time stamp among the two DAQs. Finally, the OV data is combined with data from the NUDAQ by the offline event processing.

2.8 Calibration Systems

In a two detectors scheme (FD+ND), the dominant source of systematic uncertainty falls on the differences between both detectors response, requiring a precise knowledge on the energy scale and the detection efficiency. Thus, for any oscillation analysis, it is important to determine accurately the scintillator response, the PMT gain and timing or the absolute energy scale with its non-uniformities and non-linearities, which can be checked using calibration data. In order to achieve this knowledge, several embedded and deployable calibration systems are used and can be divided into two categories: untagged radioactive sources and artificial light sources. All the calibration sources will be the same for the two detectors.

2.8.1 Radioactive Sources

Source deployment in the active volume of the detectors is essential to evaluate the detector responses against physical interactions, as the absolute energy scale and the neutrino detection efficiency. The sources used in the Double Chooz experiment are:

- ^{252}Cf: Californium-252 undergoes into spontaneous fission with average multiplicity of 3.76 neutrons/fission. The 2.223 MeV gammas emitted by the neutron capture on H are used to calibrate the energy uniformity (see section 4.4.2). Moreover it can be used to study the abundance of the Gd and H nuclei at different positions, in particular in the center of the detector.
- ^{60}Co: Cobalt-60 decays via β^- to ^{60}Ni, emitting 1.173 and 1.333 MeV gammas in the prompt energy range of interest for the $\bar{\nu}_e$ selection and it is also used to evaluate the event vertex reconstruction accuracy (see section 4.3).

- ^{137}Cs: Caesium-137 emits 0.662 MeV mono-energetic gamma after β^--decay [114], remaining between the trigger threshold (see section 5.6.1) and the IBD reaction threshold (eq. 2.4) and it can be used to calibrate the scintillator energy resolution (section 4.5) and the reconstructed position.

- ^{68}Ge: Germanium-68 decays by electron capture to ^{68}Ga, which suffers a β^+ decay, converting to stable ^{68}Zn. In the process the annihilation gammas of 0.511 MeV from the positron emitted by this source correspond to the minimum prompt signal for the IBD reaction, thus allowing to calibrate the efficiency of the trigger threshold at different positions to make sure that all IBD positrons are accepted. This source is also used to validate the resolution of the event vertex reconstruction.

All these sources are point-like sources that are encapsulated in very small capsules (approximately 0.3 cm in length and a radius of 0.08 cm) in order to reduce absorption of emitted radiation and shadowing effects.

In addition, natural radiation sources like spallation neutrons or the decay of natural radioactive contamination (^{210}Po) are used to measure the non-uniformity and time stability of the detectors response (see sections 4.4.2 and 4.4.4).

Radioactive sources are deployed into the detectors through two types of deployment systems. One is the Z-axis system to insert calibration sources into the NT and the other one is the guide tube system, allowing the circulation of the sources along the GC (fig. 2.12, left). Both systems entrance consists of a vertical opening along the central vertical axis known as chimney, which is open only during calibration periods. The source deployment into the liquid scintillators is perdormed from a light tight Glove Box, sitting above the detector. The Glove Box (fig. 2.12, right) is continually flushed with nitrogen and kept at the same pressure as the ID, in order to maintain clean and radiopure detector conditions.

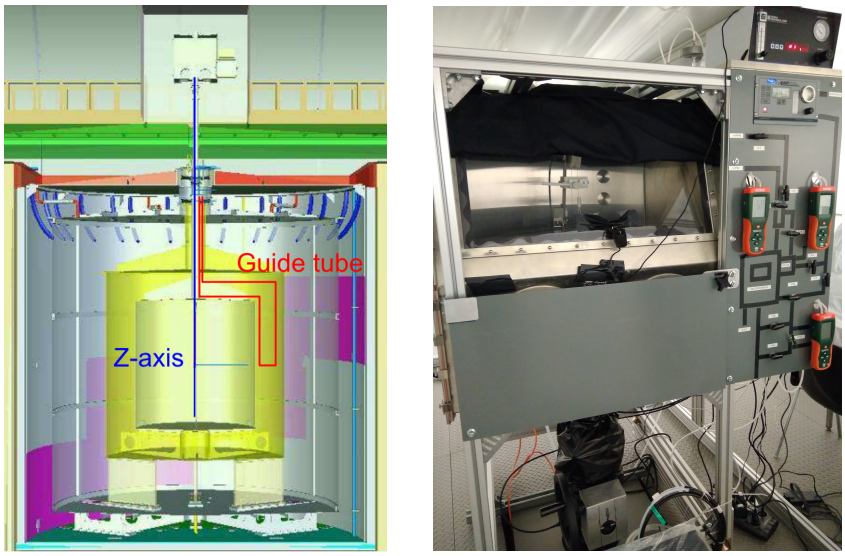

Figure 2.12: Left: Schematic representation of the Double Chooz radioactive source deployment systems. The blue line shows the Z-axis system, while the red line is the guide tube system. Right: Picture of the ND glovebox.

2.8.1.1 Z-axis

Using the Z-axis system, radioactive sources can be deployed along the central vertical axis of the NT using a micro-step motor and pulley-and-line system, which is connected through the ID chimney to the Glove Box (a picture of the system is shown in fig. 2.13). This system lies in an arm with a pulley-and-weight device controlled by a stepper motor with a step of 0.0002 mm with a thin teflon-coated stainless steel cable mounted on it. The source capsule is attached on the edge of a weight, which is tied to this cable.

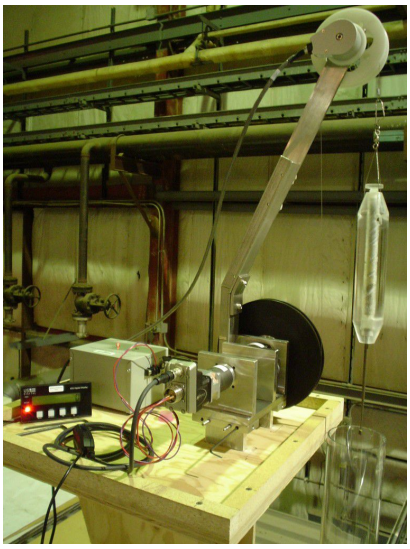

Figure 2.13: Z-axis deployment system before its installation inside the glove box.

Each source can be positioned in a range of 1 cm above the NT bottom up to the chimney, with 1 mm precision, allowing fine control over the location of the source. The system is useful to determine the absolute energy scale at the center of the detector and its position dependence along the central axis. At the top and bottom regions of the NT, it is also possible to estimate the fraction of neutrons which escape from the neutrino target.

2.8.1.2 Guide Tube

The radioactive sources mentioned above can also be deployed in the GC volume along a 5 mm–diameter rigid hermetic stainless steel tube embedded, called the Guide Tube, as shown in figure 2.14. Deployment with this system is performed using a motor-driven wire, guided through the rigid looped tube. It traverses the GC passing near the boundaries of the target and the buffer, making possible the measurement of the neutron capture in the GC volume. The source positions are known to a precision of 1 cm.

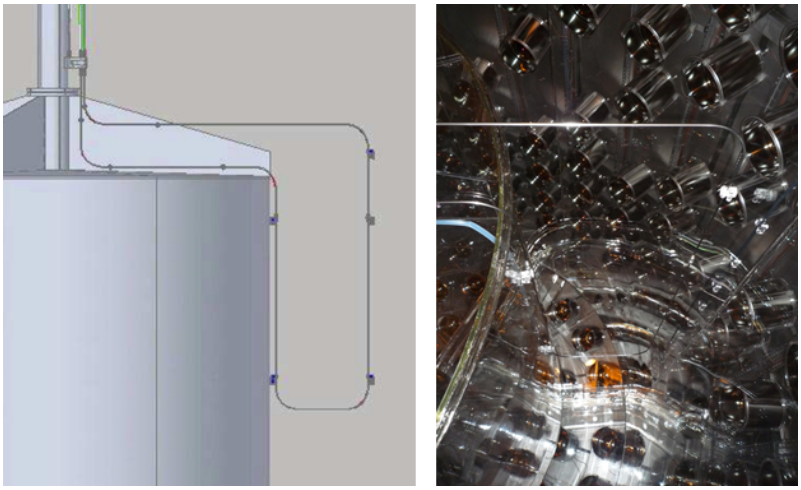

Figure 2.14: Guide Tube CAD image [115] (left) and view inside the GC acrylics vessel of the FD.

During the running period of the Double Chooz experiment, there has been 6 calibration campaigns. The last one took place on August 2017 using the Z-axis system to deploy ^{252}Cf, ^{136}Cs and ^{60}Co radioactive sources in different positions along the NT symmetry axis in both FD and ND, while the Guide Tube system was used in January 2018 for the last time.

2.8.2 Light Injection Systems

Both the ID and the IV are equipped with two dedicated light injection systems: the Inner Detector Light Injection (IDLI) and the Inner Veto Light Injection (IVLI) system, responsible for the PMT calibration of the ID and IV PMTs.

The IDLI system consists of a controller mechanism and a Light Emitting Diodes (LEDs) flasher box connected with optical fibers. These fiber cables are attached to the support structure of the ID PMTs. There are 46 injection points, each one connected with a flasher module in the LED box. These modules have three LEDs with three different wavelengths (385 nm, 425 nm and 470 nm) and a PIN-photo diode as a monitor of LED light intensity. Light emitted by the 385-nm LED is mostly absorbed in the GC, while light emitted by the 425-nm LED is partially absorbed in the GC and NT, and light emitted by the 470-nm LED is not appreciably attenuated. Among all injection points, in 32 of them the light is routed through diffuser plates which spread the beam to an opening angle of about 22°. For the remaining 14 points, the light is routed through quartz optical fibers which produce narrower pencil beams of about 7°.

The IVLI system have a conceptual design that is quite similar to the IDLI. To send light evenly at all the IV channels, light injectors are attached on every single PMT. The light pulses are produced by a board of LEDs installed outside the detector and the light enters inside the IV through quartz fibers. The LED board has 90 LEDs producing blue light (475 nm) and 6 illuminating in the UV region (365 nm).

Calibration data taken with these two systems are used to extract the conversion factor from integrated charge to number of photoelectrons (PEs) that will be de-

scribed in more details in Chapter 4 and to correct for relative timing difference for each channel. These calibration data is acquired weekly to monitor the detector and liquid scintillator properties, as well as the gain and stability of the PMTs.

Chapter 3

Reactor Antineutrino Flux Prediction

3.1 Introduction

This chapter is devoted to explain the MC simulation of the IBD signal interacting in the Double Chooz (DC) detectors, which is essential in the θ_{13} oscillation analysis. During the single-detector phase, the measurement of the mixing angle comes from the comparison of the observed data to the antineutrino prediction and its precision depends strongly on the uncertainty on the knowledge of the neutrino flux and the simulation of the detector response. In the case of the multi-detector analysis (FD and ND working simultaneously), there are two different approaches, one similar to the single-detector fit but including observed and predicted spectra of both FD and ND (Data-MC fit), and the second case (Data-Data fit), in which the ND is used to obtain the predicted spectrum of the FD. The antineutrino flux prediction is described in section 3.2 and the detector simulation is discussed in section 3.3.

The expected rate of $\bar{\nu}_e$ from a reactor R observed through the IBD reaction inside one detector at time t is given by:

$$\frac{dN_R^{\exp}(t)}{dt} = \frac{\epsilon N_p}{4\pi L_R^2} \times \frac{P_{\text{th},R}(t)}{\langle E_f \rangle_R(t)} \langle \sigma_f \rangle_R(t) \tag{3.1}$$

where ϵ is the signal detection efficiency, N_p denotes the number of protons in the detector and L_R represents the distance between the reactor R (B1 or B2) and the considered detector. P_{th} is the thermal power, $\langle E_f \rangle_R(t)$ denotes the mean energy released per fission and $\langle \sigma_f \rangle_R(t)$ corresponds to the mean cross section per fission. These last three terms depend on the composition of the reactor core R and change with respect to time (as explained in section 2.3).

Then the DC simulation consists of two parts, a reactor model corresponding to the second factor of equation 3.1 and a detector model which matches with the first factor.

3.2 Reactor antineutrino flux simulation

3.2.1 Thermal power

The instantaneous thermal power of each reactor core $P_{\mathrm{th},R}$ is provided by the power plant company Électricité de France (EDF) as a fraction of the total power and is evaluated over time steps of less than 1 minute.

In a PWR, the heat produced in the fission chain reaction rises the temperature of the water in the primary loop by thermal conduction through the fuel cladding. The hot primary coolant is pumped into a heat exchanger called the steam generator. Heat is transferred through the walls of the tubes of the steam generator to the lower pressure secondary loop where the coolant evaporates the pressurized steam and is directed to a turbine coupled to an electric generator. The instantaneous thermal power (see fig. 3.1) is derived from the in-core instrumentation, being the temperature of the water circulating in the first loop one of the most important variables.

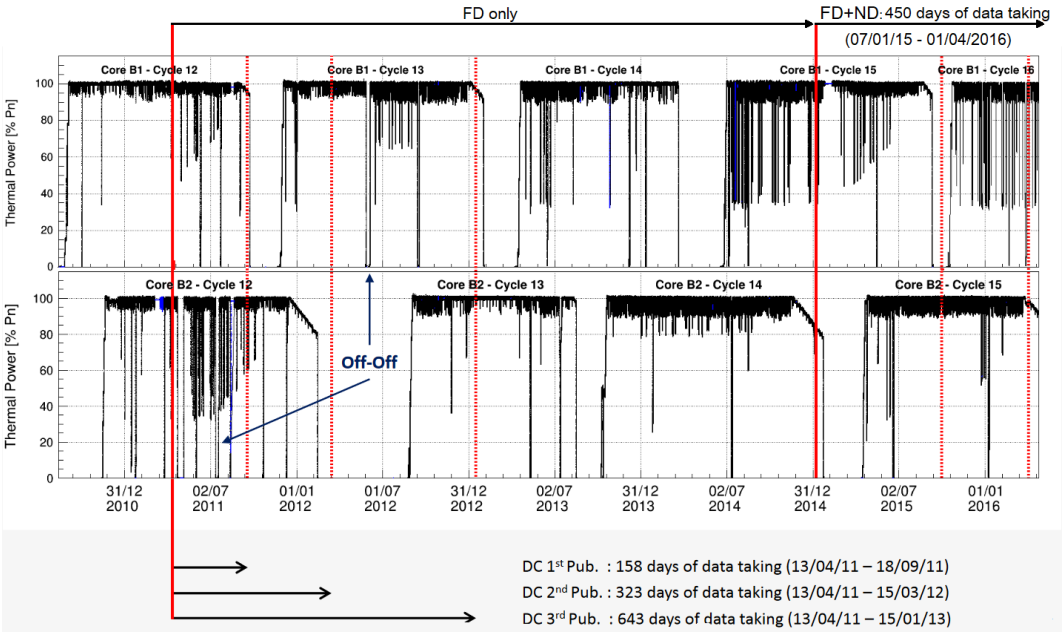

Figure 3.1: Evolution of the thermal power of the B1 and B2 cores. Figure from [117].

The calibration of the core instrumentation is performed on a weekly basis. At the nominal full power of 4250 MW, the 1σ uncertainty of $P_{\mathrm{th},R}$ results in a 0.47% [118]-[120]. Since the amount of data taken when one or the two reactors are off is small, this uncertainty is used for the mean power of both cores.

3.2.2 Mean energy released per fission

The mean energy released per fission $\langle E_f \rangle_R(t)$ depends on the mean fission energy released per isotope $\langle E_f \rangle_k$, being $k =^{235}\mathrm{U}$. $^{239}\mathrm{Pu}$, $^{238}\mathrm{U}$ and $^{241}\mathrm{Pu}$, weighted with the

fractional fission rate $\alpha_{k,R}$ of each nuclide k:

$$\langle E_f \rangle_R(t) = \sum_k \alpha_{k,R}(t) \langle E_f \rangle_k \tag{3.2}$$

Values and uncertainties of the mean energy released per fission and per isotope have been extracted from [121] and are summarized in table 3.1.

Table 3.1: Mean energy released per fission of nuclide $\langle E_f \rangle_k$.

Nuclide	$\langle E_f \rangle_k$ [MeV]	Precision (%)
^{235}U	201.92 ± 0.46	0.23
^{239}Pu	209.99 ± 0.60	0.29
^{238}U	205.52 ± 0.96	0.47
^{241}Pu	213.60 ± 0.65	0.31

The instantaneous fractional fission rate of the isotope k, α_k, of the Chooz reactors is estimated through a dedicated reactor simulation using the MURE package (MCNP Utility for Reactor Evolution) [122], which uses the Monte Carlo static particle transport code MCNP [123]. The validation of the MURE results is done comparing them with the ones obtained using the DRAGON code [124], which uses a two-dimensional deterministic simulation of the neutron transport. The systematic uncertainties of the fraction fission rates are estimated from the discrepancies between the results of the two codes. Evolution of α_k of the four dominant isotopes over time since the beginning of FD is shown in fig. 3.2, and the averaged value over this data taking period and the two reactors is summarized in table 3.2.

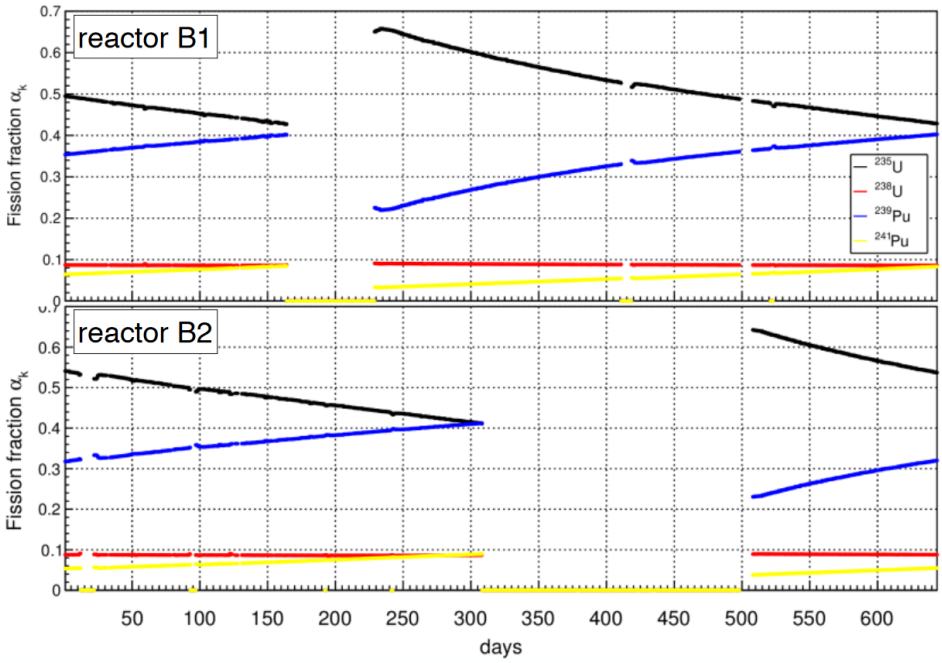

Figure 3.2: Evolution of the fractional fission rate $\alpha_k(t)$ since the beginning of FD data taking for the two reactors B1 and B2. Gaps with no data correspond to periods with reactor off.

Table 3.2: Fractional fission rate $\langle \alpha_k \rangle$ of the isotope k over the period of data taking with only the FD being operational weighted over B1 and B2 reactors.

Nuclide	$\langle \alpha_k \rangle$
^{235}U	0.496 ± 0.016
^{239}Pu	0.351 ± 0.013
^{238}U	0.087 ± 0.006
^{241}Pu	0.066 ± 0.007

3.2.3 Mean cross-section per fission

The non-oscillation flux prediction depends also on the mean cross-section per fission, given by:

$$\langle \sigma_f \rangle_R(t) = \sum_k \alpha_{k,R}(t) \langle \sigma_f \rangle_k = \sum_k \alpha_{k,R}(t) \int_0^\infty S_k(E_{\bar{\nu}_e}) \sigma_{\text{IBD}}(E_{\bar{\nu}_e}) dE_{\bar{\nu}_e} \tag{3.3}$$

where $\alpha_{k,R}(t)$ is the aforementioned fractional fission rate, $S_k(E_{\bar{\nu}_e})$ is the energy spectrum of all the $\bar{\nu}_e$ emitted by the fission of the k^{th} isotope (fig. 3.3) and $\sigma_{\text{IBD}}(E_{\bar{\nu}_e})$ is the inverse beta decay reaction cross-section.

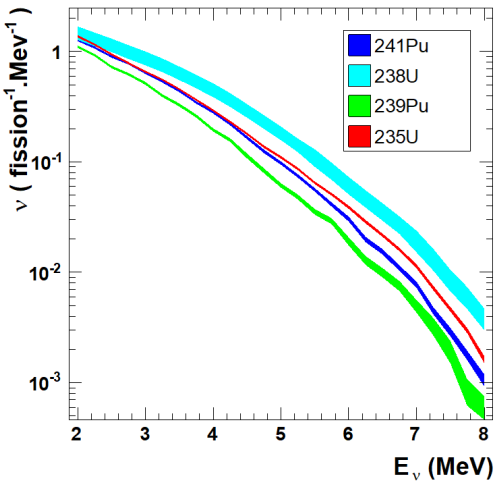

Figure 3.3: Antineutrino energy spectra per fission $S_k(E_{\bar{\nu}_e})$ for ^{235}U, ^{238}U, ^{239}Pu and ^{241}Pu.

In Double Chooz, a re-evaluation of the reference antineutrino spectra $S_k(E_{\bar{\nu}_e})$ from the ILL research reactor [125] is used for ^{235}U, ^{239}Pu and ^{241}Pu isotopes [126], [127]. For ^{238}U, the antineutrino spectrum derived from the research reactor FRM-II, the most powerfull neutron source in Germany, is used [128]. Off-equilibrium effects from [127] are also taken into account.

In order to reduce the uncertainties coming from the reference antineutrino spectra and to cancel any potential neutrino oscillation at very short baseline due to heavy sterile neutrinos, the Bugey4 measurement [129] is used as an anchor point for the

mean cross-section per fission $\langle\sigma_f\rangle_k$ following eq. 3.4:

$$\langle\sigma_f\rangle_R = \langle\sigma_f\rangle^{\mathrm{B4}} + \sum_k \left(\alpha_k^R - \alpha_k^{\mathrm{B4}}\right)\langle\sigma_f\rangle_k \tag{3.4}$$

being $\langle\sigma_f\rangle^{\mathrm{B4}} = (5.75 \pm 0.08)\cdot 10^{-43}\mathrm{cm}^2/\mathrm{fission}$.

The Bugey4 measurement was performed in the 80's at 14 m away from a PWR and having a relative uncertainty of 1.4%, it is up to now the most precise available measurement of the mean cross section per fission. This anchoring reduces largely the flux uncertainty due to its high accuracy, leading only to a small correction term given by small differences in the composition of Bugey and Chooz reactor fuels, $\alpha_k^R - \alpha_k^{\mathrm{B4}}$. The reduction of the flux uncertainty in the single-detector case due to Buyey4 anchor point is illustrated in fig. 3.4. The published fractional fission rate of the isotope k in the Bugey reactor is summarized in table 3.3 (no errors associated to α_k^{B4} since it is assumed that $\sigma_{\alpha_k^{\mathrm{B4}}} = \sigma_{\alpha_k^{\mathrm{DC}}}$).

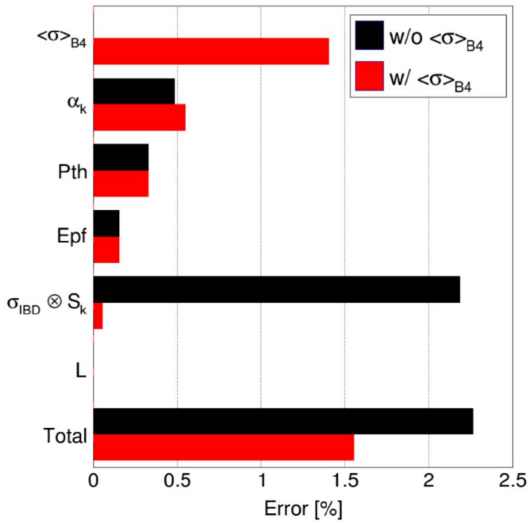

Figure 3.4: Uncertainties in the FD-I flux prediction with or without including Bugey4 anchor point.

Table 3.3: Fractional fission rate $\langle\alpha_k^{\mathrm{B4}}\rangle$ of the isotope k for Bugey4 measurement.

Nuclide	$\langle\alpha_k^{B4}\rangle$
^{235}U	0.538
^{239}Pu	0.328
^{238}U	0.078
^{241}Pu	0.056

On the other hand, the cross-section for the IBD reaction to zeroth order in $1/M_p$, where M_p is the proton mass, can be written as [97]:

$$\sigma_{\mathrm{IBD}} = \sigma(\bar{\nu}_e + p \to n + e^+) = 0.0961\cdot 10^{-42}\left(\frac{E_e\cdot p_e}{MeV^2}\right)\mathrm{cm}^2 \tag{3.5}$$

being E_e and p_e the energy and the momentum of the positron.

3.2.4 Flux uncertainties and error suppression in the oscillation analysis

In the oscillation analysis, the mixing angle θ_{13} is extracted from the comparison of the observed to the predicted neutrino spectra. The reactor flux uncertainty is taken into account in the fit via a covariance matrix. To generate the final covariance matrix, it is needed to compute:

- Predicted flux spectrum per detector (FD-I, FD-II and ND) and per reactor (B1, B2).
- Covariance matrix per detector (3), per reactor (2) and per parameter (6) used to compute the flux prediction of eq. 3.1, including also the Bugey4 anchor point.
- Inter-reactor correlations for each of the 6 parameters.
- Inter-detector correlations for each of the 6 parameters.

3.2.4.1 Predicted flux spectrum

From equation 3.1, the expected rate of $\bar{\nu}_e$ can be extracted. However in the oscillation fit the expected energy-dependant shape spectrum is also relevant. For this purpose, the expected number of $\bar{\nu}_e$ per unit of time in the energy range $[E_i, E_i+\Delta E]$ observed in the detector d in case of no oscillation could be rewritten as:

$$\begin{aligned} \frac{dN_{i,R}^{\exp,d}(t)}{dt} &= \frac{\epsilon N_p}{4\pi L_{d,R}^2} \times \frac{P_{\text{th},R}(t)}{\langle E_f \rangle_R(t)} \times \left(\frac{\langle \sigma_f \rangle_R}{\sum_k \alpha_k^R(t) \langle \sigma_f \rangle_k} \sum_k \alpha_k^R(t) \langle \sigma_f \rangle_{i,k} \right) \\ \langle \sigma_f \rangle_{i,k} &= \int_{E_i}^{E_i+\Delta E} S_k(E_{\bar{\nu}_e}) \sigma_{\text{IBD}}(E_{\bar{\nu}_e}) dE_{\bar{\nu}_e} \end{aligned} \tag{3.6}$$

In the θ_{13} oscillation fit, it is needed to compute the flux prediction per energy bin (38 bins in total, eq. 3.6) for the 3 detectors (FD-I, FD-II and ND) and the 2 reactors B1 and B2, resulting in 6 spectra ϕ_R^d, being $d = [1, 3]$ and $R = [1, 2]$. An example for the predicted spectrum for the ND can be seen in figure 3.5.

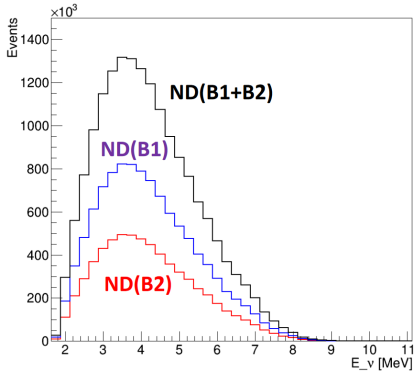

Figure 3.5: ND predicted flux spectrum for each of the reactor B1 (blue) and B2 (red) and the total flux in black.

3.2.4.2 Covariance matrices

In addition to these expected spectra, it is required to calculate the uncertainties of the 6 input parameters used to determine the flux prediction for each of the 6 spectra, that are included as covariance matrices taking into account the correlations between reactors and detectors. These 6 parameters are namely the reactor baselines $L_{d,R}$, the mean energy released per fission per fissile isotope $\langle E_f \rangle_R(t)$, the reactors thermal power $P_{\mathrm{th},R}$, the isotope fission fractions α_k, the mean cross section per fission $\langle \sigma_f \rangle_R$, represented as the product of the spectrum S_k and the IBD cross-section σ_{IBD}, and finally the Bugey-4 mean cross-section per fission as an anchor point $\langle \sigma_f \rangle^{\mathrm{B4}}$.

Each of these variables has its own error matrix M_{ij} (see the two upper rows of figure 3.6 as example), with 38 visible energy bins per detector. The correlation matrices are the lower ones in figure 3.6. $\langle \sigma_f \rangle^{\mathrm{B4}}$, P_{th}, $\langle E_f \rangle_R(t)$ and L_R uncertainties only affect the normalization (Rate-Only errors) and the correlation matrices for these variables show that the bin-to-bin correlation is equal to one. On the contrary, $S_k \otimes \sigma_{\mathrm{IBD}}$ and α_k affect both the normalization and the shape.

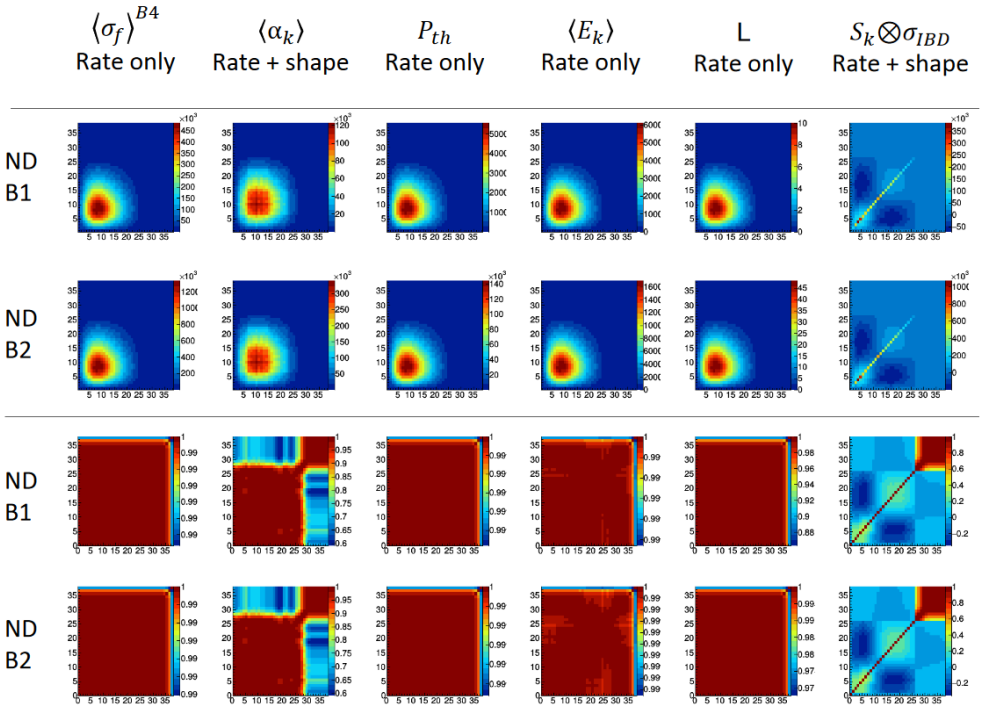

Figure 3.6: Covariance (top) and correlation (bottom) flux matrices for each of the variables involved in the ND flux prediction. X-axis and y-axis correspond to the 38 energy bins used in the oscillation fit, while z-axis represents the variable uncertainty. FD-I and FD-II matrices are obtained in a similar way.

Each element of the covariance matrix associated to the flux prediction for the

bins i and j, M_{ij}, is calculated as:

$$M_{ij} = \sum_{k,l} \frac{\delta N_i}{\delta \omega_k} \mathrm{cov}(\omega_k, \omega_l) \frac{\delta N_j}{\delta \omega_l} \tag{3.7}$$

where N_i (N_j) is the number of predicted events in the i^{th} (j^{th}) energy bin calculated from eq. 3.6, i.e. 38 energy bins of the prediction. ω are the parameters used in the reactor flux prediction, with k and l working as iterator over the 6 inputs parameters. $\mathrm{cov}(\omega_k, \omega_l)$ is the covariance between the flux parameters. Considering that all the parameters are fully uncorrelated, the sum is not null only for the case in which $k = l$.

3.2.4.3 Inter-reactor and inter-detector correlations

Furthermore the flux prediction parameters can be correlated across:

- B1 and B2 reactors
- ND and FD detectors

as can be seen in figure 3.7. These correlations can help to reduce total errors on the antineutrino flux prediction as well as $\sin^2(2\theta_{13})$ uncertainty.

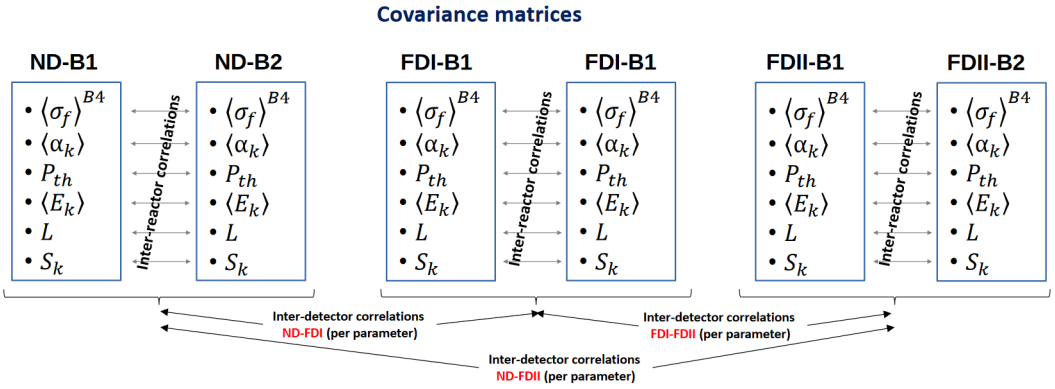

Figure 3.7: Scheme showing inter-reactor and inter-detector correlations for the 6 source of uncertainties in the flux prediction. From [130]

Correlation across reactors The $\bar{\nu}_e$ flux from reactors B1 and B2 observed in the detector d will be:

- $\phi^d_{B1} = f(P^{th}_{B1}, L^d_{B1}, \langle\alpha_k\rangle_{B1}, \langle E_f\rangle_{B1}, \langle\sigma^{B4}_f\rangle, S_k(E)\sigma_{IBD}(E))$
- $\phi^d_{B2} = f(P^{th}_{B2}, L^d_{B2}, \langle\alpha_k\rangle_{B2}, \langle E_f\rangle_{B2}, \langle\sigma^{B4}_f\rangle, S_k(E)\sigma_{IBD}(E))$

The total flux and its uncertainty observed by the detector d will be:

- $\phi^d_{tot} = \phi^d_{B1} + \phi^d_{B2}$
- $\sigma^2_{\phi^d_{tot}} = \sigma^2_{\phi^d_{B1}} + \sigma^2_{\phi^d_{B2}} + 2\rho_{\phi^d_{B1},\phi^d_{B2}}\sigma_{\phi^d_{B1}}\sigma_{\phi^d_{B2}}$

where $\rho_{\phi^d_{B1},\phi^d_{B2}}$ is the correlation coefficient between the flux coming from B1 and the flux coming from B2 and $\sigma_{\phi^d_R}$ is the uncertainty on the flux from reactor R.

Considering the uncertainties in [%], the reduction of the inter-reactor errors with the number of reactors is given by:

$$\sigma^{\alpha}_{\phi^d_{B1+B2}}[\%] = \frac{\sigma^2_{\phi^d_{B1}} + \sigma^2_{\phi^d_{B2}} + 2\rho_{\phi^d_{B1},\phi^d_{B2}}\sigma_{\phi^d_{B1}}\sigma_{\phi^d_{B2}}}{\phi^d_{B1} + \phi^d_{B2}} \tag{3.8}$$

being α any of the 6 variables involved in the flux error prediction.

As example in the case of the single-detector analysis, that is, in the period where only the FD was working (fig. 3.8a), if ϕ_{B1} and ϕ_{B2} are fully correlated, $\rho_{\phi^{FD}_{B1},\phi^{FD}_{B2}} = 1$ and consequently there is no error suppression. Nevertheless, if both are fully uncorrelated between reactors, $\rho_{\phi^{FD}_{B1},\phi^{FD}_{B2}} = 0$ and the total flux error is maximally suppressed (eq. 3.9). Subsequently uncorrelated errors across reactors reduce the uncertainty on the total flux prediction:

$$\begin{aligned} \rho_{\phi^{FD}_{B1},\phi^{FD}_{B2}} &= 1 \implies \sigma_{\phi^{FD}_{tot}} = 2\sigma_{\phi^{FD}_{B1}} \text{ or } \sigma_{\phi^{FD}_{tot}}[\%] = \sigma_{\phi^{FD}_{B1}}[\%] \\ \rho_{\phi^{FD}_{B1},\phi^{FD}_{B2}} &= 0 \implies \sigma_{\phi^{FD}_{tot}} = \sqrt{2}\sigma_{\phi^{FD}_{B1}} \text{ or } \sigma_{\phi^{FD}_{tot}}[\%] = \frac{\sigma_{\phi^{FD}_{B1}}}{\sqrt{2}}[\%] \end{aligned} \tag{3.9}$$

assuming in both cases that $\sigma_{\phi^{FD}_{B1}} = \sigma_{\phi^{FD}_{B2}}$ and $\phi^{FD}_{B1} = \phi^{FD}_{B2}$.

In the single-detector case as well as in the multi-detector case, $\sigma_{\text{IBD}} \times S_k$, $\langle E_f \rangle$ and $\langle \sigma_f \rangle^{\text{B4}}$ are considered to be fully correlated between detectors and reactors. In the case of P_{th} and α_k, one can distinguish two possibilities. The uncertainties of these variables are treated as fully correlated across reactors in the single-detector configuration, assuming a conservative approach, having no error suppression. On the contrary, in the multi-detector case, inter-reactor errors are fully uncorrelated. This way, in both cases, correlations were defined in order to maximize θ_{13} error to be conservative.

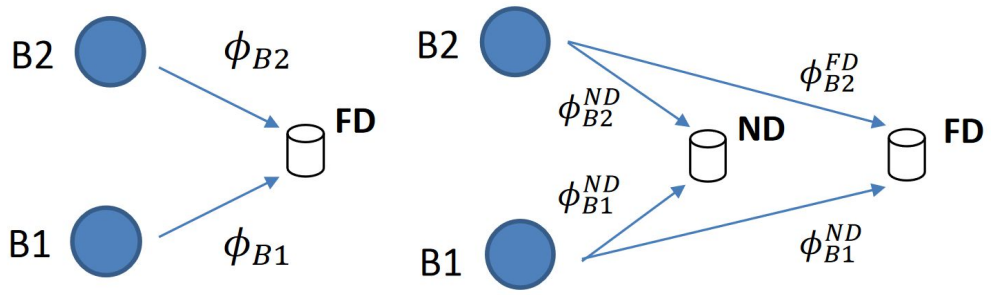

(a) (b)

Figure 3.8: Left: Scheme of the single detector (FD) configuration setup. Right: Scheme of the two detectors (FD+ND) configuration setup.

Correlation across detectors In a two-detector configuration (fig. 3.8b), $\sin^2(2\theta_{13})$ relies on the ratio of the total flux observed by the FD and ND:

$$R = \frac{\phi^{FD}_{tot}}{\phi^{ND}_{tot}} \tag{3.10}$$

with an uncertainty:

$$\begin{aligned}\sigma_R^2 &= \left(\frac{1}{\phi_{tot}^{ND}}\right)^2 \sigma_{\phi_{tot}^{FD}}^2 + \left(\frac{\phi_{tot}^{FD}}{(\phi_{tot}^{ND})^2}\right)^2 \sigma_{\phi_{tot}^{ND}}^2 \\ &- 2\frac{1}{\phi_{tot}^{ND}}\frac{\phi_{tot}^{FD}}{(\phi_{tot}^{ND})^2}\rho_{\phi_{tot}^{FD},\phi_{tot}^{ND}}\sigma_{\phi_{tot}^{FD}}\sigma_{\phi_{tot}^{ND}} \end{aligned} \tag{3.11}$$

As in the single-detector configuration, two possible cases are studied. If ϕ_{tot}^{FD} and ϕ_{tot}^{ND} are fully correlated, then there is maximal error cancellation, while if both are fully uncorrelated there is no error suppression, as can be appreciated in eq. 3.12. So as a result correlated errors across detectors reduce the uncertainty on the ratio, just the opposite scenario to the single detector case.

$$\begin{aligned}\rho_{\phi_{tot}^{FD},\phi_{tot}^{ND}} &= 1 \implies \sigma_R^2 = \left(\frac{1}{\phi_{tot}^{ND}}\sigma_{\phi_{tot}^{FD}} - \frac{\phi_{tot}^{FD}}{(\phi_{tot}^{ND})^2}\sigma_{\phi_{tot}^{ND}}\right)^2 \\ \rho_{\phi_{tot}^{FD},\phi_{tot}^{ND}} &= 0 \implies \sigma_R^2 = \left(\frac{1}{\phi_{tot}^{ND}}\right)^2 \sigma_{\phi_{tot}^{FD}}^2 + \left(\frac{\phi_{tot}^{FD}}{(\phi_{tot}^{ND})^2}\right)^2 \sigma_{\phi_{tot}^{ND}}^2 \end{aligned} \tag{3.12}$$

There is a last ingredient that has influence over the flux uncertainty, the isoflux condition. If the detectors are ideally isoflux, this implies that each detector has exactly the same flux contribution from of each reactor (although there is not necessary identical contribution of each reactor to each detector). In this scenario:

$$\frac{\phi_{B1}^{FD}}{\phi_{B2}^{FD}} = \frac{\phi_{B1}^{ND}}{\phi_{B2}^{ND}} = \alpha \tag{3.13}$$

$$R = \frac{\phi_{tot}^{FD}}{\phi_{tot}^{ND}} = \frac{\phi_{B1}^{FD} + \phi_{B2}^{FD}}{\phi_{B1}^{ND} + \phi_{B2}^{ND}} = \frac{\alpha\phi_{B2}^{FD} + \phi_{B2}^{FD}}{\alpha\phi_{B2}^{ND} + \phi_{B2}^{ND}} = \frac{\phi_{B2}^{FD}}{\phi_{B2}^{ND}} = const \tag{3.14}$$

This carries to full error cancellation whatever the type of correlation be (correlated or uncorrelated) and this is equivalent to the ideal scenario for a θ_{13} experiment: one reactor with two identical detectors. However none of the three reactor experiments are perfectly isoflux, although Double Chooz has the closest isoflux configuration, hence the largest inter-detector correlation resulting in largest suppression error.

As explained in the previous chapter, the period in which only the FD was operative is named FD-I, while in the period after the completion of the ND, the FD is named FD-II. Considering correlations between FD-I and FD-II, it must be taking into account that it is the same detector but the data taking period is different, so in this scenario, it is assumed that the inter-detector errors for P_{th} and α_k are fully uncorrelated. In the case of FD-I to ND, it is assumed that there are no correlations between both detectors.

In the FDII to ND correlation scenario, the flux error nearly cancels thanks to almost fully isoflux site. Thus a suppression factor (SF) is defined to represent the ratio of the uncorrelated error over the total error of ND and FD-II flux prediction, in order to evaluate the percentage of the reactor error uncertainty that cancels thanks to the geometry of the Double Chooz site. In other words, this factor reflects the ability of each experiment to minimize the reactor uncertainty relative to the simple case of a single detector and a single reactor, where no cancellation is expected. Looking at fig. 3.9, it can be extracted that the worst case (the highest SF) matches

SF∼0.12, when both reactors are on, while the total suppression matches SF=0 when only one reactor is on. A conservative approach was followed using finally SF=0.08 assuming that for the considered data set about 1/3 of the data were taken with only one reactor and 2/3 of the data with both reactors on. In the case of FDI to ND comparison, there is no error cancellation due to isofluxness (different period of data taking).

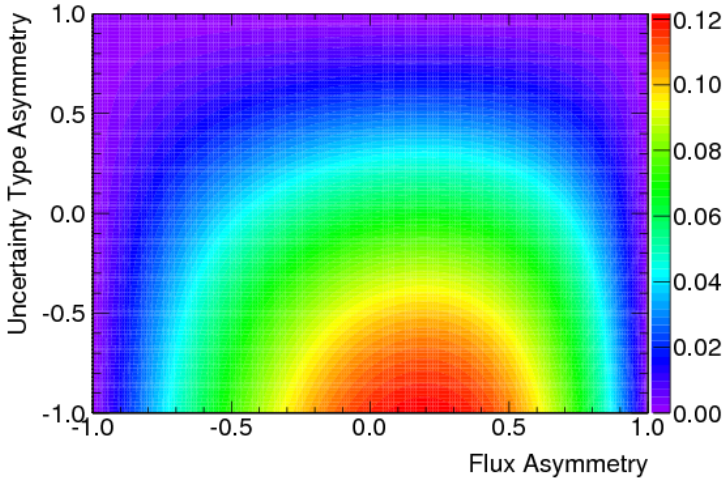

Figure 3.9: Evolution of the suppression factor (z-axis) against both the reactor power flux asymmetry (x-axis), defined as $(\phi_{B2}-\phi_{B1})/(\phi_{B2}+\phi_{B1})$, that is the flux difference between the reactors $B1$ and $B2$, and the reactor uncertainty type asymmetry (y-axis). Figure from [69].

Tables 3.4 and 3.5 show the correlation of each reactor uncertainty type following the inter-reactor correlation explained above. Correlation between ND and FD-I is estimated to be 0.825, between FD-I and FD-II is 0.829.

Table 3.4: Reactor flux uncertainty correlation between ND and FD-I. Second column shows the inter-reactor correlation for each source of uncertainty (1 meaning that is fully correlated, 0 fully uncorrelated). The total error (Tot) is divided in the uncorrelated (Unc) and correlated (Cor) error for each detector and variable.

		ND			FD-I		
Source	Inter-reactor	Unc	Cor	Tot	Unc	Cor	Tot
$\langle\sigma_f\rangle^{\text{B4}}$	1	-	1.41	1.41	-	1.41	1.41
$\langle E_f\rangle$	1	-	0.16	0.16	-	0.16	0.16
$\sigma_{\text{IBD}} \times S_k$	1	-	0.06	0.05	-	0.05	0.06
Baseline L_R	0	< 0.01	-	< 0.01	< 0.01	-	< 0.01
α_k	0	0.6	-	0.6	0.5	-	0.5
P_{th}	0	0.3	-	0.3	0.3	-	0.3
Total		0.66	1.41	1.56	0.64	1.42	1.56
ρ(ND:FD-I)	0.825						

Table 3.5: Reactor flux uncertainty correlation between FD-I and FD-II.

		FD-I			FD-II		
Source	Inter-reactor	Unc	Cor	Tot	Unc	Cor	Tot
$\langle\sigma_f\rangle^{\text{B4}}$	1	-	1.41	1.41	-	1.41	1.41
$\langle E_f\rangle$	1	-	0.16	0.16	-	0.16	0.16
$\sigma_{\text{IBD}} \times S_k$	1	-	0.06	0.05	-	0.05	0.06
Baseline L_R	1	< 0.01	< 0.01	-	< 0.01	< 0.01	-
α_k	0	0.5	-	0.5	0.6	-	0.6
P_{th}	0	0.3	-	0.3	0.3	-	0.3
Total		0.64	1.41	1.56	0.65	1.42	1.56
ρ(FD-I:FD-II)			0.829				

In the reactor correlations, it has been assumed that the inputs that are the same in two flux predictions are fully correlated, but in the case of the thermal power or the fractional fission rate uncertainties, both are considered as fully uncorrelated in the FD+ND analysis, in order to maximize θ_{13} error.

Finally, table 3.6 summarizes the normalization errors on the flux prediction induced by the error of each parameter. For ND, FD-I and FD-II this total uncertainty is the same: $\sim$1.57%, but this uncertainty is partially correlated across the three flux predictions due to the site topology and the synchronization of the period of data taking, as explained above. It can be appreciated that the signal normalization uncertainty is lower when the ND is compared to the FD-II flux than when it is compared to the FD-I, due to the simultaneous data taking. Taking into account the SF factor in the case of ND:FD-II, it can be computed the correlation between ND and FD-II, being ρ(ND:FD-II)=0.993.

Table 3.6: Reactor flux uncertainty on the signal normalization.

		Uncorrelated Error (%)		
Source	Total Error (%)	ND:FD-I	ND:FD-II	FD-I:FD-II
$\langle\sigma_f\rangle^{\text{B4}}$	1.41	-	-	-
$\langle E_f\rangle$	0.16	-	-	-
$\sigma_{\text{IBD}} \times S_k$	0.06	-	-	-
Baseline L_R	< 0.01	-	-	-
α_k	$0.78/\sqrt{2}$	0.57	0.11	0.57
P_{th}	$0.47/\sqrt{2}$	0.33	0.06	0.33
Total	1.57	0.66	0.13	0.66

The values listed in this table are not used as inputs to generate the final covariance matrix for the oscillation fit, but they are useful to demonstrate the reduction of the flux systematics from the 1.68% given in previous analyses in Double Chooz [131], [102], using only the FD data, to the 0.1% uncorrelated uncertainty between the ND and FD-II because of the iso-flux configuration and simultaneous data taking.

Once the flux spectra and the inter-reactor and inter-detector correlations have been obtained, a covariance matrix of 114×114 elements (38 bins per detector) is built for each of the 6 parameters, considering these correlations. The scheme of this

matrix is shown in figure 3.10. The final total 114×114 covariance matrix can be built as a sum of the 6 114×114 matrices associated to each parameter (see figure 3.11):

$$M_{tot} = M_{\langle\sigma_f\rangle^{B4}} + M_{\langle\alpha_k\rangle} + M_{P_{th}} + M_{\langle E_k\rangle} + M_L + M_{S_k \otimes \sigma_{IBD}} \tag{3.15}$$

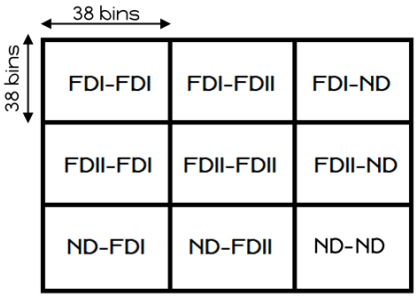

Figure 3.10: Scheme of the 114×114 covariance matrix of the flux prediction.

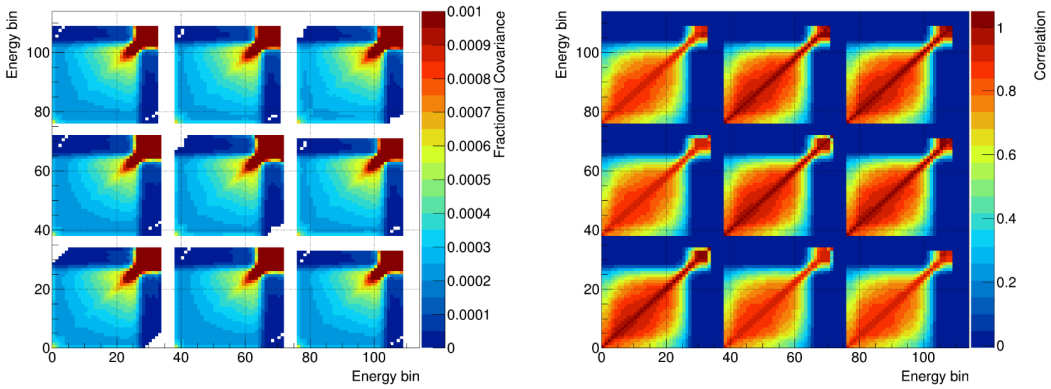

Figure 3.11: Final 114 x 114 covariance matrix (left) used as input in the oscillation fit with inter-reactor and inter-detector correlations applied. The matrix is fractional, divided by bins contents. The correlation matrix of the flux prediction is shown in the right part of the figure.

3.3 Simulation of IBD detection

3.3.1 Detector simulation

The Double Chooz detectors are modeled using a detailed Geant4 simulation based on the DCGLG4sim package [132], a toolkit for the simulation of the particles path through matter. The code has been customized in order to enhance the scintillation process, the photocathode optical surface model and the neutron thermalization process.

The optical properties of the scintillator liquids were evaluated from measurements made in the laboratory [133] and were used as inputs in the MC simulation. These

optical parameters include the light yield on the NT and GC liquid scintillators, scintillator timing and emission spectrum, light attenuation and probability of light reemission, the ionization quenching (Birk's law quenching [134]) and refractive and reflective coefficients of different detector materials.

The detector geometry, including vessels and tanks, and detector materials as well as the PMTs and support structures have been implemented in great detail. The orientation and positions of the components are known using a photographic survey with sub-mm accuracy.

3.3.2 Readout system simulation

The Readout System Simulation (RoSS) accounts for the response of the elements associated with the detector event readout, for instance, trigger system, front-end electronics, flash-ADC and the modeling of the full data acquisition (DAQ) with the PMTs. The simulation implements a probability distribution function (PDF) to characterize the response of each single photoelectron p.e. based on the measurement of the components response. These single photoelectrons are accumulated to produce a waveform signal for each PMT which is digitalized by the flash-ADC conversion with a 2 ns time bin. Channel to channel variations, such as gain, baseline and noise, are also taken into account in the same way as to data, so the simulation exhibits a similar dispersion as the IBD data (see Chapter 4 for more details).

3.3.3 MC event generator

Simulated IBD events are generated with run-by-run correspondence of MC to data by integrating equation 3.6 over time and energy range. Neutrino energy is assigned randomly, as well as the IBD interaction position, which is weighted as a function of the proton density in the detector. The momenta of the positron and neutron is estimated from the neutrino energy and the decay kinematics. To suppress statistical errors, the ND MC simulation contains 10 times more events than the expected ones, while in the case of the FD, the MC contains 100 times more events.

Chapter 4

Data event Reconstruction

4.1 Introduction

Raw events collected by the PMTs of the Double Chooz detectors need to be reconstructed in terms of energy and vertex position in order to collect information that will be used later to select the IBD candidates. The performed neutrino oscillation analysis that will be explained in Chapter 7 is energy-dependent, as was seen in the survival probability of the electron antineutrino, equation 1.48, so a precise energy reconstruction is vital for the $\bar{\nu}_e$ normalization.

4.2 Pulse reconstruction

Event reconstruction begins from pulse reconstruction, extracting the charge and the time of the signal for each PMT from the digitized waveform recorded by the flash-analog to digital converter (FADC). These waveforms cover 256 ns in 128 samples with a width of 2 ns and they are used to compute the baseline (B_{mean}) (pedestal) and its fluctuation as RMS (B_{rms}). PMT charge is calculated once the baseline B_{mean} is subtracted from the integration of the waveform in a fixed 112 ns window, reconstructed in Digitized Units of Charge (DUQ). The waveforms are also used to calculate the time variables of the pulse, which are reconstructed in ns. On one hand, there are two conditions that are imposed to avoid noise fluctuations:

- At least 2 ADC counts with respect to the baseline are required for the maximum amplitude of the waveform.
- The pulse should be above the charge threshold of $Q_{min} = B_{rms} \times \sqrt{N_{win}}$, where N_{win} is the number of samples in the integration window (56 for a 112 ns window).

And on the other hand, the timing attributes should satisfy the following requirements:

- The start time T_{start} of the integration must correspond to the 30% of the maximum amplitude (before reaching maximum).
- The end time T_{end} of the integration must correspond to the 20% of the maximum amplitude (after reaching maximum).
- The maximum T_{max} corresponds to the maximum amplitude.

Definition of the mentioned time variables are illustrated in figure 4.1.

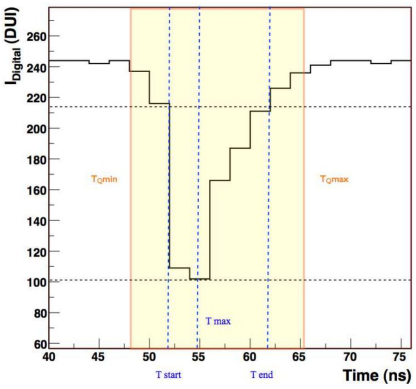

Figure 4.1: Example of a recorded digitized waveform showing pulse time definitions. Yellow band includes the charge integration window.

4.3 Vertex reconstruction

The reconstruction of the interaction vertex for each triggered event is performed using a maximum likelihood algorithm based on charge and time. It is assumed that each event is a point-like instantaneous light emission defined by $\mathbf{X} = (x_0, y_0, z_0, t_0, \Phi)$, where (x_0, y_0, z_0) is the spatial position in terms of the detector coordinates, t is the time of the light emission and Φ is the amount of light per unit solid angle in units of photons per steradian.

For each event, the amount of light deposited at the ith PMT can be predicted as:

$$q_i^{\text{pred}} = \Phi \times \Omega_i \times A_i \times \epsilon_i \tag{4.1}$$

being Ω_i the solid angle between the light emission point and the PMT, A_i is the light transmission amplitude, which includes the effects of the light attenuation and the dependence on the incident angle, and ϵ_i is the quantum efficiency for the ith PMT. Besides this, the prompt arrival time at the ith PMT can be written as:

$$t_i^{\text{pred}} = t_0 + \frac{r_i}{c_n} \tag{4.2}$$

where r_i is the distance of the ith PMT to the vertex position and c_n is the speed of light along the light path.

Taking these two predicted variables into account, an event likelihood is constructed to compare the observed PMT charge and the arrival time with the predicted ones:

$$\mathcal{L}(\mathbf{X}) = \prod_{q_i=0} f_q(0, q_i^{\text{pred}}) \prod_{q_i>0} f_q(q_i, q_i^{\text{pred}}) f_t(t_i, t_i^{\text{pred}}) \tag{4.3}$$

The first product makes reference to the PMTs that have not been hit and the second runs over the PMTs that recorded non-zero charge q_i. $f_q(q_i, q_i^{\text{pred}})$ and $f_t(t_i, t_i^{\text{pred}})$ are respectively the probability to measure a charge q_i given a predicted charge q_i^{pred} and the probability to measure a time t_i given a predicted light arrival time t_i^{pred}. These density functions PDF are obtained from laser calibration data, while the effective light attenuation length and the PMT angular response, included in A_i, are tuned with source calibration data.

The goal of the event reconstruction is to find the best parameters of $\mathbf{X}$ which maximize the event likelihood or equivalently, minimize the log-likelihood function, referred in Double Chooz as the functional value F_V:

$$F_V = -\ln \mathcal{L}(\mathbf{X}) = -\sum_{i=0}^{N_{\text{PMT}}} \ln f_q(q_i, \mathbf{X}) - \sum_{q_i>0} \ln f_t(t_i, \mathbf{X}) = F_V^q + F_V^t \tag{4.4}$$

This functional value will be used also to reject some muon induced backgrounds, described in Chapter 5.

The vertex reconstruction performance have been evaluated using calibration sources deployed at known positions in the z axis along the target. The resulted resolution is around 12 cm for the source positions, as shown in fig. 4.2 for the ^{68}Ge source [135], 17 cm for the ^{137}Cs and 12 cm for the ^{60}Co source.

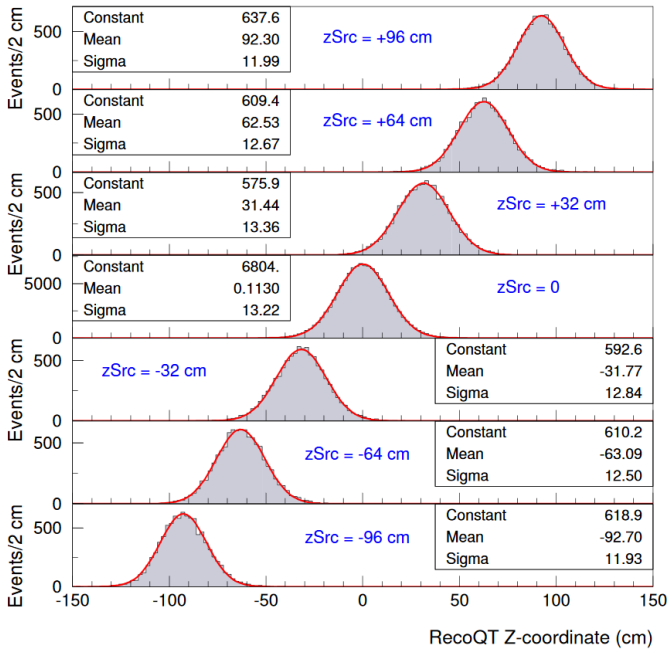

Figure 4.2: Reconstructed z coordinate for the ^{68}Ge source data deployed at 7 different positions along the z-axis.

4.4 Energy reconstruction

The visible energy (E_{vis}) provides the absolute calorimetric estimation of the energy deposited per trigger in the detector. The energy reconstruction method is based on the conversion of the total number of photoelectrons (p.e.) collected by the PMTs to the visible energy, applying correction factors for taking into account readout effects, spatial uniformities and time instabilities or non-linearities. Energy reconstruction procedure is similar between data and MC, but there are steps specific only to one of them. Despite the energy is reconstructed independently for FD and ND, the absolute energy scale is equalized between detectors and between data and MC, in order to avoid any possible bias in the oscillation fit. Thus, the visible energy is reconstructed like:

$$E_{vis}^{data} = N_{pe}^{data} \times f_u^{data}(\rho, z) \times f_{MeV}^{data} \times f_{st}^{data}(E_{vis}^0, t) \quad (4.5)$$

$$E_{vis}^{MC} = N_{pe}^{MC} \times f_u^{MC}(\rho, z) \times f_{MeV}^{MC} \times f_{nl}^{MC}(E_{vis}^0) \quad (4.6)$$

where the parameters ρ and z represent the vertex position in the detector coordinates, being ρ the radial distance from the central vertical axis and z the vertical coordinate. The event time is defined as t (elapsed days) while E_0 represents the energy after applying the uniformity correction. Each term of equations 4.5 and 4.6 will be described in more detail in the next subsections.

4.4.1 Linearized Charge to PE conversion

The total number of photoelectrons is given by:

$$N_{pe} = \sum_i \frac{q_i}{g_i(q_i, t)} \quad (4.7)$$

where i refers to all accepted PMT channels (i.e. channels with stable mean charge and pedestal), q_i is the integrated charge of each channel obtained following the procedure described in section 4.2 and g_i is a charge-to-p.e. conversion factor, known as gain. This gain is not only charge dependent but also it changes after each power cycle of electronics, so it needs to be calibrated periodically. In fact, LED light injection calibration data of different intensities is used to measure the gain of each channel, observing non-linearities especially at low energy depositions [137]. This non-linearities become from the fact that the Double Chooz FADCs are only 8-bit, which results in poor baseline estimation, biased within ±1 ADC count. The gain non-linearity of figure 4.3 is parametrized as a curve represented by three parameters, constant gain at high charge $g0$, non-linear slope at low charge and the transition point. The comparison of the calibration constants between two power cycles is displayed in figure 4.4, showing on the left the readout gain (g0) and on the right the slope for the ND channels in early 2015 versus early 2016. The gain g0 is fully correlated while the slope is fully uncorrelated, pointing out that it has to be re-calibrated periodically.

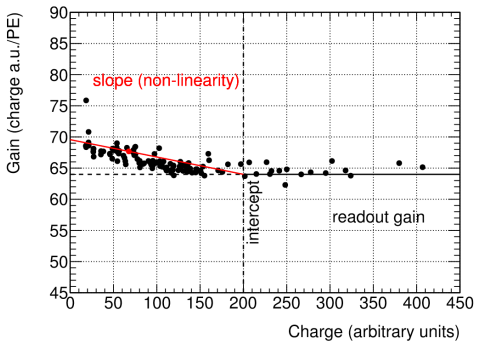

Figure 4.3: Gain as a function of the integrated charge for a ID channel. The gain function is obtained from a fit with three parameters: slope at low charge, the constant gain at high charge and the intersection of the two lines.

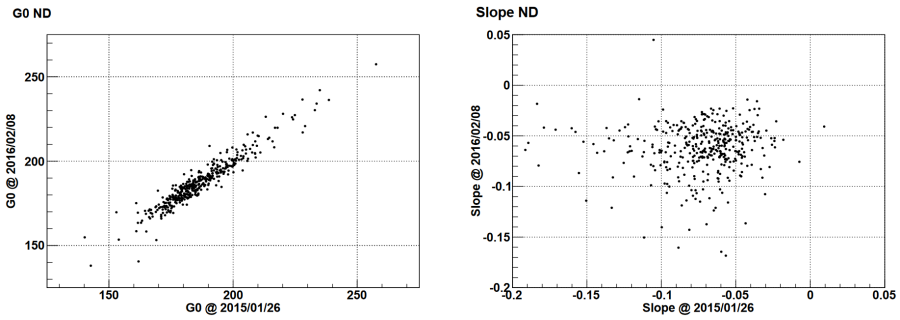

Figure 4.4: Stability of the gain calibration constants. On the left, the gain at high charge for the ND channels in January 2015 versus February 2016. On the right, the non-linearity slope at low charge.

4.4.2 Uniformity calibration

The number of collected p.e. depends on the position of the event in the detector, due to geometrical effects or differences in the PMTs or the electronic response. This effect is corrected by the uniformity calibration $f_u(\rho, z)$, which is applied in the form of a 2D map in (ρ, z) coordinates, in the way that the corrected number of p.e, $\mathrm{N}_{pe}(\rho, z) \times f_u(\rho, z)$, is equal to the one obtained at the center of the detector $\mathrm{N}_{pe}(\rho = 0, z = 0)$.

These correction maps are created both for data and MC. In the case of the data maps, spallation neutrons are used due to their large abundance and their uniformity distribution in the detector volume, while in the case of the MC maps, IBD simulations are used since there is no muon or spallation neutron simulations. To generate these maps, first of all event vertices are reconstructed following the charge+time fit of the PMT hit (see section 4.3). Secondly the detector is subdivided into 24×24 bins in (ρ, z) and $\mathrm{N}_{pe}(\rho, z)$ is measured for each bin using the capture of spallation neutrons by H-nuclei as explained in figure 4.5. Finally the 2D map is build based on:

$$f_u(\rho, z) = \frac{N_{pe}(\rho = 0, z = 0)}{N_{pe}(\rho, z)} \tag{4.8}$$

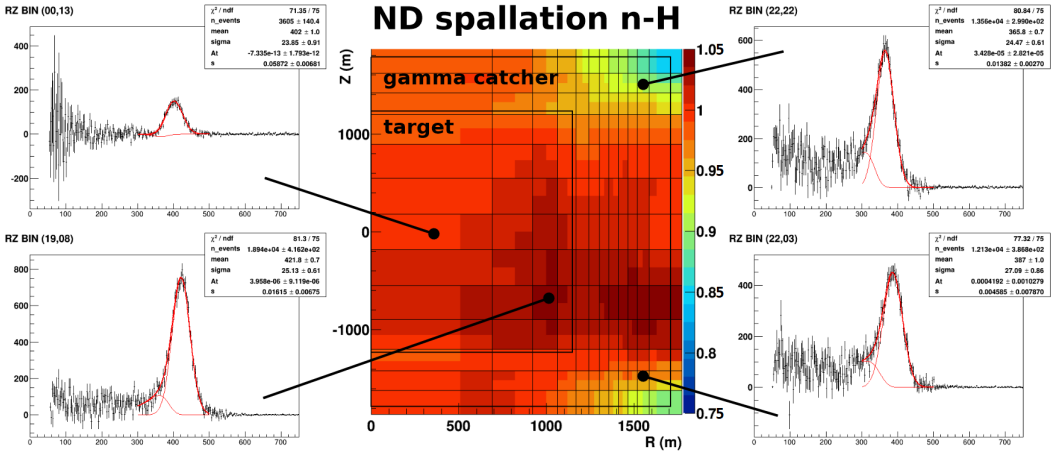

Figure 4.5: Example of the generation of the uniformity correction maps, corresponding to $f_u^{-1}(\rho, z)$ made from the Gaussian fits of the p.e. peaks corresponding to H captures. The x-axis of the gaussian fits corresponds to the number of p.e. for a specific cordinate (ρ, z).

The resulting maps for data and MC for the FD-I, FD-II and ND are shown in figure 4.6. On the other hand, the systematic uncertainty is built from another set of maps, this time generated once the full visible energy calibration is completed, and making 2D asymmetry maps between data and MC also for FD-I, FD-II and ND, which are defined as 2×(data-MC)/(data+MC) (plotted in fig. 4.7). The RMS of the 1D projection of these asymmetry maps is taken as systematic uncertainty due to the uniformity correction, obtaining thus uncertainties of 0.25% for FD-I and FD-II and 0.39% for ND in the detector volume (NT+GC).

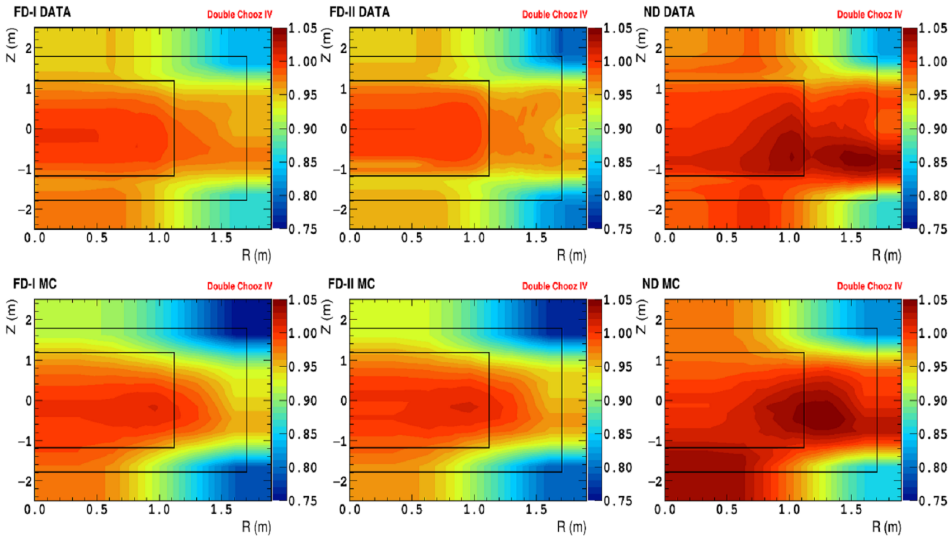

Figure 4.6: Uniformity calibration maps (corresponding to $f_u^{-1}(\rho, z)$ of equation 4.8) for FD-I (left), FD-II (middle) and ND (right). The upper maps correspond to data while the lower correspond to MC.

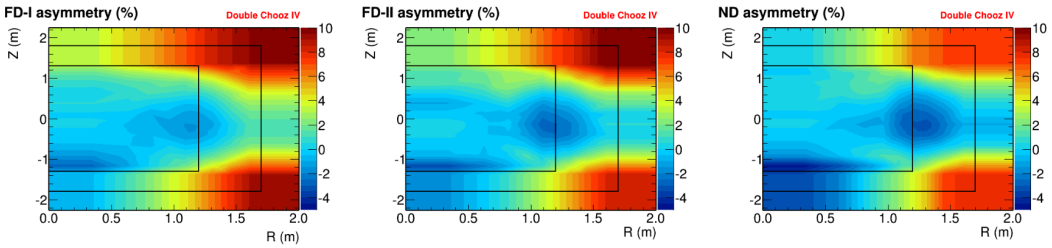

Figure 4.7: Asymmetry maps between data and MC after full visible energy calibration for FD-I (left), FD-II (center) and ND (right). Their 1D projection are considered as the systematic uncertainty of the uniformity correction.

4.4.3 Absolute energy scale calibration

The absolute energy scale correction factor $f_{pe/MeV}$ converts the number of p.e. to MeV and it is determined from the position of the 2.2 MeV capture peak of neutrons by a H nucleus, using to that effect ^{252}Cf calibration data and MC taken at the detector center (see figure 4.8). The corresponding conversion results $f_{pe/MeV}$ are summarized in table 4.1.

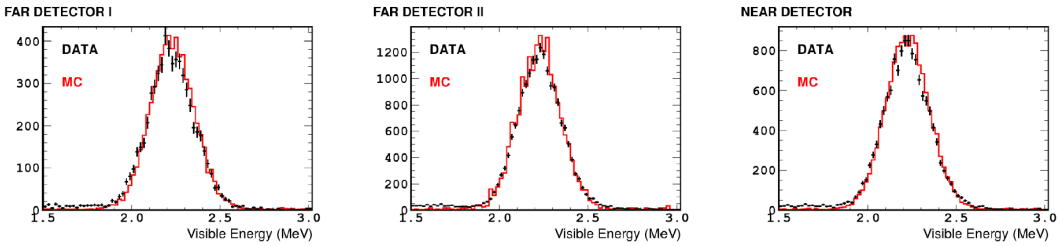

Figure 4.8: ^{252}Cf n-H energy spectra for data (black points) and MC (red solid line) at detector center used to extract the absolute energy scale correction factor $f_{pe/MeV}$ for FD-I (left), FD-II (center) and ND (right).

Table 4.1: Absolute energy scale correction factor $f_{pe/MeV}$ for FD-I, FD-II and ND.

	FD-I	FD-II	ND
Data $f_{pe/MeV}$	186.2	219.6	186.7
MC $f_{pe/MeV}$	186.6	197.9	182.8

4.4.4 Time stability correction

To account for the time dependence of the number of p.e. due to fluctuations in the electronic gain during a power cycle period or changes in the scintillator response, a stability correction factor $f_{st}^{data}(E_{vis}^{0}, t)$ is included in the energy reconstruction function. These instabilities are not taken into account in the MC, so this time stability correction is only applied to data. It is estimated using spallation neutron captures on Gd and neutron IBD captures on H as well as the energy deposited by α-decays of ^{210}Po (visible energy of $\sim$1 MeV after quenching, allowing to monitor

the lower energy neutron below the Gd and H peaks), as illustrated in figure 4.9.

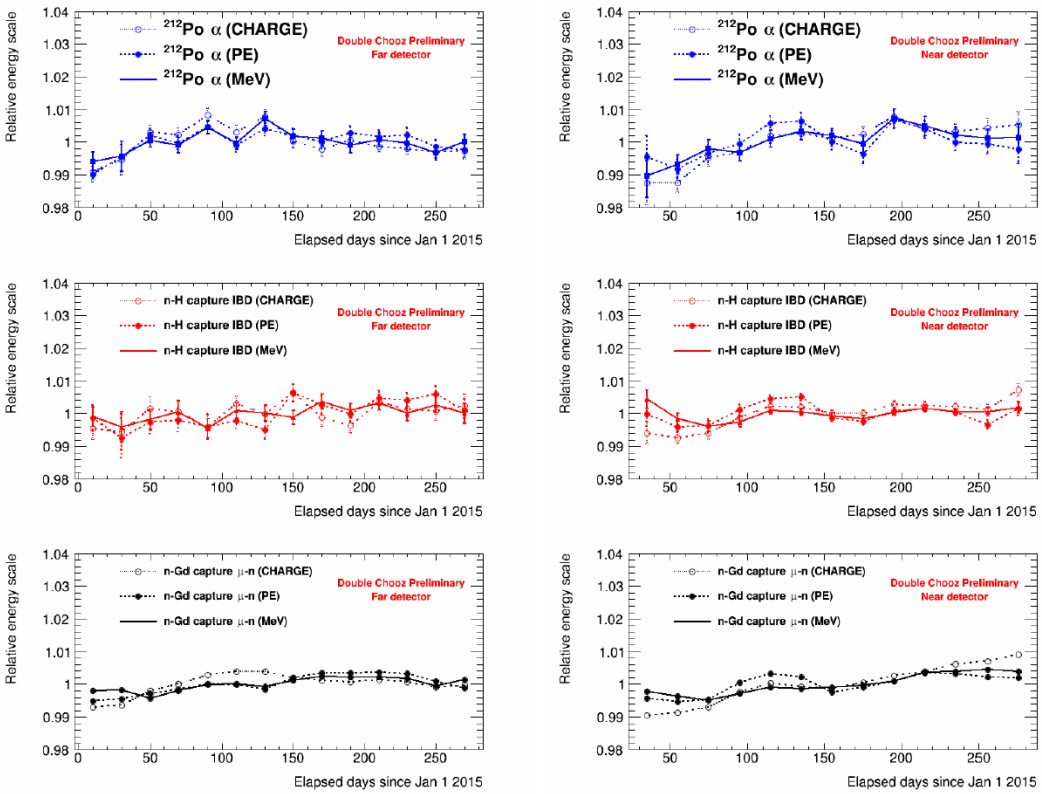

Figure 4.9: Effect of the time stability corrections for the α-decay of ^{210}Po (top plots), n-H captures (middle plots) and n-Gd captures (bottom plots). The y-axis represent the ratio of the peak energy of the three sources to their nominal value. Dotted line with empty circles represents reconstructed charge before any application of the linearized p.e. or stability corrections. Dashed line with full circles are p.e. once the linearized p.e. correction is applied and finally the solid line represents the visible energy after stability correction is also applied. Left plots correspond to FD-II while right ones correspond to ND.

The systematic uncertainty associated with this correction is obtained from a convolution of an error function which depends on the RMS of the time stability response with the non-oscillated MC prompt spectrum. This error function is anchored by the three data points, corresponding to the dispersion of the visible energy of ^{210}Po, spallation n-Gd and IBD n-H captures. The distributions involved in the convolution for each detector are plotted in fig. 4.10. The total uncertainties are defined as the integral of the convoluted histogram (named as folded spectrum in the figure), being 0.34%, 0.37% and 0.46% for FD-I, FD-II and ND respectively.

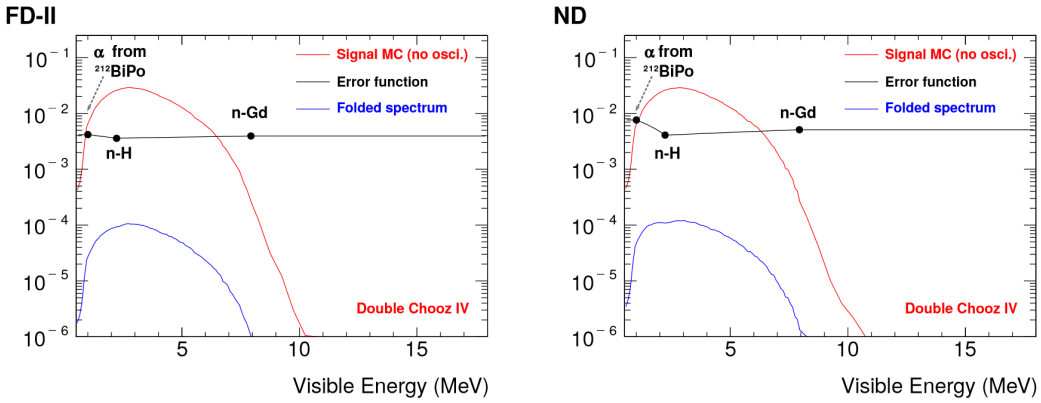

Figure 4.10: Method to obtain the systematic uncertainty associated to the time stability correction. The energy stability error function is displayed in black while the non-oscillated MC is done in red. The integral of the convoluted spectrum of both spectra provides the systematic uncertainty. The FD-II spectra are shown on the left part of the figure, the ND spectra in the right plot.

4.4.5 Non-linearity correction

The visible energy of the MC needs to be corrected for its remaining non-linearity relative to that presents in the IBD data set in order to improve the agreement between data and MC. This non-linearity arises from two sources, the charge non-linearity (QNL) and the light non-linearity (LNL), which are described separately in the following sections.

4.4.5.1 Charge non-linearity correction

This contribution is predominantly due to electronic effects, like the modeling of the readout system or the charge integration algorithm. The QNL correction is extracted from the ratio between n-Gd and n-H captures of the ^{252}Cf source at the center of the detectors. The γ emitted from the n-H capture has an energy of roughly 2.22 MeV/γ, while in the case of the n-Gd capture, three γ's are emmitted with a total energy of roughly 8 MeV. However the average energy of a single γ is 7.94 MeV / 3.6 γ's $\sim$ 2.21 MeV/γ, so the energy response should be the same in both capture peaks.

The QNL correction f_{qnl} adjusts the measured visible energy E_{vis} of the Gd-to-H peak ratio to the theoretical value 7.937 MeV/2.224 MeV with a linear function of the form $f_{qnl} = b_{qnl} + c_{qnl} \times E_{vis}$ and it is calculated for FD-I, FD-II and ND ^{252}Cf data and MC as can be appreciated in fig. 4.11. The parameters b_{qnl} and c_{qnl} for each detector are listed in table 4.2.

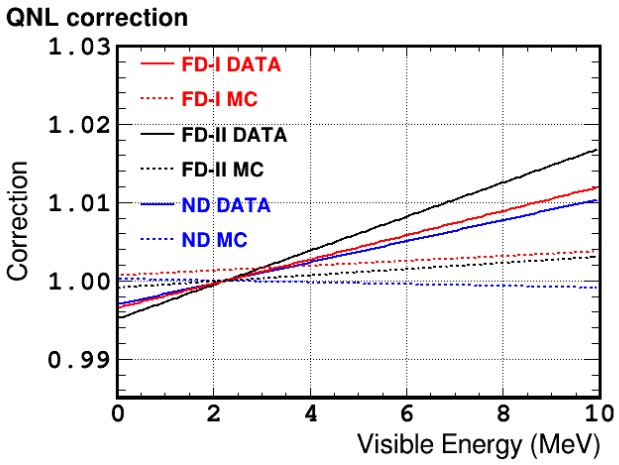

Figure 4.11: Charge non-linearity correction for ^{252}Cf data (solid line) and MC (dashed line) for FD-I (red), FD-II (black) and ND (blue).

Table 4.2: Charge non-linearity correction parameters for FD-I, FD-II and ND ^{252}Cf data and MC.

	Data	MC
FD-I	$0.998818 + 0.0005293 \times E_{\text{vis}}$	$1.000690 - 0.0003085 \times E_{\text{vis}}$
FD-II	$0.994891 + 0.0023134 \times E_{\text{vis}}$	$0.999119 + 0.0003950 \times E_{\text{vis}}$
ND	$0.996522 + 0.0015700 \times E_{\text{vis}}$	$1.000254 - 0.0001136 \times E_{\text{vis}}$

The systematic uncertainty is computed from the remaining non-linearity observed in the data to MC ratio along the z-axis using once again the ^{252}Cf source (z positions for FD: -1272 mm, -960 mm, 0 mm, +960mm; z positions for ND: -906 mm, 0 mm, +960 mm, +1160 mm, +1210 mm). Studing the correlation between the values of the slope c_{qnl} and the intercept b_{qnl} for the different positions, the uncertainties of these parameters are determined from their standard deviations, as seen in figure 4.12.

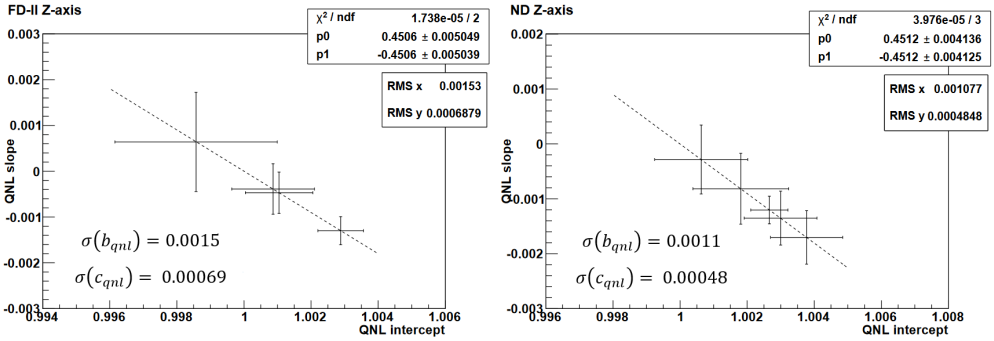

Figure 4.12: Variation of the QNL correction along z-axis using ^{252}Cf source for FD-II (left) and ND (right). The error on slope c_{QNL} and intercept b_{QNL} central values are extracted from RMS.

IBD n-H scale equalisation Once the QNL correction is applied, an ultimate correction factor is also used to align the absolute energy scale for the six ^{252}Cf data and MC configurations (FD-I, FD-II and ND) to adjust their H neutron capture peak to the theoretical 2.224 MeV, which also brings the Gd peak to 7.937 with QNL. This way, this corrects all the remaining imperfections of calibration. The combined effect of applying the QNL correction and this scale equalisation can be observed in fig. 4.13.

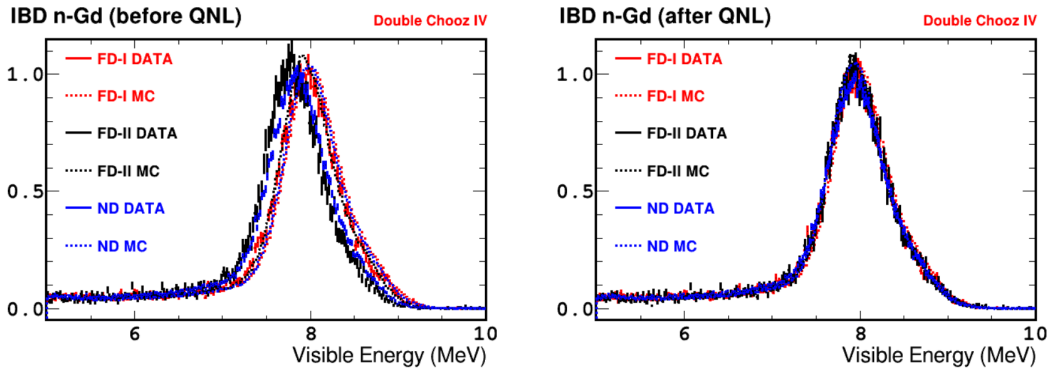

Figure 4.13: n-Gd capture peak for ^{252}Cf data and MC before and after the total QNL correction is applied. Data (solid line) and MC (dashed line) for FD-I (red), FD-II (black) and ND (blue).

4.4.5.2 Light non-linearity correction

In this case, for the correction of the light non-linearities (LNL) is necessary to take into account that the incorrect modeling of scintillation quenching (Birks' constant) or the scintillator light yield could alter the ratio of scintillation to Cherenkov light and cause a discrepancy between data and MC.

To evaluate this non-linearity, MC simulations are generated with several combinations of Birks' quenching parameters k_B and the light yield of the liquid scintillator ([133], [138]), taking into consideration that the LNL is particle-dependent, so this calibration is only implemented for positron events. Calibration source data (^{137}Cs and ^{252}Cf) is used to find out which combinations of the MC parameters achieve the best agreement to the data.

Once these parameters are fixed, the non-linearity observed in this data-like simulation with respect to the default MC is fitted following the form $f_{lnl} = a_{lnl}/E_{\text{vis}}+b_{lnl}$. The integrated detection volume corresponds to both NT and GC, so a weighted mean is calculated obtaining a combined correction for the total volume. For the θ_{13} oscillation analysis, a_{lnl} and b_{lnl} are considered as free parameters and fully correlated for all detectors. The resulting parameters are taken then as the average of the FD-I, FD-II and ND measurements (see fig. 4.14), being $a_{lnl} = 0.0091 \pm 0.0157$ MeV and $b_{lnl} = 0.9959 \pm 0.0071$.

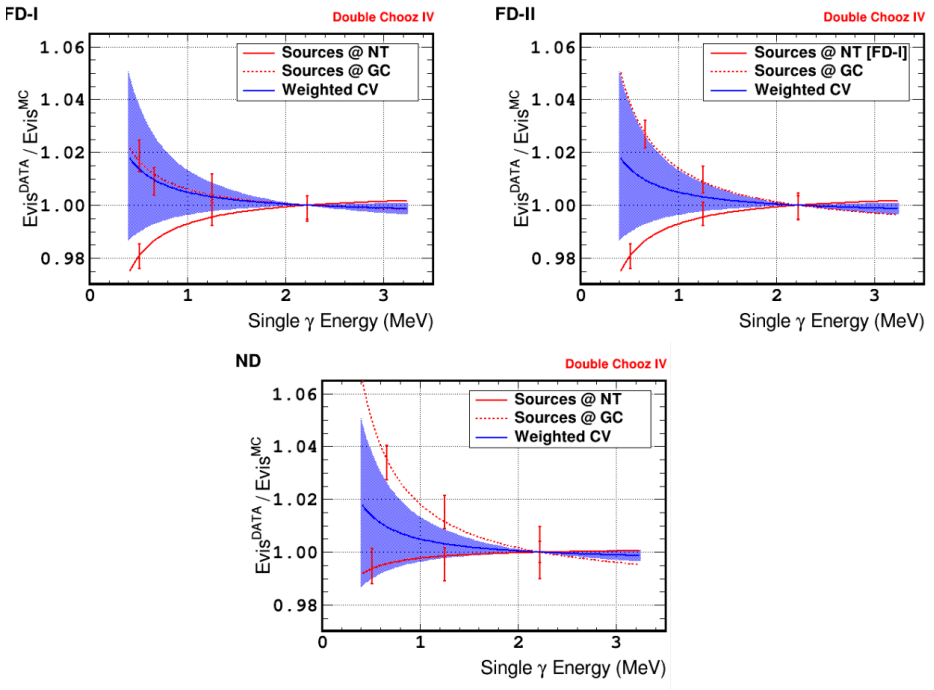

Figure 4.14: LNL correction curves for FD-I (left), FD-II (center) and ND (right), using calibration sources deployed in NT and GC. Blue bands corresponds to the uncertainty of the LNL correction.

4.5 Energy resolution

Once the energy calibration has been carried through to completion, Double Chooz has achieved a remarkable agreement between data and MC, as can be seen in fig.4.15. The energy resolution σ/E_{vis} is plotted as a function of the visible energy for data and MC points (using radioactive sources and also spallation neutrons) that is defined as:

$$\frac{\sigma}{E_{\text{vis}}} = \sqrt{\frac{a^2}{E_{\text{vis}}} + b^2 + \frac{c^2}{E_{\text{vis}}^2}} \tag{4.9}$$

where a is the stochastic term, b is the constant term and c is linked to electronic noise. The value of these parameters for each detector are summarized in table 4.3.

Table 4.3: Energy resolution parameters from fit for FD-I, FD-II and ND.

	FD-I	FD-II	ND
a ($\text{MeV}^{1/2}$)	0.0784 ± 0.0010	0.0792 ± 0.0017	0.0846 ± 0.0009
b	0.0187 ± 0.0006	0.0166 ± 0.0011	0.0158 ± 0.0010
c (MeV)	0.0249 ± 0.0029	0.0213 ± 0.0035	0.0232 ± 0.0021

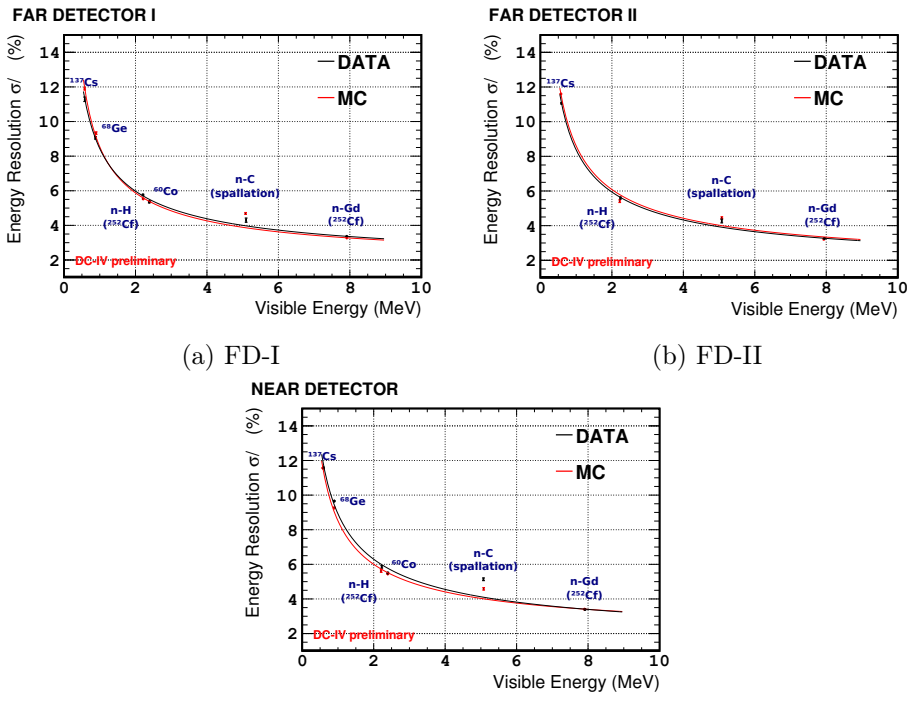

(a) FD-I

(b) FD-II

(c) ND

Figure 4.15: Energy resolution as a function of the visible energy for FD-I, FD-II and ND from data (black) and MC (red). Circles correspond to calibration sources deployed in the target center, except ^{137}Cs that was deployed in the guide tube. n-C (neutron captures in Carbon) resolution was extracted from spallation neutrons.

4.6 Energy scale in the θ_{13} oscillation fit

In the oscillation fit analysis, it is needed to take into account the remaining differences between data and MC model. The visible energy of the MC simulation (after all the previous pointed out corrections have been applied) can be rewritten as:

$$E^{\mathrm{MC}}_{\mathrm{vis,fit}} = E^{MC}_{\mathrm{vis}} \times (a_{lnl}/E^{MC}_{\mathrm{vis}} + b_{lnl}) \times b_{st,u} \times (b_{qnl} + c_{qnl} \times E^{MC}_{\mathrm{vis}}) \tag{4.10}$$

where E^{MC}_{vis} is extracted from equation 4.6. The parameter $b_{st,u}$ corresponds to the time stability and uniformity correction factor. This parameter is initialized to 1 in the fit, since no further correction is needed, but this allows to take into account its associated uncertainty. In the same way, the QNL correction has been already applied, so the parameters b_{qnl}, c_{qnl} are only used to propagate errors. The implementation of the light no-linearity correction has been postpone until now.

The energy systematics summary is resumed in the table 4.4 [139].

Table 4.4: Systematic uncertainties on energy scale for for FD-I, FD-II and ND. Last column shows the average values for a_{lnl} and b_{lnl} among detectors since they are assumed to be fully correlated.

	FD-I	FD-II	ND	correlated
a_{lnl}	0.0009 ± 0.0043	0.0092 ± 0.0056	0.0172 ± 0.0076	0.0091 ± 0.0157
b_{lnl}	0.9996 ± 0.0019	0.9959 ± 0.0026	0.9923 ± 0.0035	0.9959 ± 0.0071
$b_{st,u}$	1.0000 ± 0.0042	1.0000 ± 0.0045	1.0000 ± 0.0060	-
b_{qnl}	1.0000 ± 0.0012	1.0000 ± 0.0015	1.0000 ± 0.0011	-
c_{qnl}	0.00000 ± 0.00053	0.00000 ± 0.00069	0.00000 ± 0.00048	-

Equation 4.10 could be then rewritten as:

$$E^{\mathrm{MC}}_{\mathrm{vis,fit}} = a' + b' \times E^{MC}_{\mathrm{vis}} + c' \times \left(E^{MC}_{\mathrm{vis}}\right)^2 \tag{4.11}$$

being

$$\begin{aligned} a' &= b_{st,u} \times b_{qnl} \times a_{lnl} \\ b' &= b_{st,u} \times (b_{qnl} \times b_{lnl} + c_{qnl} \times a_{lnl}) \\ c' &= b_{st,u} \times c_{qnl} \times b_{lnl} \end{aligned} \tag{4.12}$$

These final input parameters for each detector are the ones shown in table 4.5. The correlations among them are also shown in figure 4.16, considering that there is an anticorrelation between the parameters b_{qnl} and c_{qnl} for the three detectors of -0.45 and also that the parameters a_{lnl} and b_{lnl} are fully correlated so the correlation is equal to -1.

Table 4.5: Parameters introduced in the energy scale correction function of equation 4.11 for FD-I, FD-II and ND.

	FD-I	FD-II	ND
a'	0.009 ± 0.016	0.009 ± 0.016	0.009 ± 0.016
b'	0.9959 ± 0.0083	0.9959 ± 0.0085	0.9959 ± 0.0093
c'	0.00000 ± 0.00053	0.00000 ± 0.00069	0.00000 ± 0.00048

		FDI			FDII			ND		
FDI	a'	1	-0.85	0	1	-0,83	0	1	-0,76	0
	b'	-0.85	1	-0.06	-0,85	0,71	0	-0,85	0,65	0
	c'	0	-0.06	1	0	0	0	0	0	0
FDII	a'	1	-0,85	0	1	-0.83	0	1	-0,76	0
	b'	-0,83	0,71	0	-0.83	1	-0,08	-0,83	0,63	0
	c'	0	0	0	0	-0.08	1	0	0	0
ND	a'	1	-0,85	0	1	-0,83	0	1	-0.76	0
	b'	-0,76	0,65	0	-0,76	0,63	0	-0,76	1	-0.05
	c'	0	0	0	0	0	0	0	-0.05	1

Figure 4.16: Correlations across energy scale parameters in the 3 parameters case.

With these parameters in hand, and taking into consideration the existing correlations, a covariance matrix is built. First a randomization of the energy scale function (equation 4.11) is performed, including uncertainties and correlations across parameters. An example of the resulted randomized curve is shown in figure 4.17. The difference per energy bin between the nominal value and the value obtained after 10^5 randomizations defines the elements of the covariance matrix that are introduced in the oscillation fit. The final fractional energy correlation and covariance matrices are shown in figure 4.18.

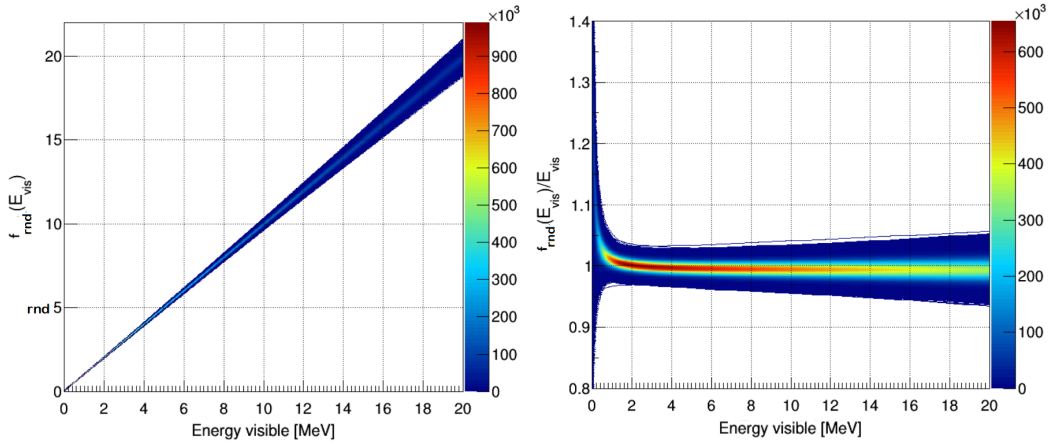

Figure 4.17: Example of a randomized energy scale function used to generate the covariance energy response matrix.

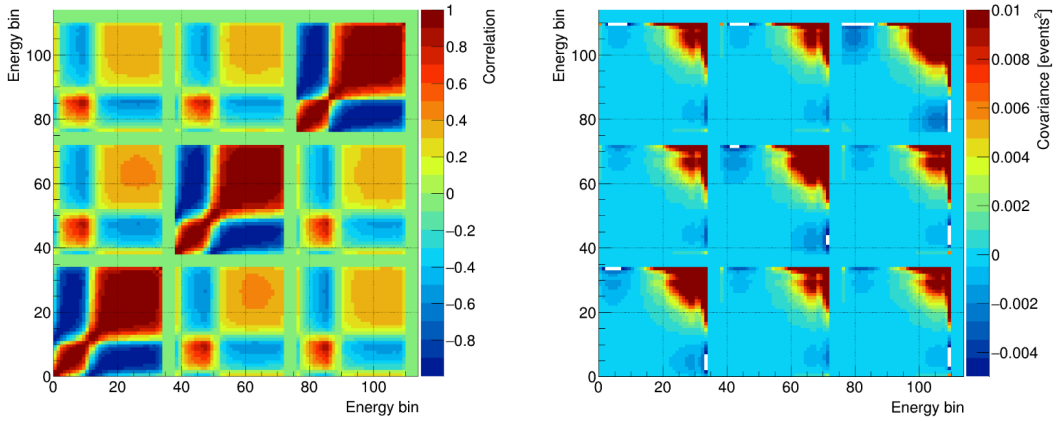

Figure 4.18: Correlation (left) and fractional covariance (right) matrices for the energy scale uncertainty.

Chapter 5

IBD Data Selection Analysis

5.1 Introduction

The electron antineutrinos emitted by the nuclear reactors interact with the protons present in the liquid scintillator of the detectors through the inverse β decay (IBD): $\bar{\nu}_e + \mathrm{p} \rightarrow \mathrm{e}^+ + \mathrm{n}$, producing the spatial and temporal coincidence of two signals that allows an efficient suppression of the backgrounds. The positron will lose its kinetic energy and will be quickly annihilated, being observed as the prompt signal. The delayed signal corresponds to the neutron capture either by a Gadolinium (Gd) nucleus after 30 μs emitting gammas of 8 MeV or by a Hydrogen (H) nucleus after 200 μs, emitting gammas of 2.2 MeV, thus providing two independent samples.

Double Chooz has developed a new IBD detection method based on the Total neutron Capture (TnC) technique, which considers neutron captures over all possible isotopes (mainly Gd and H, with almost neglibible contribution of C) in the full detector volume [140]. The TnC provides remarkable advantages over any single isotope dependent detection. It increases the detection efficiency volume, yielding higher statistics, and causes a significant reduction of the detection systematics.

To perform the θ_{13} measurement, the total number of selected neutrino candidates as well as the MC predicted events with no oscillation are needed. Since the MC does not include any background simulation, additionally the spectral shape and rate of the background sources are also used as inputs for the oscillation fit.

Analyses and selection criteria performed to find the characteristic trigger coincidence of the IBD, that have been used in Double Chooz publications previous to this thesis, are briefly described in section 5.2. The main reasons why Double Chooz has adopted the combined selection Gd+H are justified in section 5.3. The data sets used for this analysis are listed in section 5.4 and the background sources present in it are described in section 5.5. Section 5.6 is devoted to explain the selection used in the TnC analysis, while the vetoes used to eliminate the background that masks the IBD signal are accounted for in section 5.7. These vetoes produce an inefficiency in the neutrino selection that is resumed in section 5.8. Finally the remaining background and the selected IBD candidates are estimated in sections 5.9 and 5.10.

5.2 Review of previous data selection in Double Chooz analyses

The Double Chooz group was the first experiment to report for the first time an indication of reactor $\bar{\nu}_e$ disappearance, given the first indication of non-zero θ_{13} in November 2011 at LowNu2011 conference in Korea and the result $\sin^2(2\theta_{13}) = 0.086 \pm 0.041$, using only the far detector data, was published in March 2012 [66]. This first analysis was based on the IBD captures on Gd nuclei, due to the delayed energy around the 8 MeV peak, well above the radioactive background energy region, and the well defined fiducial volume (Gd signal only happens in the neutrino target). This analysis was updated some months later, measuring non-zero θ_{13} at 2.9σ [108] and improved in 2014 with $\sin^2(2\theta_{13}) = 0.090^{+0.032}_{-0.029}$ [131].

On the other hand, Double Chooz also developed a novel analysis based only on hydrogen captures, being the first time that a reactor experiment used this alternative channel. It was published in 2013 [101], with a systematic uncertainty worse than in the Gd analyses but the statistic becomes 3 times higher. This analysis has been also improved in 2016, due to the inclusion of novel techniques for background reduction. In this case the signal to background ratio was improved from 0.93 to 9.7. This was the last result of Double Chooz using the single detector data [102], with $\sin^2(2\theta_{13}) = 0.124^{+0.030}_{-0.039}$.

In addition, Double Chooz was the first collaboration that fitted the data to prediction using both rate and spectral shape information (R+S). Complemetary to the above results, a background model independent θ_{13} measurement was published in 2014 [141]. A fit, called Reactor Rate Modulation (RRM), is performed comparing the predicted IBD rate with the measured one at different reactor power regimes, thanks to the simplicity of the experiment setup: 2 reactors and 2 detectors. The best result obtained with this analysis is $\sin^2(2\theta_{13}) = 0.088 \pm 0.033$ [102].

This chapter is devoted to describe the analysis used to select IBD candidates taking into account equally the neutron captures by Gd and H nuclei, providing finally the first multi-detector θ_{13} measurement in the Double Chooz history.

5.3 Motivation for the TnC technique

The Total neutron Capture technique relies on a larger delayed energy range ($1.3 < E_{del} < 10$ MeV) to allow for neutron captures over all isotopes available in the liquid scintillator volumes, that is, captures in H and loaded Gd present in the detector. Three main features are achieved by adopting this novel selection.

First of all an increase of signal statistics by more than a factor of two is accomplished as compared to the Gd-only channel due to the addition of the Gamma Catcher (GC) volume, since the $\bar{\nu}_e$ is detected regardless of the capturing isotope. The GC region was not originally designed as an IBD-sensitive capture region, so the knowledge of the number of target protons in this volume is poor, eventually increasing the systematic uncertainty of θ_{13}. To improve this knowledge, some measurements will be carried out during the dismantling of the detectors, now in progress.

Once the proton number be measured, the increased of the statistics will have a large impact on the overall sensitivity in the value of θ_{13}.

A major increase of the detection efficiency volume can be appreciated in figure 5.1. The efficiency of the Gd-only selection [131] (left part of the figure) confines the IBD captures only in the neutrino target region, while the TnC selection (right part) increases its efficiency in both, the neutrino target and the GC. In particular, the selection efficiency is close to 100% in the target, since all the captures are considered without distinguishing among isotopes.

Furthermore the TnC method provides a major reduction of the detection systematics, since there is no need to compute the complex neutron spill in/out currents between the NT and GC vessels, and due to the integration over Gd and H captures simultaneously, the determination of the Gd or H fractions are not needed in this new analysis. This way the detection efficiency uncertainty is improved from 0.5% for the FD Gd-only analysis to 0.3% in the FD and 0.2% in the ND for the TnC analysis (without considering proton number uncertainty). This numbers will be explained in more detail in Chapter 6.

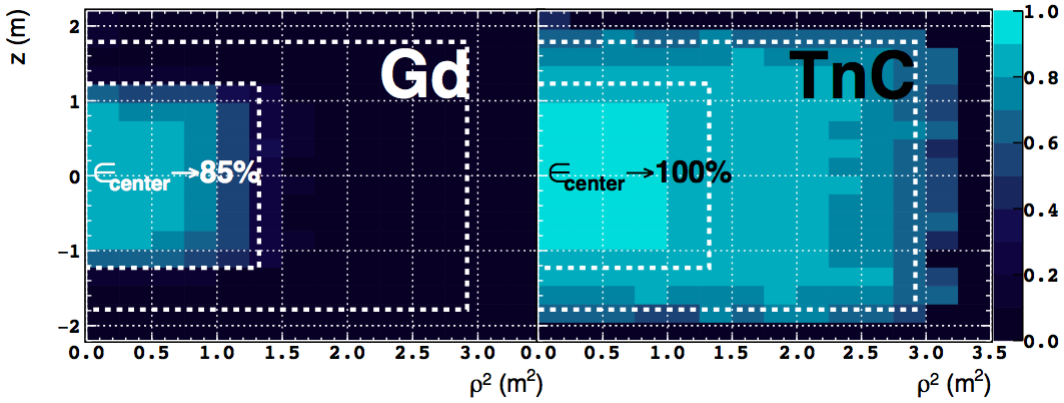

Figure 5.1: IBD selection efficiency in the detector volume (z, ρ). The inner dashed line delimits the NT, the outer dashed line demarcates the GC. On the left plot the efficiency for the Gd-only channel is represented, while on the right, it is plotted the efficiency for the TnC analysis.

Finally, the TnC technique is inter-volume leak insensitive. This is in fact very relevant since a small amount of Gd in the upper part of the near detector GC volume has been discovered due to the presence of neutron captures on Gd within the GC fiducial volume. It results in a higher relative fraction of captures on Gd in the near detector in comparison to the far detector. This can be seen in figure 5.2, where the plot shows the delayed energy distribution for the neutron captures from the Cf source used in the calibration campaigns in the FD (black) and in the ND (blue) that take place in the right top corner of the GC region. In the asymmetry plot it can be observed that the Hydrogen peak (∼2.2 MeV) matchs between both detectors. Nonetheless, the energy range of Gd-capture events (region between 6-8 MeV) presents a significant excess of events in the near detector data, showing an asymmetry of almost 200%.

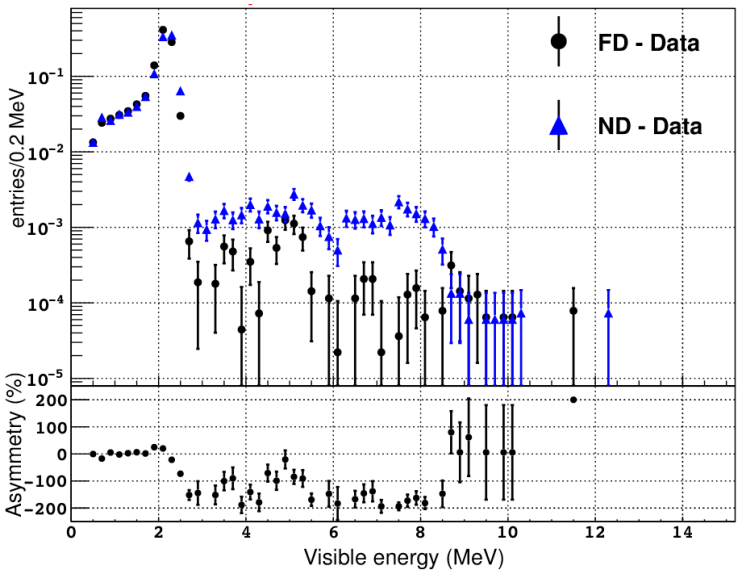

Figure 5.2: Delayed energy spectra for far (black points) and near (blue triangles) detectors data for the right top corner of the GC. Events are normalized to the [1.3, 3] MeV region (H-peak). Asymmetry plots corresponds to $2\frac{\mathrm{N(FD)\text{-}N(ND)}}{\mathrm{N(FD)+N(ND)}}$ where N is the number of events.

The GC leak can also be appreciated studying the r^3 distribution (reconstructed position vector cubed) for Gd capture events along the detector for FD and ND using the IBD neutrons and also the fast neutrons (FN) induced by muon spallation (fig. 5.3). It can be seen that the behaviour of FN and IBD neutrons is very similar in the NT region, where no assymmetry is found, but as the r^3 increases, the asymmetry becomes higher.

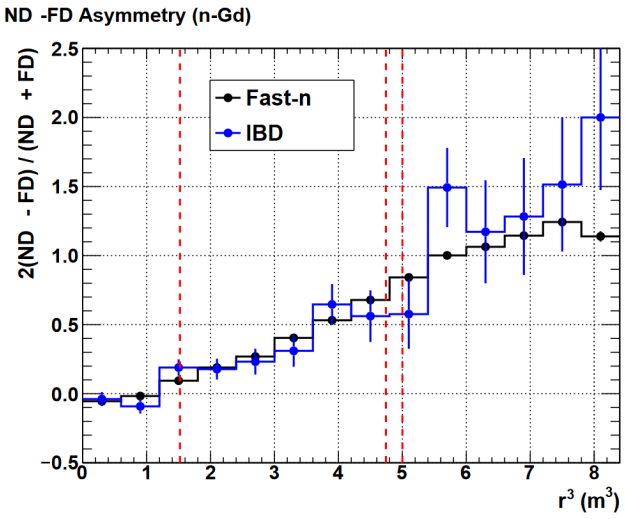

Figure 5.3: Asymmetry between ND and FD in r^3 distribution for Gd capture events (IBD in blue and fast neutrons in black). Red lines represent NT wall ($\sim$1.5 m^3), intersection of the NT wall and lid ($\sim$4.7 m^3), and GC wall ($\sim$5 m^3). Relative excess in ND w.r.t. FD is seen outside of NT region.

Different approaches have been carried out to understand the impact of the presence of this leak in the GC. In particular, using fast neutrons sample (after a muon, huge number of fast neutrons are emitted), and the r^3 asymmetry, four MC simulations with different concentrations (0.00, 1.10, 1.55 and 2.40 $\mu g/cm^3$) of Gd in the GC have been generated (see fig. 5.4).

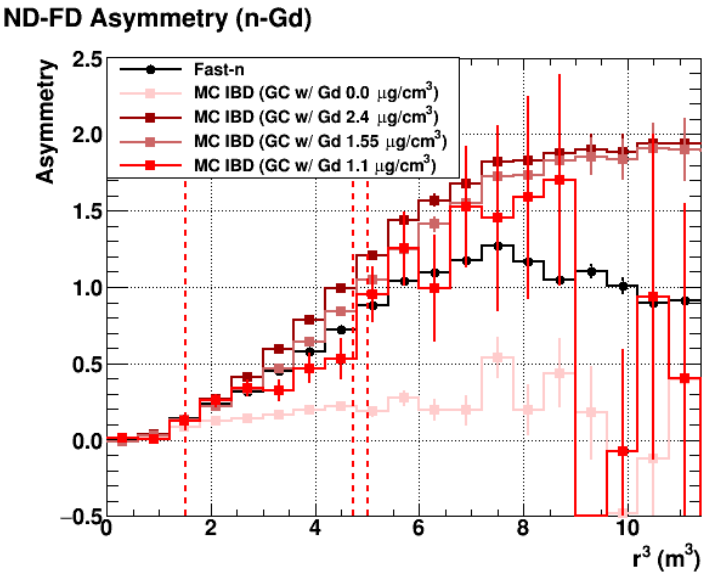

Figure 5.4: ND:FD asymmetry between FN sample and MCs with different concentrations of Gd in GC in r^3 distribution for Gd capture events. Dashed red lines represent NT wall (∼1.5 m^3), intersection of the NT wall and lid (∼4.7 m^3), and GC wall (∼5 m^3).

These 4 MC have been tested via the IBD selection efficiency that will be explained in detail in Chapter 6. As illustrated by figure 5.5, it can be seen that the MC with 1.10 or 1.55 $\mu g/cm^3$ are the most representative of the data, being the first one used in the final θ_{13} oscillation analysis. In the Gd-only analysis the presence of Gd in the ND GC would have introduced some challenges to be considered, for instance, the correct generation of the MC that should reproduce the ND behaviour, since the exact amount of Gd in the ND GC is still unknown as well as the exact region it occupies. On the contrary the TnC analysis is leak immune since it integrates over the full scintillating volume (both NT and GC), showing the same IBD selection efficiency for data and MC.

Thus in summary, with the TnC analysis the Double Chooz experiment provides the breakdown of the statistics limitation and a new robust and accurate detection framework that is isotope independent with a significant reduction of detection systematics.

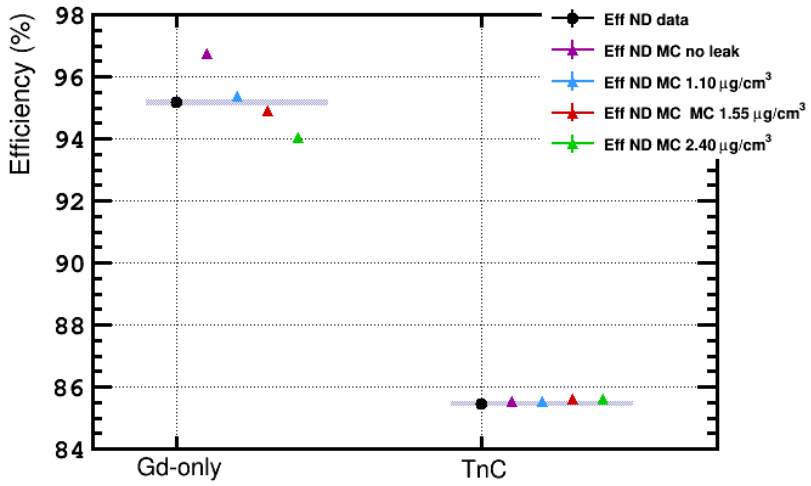

Figure 5.5: IBD selection efficiency in Gd-only and TnC analysis for ND data (black point) and the four ND MC, i.e, no Gd in GC simulated (magenta triangle), 1.10 μg/cm^3 of Gd in GC (blue triangle), 1.55 μg/cm^3 (red triangle) and 2.4 μg/cm^3 (green triangle). Errors are included

5.4 Data Sets

In order to obtain the neutrino mixing angle θ_{13}, the Double Chooz collaboration has developed its analyses using data from the single-detector (Far Detector only) and the multi-detector (Far and Near Detector operating simultaneously) periods. To distinguish both periods, FD-I will denote the data taking with the FD during the single-detector period and FD-II the multi-detector one. There was also an interval of 7 days during the FD-I period in which the 2 reactors of the Chooz nuclear plant were under maintenance service that will help to measure the background present in the detectors (referred as 2-Off or off-off period). Runtime and lifetime (once the veto to tag muons is applied) for the data taking between 2011-2012 for the FD-I and 2015-2016 for the MD period, used to extract θ_{13} are summarized in table 5.1.

Table 5.1: Runtime and lifetime for the different data sets used to extract θ_{13}.

Data set	Runtime (days)	Lifetime (days)
FD-I	481.20	455.21
2-Off	7.60	7.16
FD-II	384.00	362.97
ND	346.30	257.96

In addition, some particular analyses, as the selection efficiency temporal stability explained in section 6.6, have been updated including 23 months of data taking with

FD and ND. In this case, the run and lifetime are listed in table 5.2.

Table 5.2: Runtime and lifetime for 23 months of FD+ND data.

Data set	Runtime (days)	Lifetime (days)
FD-II	592.84	560.35
ND	525.30	391.04

The full detector data set characteristics is shown in table 5.3. In this table FD-I includes also the data used to make some commisioning and upgrades that improved the electronic of the detector: 14 PMTs were back on (they had been switched off due to strong flasher/noise emitter), the electronic gain was increased by a factor of two and the after-muon response was also improved.

Table 5.3: Runtime and lifetimes for the full DC data set.

Data set	Runtime (days)	Lifetime (days)
FD-I	860.63	814.35
2-Off	7.60	7.16
FD-II	910.85	860.92
ND	834.64	621.34

5.5 Main background sources

This section is focused on the explanation of the backgrounds involved in the reactor neutrino experiments, which mimic the IBD prompt or delayed events making hard to distinguish them from the IBD signal. The backgrounds in Double Chooz are divided into two major groups: uncorrelated backgrounds called accidental background, which are random coincidences of two uncorrelated triggers, and correlated backgrounds, in which there is a physical correlation between the prompt and the delayed signal. This subsample can be divided, in turn, into two categories: correlated events due to the muons passing through or close to the detector (like stopping muons or fast neutrons) or long-lived cosmogenic isotopes (^{9}Li, ^{8}He).

5.5.1 Accidental Background

This background is conformed by the random coincidence of two triggers that are not physically correlated. In the TnC analysis, the prompt and delayed energy range are similar ($1.0<E_p<20$ MeV and $1.3<E_{del}<10$ MeV) so both signals are populated with the gamma rays from natural radioactivity originated in the PMTs or by other detector materials or the surrounding rock.

The energy region of the natural radioactivity spreads up to ∼4 MeV, so the Hydrogen channel suffers from very large contamination of accidental background (fig. 5.6). As a result of this, the accidental background represents an important fraction of the neutrino candidates in the oscillation region. An accurate measurement of

the rate and a correct estimation of the associated errors are needed to subtract this background from the IBD data. Fortunately the accidental rate and spectral shape are known with high precision by using the Off-time method, that will be explained in section 5.9.1.1.

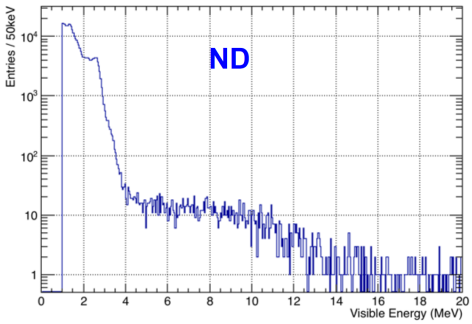

Figure 5.6: Prompt energy spectrum of accidental events using the Off-time method. These events are dominated by natural radioactivity decays with a non-correlated neutron capture.

5.5.2 Stopping Muon background

This background is conformed by the low energy muons which stop and decay into the detector. Inside the detector, they lose their energy by ionization producing a prompt-like signal and decay producing a Michel electron. The coincidence of the energy deposition and the Michel e^- can mimic the IBD prompt and delayed signals. A set of vetoes has been developed to reject this kind of events, described in section 5.7, achieving a negligible contamination of stopping muons. Entering muons are identified by the IV with 100% efficiency, but those penetrating through the chimney may enter the ID without clear activities in the IV.

5.5.3 Fast Neutron background

Fast neutrons are high energy spallation neutrons produced by muons that interact with the rock surrounding the detectors. One of these neutrons interacts with a proton present in the liquid scintillator causing a recoiled proton that mimics the prompt signal and finally the neutron thermalizes in the detector and is captured on Gd or H, simulating the IBD signal.

Muons and their products get in the detector going through the OV and IV, where they can deposit part of their energy. Then it is possible to estimate this background by analysing the signals picked by the PMTs of the IV, following a procedure called IV-tagging method, which will be described in more detail in section 5.7, and also by looking if these events have crossed the OV region.

5.5.4 Cosmogenic background

Cosmic muons passing through the detector are able to create unstable cosmogenic isotopes, being the ^{9}Li and ^{8}He the most dangerous for the Double Chooz analyses. After their decay, a neutron is emitted together with a β^- particle [114], making

difficult to distinguish this process from the IBD products:

$$\begin{aligned} {}^{9}\mathrm{Li} &\rightarrow \beta^{-} + 2\alpha + n \ (\mathrm{BR}\ 51\%) \\ {}^{8}\mathrm{He} &\rightarrow \beta^{-} + {}^{7}\mathrm{Li} + n \ (\mathrm{BR}\ 16\%) \end{aligned} \tag{5.1}$$

Due to their long lifetimes (257.2 ms for ^{9}Li and 171.8 ms for ^{8}He), it is not viable to reject them by applying a dead time after the detection of the muon (muon veto section 5.6.1.1).

Double Chooz has developed a dedicated condition based on a likelihood function $\mathcal{L}$ that is able to estimate the probability that an IBD-like event is produced as a result of a cosmogenic isotope decay, using the fact that a high neutron multiplicity production follows the muon spallation process. This likelihood is explained in more detail in section 5.7. Then any event that is preceded by a muon followed by multiple neutrons and spatially close to that muon, has a huge probability to be produced by a cosmogenic isotope.

5.5.5 Light Noise background

Light Noise (LN) is an unexpected background caused by spontaneous light emission from the bases of the PMTs installed in the ID. This effect was discovered and understood before the ND construction, making possible its correction by covering the PMTs bases. Random coincidences of LN events manifest as accidental background. A set of requirements based on the event topology has been used to reject this instrumental background and are described in section 5.6.1.2. LN events are characterized by a long light emission which spanned in time from a few tens to hundreds of nanoseconds. In figure 5.7 [142], it is compared a LN event (left) with an IBD event (right). In the case of LN, larger pulses are detected by one specific PMT, while in the case of a neutrino interaction, similar light signal is detected by all PMTs.

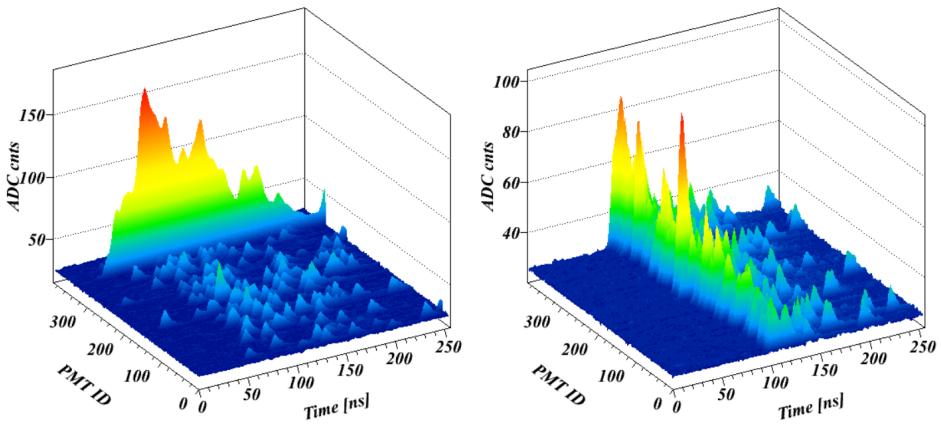

Figure 5.7: Comparison of the time profile of the PMT waveform for a LN event (left) and a neutrino interaction (right). In the first case, only a single PMT sees the LN events and some ns later, other PMTs see some light, while in the IBD case, all PMTs see some light at similar times.

The rate of LN has been observed to increase with the temperature, as can be seen in fig. 5.8. After several studies in the laboratory, it has been demonstrated that there is no light emission when the epoxy resin used to insulate the PMT components from the buffer mineral oil is removed. Consequently it was concluded that the combined effect of the heat and high voltage on the epoxy resin produces the light emission of the PMTs.

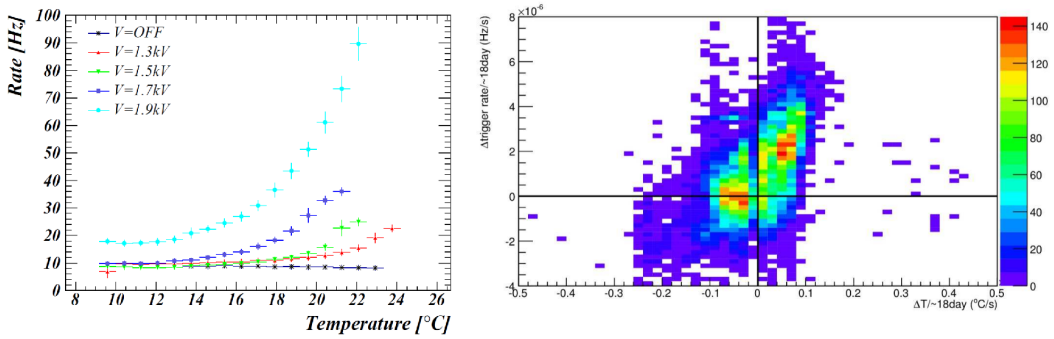

Figure 5.8: Left plot: Variation of the light emission rate for different PMT high voltage values, changing the PMT temperature. A rise of the temperature always corresponds to higher rates of the detected signals. Right plot: Correlation of the trigger rate with the temperature.

5.6 IBD Selection

This section describes the pre-selection and the selection used to search for the coincidence of the two valid triggers characteristic of the IBD signature. This steps can be resumed as:

$\bar{\nu}_e$ selection
- **Preselection**
  - Trigger energy
  - Muon rejection
  - LN rejection
- **Selection**
  - Prompt Energy
  - Delayed Energy
  - Time Coincidence
  - Spatial Coindicence
  - Isolation Condition
  - Artificial Neural Network

5.6.1 Preselection

Only the valid triggers (called singles) are considered to look for the IBD coincidence. These valid triggers are defined as:

- Not a muon (see section 5.6.1.1)

- If a muon is tagged, all the events recorded 1.25 ms after the muon are discarded
- Not a LN event (see section 5.6.1.2)
- The minimum trigger energy must be 0.3 MeV and the maximum, 100 MeV, in order to get a trigger efficiency of 100%.

5.6.1.1 Muon veto

In section 5.5 it was mentioned that most of the correlated background can be rejected if the signals produced after a muon are removed. The muons that cross the detector deposit a large amount of energy in the ID or IV or both, satisfying this way the following conditions:

- Visible energy in ID: $E_{vis}(ID) > 100$ MeV
- Charge deposited in IV: Q(IV) $>$ 50000 DUQ in the FD-II and Q(IV) $>$ 30000 DUQ in the FD-I and ND.

The difference present in the selection cuts or vetoes between FD-I and FD-II is due to an electronic upgrade that took place between both periods of data taking, while the discrepancy between FD-II and ND is due to the different backgrounds, since the overburden is not equivalent in both detectors.

The rate of muons passing through the detector that are tagged with the previous muon definition is 45.2 Hz in the FD and 239.7 Hz in the ND. Moreover all the triggers in the 1.25 ms after a muon are discarded. This veto acts as a dead time in the detectors, which has to be considered in the comparison of the data to the MC, since the muon background is not simulated in the MC.

5.6.1.2 Light Noise cuts

As explained in section 5.5.5, the LN events have a characteristic pattern that allows to distinguish them from an IBD event. There are four variables used for the LN rejection based mainly on the charge collected by the PMTs. In the TnC analysis, the following cuts are applied:

- FD-I
  - $Q_{max}/Q_{tot} < 0.12$
  - $Q_{diff} < 30000$ DUQ
  - $RMS(t_{start}) < 36$ ns or $RMS(Q) < 464 - 8 \times RMS(t_{start})$
- FD-II and ND
  - $Q_{max}/Q_{tot} < 0.20$
  - $Q_{diff} < 100000$ DUQ
  - $RMS(t_{start}) < 36$ ns or $RMS(Q) < 1680 - 28 \times RMS(t_{start})$

Q_{max} corresponds to the maximum charge collected by a single PMT while Q_{tot} is the total charge of the event collected by all PMTs. If Q_{max}/Q_{tot} is large means that a single PMT has seen most of the event light which is typical of a LN event.

Q_{diff} is defined as:

$$Q_{diff} = \frac{1}{N} \sum_{i}^{N} \frac{(Q_{max} - Q_i)^2}{Q_i} \tag{5.2}$$

where N is the number of PMTs surrounding the PMT with maximum charge within a sphere of 1m radius. From this equation it can be concluded that a large Q_{diff} implies a very localized charge distribution, which is typical of a LN event.

The last two variables used are RMS(t_{start}) and RMS(Q), standard deviations of the PMTs hit time and charge distributions respectively. Physics events take place in the liquid scintillator so RMS(t_{start}) has small values (less than 40 ns). Additionally it was seen that there is a correlation between both variables and a two-dimensional cut is powerful to ensure that the light is delivered homogeneously and simultaneously to all the PMTs. This can be appreciated in figure 5.9, where two populations can be easily distinguished. The left cluster corresponds to the physics events, with small spread in the PMT hit times, while the right cluster contains LN events.

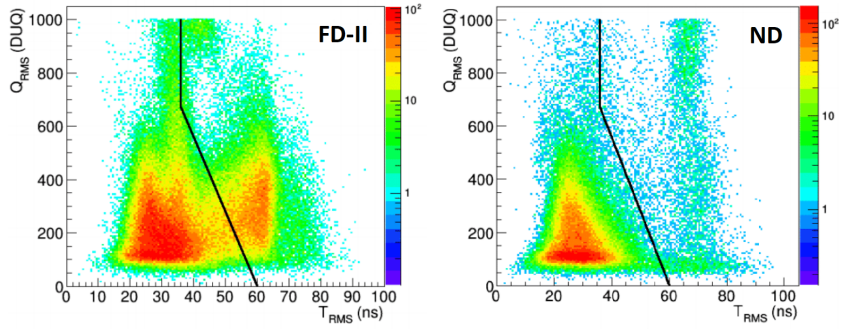

Figure 5.9: Left plot: Standard deviation of the PMTs charge distribution vs. standard deviation of the PMTs hit time distribution for FD-II. The RMS(t_{start}) vs RMS(Q) cut is indicated by the black line. Rejected events are the one on the right side of the line. Right plot: Same as left plot but for ND. It can be appreciated that the LN cluster has been highly suppressed.

5.6.2 Selection

Once the pre-selection has been carried out, the signature of the $\bar{\nu}_e$ interacting in the detector is looked for, resulting in the coincidence of a prompt trigger, given by the annihilation of the positron, and a delayed trigger given by the capture of the neutron. This coincidence allows major accidental background rejection. Then, to be considered as an IBD event, the pair of triggers needs to satisfy the following requirements:

- Prompt energy window: $1.0 < E_{prompt} < 20$ MeV
- Delayed energy window: $1.3 < E_{delayed} < 10$ MeV
- Prompt-Delayed time correlation: $0.5 < \Delta T < 800$ μs
- Prompt-Delayed space correlation: $\Delta R < 1200$ mm

Although there is no neutrinos expected beyond 8.5 MeV, the prompt energy range is open until 20 MeV to better constraint the normalization of cosmogenic and correlated backgrounds in the spectral oscillation fit. In the past, for the Gd-only analysis the prompt energy was settled to a range [0.5, 20] MeV. However now the region from 0.5 to 1 MeV is excluded to avoid the antineutrino interactions in the Buffer region. It could happen that one of the two gamma rays produced in the e^+ annihilation reaches the GC scintillator, producing a prompt signal of 0.511 MeV. Accordingly the lower energy cut is set to 1 MeV to avoid a possible cut around the 0.511 MeV peak, which would be sensitive to the energy scale uncertainty. Such events are specific to n-H events in the GC, therefore they do not represent a problem in the Gd-only analysis.

The delayed energy window is maximally opened to allow neutron captures over all available isotopes in the liquid scintillator volumes, i.e captures on the natives H ($E_{delayed}$ peak at 2.2 MeV) and the loaded Gd ($\sim$ 8 MeV).

IBD interactions have a temporal and spatial correlation between the prompt and the delayed signal. IBDs have a mean neutron capture time of $\sim$30 μs if the capture is on Gd and $\sim$200 μs if is on H. However due to the presence of Gd in the ND GC, there is a competitiveness between the Gd and H, and the neutrons that are finally captured on Gd need more time to be captured (>200 μs). This can be seen in fig. 5.10, where the ΔT distribution, allowing only for captures by Gd nuclei, is plotted for the 4 MCs with different Gd concentrations in the GC, refereed in section 5.3. It can be appreciated that the highest Gd concentration in GC, the largest number of events with larger ΔT. As a consequence, the upper limit of the temporal coincidence is chosen up to 800 μs. In contrast, the accidental coincidences have a flat ΔT as a result of the fact that the probability to get random coincidences is the same over time.

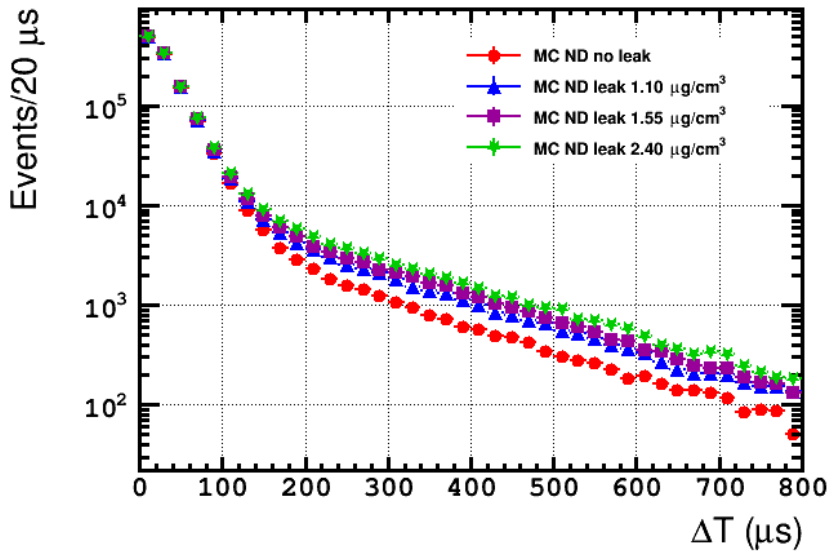

Figure 5.10: Time coincidence between prompt and delayed events considering only Gd captures using MCs with different concentrations of Gd in the GC.

The next variable is the distance between the prompt and delayed vertex of the IBD event. This cut has been tuned to maximize the accidental rejection while keeping the IBD selection efficiency. The agreement has been found taking into account that the correlation distance ΔR in the accidental background tends to be larger because there is no correlation between prompt and delayed-like events.

Finally a last cut is imposed to guarantee that the IBD events are isolated pairs, ensuring that the trigger can not be considered prompt and delayed simultaneously. Moreover these isolation cuts will help to avoid multiple neutrons from spallation muons, since it is required no valid trigger in the prompt isolation window before a prompt candidate and only one delayed candidate in the delayed isolation window:

- No valid triggers allowed in 800 μs preceding the prompt candidate
- Time window from 0.5 μs to 900 μs following the prompt candidates contains only the delayed trigger. The event is rejected if a valid trigger exists within 0.5 μs after the prompt event.

5.6.2.1 Artificial Neural Network

As said in previous sections, accidental coincidences represent an important fraction of the neutrino candidates in the oscillation region, even after applying the selection cuts. However there are three variables which are effective for accidental background rejection, the temporal and spatial coincidence of the prompt-like and the delayed-like event and the delayed energy distribution, that comes from the energy deposition of environmental gamma rays at low energies. These distributions for accidental events and also IBD MC can be seen in figure 5.11.

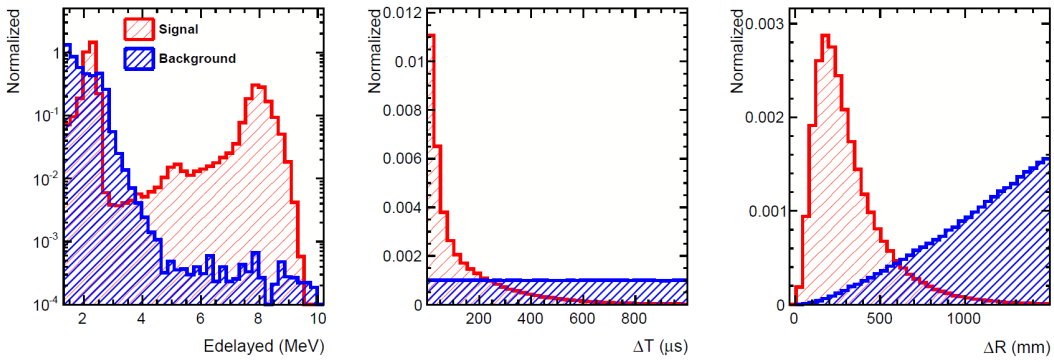

Figure 5.11: Delayed energy E_{del} (left), temporal ΔT (right) and spatial ΔR (right) coincidence between prompt and delayed trigger for accidental background in blue and signal MC in red.

In Gd-only analysis, due to the high neutron capture energy (E_{del} ~8 MeV) and the short capture time (ΔT~30 μs), a set of one-dimensional cuts is efficient when it comes to reject accidental coincidences. However when H captures are as well involved (E_{del} ~2.2 MeV and ΔT~200 μs), one needs to find a compromise between a high signal efficiency but a large background contamination or vice-versa. Fortunately Double Chooz has developed an Artificial Neural Network (ANN) classifier, a multivariate analysis and powerful tool to reject accidental coincidences. This ANN,

designed originally for the H-only channel analysis [102] and improved for the TnC analysis, uses the variables $E_{delayed}$, ΔT and ΔR as inputs and a cut optimization in the 3-dimensional space yields major accidental background rejection while keeping high signal selection efficiency (∼86 % as will be described in Chapter 6).

The neural network used is a Multi-layer Perceptron (MLP) network with back propagation from the Toolkit for Multivariate Analysis (TMVA) package in ROOT [143]. This package provides a set of multivariate analysis (MVA) methods, including one-dimensional and multi-dimensional likelihoods, boosted decision trees or artificial neural networks. The ANN structure includes an input layer with four nodes (the three input variables written before and a bias node), a single hidden layer with nine nodes (including also a bias node) and a single output parameter (classifier output), as can be distinguish in figure 5.12. The training cycle number was set to 600. The inclusion of more input parameters was tested, as spatial events coordinates, concluding that they did not improve the ANN performance.

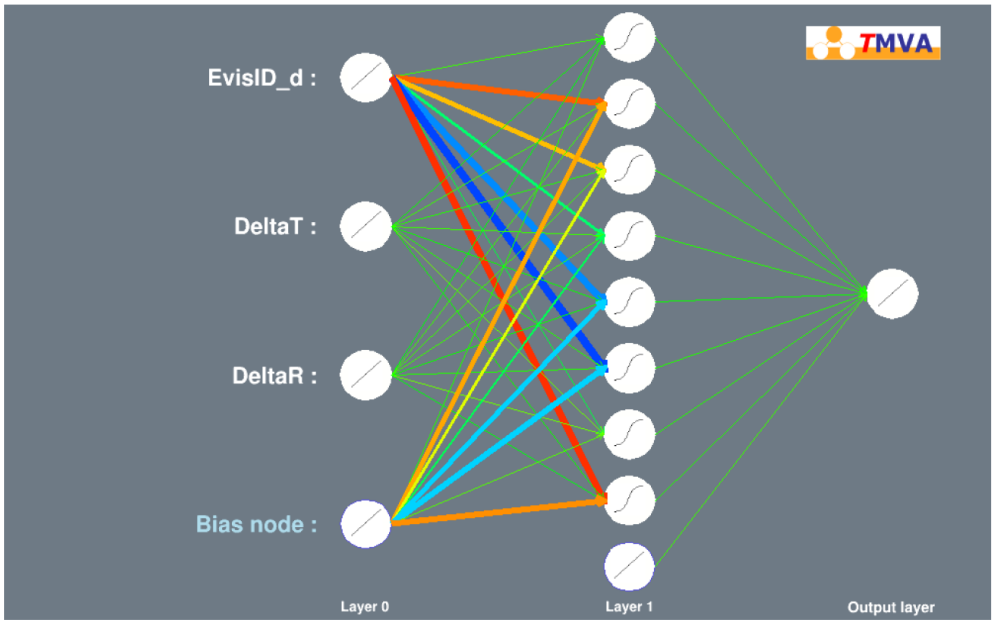

Figure 5.12: Schematic representation of the ANN for the TnC analysis.

Three neural networks were trained, one for each detector set of data (FD-I, FD-II and ND), using unique samples of IBD Monte Carlo signals and samples of accidental coincidences extracted using the off-time method explained in section 5.9.1.1 but with 200 off-time windows and a time offset of 2s to get independent accidental samples different from the ones used in the θ_{13} oscillation analysis. It should be noticed that the composition of the background sources are not identical for FD and ND due to the distinct external shield used (steel or water, as explained in section 2.5.3) and overburden, causing different muon rates. This will result in slightly different ANN output distributions. The same number of signal MC and accidental background events were used in the training (600000 in FD-I, 405900 in FD-II and 406000 events in ND). The ANN output for the ND data set is shown as example in figure 5.13.

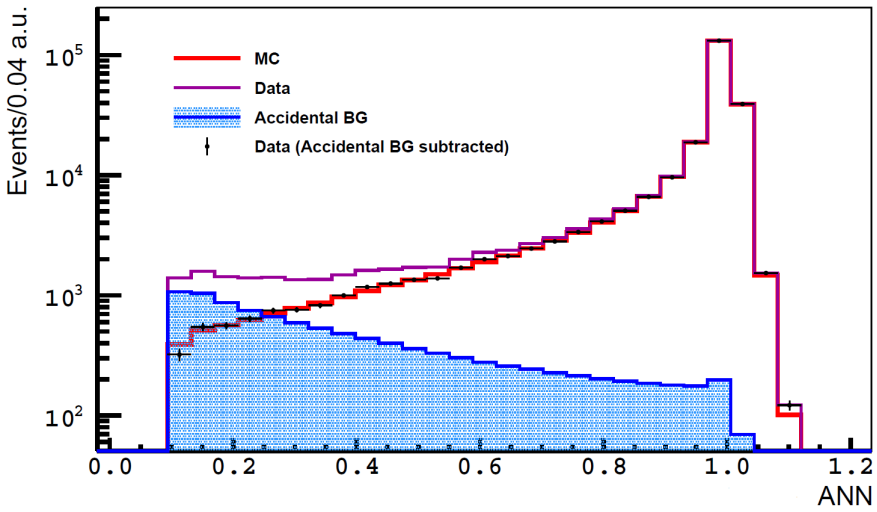

Figure 5.13: ANN output for ND. Accidental background is shown in blue area, signal MC in solid red line, antineutrino data without accidental subtraction in magenta line and final data with accidental background subtracted in black points.

The cut for the ANN output is chosen in each detector to maximize the signal to background ratio (S/N) keeping signal efficiency at around 85% (see figure 5.14).

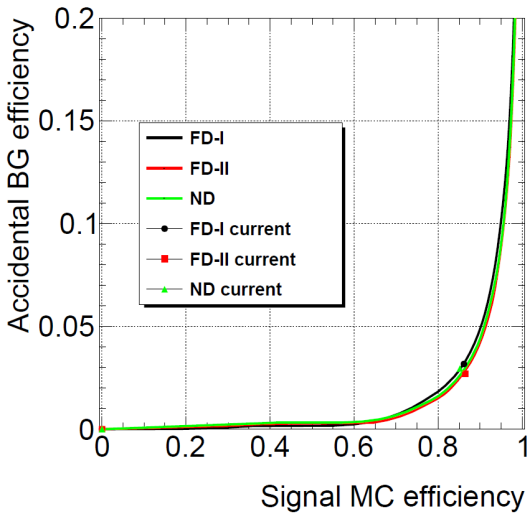

Figure 5.14: Accidental background efficiency (up to 20%) vs. signal MC efficiency for FD-I (black), FD-II (red) and ND (green). Points represent the current optimized ANN cuts.

Moreover since neutrino oscillation comes from the deficit in the observed prompt energy spectrum with respect to the prediction without oscillation, it is important to look for any systematic bias affecting the prompt spectrum that could imply a bias in the oscillation result. Even if the ANN does not use the prompt energy information as input, the ANN cut was also optimized to achieve the same efficiency

curve plotted against prompt energy in FD and ND, as it is illustrated in figure 5.15. The ANN efficiency is defined as the ratio of the number of signal MC events with and without applying the ANN cut:

$$\epsilon_{\mathrm{ANN}} = \frac{(1.3 < \mathrm{E_{del}} < 10)\ \mathrm{MeV} \cap (0.5 < \Delta\mathrm{T} < 800)\ \mu\mathrm{s} \cap \Delta\mathrm{R} < 1200\ \mathrm{mm} \cap \mathrm{ANN}}{(1.3 < \mathrm{E_{del}} < 10)\ \mathrm{MeV} \cap (0.5 < \Delta\mathrm{T} < 800)\ \mu\mathrm{s} \cap \Delta\mathrm{R} < 1200\ \mathrm{mm}} \tag{5.3}$$

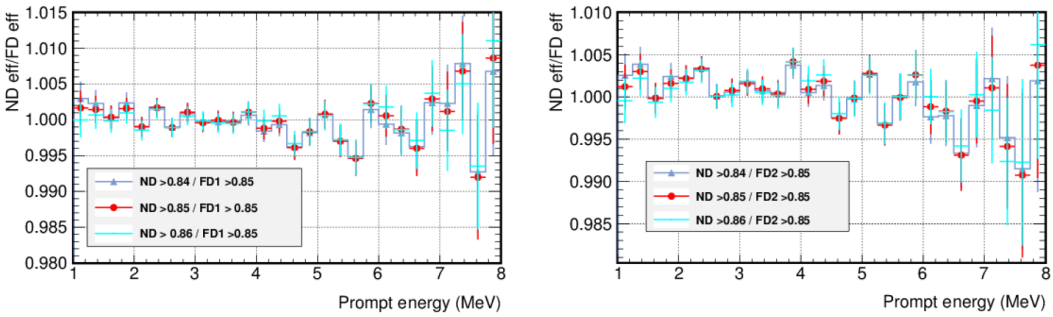

Figure 5.15: Ratios of MC signal ANN efficiency as a function of the prompt visible energy for three ND ANN cut values. The ratio ND/FD-I is shown on the left while in the right the ratio ND/FD-II is shown. In both cases the ratio closest to 1 is the corresponding to the ND ANN cut > 0.86 [144].

As a result, the ANN cut values that ensure the prompt energy selection efficiency identical across detectors match with ANN>0.85 for the FD and ANN>0.86 for the ND. Although they are slightly different between FD and ND, these differences are cancelled in comparison with the MC, as the same ANN cut values are applied to the data and MC for each data set.

Table 5.4 summarizes the chosen ANN cut and the Signal MC to background ratio (S/N) for FD-I, FD-II and ND.

Table 5.4: Summary of the optimized value of the ANN cut for FD-I, FD-II and ND and the signal to background ratio for these ANN cuts.

	FD-I	FD-II	ND
ANN cut	ANN > 0.85	ANN > 0.85	ANN > 0.86
S/B	25.64	27.08	250.57

After this, the ANN efficiency with respect to the prompt energy is compared between data and MC for the three detectors (fig. 5.16.), showing a discrepancy at low energy (below 1.5 MeV) in the FD-I. Several analyses have been developed, like studying the efficiency for different periods of FD-I, but the cause has not been clarified yet. Initially to account for this discrepancy, an additional 10% normalization error on the MC prediction was accounted in the first bin (1.00-1.25 MeV) of the θ_{13} oscillation fit. However the result of θ_{13} is not impacted in a significant way by adding this systematic, so finally it was decided not to include it in the fit.

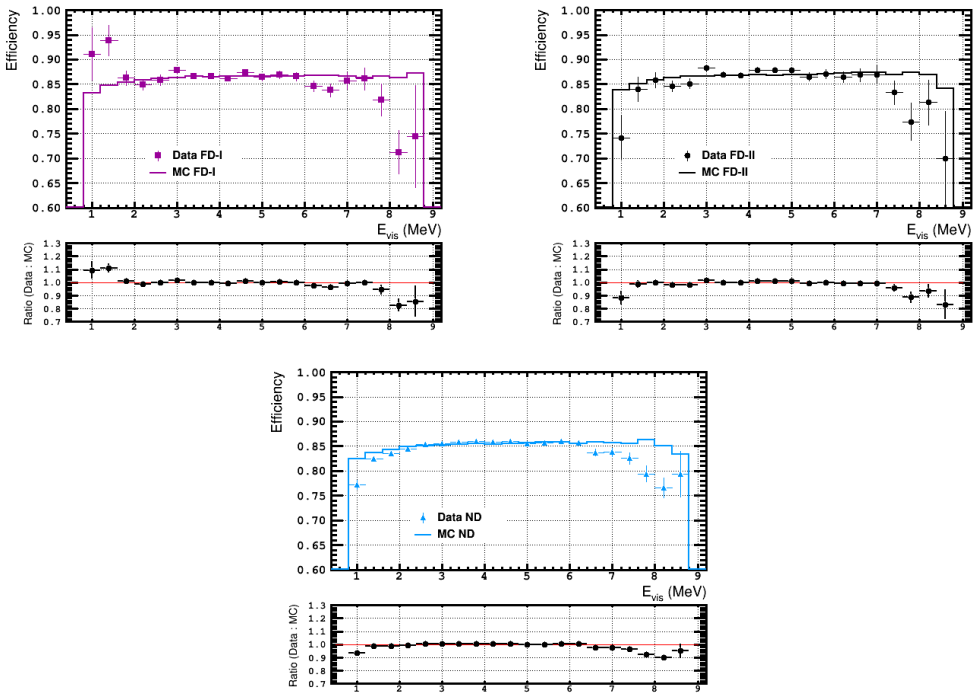

Figure 5.16: Comparison of data and MC ANN efficiency vs prompt energy for FD-I (upper left), FD-II (upper right) and ND (bottom).

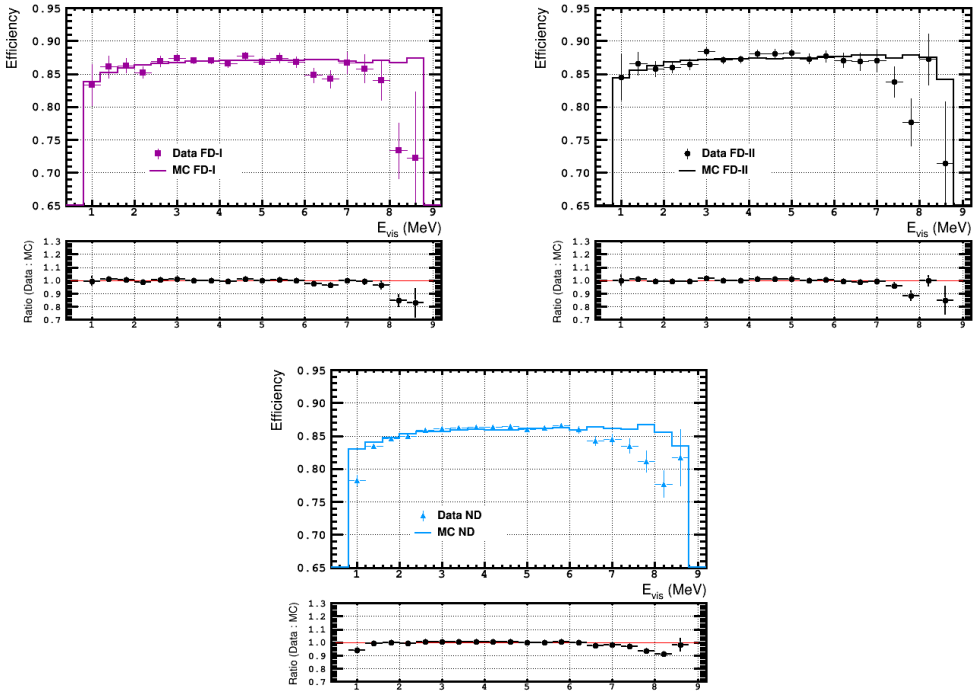

Figure 5.17: Comparison of data and MC ANN efficiency, including an extra cut for the ANN variable in the denominator.

Furthermore this disagreement between IBD data and MC is highly suppressed when in the denominator of equation 5.3, an ANN>0.1 cut is also added, which reduces the subtracted accidental background while integrating over ∼98% of the detectable IBDs. In this case, the agreement between IBD data and MC ANN efficiency is better for the three detectors as can be seen in fig. 5.17

To show the rejection power of the neural network, the energy delay distribution for the accidentals is shown prior and after the ANN implementation (fig. 5.18).

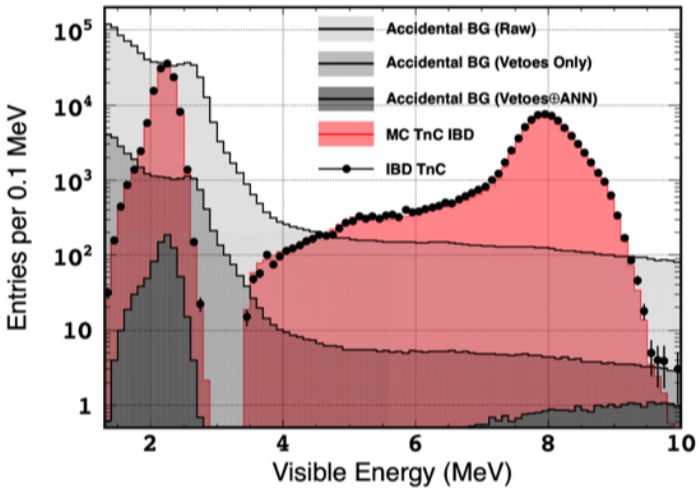

Figure 5.18: Delayed energy distribution E_{del} for accidental coincidences (in gray) before and after ANN is applied. MC (in red) and IBD events once accidentals have been subtracted (black dots) are also shown, finding excellent agreement after the accidental background rejection.

To sum up the IBD preselection and selection cuts are listed in table 5.5.

Table 5.5: Neutrino selection cuts for FD-I, FD-II and ND, including all the preselection and selection cuts described in the text.

Variable	FD-I	FD-II	ND
Single Energy	$0.3 < E_{singles} < 100$ MeV		
Muon Veto	E_{vis}(ID)<100 MeV		
	Q(IV)<30M DUQ	Q(IV)<50M DUQ	Q(IV)<30M DUQ
LN Veto	$Q_{max}/Q_{tot} < 0.12$ $Q_{diff} < 30$M DUQ RMS(t_{start}) < 36 ns or RMS(Q) < 464 - 8 × RMS(t_{start})	$Q_{max}/Q_{tot} < 0.20$ $Q_{diff} < 100$M DUQ RMS(t_{start}) < 36 ns or RMS(Q) < 1680 - 28 × RMS(t_{start})	
Prompt Energy	$1.0 < E_{prompt} < 20$ MeV		
Delayed Energy	$1.3 < E_{delayed} < 10$ MeV		
Time Coincidence	$0.5 < \Delta T < 800$ μs		
Spatial Coincidence	$\Delta R < 1200$ mm		
Isolation	no signals in [-800, 900] μs from the prompt		
ANN	ANN > 0.85	ANN > 0.85	ANN > 0.86

5.7 Background rejection

Essentially correlated background rejection relies on direct muon tagging using ID, IV and OV detectors and making use of these identifications, several vetoes are defined. The following conditions have been defined using the IBD data sample, since the IBD MC doesn't include background simulations.

5.7.1 IV veto

This veto is dedicated to reduce fast neutrons that deposit energy in the IV before entering the ID but this energy is below the threshold of tagged muons. In order to discriminate the fast neutron background, correlation in space and time among events than deposit energy in the ID and also in the IV is looked for. If the prompt and delayed signals satisfy the conditions included in table 5.6, the event is rejected.

Table 5.6: IV veto conditions for the prompt (p) and delayed (d) events, including the number of hits IV PMTs, the hit time difference between the ID and the IV and the distance between the reconstructed vertices in the ID and the IV, as well as the charge and energy deposition in the IV.

Condition	Signal	FD-I	FD-II	ND
N_{IV}^{HIT} PMT	p, d	>1	>1	>1
Q_{IV}	p, d	>400 DUQ	>300 DUQ	>300 DUQ
ID-IV ΔR	p, d	ΔR<3.7 m	ΔR<3.7 m	ΔR<3.7 m
ID-IV ΔT	p	-100<ΔT<-10 ns	-40<ΔT<70 ns	-40<ΔT<70 ns
ID-IV ΔT	d	-100<ΔT<-30 ns	-30<ΔT<60 ns	-30<ΔT<60 ns
E_{vis}	d	<3 MeV	<3 MeV	<3 MeV

Furthermore, it was seen in [102] that the IV veto also rejects a significant amount of accidental background in the low energy region arising from multiple Compton scattering of γ's in the IV and ID. These γ rays are emitted from radioactive nuclei in the surrounding rock, being dominant the γ's from ^{208}Tl with an energy of 2.6 MeV.

5.7.2 OV veto

Cosmic muons passing through the detector leave energy in the OV and are tagged thanks to this volume. IBD prompt candidates that are coincident with an OV trigger (within 224 ns) are rejected.

5.7.3 Chimney-Pulse-Shape (CPS) veto

As described in the detector section (Chapter 2), there is a central chimney, connected to all detector layers, that allows the introduction of liquids and calibration sources. Muons that enter through this chimney, can enter the detector being unseen by the IV veto. For stopping muon (SM) events entering through the chimney, reconstructed vertices are often displaced due to the small volume and the lack of direct view of

the PMTs. The CPS veto is based on a pulse shape discriminator which looks for the probability that the reconstructed position of a delay signal happens in the chimney instead of the central region of the detector via a likelihood function. This means that the ratio $\mathcal{L}_{\rm chm}/\mathcal{L}_{\rm vtx}$ is smaller for stopping muons than for IBD events. Hence the following condition is taken in the FD-I, FD-II and ND and the events that satisfy it are rejected:

$$\mathcal{L}^{\rm del}_{\rm chm}/\mathcal{L}^{\rm del}_{\rm vtx} < 0.95 \tag{5.4}$$

5.7.4 Functional Value (FV) veto

This veto makes use of the vertex reconstruction algorithm in Double Chooz called RecoBAMA [108], which is based on a maximum likelihood function that uses PMT charge and time variables assuming the event to be a point-like source $\mathcal{L}(\vec{x})$. This maximization is equivalent to minimizing the negative log-likelihood function, i.e, the goodness of the reconstruction parameter $F_V = F^t_V + F^q_V = -ln\mathcal{L}(\vec{x})$. A high FV means that the event is not a point-like event, characteristic of a SM or LN due to highly asymmetric light deposition. This condition is applied as a function of the energy of the delayed event and the events that obey it are rejected:

$$\begin{aligned}
\text{FD-I: } \mathrm{E_{vis}} &< 0.36 \times e^{F_V/2.4} \;\&\; \mathrm{E_{vis}} < 0.06 \times e^{F_V/1.2} \\
\text{FD-II: } \mathrm{E_{vis}} &< 0.2 \times e^{F_V/1.8} \;\&\; \mathrm{E_{vis}} < 0.05 \times e^{F_V/1.2} \\
\text{ND: } \mathrm{E_{vis}} &< 0.32 \times e^{F_V/2.1} \;\&\; \mathrm{E_{vis}} < 0.07 \times e^{F_V/1.2}
\end{aligned} \tag{5.5}$$

A novel analysis developed for the TnC analysis [145] has evinced that the time component of the functional value veto F^t_V is more powerful to separate SM than the charge component F^q_V. This way in addition to the previous FV requirement, another set of cuts focused on the time component has been carried out:

$$\begin{aligned}
\text{FD-I: } & \left[\frac{(F^t_V + 0.11 \times \mathrm{E_{vis}}) - 4.1}{0.14}\right]^2 + \left[\frac{\Delta BJ_z + 0.03}{0.21}\right]^2 > 4^2 \\
& \quad || \quad F^t_V + 0.11 \times \mathrm{E_{vis}} > 4.3 \\
\text{FD-II: } & \left[\frac{(F^t_V + 0.12 \times \mathrm{E_{vis}}) - 4.1}{0.15}\right]^2 + \left[\frac{\Delta BJ_z - 0.01}{0.21}\right]^2 > 5^2 \\
& \quad || \quad F^t_V + 0.11 \times \mathrm{E_{vis}} > 4.3 \\
\text{ND: } & \left[\frac{(F^t_V + 0.097 \times \mathrm{E_{vis}}) - 4.0}{0.14}\right]^2 + \left[\frac{\Delta BJ_z - 0.01}{0.19}\right]^2 > 5^2 \\
& \quad || \quad F^t_V + 0.11 \times \mathrm{E_{vis}} > 4.3
\end{aligned} \tag{5.6}$$

Where ΔBJ_z is the difference in the reconstructed vertical component from the center of the detector (z) between the RecoBAMA algorithm and a second algorithm called RecoJP [146], which reconstructs the event vertex position using only hit timing information in the likelihood function. The difference between both algorithms is smaller for the IBD events but increases when there are inhomogeneities like asymmetric light deposition, such as the SM signature.

5.7.5 Cosmogenic Isotopes veto

This B+Li+He veto is based on a likelihood calculation for each prompt event and the preceding muons, taking into account the distance between the muon track and the prompt IBD signal along with the neutron multiplicity following the muon in a time window of 700 ms. The likelihood is trained using ^{12}B, since it is produced in large abundance by muons and this distribution is consistent with ^{9}Li+^{8}He distribution [142]. Finally it is required that all the prompt events satisfying the following condition are considered as background and are rejected:

$$\mathcal{L}_{Li} > 0.4 \tag{5.7}$$

5.8 Vetoes inefficiencies

The background vetoes described in previous section are only applied to the neutrino candidate sample. The determination of the vetoes inefficiency is detailed below:

- **Muon veto:** After tagging a muon, a 1.25 ms veto time is imposed, acting as a dead-time. In the FD-I this dead-time is around 26 days of data taking, 21 days in the FD-II and 88 days in the ND, which involves an inefficiency of 5.43% in the FD and 25.52% in the ND.
- **LN veto:** The inefficiency of the LN cuts is calculated from the antineutrino fraction that satisfy these cuts in the MC, where there is not such background simulated.
- **Isolation cut:** This inefficiency is calculated as the probability to have a valid trigger within the 1.7 ms isolation window open around the prompt trigger.
- **IV veto:** The inefficiency is extracted from the fraction of accidental candidates selected with the off-time method which are rejected by the IV veto.
- **OV veto:** The inefficiency is calculated by counting the number of prompt triggers which are coincident with an OV trigger.
- **Li+He veto:** To obtain this inefficiency it is needed to compute the number of IBD candidates that are paired with a muon collected using an off-time selection and are vetoed.
- **Stopping Muon veto:** This veto is a concatenation of the three following conditions: FV, CPS and ΔBJz. The inefficiency of these cuts is computed as the ratio of the estimated number of IBD rejected by the cut over the total estimated number of IBD in the original IBD sample: $N_{IBD^{rej}}/N_{IBD^{tot}}$. Since this sample of rejected events also contains background events, the number of antineutrinos lost is estimated once this remaining background is subtracted.

The table 5.7 shows the efficiency for any cut and any detector:

Table 5.7: Inefficiency in the TnC neutrino selection due to the background vetoes.

Condition	FD-I ineff. (%)	FD-II ineff. (%)	ND ineff. (%)
Muon veto	5.43 ± (<0.01)	5.43 ± (<0.01)	25.52 ± (<0.01)
μ-IBD veto	0.49 ± (<0.01)	0.49 ± (<0.01)	2.37 ± (<0.01)
Light noise	0.01 ± (<0.01)	0.00 ± (<0.01)	0.00 ± (<0.01)
Isolation	2.71 ± (<0.01)	3.80 ± (<0.01)	3.14 ± (<0.01)
IV veto	0.06 ± 0.01	0.05 ± 0.01	0.08 ± 0.01
OV veto	0.06 ± (<0.01)	0.06 ± (<0.01)	0.01 ± (<0.01)
Li+He veto	0.52 ± (<0.01)	0.53 ± (<0.01)	0.12 ± (<0.01)
SM veto	0.17 ± 0.02	0.32 ± 0.04	0.12 ± 0.01
Total	9.14 ± 0.02	10.29 ± 0.04	29.76 ± 0.01

5.9 Estimation of the remaining background

In spite of the used of the background vetoes, there is an amount of irreducible background that has to be taken into account in the θ_{13} oscillation analysis, so the rate and the spectral shape of each type of background source need to be known.

5.9.1 Final Accidental Sample

As explained in section 5.5.1, the accidentals rate and shape are determined using the Off-time method [147], described below.

5.9.1.1 Off-time method

In the neutrino candidate sample, it is required that the time interval between the prompt and delayed signal be (0.5,800) μs. In the accidental sample this interval is replaced by:

$$(0.5\mu s + T_{\text{off}}) < \Delta T < (800\mu s + T_{\text{off}}) \tag{5.8}$$

where T_{off} must be chosen large enough to guarantee that there is no possible physical correlation between the prompt and the delayed trigger. It is given by:

$$T_{\text{off}} = 1s + n_{\text{window}} \times T_{\text{iso}} \tag{5.9}$$

In the TnC analysis, the accidental sample is collected using 500 off-time windows of $T_{\text{iso}} = 1.7$ ms each, starting 1s after the prompt trigger is opened (see fig. 5.19). The use of 500 consecutive windows increases the statistics of the accidental sample.

In the case of data sample, an isolation time window is applied before and after the prompt candidate as explained in section 5.6.2. In the accidental sample, since the interval between the two valid triggers is larger, it is needed to introduce an extra isolation cut:

- No valid trigger in the 800 μs before and in the 900 μs after the prompt.

- No valid trigger in the 800 μs before the time $t_{prompt}+T_{off}$ and only the delayed trigger in the 900 μs after it.

being t_{prompt} the prompt trigger time.

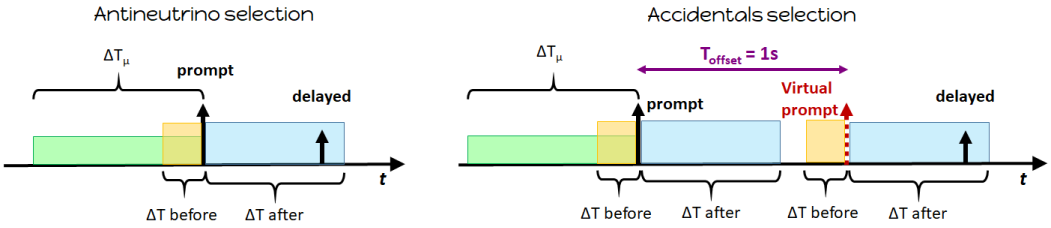

Figure 5.19: Scheme of the Off-time method.

The accidental background prompt spectra for FD-I, FD-II and ND data obtained by this method is given in figure 5.20.

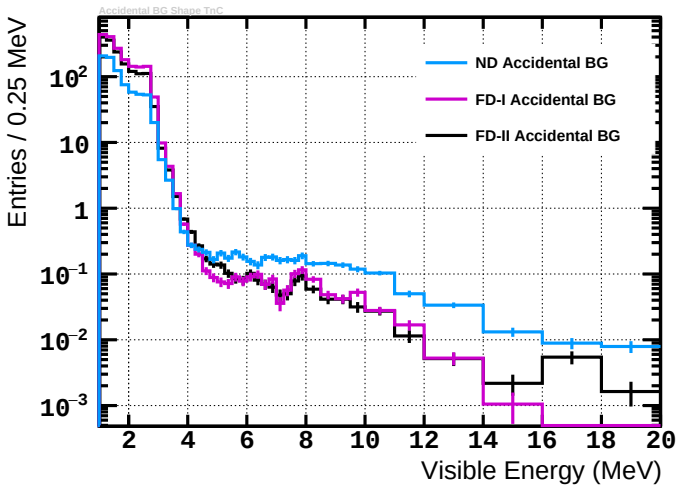

Figure 5.20: Prompt energy spectra of accidental background. FD-I sample in magenta, FD-II in black and ND in blue.

Hence with the Off-time method, a pure sample of accidentals with high statistics is obtained. However the selection cuts depending on time have different effects in the neutrino candidates (called on-time sample) and in the pure accidental sample (off-time sample). Thus the thereby achieved accidental rate has to be corrected accounting for four systematic effects, via a correction factor:

$$f_{acc} = f_{run} \times f_{\mu} \times f_{iso} \times f_{Li} \tag{5.10}$$

- **Run length correction** f_{run}: in the case of the on-time sample, if the prompt candidate is at the end of the data taking run, the coincidence window is included in the run. But in the off-time case, due to the virtual prompt signal, some of the off-time windows could be out of the run range. Thus the accidental background rate at the end of each run in the off-time sample is underestimated.

- **Muon veto correction** f_μ: In the TnC analysis, there is a muon veto that requires that 1.25 ms after a muon, no signal could be defined as a valid trigger. The probability that a prompt signal be vetoed is the same in the on and the off-time sample. However once the prompt signal is accepted, the probability of vetoing the delayed signal is different between the on-time and the off-time sample. This is due to the fact that in the on-time case, the only requirement must be that there is no muon between the two valid triggers, but in the off-time sample, since the interval between the prompt and the delayed signal is wider, the probability of vetoing the delayed event is higher than in the on-time case. Thus more events are vetoed and the accidental coincidences are underestimated.
- **Isolation cut correction** f_{iso}: In the on-time sample only one isolation cut is applied around the prompt event but in the off-time, this cut is applied a second time around the virtual prompt signal. This induces an increase of the rejection probability and again underestimates the accidental background.
- **Lithium veto correction** f_{Li}: Cosmogenic background events are rejected using a likelihood cut that it is applied to the prompt event (explained in section 5.7). This likelihood is based on the distance between the muon track and the prompt event reconstructed vertex and also on the number of neutron captures following the muon in a 1 ms. In the case of the on-time sample, a cosmogenic β-decay (as ^{1}2B) is likely to be rejected due to the required correlation in time and space with the prompt signal, while in the off-time one, the delayed event is farther in time and there is no possible correlation with any cosmogenic trigger acting as prompt trigger. As a consequence of this, the accidental background is overestimated in the off-time sample.

The total correction factor applied to the accidental rate for each detector is shown in table 5.8.

Table 5.8: Global accidental correction factors for FD-I, FD-II and ND.

	FD-I	FD-II	ND
f_{run}	1.00044	1.00042	1.00053
f_μ	1.049 ± 0.001	1.049 ± 0.002	1.289 ± 0.001
f_{iso}	1.025201	1.035226	1.021859
f_{Li9}	1.000 ± 0.004	1.000 ± 0.003	1.000 ± 0.001
Total	1.077 ± 0.004	1.087 ± 0.004	1.318 ± 0.002

Once these four corrections are taken into account, the resulting accidental background rates for the three data samples used in the θ_{13} oscillation analysis are:

- FD-I: 3.930 ± 0.010 day^{-1}
- FD-II: 4.320 ± 0.020 day^{-1}
- ND: 3.110 ± 0.004 day^{-1}

Differences in the accidental rate observed between FD and ND come from the fact that there is no Light Noise observed in the Near detector. Differences between

FD-I and FD-II samples mainly come from the 14 PMTs more that were switched on during the FD-II period, with the largest Light Noise contribution. Cosmic muon induced background rate is higher in ND resulting in a higher rate of high-energy accidental events.

5.9.2 Final Fast Neutron sample

Estimation of the FN sample spectral shape used in the θ_{13} oscillation fit is done by fitting the IVV tagged events, that is, IBD candidates passing all selection criteria but rejected by the IV veto (section 5.7.1). All these events in the [0, 100] MeV range of visible energy (figure 5.21) are adjusted by a third degree polynomial. This shape is included analytically in the oscillation fit together with the parameter correlations and errors.

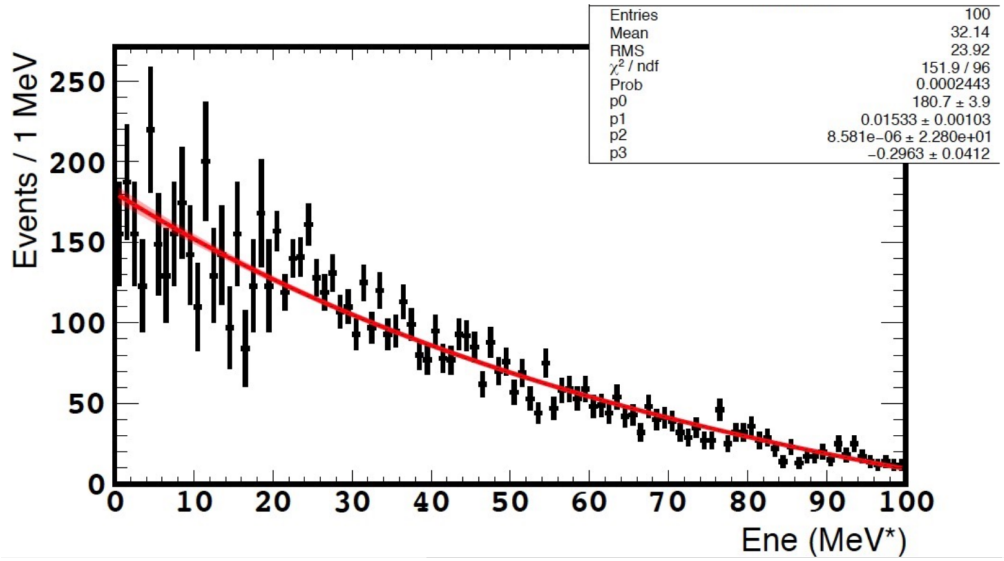

Figure 5.21: Prompt energy spectrum of fast neutrons in the ND with analytical shape used in the θ_{13} fitted in red.

The rate is obtained by normalizing the previous fit function into the range [20, 100] MeV where the FN sample is dominant (neutrinos are confined in the region of energy lower than 10 MeV), and then integrating the region below the fit function between 1 and 20 MeV, resulting in:

- FD-I: 2.60 ± 0.11 day^{-1}
- FD-II: 2.48 ± 0.10 day^{-1}
- ND: 20.77 ± 0.43 day^{-1}

Given that no difference is expected between the FD-I and FD-II rates of correlated background, they are set in the fit as a single parameter, considering the rate of FD 2.54 ± 0.07 day^{-1}.

5.9.3 Final Cosmogenic background sample

The prompt energy spectrum of this cosmogenic contamination is obtained directly from the IBD data using events with high likelihood $\mathcal{L} > 0.4$. This spectrum is extracted for FD-I, FD-II and ND and combined in a single spectrum since the physics behind the cosmogenic isotope production and its decay is the same for the three samples. The resulting spectrum is compared with a MC simulation of the ^{9}Li decay, as is displayed in the figure 5.22, showing good agreement between both spectra. This MC simulation was also used to find the production rate of ^{8}He radioisotope, and the results were consistent with no fraction of ^{8}He in the sample [148].

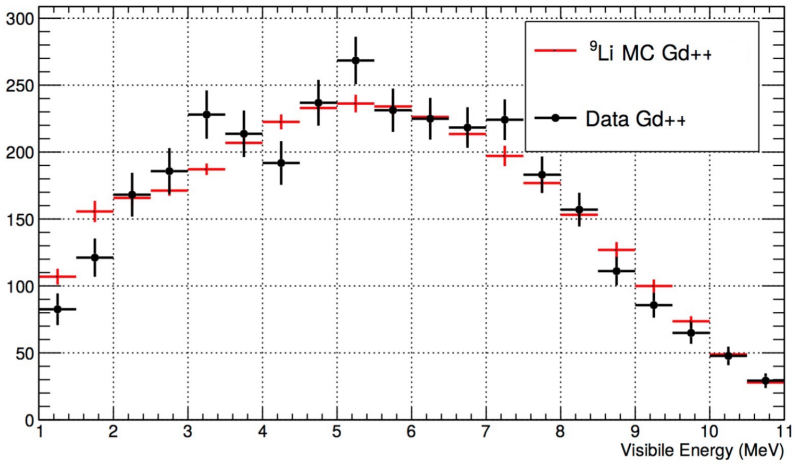

Figure 5.22: Prompt energy spectrum of the ^{9}Li/^{8}He candidates selected by the likelihood function $\mathcal{L}$. Data are shown as black dots while the ^{9}Li MC is shown in red, pointing out the consistency between both spectra.

The rate of the remaining background is estimated from a fit to the time difference between the IBD candidates and the previous tagged muons (called $\Delta T_{\mu-IBD}$) before applying the likelihood veto.

To increase the statistics of the ^{9}Li sample and reduce accidental coincidences, it is required that there is at least one or more neutron candidate after a muon and the energy of the muon is above 600 MeV* (MeV-equivalent scale since the energy reconstruction is not ensured at high energy due to non-linearity processes related to flash-ADC saturation effect). The distribution of this enriched distribution is shown in figure 5.23 where it can be appreciated that the cosmogenic background causes an exponential shape while IBD candidates, as they do not have correlation with muons, show a flat component. This fit provides an upper limit for the cosmogenic background rate.

On the other hand, the lower limit is computed from a muon sample with energy above 300 MeV* if the muon is followed by at least one neutron capture in the subsequent 1ms or from a muon sample with energy above 500 MeV* if there is no a neutron.

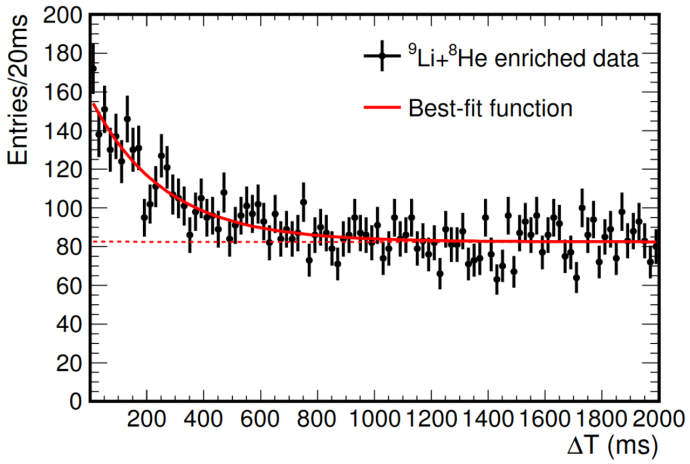

Figure 5.23: $\Delta T_{\mu-IBD}$ distribution of the ^{9}Li enriched sample. The red line shows the best fit. The exponential shape is due to the Li contribution.

After this, both upper and lower limits given by the previous fits are combined. Finally the fraction of vetoed events with the likelihood veto of section 5.7.5 is subtracted from the combined rate, being the remaining rate for each detector:

- FD: 3.010 ± 0.600 day^{-1}
- ND: 12.320 ± 2.010 day^{-1}

Since there is a strong correlation between the IBD candidates and cosmogenic background rate, to avoid a possible bias in the oscillation fit analysis, the Li rate is treated as an unconstrained value. Previous studies demonstrated that there was a tension between the output values extracted from θ_{13} fit and the input values for the Li rate [131]. However it was checked that the uncertainties on the background rates are strongly constrained in the θ_{13} fit by the spectral shape information and the output value of $\sin^2(2\theta_{13})$ is consistent with and without constraining the background rates.

5.10 Final Selected Candidates and Remaining Background

Once the preselection and selection cuts and also the background vetoes has been applied to the neutrino candidates sample and the MC simulation, the number of IBD candidates for data and MC and also the remaining background events are summarized in table 5.9.

The signal to background ratio is ∼11 in the FD and ∼21 in the ND, being the impact of the BG larger in the FD due to the lower signal rate. The total BG precision is 6.3% in the FD and 5.7% in the ND. It can be seen that accidental background is dominant in the FD, while it is the cosmogenic background (^{9}Li) the dominant one in the ND due to the smaller overburden.

Table 5.9: Rate of selected IBD candidates in data and MC and remaining background rates working as inputs for the θ_{13} oscillation analysis.

	FD-I	FD-II	ND
Lifetime [day]	455.207	362.974	257.959
Signal MC (no osc.) [day^{-1}]	101.72	115.30	786.73
IBD candidates [day^{-1}]	105.77	117.53	815.94
Accidentals [day^{-1}]	3.930 ± 0.010	4.320 ± 0.020	3.110 ± 0.004
FN + SM [day^{-1}]	2.54 ± 0.07	2.54 ± 0.07	20.77 ± 0.43
^{9}Li+^{8}He [day^{-1}]	3.01 ± 0.60	3.01 ± 0.60	12.32 ± 2.01
IBD cand - BG [day^{-1}]	96.29	107.66	779.74

These rates are going to be introduced as inputs for the θ_{13} oscillation fit. Comparing the number of IBD candidates once the remaining background is subtracted with the MC prediction, there is a deficit of ∼7% in the FD and ∼1% in the ND. This deficit is interpreted as the result of the neutrino oscillations.

5.10.1 Direct measurement of the background rates

In the period in which the two reactors of the power plant are shut down, a direct measurement of the background rate has been carried out, see 5.10. During this period, 68 events were selected by the FD-I after the full neutrino selection was performed. The measured number of residual neutrino candidates was 4.18 ± 1.25, where a conservative error of ∼30% is assigned. So the background rate measured during this period is 8.91 ± 1.16 day^{-1}. Taking into account that the estimation based on the DC background model is 9.48 ± 0.60 day^{-1}, it can be concluded that there is a remarkable agreement between the background model and the off-off measurement.

Table 5.10: Rate of selected IBD candidates (residual neutrinos included) and expected and measured BG during the period with two reactors off.

	FD-I Off-Off
Lifetime [day]	7.16
IBD candidates [day^{-1}]	9.5
Residual $\bar{\nu}_e$ [day^{-1}]	0.584 ± 0.175
Expected BG rate [day^{-1}]	9.48 ± 0.60
Measured BG rate [day^{-1}]	8.91 ± 1.16

There is a new period in which Double Chooz has taken data while the two reactors are off as can be seen in figure 5.24. With these new events collected during 17 days in both ND and FD-II, the background model accuracy has been scrutinised, applying to these events the selection cuts and background vetoes. The final rates for each background source are listed in table 5.11. The agreement with the results of the BG model shown in table 5.9 is within 1σ. In this case, there is not yet an estimation of the residual neutrino candidates emitted during this 17 days.

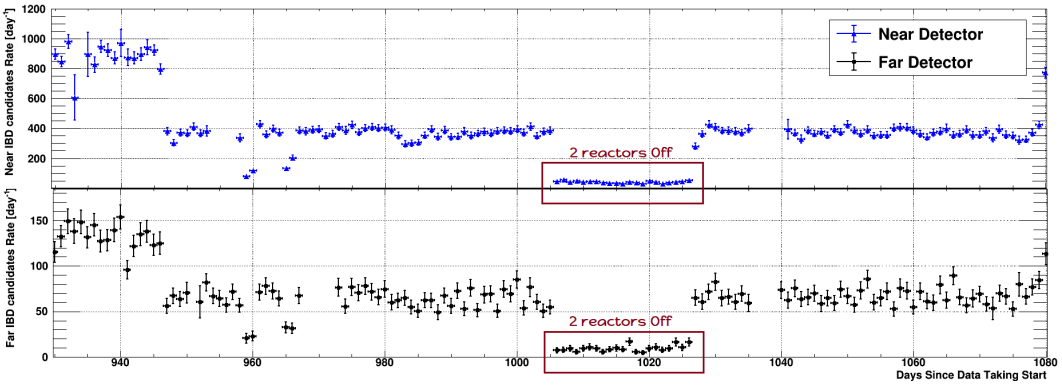

Figure 5.24: Daily rate of IBD candidates for ND (blue) and FD-II (black). The 2-Off period used to check the background model is marked with a red square.

Table 5.11: Rate of selected IBD candidates during the new 2-Off period and remaining background rates.

	FD-II	ND
Lifetime [day]	16.905	12.736
IBD candidates [day^{-1}]	9.17	42.09
Accidentals [day^{-1}]	4.453 $\pm$ 0.030	3.027 $\pm$ 0.026
FN + SM [day^{-1}]	3.00 $\pm$ 0.40	20.0 $\pm$ 1.8
^{9}Li+^{8}He [day^{-1}]	2.04 $\pm$ 0.82	11.5 $\pm$ 2.0

Chapter 6

IBD Detection Efficiency

6.1 Introduction

During the period of data taking with only one detector, the mixing angle θ_{13} is estimated from the comparison between the antineutrino candidates collected with the Far Detector and the Monte Carlo (MC) simulation of the antineutrino flux explained in Chapter 3. Therefore it is needed to guarantee that the detection efficiency of both samples is properly determined and the simulation matches the one from the data. However since there are some effects that are not well reproduced in the simulation, the normalization of the predicted spectra is adjusted to avoid a systematic bias.

Once the Near Detector is working, two possibilities to extract θ_{13} arise. The first one consists of a data to MC comparison using both far and near detectors neutrino candidates, in a similar way as in the single detector fit explained above. The second one falls on the comparison of the neutrino candidates collected with the FD and the ND. Then the relative difference between both sets of data becomes a relevant parameter in the θ_{13} oscillation analysis. Uncertainties in the detection efficiency are divided into correlated components, common for both detectors and therefore cancelled when comparing the ratio of the signals in the far versus near detector, and uncorrelated components which lead to potential variations in the efficiency between detectors.

The most dominant uncertainty on the θ_{13} measurement is introduced by the antineutrino flux prediction error explained in Chapter 3, followed by the IBD detection efficiency error, i.e, the quantification of how many of the neutrino interactions occurring in the detector are identified by the experiment. This chapter is going to focus on its measurement for the antineutrino data sample as well as for the MC simulation and the residual difference between both efficiencies is accounted by the efficiency correction factor. This detection uncertainty falls on four main contributions that are described in section 6.2.

One of these contributions is the selection efficiency. As seen in Chapter 5, the antineutrino selection is based on an Artificial Neural Network (ANN), allowing to refuse the accidental coincidences that hide the signals of the neutron capture and the positron annihilation. The selection efficiency, detailed in section 6.3, is defined

as the ratio of IBD candidates selected with the standard and loose ANN cut Some perturbations on the selection conditions have been performed to study any possible systematics on the selection efficiency determination, getting efficiency values consistent with the reference one, testing this way the robustness of the method. This analysis is . Furthermore the presence of some Gd in the ND GC could introduce some bias in the calculated efficiency correction factors, so the impact of the leak in the TnC analysis is studied in section 6.4.

In previous Double Chooz publications, the detection efficiency was focused on the estimation of the neutron captures only by Gd nuclei [131]. In this case, the energy of the neutron captures peak around 8 MeV and there is no need to use the ANN since the accidental coincidences are concentrated mainly in the low energy regions (1-3 MeV). The leak impact on this analysis has been as well studied in section 6.5.

Moreover the time stability of the selection efficiency has been checked in section 6.6. Finally, section 6.7 explains how the total efficiency correction factors and their uncertainties are introduced in the oscillation fit analyses that will be detailed in Chapter 7.

6.2 IBD detection efficiency on the TnC analysis

In order to extract the mixing angle θ_{13}, the oscillation analysis is performed following two possible approaches:

- Comparing the observed rate of IBD candidates with the expected one extracted from the MC prediction.
- Comparing directly the FD with the ND observed data.

In both cases, every spectrum needs to be normalized properly via the IBD detection efficiency, that considers any difference in the antineutrino selection criteria as well as differences in the detector response or detector modelling. This way the detection efficiency of the IBD signal can be factorized into four components:

$$\epsilon_{\text{det}}^{\text{IBD}} \equiv \epsilon_{\text{sel}} \cdot \epsilon_{\text{BG}} \cdot \epsilon_{\text{p\#}} \cdot \epsilon_{\text{bound}} \tag{6.1}$$

ϵ_{sel} denotes the efficiency of the IBD candidates selection described in section 5.6, while ϵ_{BG} takes into account the inefficiency of the background vetoes described in table 5.7. The third component, $\epsilon_{\text{p\#}}$ accounts for any differences between data and MC associated to the estimation of the number of protons in the scintillator volume. Last term, ϵ_{bound}, allows to consider the spill events involving either the buffer or the gamma-catcher acrylic tank volumes. This chapter is devoted to explain the selection efficiency term ϵ_{sel}. The three other terms are described in section 6.7, focusing on how they are introduced in the θ_{13} oscillation fit.

Despite the detectors have been designed to be almost identical, there are some discrepancies that are taken into account in the θ_{13} oscillation fit via an efficiency correction factor of the form:

$$\text{R}_{\epsilon_{\text{det}}}(\text{data:data}) = \frac{\epsilon_{\text{det}}^{\text{FD}}}{\epsilon_{\text{det}}^{\text{ND}}} \tag{6.2}$$

On the other hand, the MC simulation has been designed to replicate step by step the data from the generation of the $\bar{\nu}_e$ in the reactor to their interaction in the detectors, as was explained in the Chapter 3. Thus the IBD detection efficiency for the MC can be factorized analogously to the one for the signal following equation 6.1. Comparably to equation 6.2, another efficiency correction factor is defined to account for any effects not included in the simulation:

$$\mathrm{R}_{\epsilon_{\mathrm{det}}}(\mathrm{data{:}MC}) = \frac{\epsilon_{\mathrm{det}}^{\mathrm{data}}}{\epsilon_{\mathrm{det}}^{\mathrm{MC}}} \tag{6.3}$$

6.3 Selection efficiency

This section is devoted to describe the efficiency of the IBD selection criteria for the TnC analysis, ϵ_{sel}, and its efficiency correction factor $\mathrm{R}_{\epsilon_{\mathrm{sel}}}$. The performance of this analysis is carried out with the neutrons coming directly from the IBD reaction [149]. The major advantage of these neutrons is that they are homogeneously distributed inside the whole detector volume, so they are especially appropriated for volume-wide studies of the detector performance.

In the latest Double Chooz Gd-only analysis [131], the selection efficiency had been also estimated using the data extracted from the deployment of the ^{252}Cf calibration source, with large statistics. However the source can be deployed only along the neutrino target central axis (z-axis) and in certain positions of the GC along the Guide Tube (see section 2.8), limiting the possibility to obtain full detector volume efficiency.

Since integration over all neutron captures on the full detector volume of the detectors is done, this analysis does not care about the number of capture fractions either in Gd or H. The neutron spill in/out currents among the detector volumes (Target $\leftrightarrow$ Gamma Catcher) can also be neglected. However these two sources are relevant in the Gd-only analysis, so they are described in the Appendix A.

The selection efficiency is established from the three characteristic variables of the IBD reaction, i.e. the delayed energy of the neutron capture $\mathrm{E}_{\mathrm{del}}$ and the spatial $\Delta\mathrm{R}$ and temporal $\Delta\mathrm{T}$ coincidence between the reconstructed prompt and delayed signals. However the region of the H captures is contaminated with low energy backgrounds coming from the natural radioactivity. To maximize the signal to background ratio, a multivariable analysis using the ANN described in Chapter 5 is developed.

The following definitions for the selection efficiency are adopted:

$$\begin{aligned} \epsilon_{\mathrm{sel}}^{\mathrm{data}}(\mathrm{FD}) &= \frac{\mathrm{N}(\mathrm{IBD} \cap \text{all vetoes} \cap \mathrm{ANN} > 0.85)}{\mathrm{N}(\mathrm{IBD} \cap \text{all vetoes} \cap \mathrm{ANN} > 0.1)} \\ \epsilon_{\mathrm{sel}}^{\mathrm{data}}(\mathrm{ND}) &= \frac{\mathrm{N}(\mathrm{IBD} \cap \text{all vetoes} \cap \mathrm{ANN} > 0.86)}{\mathrm{N}(\mathrm{IBD} \cap \text{all vetoes} \cap \mathrm{ANN} > 0.1)} \end{aligned} \tag{6.4}$$

$$\begin{aligned} \epsilon_{\mathrm{sel}}^{\mathrm{MC}}(\mathrm{FD}) &= \frac{\mathrm{N}(\mathrm{IBD} \cap \mathrm{ANN} > 0.85)}{\mathrm{N}(\mathrm{IBD} \cap \mathrm{ANN} > 0.1)} \\ \epsilon_{\mathrm{sel}}^{\mathrm{MC}}(\mathrm{ND}) &= \frac{\mathrm{N}(\mathrm{IBD} \cap \mathrm{ANN} > 0.86)}{\mathrm{N}(\mathrm{IBD} \cap \mathrm{ANN} > 0.1)} \end{aligned} \tag{6.5}$$

where

$$\begin{aligned} \text{IBD} \;=\; & \text{preselection} + (1.0 < \mathrm{E_p} < 8.5)\ \text{MeV} \cap (0.5 < \Delta\mathrm{T} < 800)\ \mu\text{s} \\ & \cap\ (1.3 < \mathrm{E_{del}} < 10)\ \text{MeV} \cap \Delta\mathrm{R} < 1200\ \text{mm} + \text{isolation cond.} \end{aligned} \quad (6.6)$$

and N is the number of events passing all the requirements.

The conditions shown in the numerator of each fraction are very similar to the full IBD selection described in previous chapter, i.e. preselection (section 5.6.1), selection (section 5.6.2) and background vetoes (section 5.7). The extension of the prompt energy window up to 20 MeV to accumulate background events that helps constraining the background rate for the θ_{13} analysis, is not useful in this analysis so the prompt energy window is restricted to the interval in which the antineutrinos are expected, that is, 1 MeV $< \mathrm{E_{prompt}} <$ 8.5 MeV. In the denominator the ANN cut is open and set to 0.1 to exclude accidental background contamination at low energy as can be seen in figure 6.1. Below ANN=0.1, the accidental background dominates the data sample, so removing this region of the ANN distribution allows to improve the signal to background ratio. The denominator integrates over ∼98% of the detectable IBD candidates, having the ANN>0.1 cut an inefficiency of ∼0.5%.

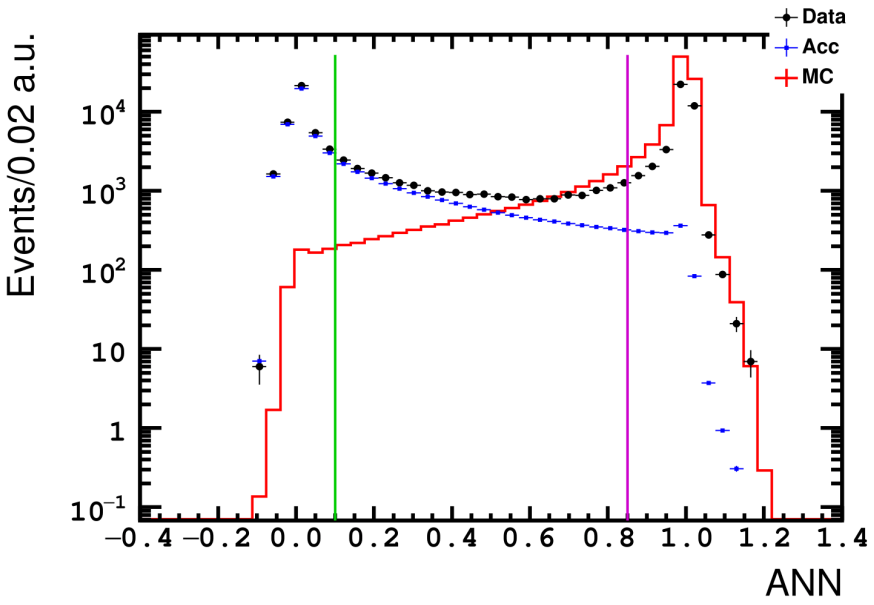

Figure 6.1: Neutral network output distribution (ANN) for FD. The data distribution (without accidental subtraction) is shown with black circles. Blue squares are used to plot the accidental sample while MC is displayed as a red line. The green and the magenta lines point out the cuts that are applied in previous efficiency definition (0.85 for the IBD selection and 0.1 for the open selection). One can see that for an ANN value smaller than 0.1, the data distribution corresponds to a pure accidental sample, so this region can be eliminated without loosing signal.

In the θ_{13} data to MC oscillation fit, remaining differences between the data and MC selection efficiencies (for FD and ND) are corrected by applying an efficiency correction factor. In the case of the data to MC comparison, this factor is calculated as:

$$\mathrm{R}_{\epsilon_{\mathrm{sel}}}(\text{Data XD} : \text{MC XD}) \equiv \frac{\epsilon_{\mathrm{sel}}^{\mathrm{data}}(\mathrm{XD})}{\epsilon_{\mathrm{sel}}^{\mathrm{MC}}(\mathrm{XD})} \qquad \mathrm{X} = \mathrm{FD},\ \mathrm{ND} \tag{6.7}$$

and it is applied directly to the normalization of the MC prompt energy spectrum. The uncertainty of the previous ratio, computed taking into account the correlations between detectors, is added as a pull term that affects to the detector normalization, representing the deviations from the central value. The inputs for the fit concerning detection efficiency are explained in more detail in section 6.7.

In the case of the data to data comparison, the efficiency correction factor is defined as:

$$\mathrm{R}_{\epsilon_{\mathrm{sel}}}(\text{Data FD} : \text{Data ND}) \equiv \frac{\epsilon_{\mathrm{sel}}^{\mathrm{data}}(\mathrm{FD})}{\epsilon_{\mathrm{sel}}^{\mathrm{data}}(\mathrm{ND})} \tag{6.8}$$

To crosscheck these data to data efficiency ratios, an extra correction factor could be defined by comparing FD MC to ND MC sample:

$$\mathrm{R}_{\epsilon_{\mathrm{sel}}}(\text{MC FD} : \text{MC ND}) \equiv \frac{\epsilon_{\mathrm{sel}}^{\mathrm{MC}}(\mathrm{FD})}{\epsilon_{\mathrm{sel}}^{\mathrm{MC}}(\mathrm{ND})} \tag{6.9}$$

6.3.1 Accidental background subtraction

The background vetoes described in section 5.7 are included in the selection efficiency definition of equation 6.4 to avoid correlated backgrounds as fast neutrons, cosmic muons and cosmogenic isotopes. These vetoes inefficiencies have been evaluated in section 5.8. Therefore the accidental coincidences are the main background contribution to this analysis. The technique to measure the accidental background from the data is the off-time method explained in section 5.9.1.1. The accidental sample obtained for each detector is corrected using the accidental correction factors from table 5.8.

The accidental background subtraction implies to apply different accidental correction factors for the normalization of the off-time sample introduced in the numerator and denominator of eq. 6.4. Factors f_μ and f_{iso} depend on the ANN cut since the shape of the ΔT distribution, used to calculate these two factors, is modulated by the ANN, being close to an exponential for large values of ANN (neutrino-like events) and almost flat for small values of ANN (accidental-like events), as can be noticed in figure 6.2. Accidental correction factors for ANN>0.1 are shown in table 6.1, analogously to the table 5.8.

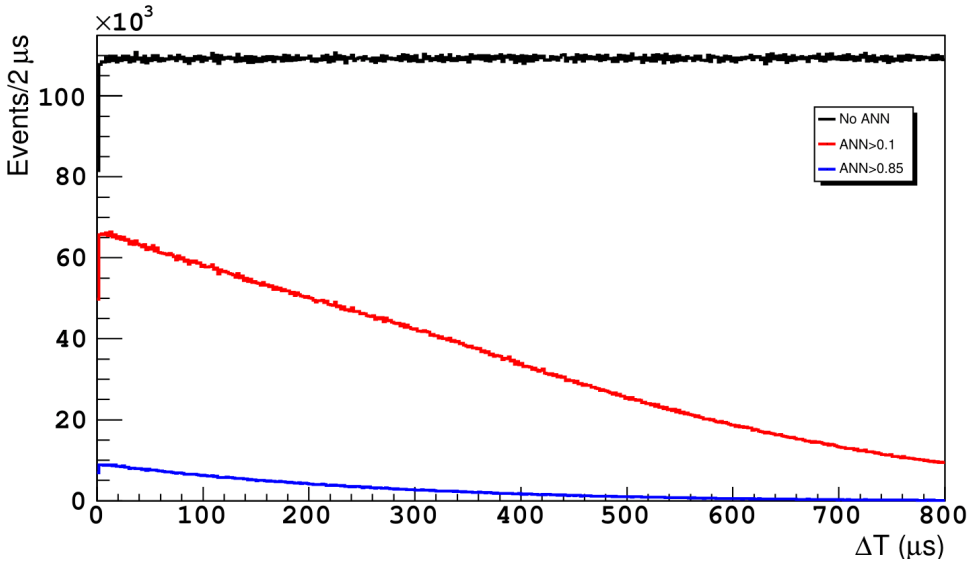

Figure 6.2: Prompt-delayed temporal distribution ΔT for the off-time sample. In black, it can be seen a flat distribution since no ANN cut is applied. The curves with ANN > 0.1 in red and ANN > 0.85 in blue show that the ΔT distribution is not flat anymore once the ANN cut comes into play.

Table 6.1: Global accidental correction factors for FD-I, FD-II and ND for the ANN cut>0.1.

ANN>0.1	FD-I	FD-II	ND
f_{run}	1.00044	1.00042	1.00053
f_{μ}	1.044 ± 0.001	1.044 ± 0.001	1.258 ± 0.001
f_{iso}	1.025442	1.035746	1.021308
f_{Li9}	1.000 ± 0.004	1.000 ± 0.003	1.000 ± 0.001
Total	1.071 ± 0.004	1.082 ± 0.004	1.285 ± 0.001

The combination of both FD-I and FD-II periods also implies a combined accidental correction factor that is calculated from the weighted correction factors of each detector (table 6.2).

Table 6.2: Global correction factors for FD-I+FD-II combination.

	ANN > 0.85	ANN > 0.1
Total	1.082 ± 0.003	1.076 ± 0.003

6.3.2 Selection efficiency results

The main concern on this analysis is based on computing the number of events that satisfy equation 6.4 for the on-time (antineutrino candidates) and the off-time samples (accidentals). Because the off-time method used to measure the accidental background can collect an arbitrarily large number of events through the use of

multiple coincidence windows, this background is measured with high precision and it can be subtracted with negligible statistical uncertainty following the next equation:

$$\epsilon_{\text{sel}}^{\text{data}} = \frac{N_{\text{on}} - \dfrac{f_{acc}(N)}{N_w} \times N_{\text{off}}}{D_{\text{on}} - \dfrac{f_{acc}(D)}{N_w} \times D_{\text{off}}} \tag{6.10}$$

where N_{on} and N_{off} are the number of IBD candidates and accidentals passing the IBD selection defined in numerator of equation 6.4 respectively. D_{on} and D_{off} are the number of IBD candidates passing the looser set of cuts of the denominator. Hence, the events selected by the cuts of numerator are a subset of the events selected by denominator cuts. N_w are the 500 coincidence windows used in the off-time method and f_{acc}(N) and f_{acc}(D) are the global accidental correction factors explained in section 6.3.1 for each detector.

In the MC selection efficiency calculation, the accidental background subtraction is not needed and therefore the equation 6.4 is directly used.

The events passing the numerator and denominator conditions of equation 6.4 are shown in Appendix B. The delayed energy distributions are plotted in figure B.1, the temporal coincidence distribution in fig. B.2 and the spatial coincidence distribution in fig. B.3. Besides the selection efficiency can be seen as a function of the spatial variables ρ and z in figures B.4 - B.6 and also as a projection of these two variables in figures B.8 - B.14. In these plots, the good agreement between the data and MC simulation can be checked as well as the performance of the accidental background subtraction.

Selection efficiencies for every detector for data and MC samples are summarized in table 6.3 (only statistical errors are shown). The overall efficiency is slightly lower in ND, in data as well as in MC, due to the different cut of the ANN variable.

Table 6.3: Selection efficiency data and MC in the full detector volume.

	FD-I	FD-II	FD	ND
$\epsilon_{\text{sel}}^{\text{data}}(\%)$	86.566 ± 0.281	87.032 ± 0.284	86.778 ± 0.205	85.469 ± 0.079
$\epsilon_{\text{sel}}^{\text{MC}}(\%)$	86.555 ± 0.014	86.958 ± 0.014	86.747 ± 0.010	85.539 ± 0.019

The calculation of the statistical errors is now described. Being Eff_{on} the efficiency of the on-time sample, i.e $\text{Eff}_{\text{on}}=\text{N}_{\text{on}}/\text{D}_{\text{on}}$, and Eff_{off} the efficiency of the off-time sample $\text{Eff}_{\text{off}}=\text{N}_{\text{off}}/\text{D}_{\text{off}}$, then eq. 6.10 can also be rewritten as:

$$\epsilon_{\text{sel}}^{data} = \frac{\text{Eff}_{\text{on}} \times D_{\text{on}} - \dfrac{f_{acc}(N)}{N_w} \times \text{Eff}_{\text{off}} \times D_{\text{off}}}{D_{\text{on}} - \dfrac{f_{acc}(D)}{N_w} \times D_{\text{off}}} \tag{6.11}$$

The statistical errors of the selection efficiency values have been computed using a Toy MC. This Toy MC counts with 20000 simulations and for each simulation an efficiency value from equation 6.11 is calculated. The value of the accidental correction factors f_{acc}(N) and f_{acc}(D) is varied from a Gaussian of width equal to the

error of the accidental correction factor itself, taken directly from tables 5.8 and 6.1. The efficiency of the on-time $\mathrm{Eff_{on}}$ and off-time sample $\mathrm{Eff_{off}}$ is assumed to follow a binomial probability distribution. On the other hand, the data candidates that satisfy denominator cuts, $\mathrm{D_{on}}$, do not have any statistical error since this number is treated as a constant. This is an example of conditioning on an ancillary statistic [150]. The accidental background fluctuates poissonsly as $\sqrt{D_{\mathrm{off}}}$. N_w has no error.

Finally a gaussian asymmetric fit of the different efficiency values obtained with the simulation is made in the range (mean±3RMS) to model the final distribution of all the simulated values of the efficiency (see figure 6.3). The mean of this gaussian will be the value of the final selection efficiency for each detector and the sigma will be the final efficiency uncertainty, written in table 6.3.

This procedure has been analytically checked [151] using the Clopper-Pearson confidence interval [152] implemented in the ROOT framework [153] as a function of the TEfficiency class [154].

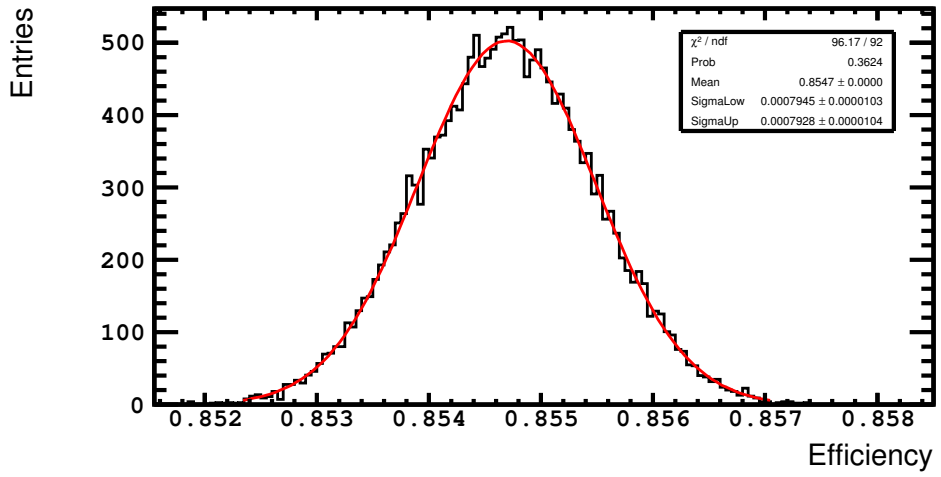

Figure 6.3: Distribution of the selection efficiency for ND data using a Toy MC and a gaussian fit. The mean of the gaussian gives the efficiency value while the width is related to its statistical uncertainty.

For the MC selection efficiency, the statistical uncertainty has been calculated following a binomial error:

$$\sigma_{\mathrm{stat}} = \sqrt{\frac{\epsilon(1-\epsilon)}{N}} \tag{6.12}$$

being ϵ the selection efficiency of equation 6.5 and N the number of candidates that satisfy the denominator of this equation.

Finally the selection efficiency correction factors, that is the ratio between the data and MC efficiency for FD and ND as well as the ratio between FD data and ND data efficiency, have been computed following equations 6.7, 6.8 and 6.9. The results, including statistical errors, are shown in table 6.4.

Table 6.4: Selection efficiency correction factors data to MC, data to data and MC to MC. Only statistical errors are shown.

$R_{\epsilon_{sel}}$(Data:MC)	FD-I:FD-I	FD-II:FD-II	FD:FD	ND:ND
	1.0001 ± 0.0033	1.0009 ± 0.0033	1.0004 ± 0.0024	0.9992 ± 0.0009
$R_{\epsilon_{sel}}$(Data:Data)	FD-I:ND	FD-II:ND	FD:ND	
	1.0128 ± 0.034	1.0183 ± 0.0035	1.0153 ± 0.0026	
$R_{\epsilon_{sel}}$(MC:MC)	FD-I:ND	FD-II:ND	FD:ND	
	1.0119 ± 0.0003	1.0166 ± 0.0003	1.0141 ± 0.0003	

As a reminder the MC with 1.1 μg/cm^3 of Gd in GC is set as the baseline MC for ND (see section 5.3).

The discrepancy appreciated between FD and ND is due to the different value of the ANN cut used (ANN>0.85 in FD, ANN>0.86 in ND), but it can be found that the results of the ratios between data:data and MC:MC are in perfect agreement. Moreover the ratios data:MC shows that the data selection efficiency for each detector is well reproduced within errors by its respective MC simulation.

The systematic error comes from the difference between the selection efficiency value of the two ND MCs (table 6.5) that are more representative of the data, that is, the one with 1.55 and the one with 1.1 μg/cm^3 of Gd concentration in the GC (as seen also in section 5.3):

Table 6.5: ND MC selection efficiency for the MCs with 1.1 and 1.55 μg/cm^3 of Gd concentration in the GC.

	MC ND (1.1 μg/cm^3)	MC ND (1.55 μg/cm^3)
ϵ_{sel}^{MC}(%)	85.539 ± 0.019	85.611 ± 0.019

$$R_{\epsilon_{sel}}(MC_{1.1}ND : MC_{1.55}ND) = 0.9992 \pm 0.0003 \rightarrow \text{Systematic error} = 0.0008$$

This uncertainty is added to any ratio involving the ND MC, to cover the lack of awareness of the quantity of Gd in the ND GC. The final numbers, including this systematic error, are shown in table 6.6 and for simplicity only the FD (total efficiency of FD-I + FD-II) to ND ratios are listed, since they are enough to indicate any discrepancy between detectors and also between data and MC.

Table 6.6: Selection efficiency correction factors for TnC analysis.

$R_{\epsilon_{sel}}$(Data:MC)	FD:FD	ND:ND
	1.0004 ± 0.0024	0.9992 ± 0.0012
$R_{\epsilon_{sel}}$(Data:Data)	FD:ND	
	1.0153 ± 0.0026	
$R_{\epsilon_{sel}}$(MC:MC)	FD:ND	
	1.0141 ± 0.0009	

6.3.2.1 Extra systematic studies

Further investigations were performed to search for any additional sources of systematic uncertainties. The stability of the data to MC selection effiency correction factors against any perturbation in the efficiency definition was also checked by loosening or tightening the cuts imposed in the denominator of equation 6.4:

1. Original
   $(0.5 < \Delta t < 800)\ \mu s \cap (1.3 < E_{del} < 10)$ MeV $\cap$ $(0 < \Delta R < 1200)$ mm $\cap$ ANN > 0.1
2. With ANN > 0
   $(0.5 < \Delta t < 800)\ \mu s \cap (1.3 < E_{del} < 10)$ MeV $\cap$ $(0 < \Delta R < 1200)$ mm $\cap$ ANN > 0.0
3. Without ANN cut
   $(0.5 < \Delta t < 800)\ \mu s \cap (1.3 < E_{del} < 10)$ MeV $\cap$ $(0 < \Delta R < 1200)$ mm
4. Without ANN cut and $E_{del} > 1.2$ MeV
   $(0.5 < \Delta t < 800)\ \mu s \cap (1.2 < E_{del} < 10)$ MeV $\cap$ $(0 < \Delta R < 1200)$ mm

In all cases, no significant deviation was observed from the original value obtained with eq.6.4 as it can be noticed in figure 6.4 and there is no need to include an extra systematic in the selection efficiency correction factors of table 6.6.

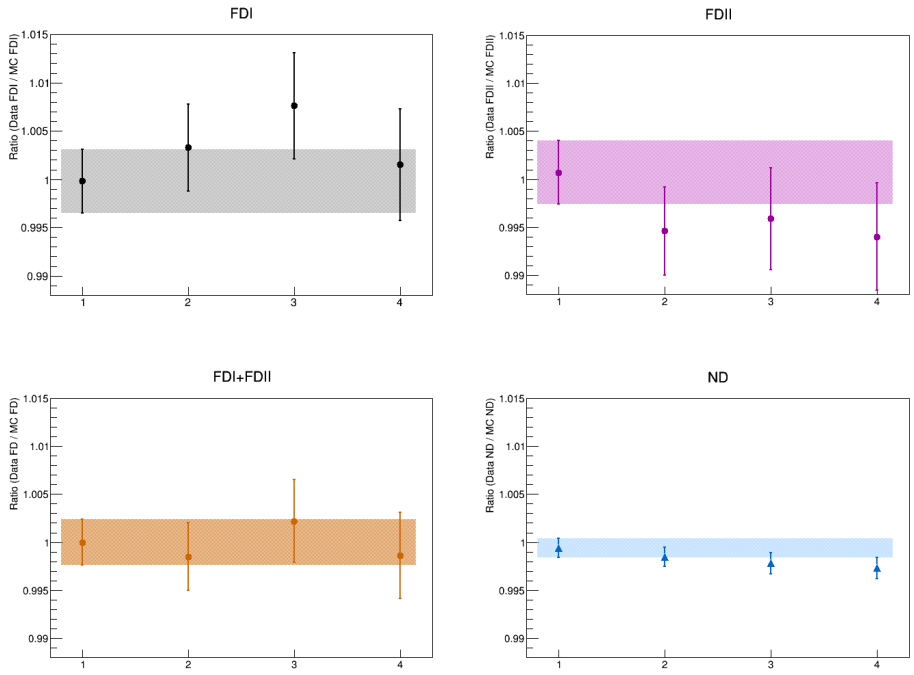

Figure 6.4: Selection efficiency correction factors data to MC for FD-I, FD-II, FD and ND, where the x axis represent the four possible variations of the denominator cuts explained in the text (original, ANN > 0, no ANN cut and no ANN cut + $E_{del} > 1.2$). All the results are compatible within 1 sigma error indicated as the colour bands.

6.4 Leak impact on the TnC selection efficiency analysis

To check that the Gd leak in the ND GC (section 5.3) has no impact on the selection efficiency calculation, the efficiency of the four ND MCs with different concentration of Gd in GC (no Gd in GC, 1.1 μg/cm^3, 1.55 μg/cm^3 and 2.4 μg/cm^3 of Gd) has been tested compared with ND and FD selection efficiency data, as can been seen in figures 6.5, 6.6 and 6.8. Moreover, to study the impact of the volume integration in the efficiency calculation, the spatial limits have been restricted to one meter of the target volume ($|z|<1000$ mm, $\rho<1000$ mm) and also to a fiducial volume that includes the target region plus 20 cm of GC ($|z|<1429$ mm, $\rho<1350$ mm).

In the target region, due to the predominance of the neutron captures on Gd over H, the ΔT between the prompt and delay signal is around 30 μs, but once the full volume is integrated, the competitiveness of the H nuclei is increased, making larger ΔT. Since the ANN rejects more events with larger ΔT, the more detector volume is integrated out of the NT, the lower efficiency is.

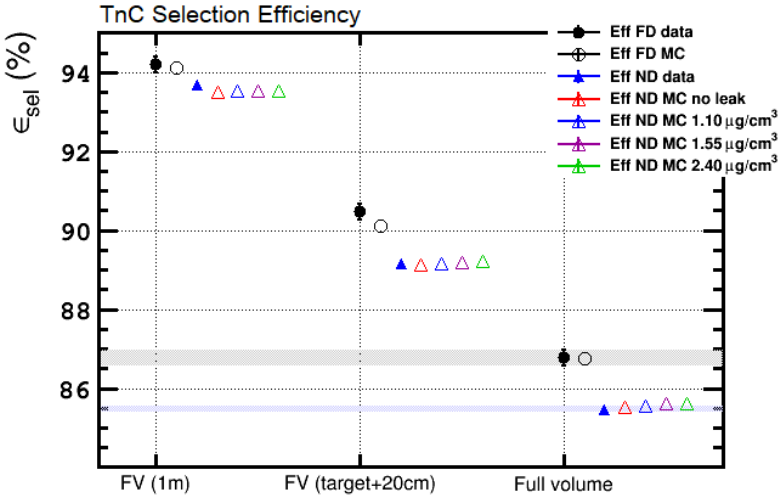

Figure 6.5: Selection efficiency for FD data, FD MC, ND data and the 4 different Gd concentration ND MCs as a function of three different detector volumes: the inner detector volume of 1m in z and 1m in ρ, the target volume + 20 cm in z and ρ and the full detector volume. The gray and blue bands indicate the efficiency values explained in the previous section for FD and ND data. Changes in the Gd concentration in GC have no impact in the ND selection efficiency. Statistical errors of table 6.3 are included.

In figure 6.5, it can be appreciated that the MC selection efficiency is compatible within error with the data efficiency for ND and FD detectors. In the case of the FD, represented as circles, the discrepancy between data and MC is less than 0.2σ in the full detector volume. Focusing on the ND, the biggest discrepancy is found when the data is compared to the MC with 2.4 μg/cm^3, being even so less that 2σ. When the ND data is compared with the baseline MC (with 1.1 μg/cm^3), the difference is less than 0.9σ in the full detector volume.

The evolution of the selection efficiency correction factors is consistent with a flat trend, as can be seen in figure 6.6. There is a small bias, whithin 1σ error, in the FD data to MC correction efficiency in the fiducial volume of the NT+20 cm. This could come from an inefficiency of the FD MC close to the target boundary region. In figure 6.7, it can be appreciated that, when the efficiency correction factor is plotted as a function of $\rho^2 = x^2 + y^2$ (the radial square distance to the center of the detector), the efficiency of the MC is lower than the data efficiency in the limit of the target region. A little excess in this region is also observed in the ND (right plot).

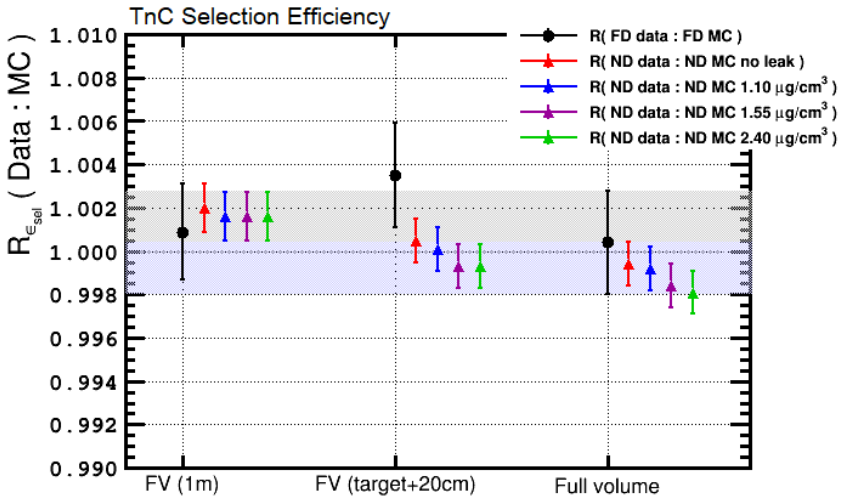

Figure 6.6: Ratios of FD data vs MC selection efficiency and ND data vs the four different Gd concentration ND MC efficiencies as a function of three different detector volumes. The gray and blue bands indicate the values of the ratios explained in section 6.3.2 for FD and ND data to MCs. Changes in the Gd concentration in GC have minor impact in the ratio ND data to MC efficiencies. Errors of table 6.4 are considered.

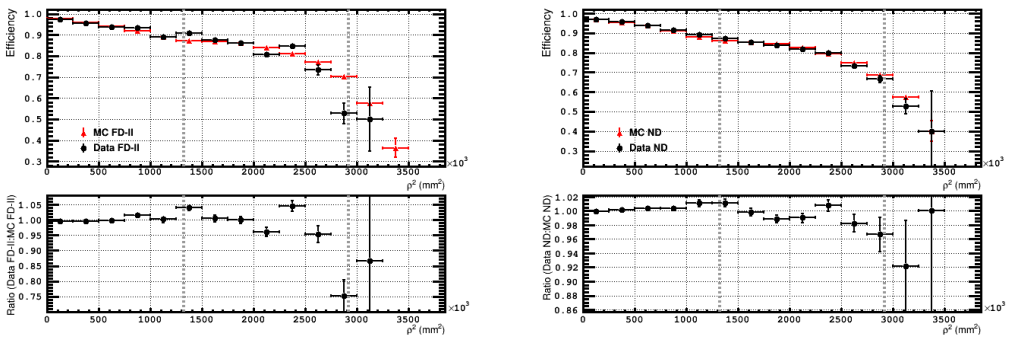

Figure 6.7: Selection efficiency correction factor $R_{\epsilon_{sel}}$(FD data:FD MC) (left) and $R_{\epsilon_{sel}}$(ND data:ND MC) as a function of ρ^2. The inner (outer) pair of dashed lines enclose the Target (GC).

Finally on figure 6.8, the selection correction factor data to data and MC to MC is shown. As explained above, there is a consistency between both data:data and MC:MC ratios for the different volumes, showing that there is no space for any bias in the data to MC ratio. Due to the different ANN cut chosen to guarantee that the prompt energy selection efficiency is identical across detectors, shown in figure 5.15, there is a ∼1.3% discrepancy between FD and ND data selection efficiency. This difference is matched by the MC to MC ratio within 0.1%, for every ND MC.

On the other hand, it can be appreciated that the correction factor is closer to one in the neutrino target fiducial volume than in the full detector volume. The explanation falls on the ANN output behaviour. In figure 6.9, it can be noticed that in the case of the full detector volume, any perturbation around the ANN cut ∼ 0.8 has more impact in the number of selected events than in the case of the reduced 1m volume. This effect is produced since in the 1m region Gd captures predominates over H captures and there are scarcely any accidentals in the Gd time/delayed energy region (ΔT∼150 μs and E_{del} ∼8 MeV). So the difference in the chosen ANN cut for FD and ND is more evident in the full detector volume.

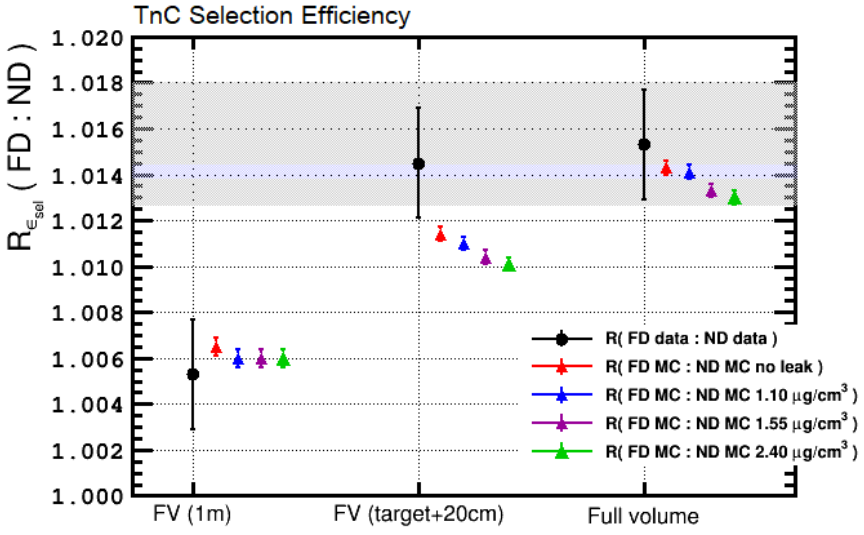

Figure 6.8: Ratios FD data vs ND data efficiency and FD MC vs the four different Gd concentration ND MC efficiencies as a function of three different detector volumes. The gray and blue bands indicate the values of the ratios explained in section 6.3.2. Changes in the Gd concentration in GC has minor impact in the agreement between data and MC efficiency ratios. Errors of table 6.4 are considered.

This way it has been demonstrated that any change on the Gd concentration in the GC has no impact in the ND MC selection efficiency. The TnC analysis is insensitive by construction to the leak since it integrates over all neutron captures in the full detector volume.

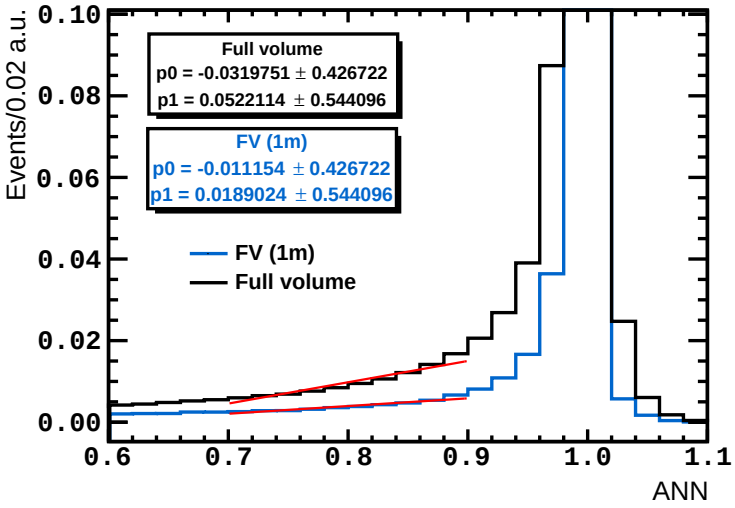

Figure 6.9: ND MC ANN output distribution considering the full detector volume (black line) or only the 1m fiducial volume (blue line). A linear fit is performed in the region of interest (ANN∼0.8). Since the slope of the fit is higher in the full volume than in the 1m volume, any perturbation around the ANN cut has higher impact in the number of selected candidates.

6.5 Leak impact on Gd-only selection efficiency analysis

The ND MC Gd-leak concentration was tuned using fast neutrons sample and was obtained that Gd ND-GC concentration is within [1.10,1.55] $\mu g/cm^3$ [157], as explained in section 5.3. To verify this independent analysis, a crosscheck with IBD neutrons has been carried out through the study of the Gd-only selection efficiency in data and different MCs, since the Gd-only selection is not immune to the Gd leak. For this purpose, these selection efficiencies have been calculated following an analogous procedure to the TnC analysis. This calculation is explained in detail in the Appendix A. The Gd-only selection efficiency is based on a set of sequential 1D cuts defined as:

$$\epsilon_{\text{sel}}^{\text{Gd}} = \frac{N(\text{IBD} \cap \text{Gd BG vetoes})}{N(\text{IBD*} \cap \text{Gd BG vetoes})} \tag{6.13}$$

where:
IBD = $(0.5 < \text{E}_{\text{prompt}} < 8.5)$ MeV $\cap$ $(0.5 < \Delta\text{T} < 150)$ μs $\cap$ $(4 < \text{E}_{\text{del}} < 10)$ MeV $\cap$ $\Delta\text{R} < 1000$ mm
IBD* = $(0.5 < \text{E}_{\text{prompt}} < 8.5)$ MeV $\cap$ $(0.5 < \Delta\text{T} < 800)$ μs $\cap$ $(3.5 < \text{E}_{\text{del}} < 10)$ MeV $\cap$ $\Delta\text{R} < 1200$ mm.

In this case there is no need to use the ANN, since the Gd-captures energy region is well above the natural radioactivity energy. As a remark, the ΔT cut in the denominator is open up to 800μs to consider also the Gd captures that take place in the ND GC.

In figure 6.10, the FD Gd-only selection efficiency for data and MC as well as the ND Gd-only selection efficiency, using data and the four MC, are presented as a function of the 3 different detector volumes used already in section 6.4, that is, the inner detector volume of 1 meter in z and 1 meter in ρ coordinates, the target volume plus 20 cm in z and ρ and the full detector volume. If a fidualization in 1m region is done, the efficiency for FD and ND is almost the same $\epsilon_{\text{sel}}^{\text{Gd}}$(FD data) = 98.674 ± 0.170 %, $\epsilon_{\text{sel}}^{\text{Gd}}$(ND data) = 98.665 ± 0.0055 %. However once the full detector volume is integrated, changes in the Gd concentration in GC turn into different efficiency values, being the MC with 1.55 and the one with 1.1 μg/cm^3 the most representatives of the data sample. Therefore the difference between FD and ND selection efficiency is due to the Gd leak in ND GC, since the behaviour of FD data and MC efficiency is well reproduced by the ND MC without Gd in GC.

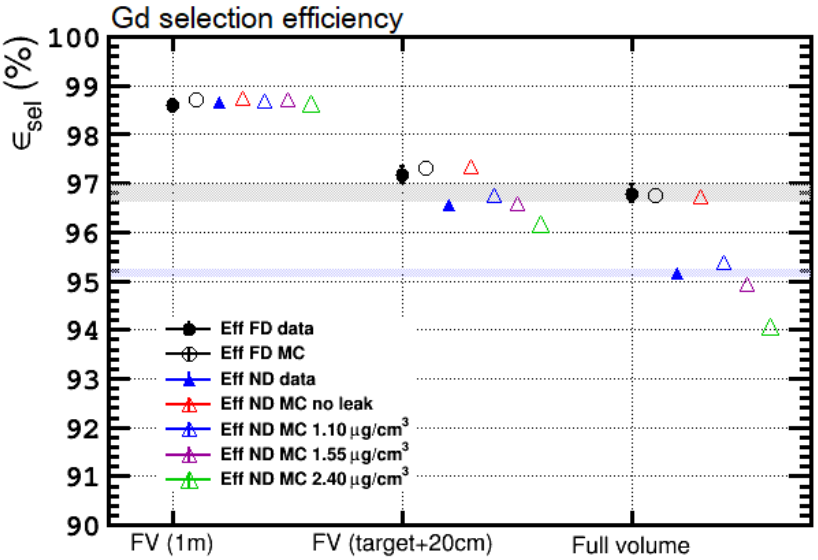

Figure 6.10: Selection efficiency for FD data, FD MC, ND data and the 4 different Gd concentration ND MCs as a function of three different detector volumes. The gray and blue bands indicate the efficiency values explained in section A.1. Changes in the Gd concentration in GC cause changes in the Gd-only single efficiency. Statistical errors of table A.5 are considered.

Besides the ratio between the selection efficiency of the data and the MC is studied in figure 6.11. Again the behaviour of ND data is well reproduced by all the MCs in the fiducial volume of 1 meter. It is important to see how the ratio between FD data and MC is similar in the three considered volumes, while in the case of the ND the MCs with 1.55 and 1.1 μg/cm^3 are the most representatives of ND data.

Figure 6.12 shows the ratio of the FD data to ND data and the ratio of FD MC to the 4 different MC, establishing that the $R_{\epsilon_{\text{sel}}^{\text{Gd}}}$(FD MC:ND MC) being ND MC the MC with 1.55 or 1.1 μg/cm^3 again the ones that reproduce the $R_{\epsilon_{\text{sel}}^{\text{Gd}}}$(FD data:ND data). As seen in figure 6.10, the ND Gd-only selection efficiency decreases when the GC is considered, since the denominator of the Gd-only selection efficiency definition

(eq. 6.13) selects the Gd-captures in the GC. Thus, the ratio between FD and ND rises when more detection volume is considered, being this ratio higher with the increase of Gd concentration in the GC.

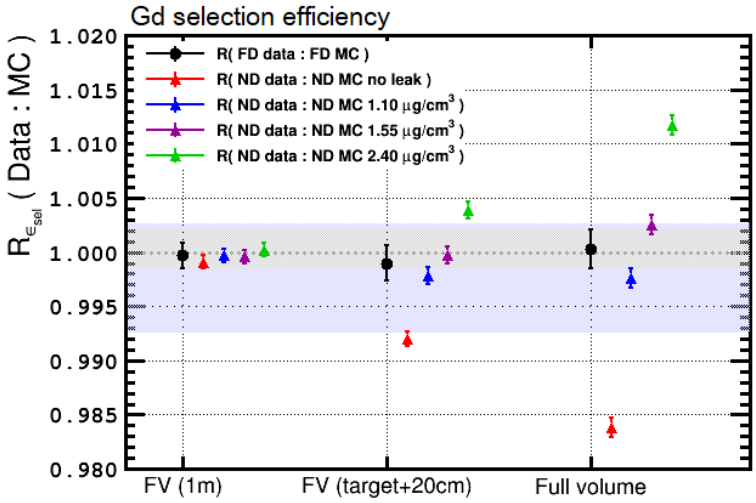

Figure 6.11: Ratios of FD data vs MC selection efficiency and ND data vs the four different Gd concentration ND MC efficiencies as a function of three different detector volumes. The gray and blue bands indicate the values of the ratios explained in section A.1 for FD and ND data to MCs. Errors of table A.6 are considered.

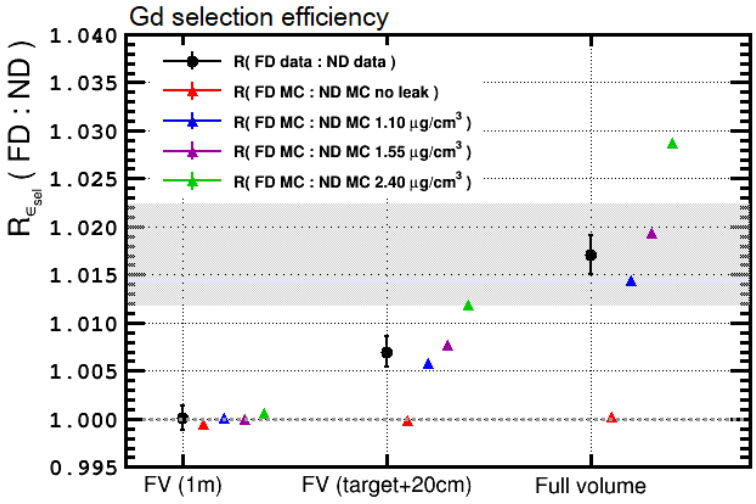

Figure 6.12: Ratios FD data vs ND data efficiency and FD MC vs the four different Gd concentration ND MC efficiencies as a function of three different detector volumes. The gray and blue bands indicate the values of the ratios explained in section A.1. Errors of table A.6 are considered.

6.6 Detectors efficiency stability

6.6.1 TnC analysis

The best way to see if the detector response is constant in terms of time is studying the selection efficiency. For this purpose 23 months of data have been subdivided in periods of around 3 months and the selection efficiency of each period has been calculated following equation 6.4.

In figures 6.13 and 6.14 it can be seen that the TnC selection efficiency seems stable with time for ND and FD-II, named as FD in this section. A linear fit (blue line) has been implemented to crosscheck that the selection efficiency of these periods is the same as the total selection efficiency of the whole data sample of 23 months, finding a really good agreement for the ND: $\epsilon_{\text{fit}}^{\text{data}}(\text{ND}) = (85.420 \pm 0.060)\%$ vs $\epsilon_{\text{sel}}^{\text{data}}(\text{ND}) = (85.416 \pm 0.066)\%$ and for the FD $\epsilon_{\text{fit}}^{\text{data}}(\text{FD}) = (86.900 \pm 0.221)\%$ vs $\epsilon_{\text{sel}}^{\text{data}}(\text{FD}) = (86.941 \pm 0.255)\%$. The same procedure has been followed with the 1.1 μg/cm^3 ND MC (red line) and the FD-II MC, but only 15 months of data have been simulated, so the total MC selection efficiency is the one shown already in table 6.3.

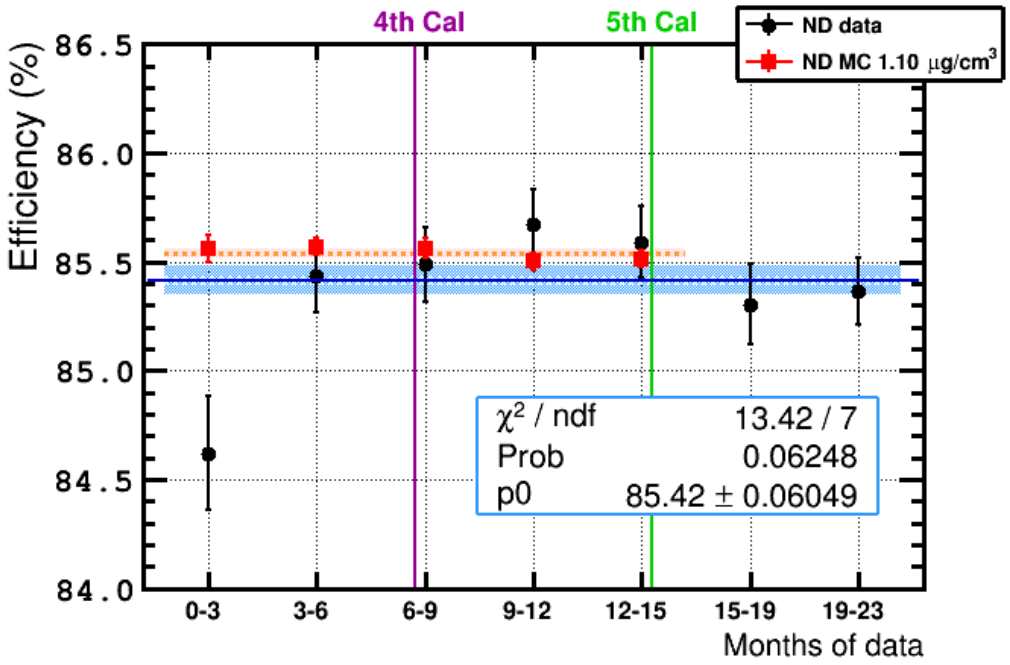

Figure 6.13: ND TnC selection efficiency for each period of the 23 months of data. The blue region shows the selection efficiency using the whole 23 months of data. MC is only produced for 15 months of data and the red line is the fit to the MC points. Black points represent the data efficiency and red squares tag the MC with 1.1 μg/cm^3 of Gd in GC efficiency. The magenta and the green vertical lines mark the dates of the fourth and fifth source calibration campaigns. Only statistical errors are considered.

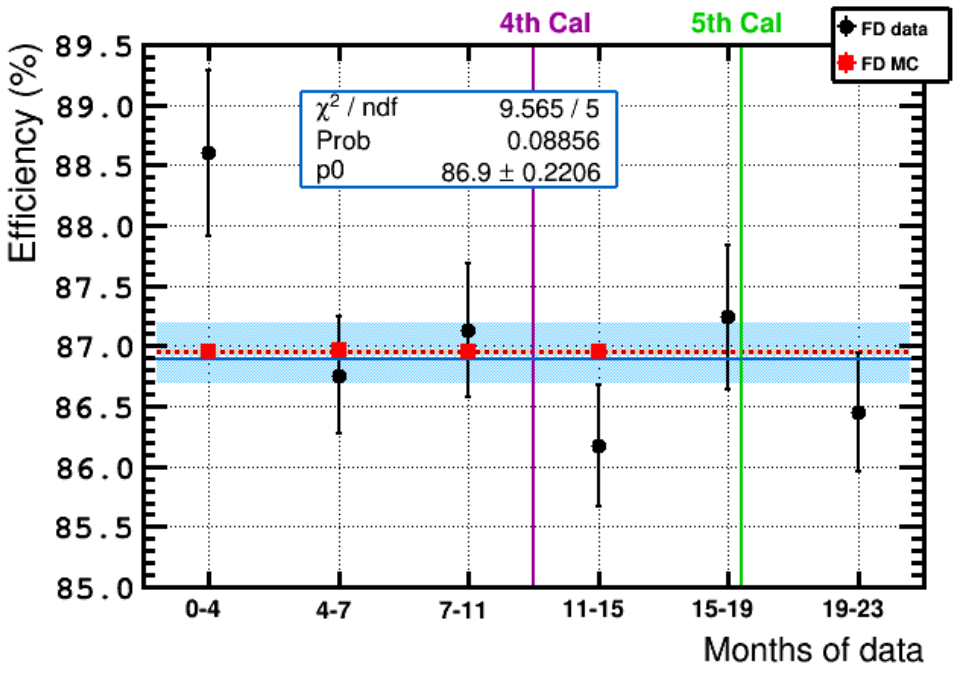

Figure 6.14: FD-II TnC selection efficiency values for each period of the 23 months of data. The blue region shows the TnC efficiency using the whole 23 months of data. MC (without Gd leak) is only produced for 15 months of data. The color and markers follow the ones of figure 6.13. Only statistical errors are considered.

The vertical green and magenta lines correspond to the 4^{th} and 5^{th} source calibration campaigns explained in section 2.8 and they are included to confirm that no liquid perturbation has taken place during the calibration campaigns and the detectors behaviour remain stable.

The subtraction of the off-time sample is carried out from the computation of the accidental events present in each period and the normalization of this quantity with the accidental correction factors of table 6.7, computed analogously to the correction factors of tables 5.8 and 6.1, but for the 23 months.

Table 6.7: Accidental correction factors for FD-II and ND in the TnC analysis for 23 months of data.

	ANN>0.85 or 0.86	ANN>0.1
FD-II	1.086 ± 0.004	1.081 ± 0.004
ND	1.319 ± 0.001	1.286 ± 0.002

Both FD and ND selection efficiency show a stable behaviour in terms of data taking time. In the case of the ND, due to the Gd leak in the GC, the efficiency of the MC without Gd in the GC (orange triangles) and the MC with 1.55 $\mu g/cm^3$

of Gd in GC (purple bottom triangles) have been also calculated for each period to verify that the TnC selection efficiency is not affected by the Gd leak in ND GC, as can be seen in fig. 6.15.

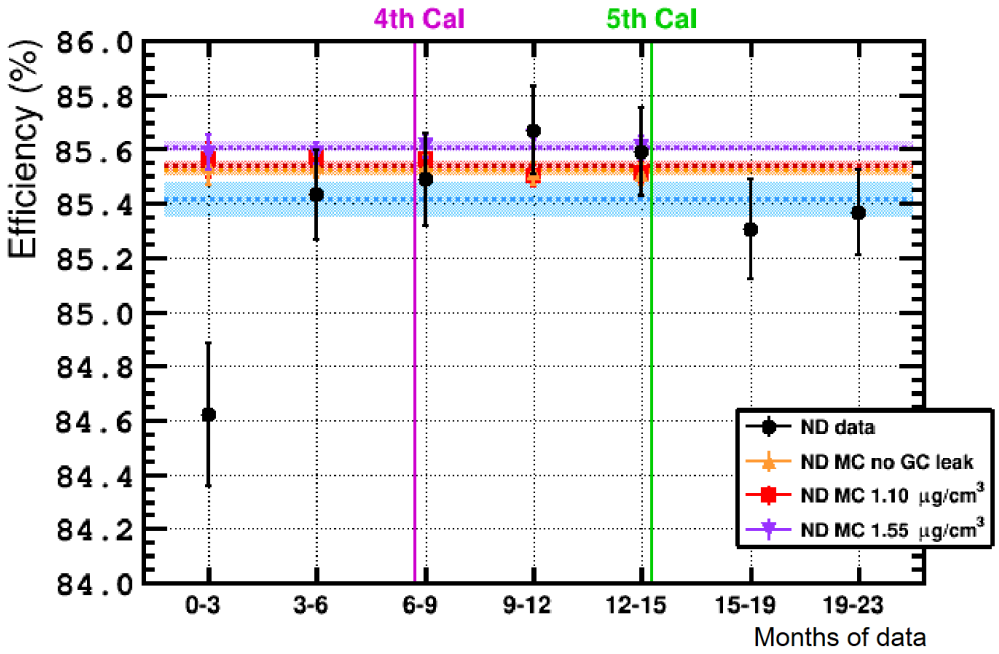

Figure 6.15: ND TnC selection efficiency values for each period of the 23 months of data. The blue region shows the ND data selection efficiency using the whole 23 months of data. MC is only produced for 15 months of data. Orange triangles depict the MC without Gd in GC efficiency, red squares tag the MC with 1.1 μg/cm^3 of Gd in GC efficiency and finally the purple inverted triangles symbolize the MC with 1.55 μg/cm^3 of Gd in GC efficiency.

However it can be appreciated that the first point corresponding to the three first months of data, taken simultaneously with FD and ND, shows a 1 sigma deviation from the efficiency central value, being this deviation positive in the case of the FD and negative in the case of the ND.

This behaviour has been studied dividing the detector in two regions: the upper part (z>0) and the bottom part (z<0), see figure 6.16 as example for the ND. The first period shows a discrepancy only in the upper part of the detector, while in the bottom part, it is compatible with the rest of months. However even with this perturbation in the upper part, the difference between the efficiency of the two volumes is about a 0.27%, being the upper efficiency $\epsilon_{\text{up}}^{\text{data}}$(ND)=(85.303 $\pm$ 0.094)% and the bottom efficiency $\epsilon_{\text{bot}}^{\text{data}}$(ND)=(85.531 $\pm$ 0.092)%. In the case of the MC, this distortion of the first point does not happen and the difference between both volumes is about 0.17%.

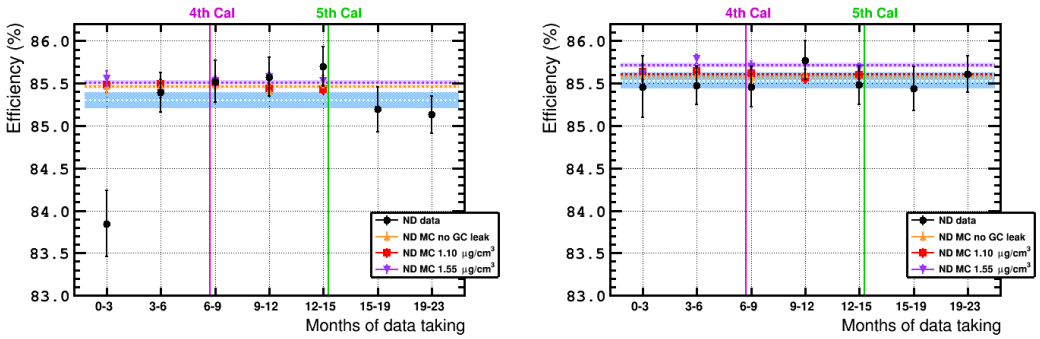

(a) ND Top (b) ND Bottom

Figure 6.16: ND TnC selection efficiency values for each period of the 23 months of data. On the left plot is shown the efficiency for the upper part of the detector and on the right the efficiency for the bottom part. The color and markers follow the ones of figure 6.15.

To find out which could be the origin of the discrepancy with the first point, the rate of accidentals has been checked. In figure 6.17, it can be seen that in FD the rate of accidentals is increasing in time due to the light noise explained in section 5.5.5, having the lowest rate during the first months. However in ND the behavior is the opposite and the rate is decreasing in time during the first months, then the rate is stable in time.

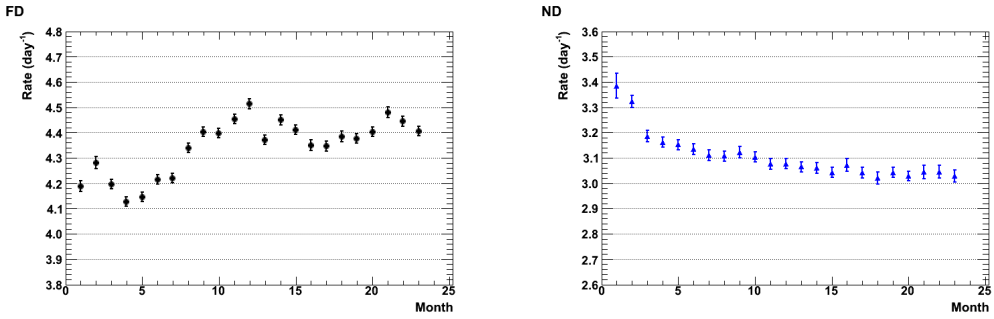

(a) FD (b) ND

Figure 6.17: Accidentals rate for the FD (left) and ND (right) using the 23 months of data taken simultaneously with the two detectors.

In fact, if the accidental rate is considered only in the bottom part of the ND, the rate follows a straight line in time, but if one focus only in the upper part, there is a clear negative slope during the first 100 days of data taking, figure 6.18. The reason for this tendency is still unknown, but this could be due to the contamination of some isotope in the top of the detector, with a lifetime of some weeks.

In the formula 6.10, the efficiency is calculated from the subtraction of the off-time sample to the on-time sample using a normalization correction factor that depends

on the rate of accidentals during the total period of data taking, as was explained in section 6.3.1. Due to the fact that during the first 3 months of data taking the accidentals rate on ND is higher than the average, the accidental correction factor should be higher than the global correction factor described in table 5.8. An accidental correction factor per period could solve the discrepancy, however since the strategy of dividing the data sample in periods is only used for this analysis and the impact on the full sample efficiency has been proved to be really small, this procedure was deemed unnecessary.

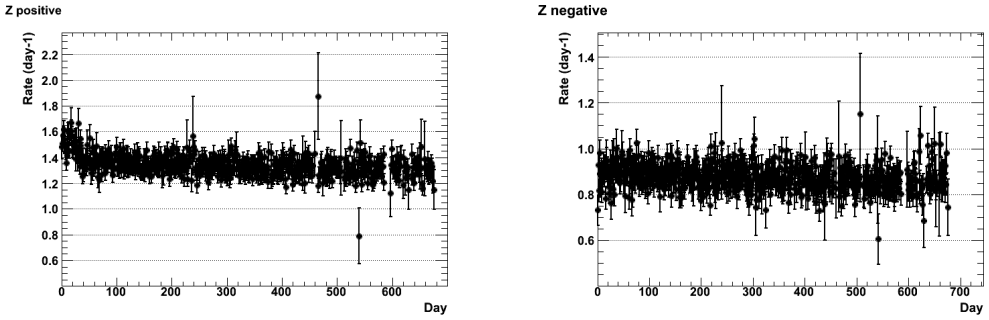

(a) ND Top (b) ND Bottom

Figure 6.18: ND accidentals rate for the upper (left) and bottom part (right) of the detector.

So as a conclusion, from these results it is possible to extract that a time stability on the TnC selection efficiency of both detectors is given and the discrepancy in the first point of data is due to a non properly well done accidental subtraction for this particular analysis.

6.6.2 Gd-only analysis

In this subsection the same procedure as in 6.6.1 has been followed but using the Gd-only efficiency definition written in equation A.3. As explained previously, the definition of Gd-only efficiency allows to tag the Gd captures that happen in the GC, since these events have a large $\Delta T > 150$ μs. This way, if there is any change in the leak, this will imply a change in the Gd-only efficiency.

In figure 6.19 it can be seen that the leak was present since the beginning of the data taking (the ND data does not match the MC without leak at any period). The same procedure has been carried out with the 1.1 $\mu g/cm^3$ MC (red line). Also the efficiency of the MC without Gd in the GC (orange triangles) and the MC with 1.55 $\mu g/cm^3$ of Gd in GC (purple bottom triangles) have been calculated for each period. The leak seems stable during the first 9 months, but after that the efficiency starts decreasing so it can be conclude that the leak of Gd in the GC is increasing in time.

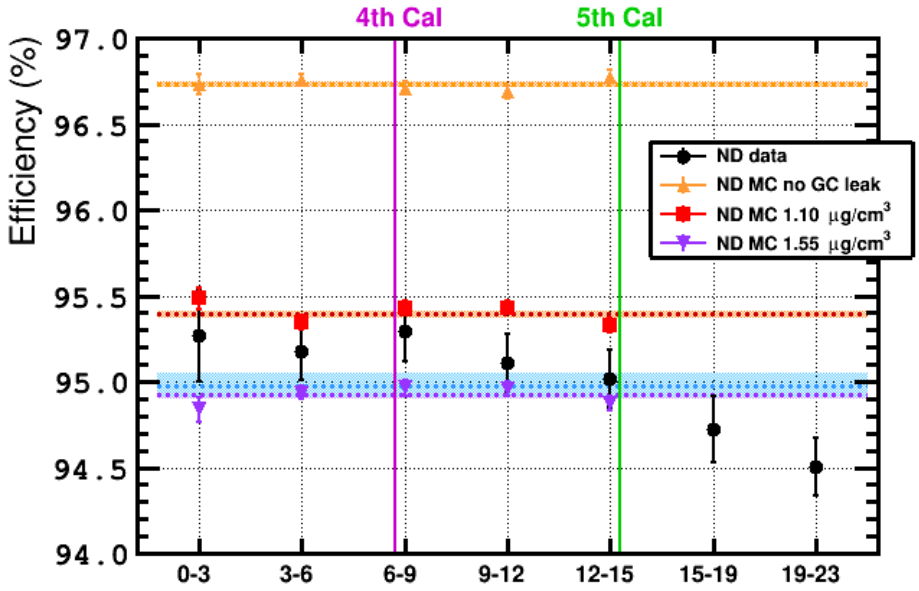

Figure 6.19: ND Gd-only selection efficiency values for each period of the 23 months of data. The color and markers follow the ones of figure 6.15.

Analogously as in the TnC temporal study, the detector has been divided in an upper and a bottom part to monitor the leak, as can be observed in figure 6.20. Looking at the full detector volume, it seems that during 9 first months the behaviour of data is compatible with MC doped with Gd, which simulates a Gd concentration uniformly distributed through GC. However after these 9 months, in the upper (bottom) part of the detector there is more (less) Gd than the simulated in the MC. The discrepancy between the upper part $\epsilon_{\text{up}}^{\text{data}} = (94.159 \pm 0.104)\%$ and the bottom part $\epsilon_{\text{bot}}^{\text{data}} = (95.832 \pm 0.090)\%$ in data selection efficiency is around 1.78%, while in the MC doped with 1.1 μg/cm^3 of Gd in GC this discrepancy is only 0.08 %.

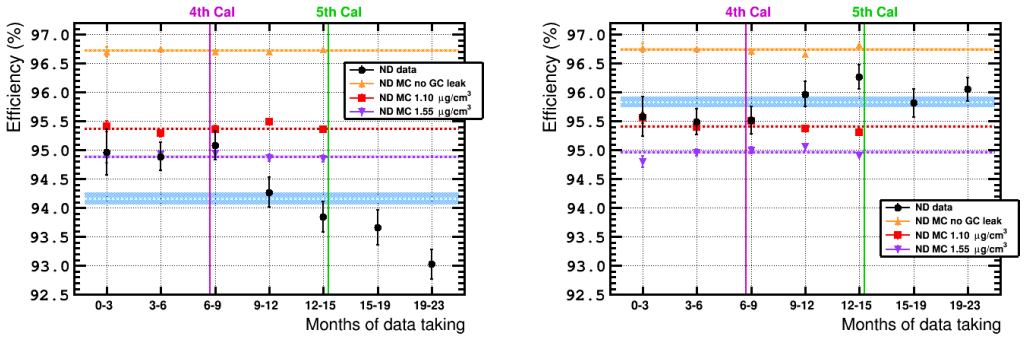

Figure 6.20: ND Gd-only selection efficiency values for each period of the 23 months of data. On the left plot it is shown the efficiency for the upper part of the detector and on the right for the bottom part. The color and markers follow the ones of figure 6.15.

The same study is performed taking into account only captures in the fiducial volume of 1m reduced target (the center of the detector) and only captures in the GC. In the target the data selection efficiency matches the MC, as expected. Focusing on the GC, the data is well reproduced by the MCs doped with 1.1 and 1.55 $\mu g/cm^3$ of Gd. Dividing again the detector in two regions (see figure 6.21), the upper part of the GC shows that the efficiency of data is always below the doped MC. On the contrary in the bottom part there is a soft agreement with $1.1 \mu g/cm^3$ MC during the first 9 months, but after that, the data is more efficient than the MC. This implies that although there is some Gd present in the bottom part of the GC, its quantity is less than the simulated by the MC with 1.10 $\mu g/cm^3$.

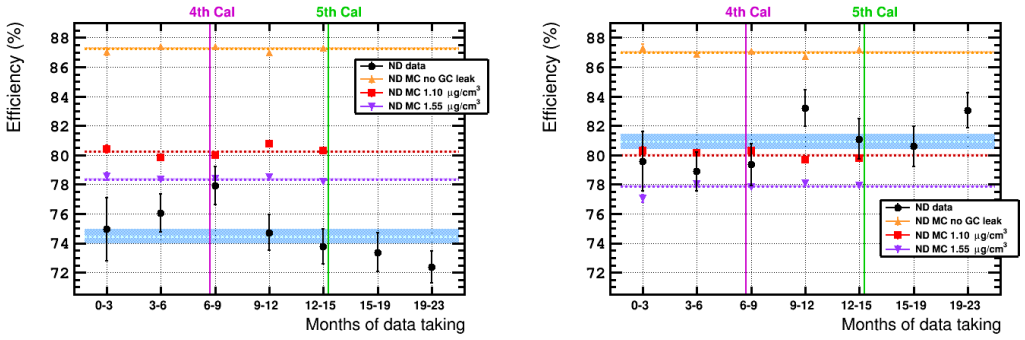

(a) ND GC Top

(b) ND GC Bottom

Figure 6.21: ND Gd-only efficiency values for each period of the 23 months of data considering the neutron captures only in the CG. The left (right) plot shows the efficiency for the upper (bottom) part of the detector. The color and shape of the data markers follow the ones of figure 6.13.

Finally the FD temporal stability has been also studied in the full detector volume. The Gd-only efficiency for FD is stable in time (figure 6.22), showing good agreement between data and MC, with no evidence of a leak in the FD.

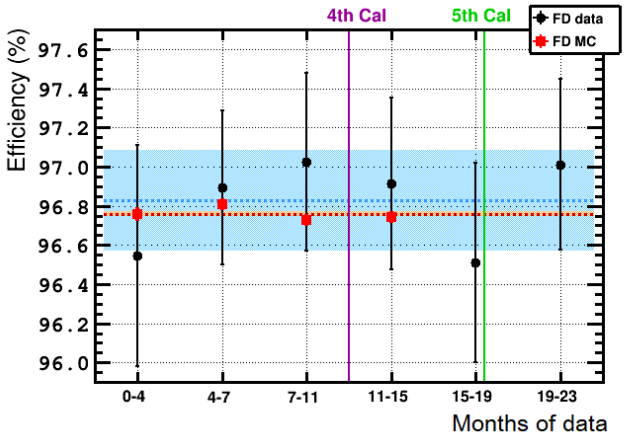

Figure 6.22: FD Gd-only efficiency values for each period of the 23 months of data. The color and markers follow the ones of figure 6.14.

6.7 Detection systematic inputs for oscillation fit

The total uncertainty on the signal detection efficiency in both the ND and FD depends on the antineutrino selection efficiency ϵ_{sel}, the inefficiency of the background vetoes ϵ_{BG}, the boundary effect ϵ_{bound} and the uncertainty on the proton number $\epsilon p\#$.

As it has been mentioned above, the discrepancies between data and MC are introduced in the MC normalization through some efficiency correction factors.

This section is devoted to describe all the individual efficiency correction factors and uncertainties that intervene in the computation of the total MC efficiency correction factor (with the exception of the neutron selection efficiency that has been detailed in previous sections). Also the efficiency inputs used on the oscillation analysis code are introduced.

Then the detection efficiency uncertainty can be treated by either Covariance Matrix or Nuance Parameters, and in both cases the uncertainty for each detector and their correlations are used. Since it's an effect on the event rate, the Covariance Matrix is fully bin-to-bin correlated for a single detector. The uncertainty, given in terms of an inefficiency to be applied in the MC, needs to be normalized to the unity, as it is explained in section 6.7.4.

6.7.1 Proton Number

The expected energy spectrum of detected antineutrinos is:

$$N_{\nu}^{exp}(E, s^{-1}) = P_{\bar{\nu}_e\bar{\nu}_e} \cdot \frac{N_p \cdot \epsilon_{\text{abs}}}{4\pi L^2} \cdot \frac{P_{th}}{\langle E_f \rangle} \langle \sigma_f \rangle \tag{6.14}$$

where E is the neutrino energy, $P_{\bar{\nu}_e\bar{\nu}_e}$ is the oscillation probability, N_p is the number of protons in the interaction volume, L the baseline of the experiment, P_{th} the thermal power, $\langle E_f \rangle$ the mean energy released per fission in the reactor, and $\langle \sigma_f \rangle$ the mean cross-section per fission (the explanation of this term was mentioned in section 3.2.3). ϵ_{abs} is the absolute efficiency, that is the proportion of remaining IBD neutrino candidates after the selection versus the total number of neutrinos that interact in the detector. The proton number directly relates to the rate of detected neutrinos and therefore any uncertainty on it directly contributes to an uncertainty in the rate of detected neutrinos.

To calculate the proton number N_p in target and GC there are two parameters which need to be known: the absolute liquid mass M_{liquid} and the relative H fraction f_H in the scintillator molecules:

$$N_p = \frac{f_H \cdot M_{liquid}}{m_H} \tag{6.15}$$

being m_H the hydrogen mass. Whereas masses can be measure at the 0.1% level and even below, the H fraction can be determined at the 1% level with the standard technologies as CHN elemental analysis (Carbon, Hydrogen, Nitrogen) performed at BASF company in Ludwigshafen [165].

The target liquid was produced in an unique batch. Therefore the H fraction is assumed to be identical between both detectors and the uncertainty is estimated

from its mass determination including temperature effects, as temperature variations could change the liquid density.

In contrast, the GC liquid scintillator was mixed separately for far and near detector with slightly different chemical compositions. Therefore the H fraction has to be measured individually for both batches.

Target The hydrogen fraction f_H, including an estimate of uncertainties, was calculated from the hydrogen fractions in the 6 individual components of the liquid scintillator (n-dodecane, ortho-PXE, Tetrahydrofuran (THF), PPO, Bis-MSB and a metal-organic Gd-complex) as determined from their chemical formulas and weight measurements of these components during the mixture of the Target scintillator, given a result of $f_H = 0.1360 \pm 0.0004$ [166],[100].

In the case of the target, the liquids for FD and ND are coming from the same batch and only one measurement of the f_H was performed, so both the near and the far use the same central value of f_H (f_H(ND)=f_H(FD)) and the same associated uncertainty, being fully correlated. However the liquid mass estimation M_{liquid} is based on the uncorrelated mass measurement between ND and FD. The scintillator mass M_{liquid} was determined by a measurement with the weighting tank [167, 169], which was part of the filling procedure and the next parameters values are obtained:

$$\begin{aligned} M_{liquid}^{ND} &= (8326.5 \pm 3.8)\ \text{kg} \\ M_{liquid}^{FD} &= (8291.5 \pm 7.3)\ \text{kg} \end{aligned}$$

Finally the atomic mass $m_H = 1.007825u$ from [114] must be used and re-written as $m_H = 1.673533 \cdot 10^{-27}$ kg to obtain the number of protons in the target:

$$\begin{aligned} N_p^{\text{NT}}\ (\text{ND}) &= (6.767 \pm 0.020) \cdot 10^{29} \\ N_p^{\text{NT}}\ (\text{FD}) &= (6.739 \pm 0.021) \cdot 10^{29} \end{aligned}$$

Gamma Catcher The Gamma Catcher scintillator consists of ortho-PXE, n-dodecane and mineral oil (Shell Ondina 909) and the wavelength shifters PPO and BisMSB [100]. The proton number in the Gamma Catcher is also calculated using eq. 6.15.

The hydrogen fraction in GC samples was measured at BASF and TU München (TUM) by the CHN analysis. In this case, the liquids for FD and ND are coming from different batches. For each near and far GC batch, 10 measurements of f_H were performed [170]. These 20 measurements (10 for the near and 10 for the far) were performed with the same experimental setup and by consequence share a common correlated uncertainty. This common correlated uncertainty is of 1%. The precision is worse for the GC than for the target, since for the target this number is calculated from the chemical composition. In the GC there is commercial mineral oil containing many different molecules, making impossible any calculation by composition. The hydrogen fraction for each detector is:

$$\begin{aligned} f_H^{ND} &= 0.1453 \pm 0.0015 \\ f_H^{FD} &= 0.1457 \pm 0.0015 \end{aligned}$$

The mass of the GC liquid can be measured directly using the flow meter data and by measuring the weight of the transport truck before and after filling [171]:

$$\begin{aligned} M_{liquid}^{ND} &= (18200.14 \pm 87.22)\ \text{kg} \\ M_{liquid}^{FD} &= (18056.22 \pm 78.99)\ \text{kg} \end{aligned}$$

Applying these numbers, the final results for the GC proton numbers in the two detectors are:

$$\begin{aligned} N_p^{\text{GC}}\ (\text{ND}) &= (1.580 \pm 0.018) \cdot 10^{30} \\ N_p^{\text{GC}}\ (\text{FD}) &= (1.573 \pm 0.017) \cdot 10^{30} \end{aligned}$$

MC Correction Factors Proton number estimations are introduced in the Double Chooz custom MC event generator, DCRxtrTools [172]. However the proton numbers shown above were the result of several corrections and iterations not available at the time of the MC simulation, so there are some discrepancies between the data estimate and the proton numbers used in the MC, the last ones listed in table 6.8.

Table 6.8: NT and GC proton numbers used in MC simulations for each detector.

	ND	FD-I	FD-II
Target	$(6.767 \pm 0.020) \cdot 10^{29}$	$(6.747 \pm 0.021) \cdot 10^{29}$	$(6.739 \pm 0.021) \cdot 10^{29}$
GC	$(1.586 \pm 0.018) \cdot 10^{30}$	$(1.586 \pm 0.018) \cdot 10^{30}$	$(1.586 \pm 0.018) \cdot 10^{30}$

The proton number correction factors to account for these differences are computed in table 6.9, for the target and the GC volumes.

Table 6.9: NT and GC proton number correction factors using MC simulations for each detector.

	ND	FD-I	FD-II
Target only	1	0.9981	1
GC only	0.9962	0.9918	0.9918

Since in the TnC analysis the NT and the GC volumes are used simultaneously, an effective proton number correction factor considering both volumes must be extracted. The proton numbers have to be weighted by the contribution of each volume to the total selected IBD sample in the Monte Carlo simulation. The proportion of IBD interactions that occurs in the different volumes of each detector is [173]:

Table 6.10: Proportion of IBD interactions (w_i) in percent in each volume of the detector from the MC.

	ND	FD-I	FD-II
Target	41.014	41.021	40.730
GC	58.258	58.225	58.529

So the final proton number correction factor for the TnC is listed in table 6.11.

Table 6.11: Proton number correction factor in the TnC analysis

	ND	FD-I	FD-II
NT+GC	0.9988 ± 0.0066	0.9958 ± 0.0066	0.9961 ± 0.0066

The calculation of the uncertainty of the proton number correction factor can be found at the Appendix C.

6.7.2 Vetoes inefficiencies

For the calculation of the total MC correction factor due to the detection efficiency, it is required to compute the inefficiencies in the $\bar{\nu}_e$ selection due to the background reduction cuts and the associated correction factors to the normalization of the MC simulation. Since these cuts are not applied to the MC, the correction factor is simply the cut efficiency in the data (which is complementary to the inefficiency). Since each background veto has been detailed in section 5.7, only the efficiency for any cut is shown in table 6.12:

Table 6.12: MC correction factor in the TnC selection due to the background vetoes.

Correction factor (%)	ND	FD-I	FD-II
Muon veto	94.57 ± (<0.01)	94.57 ± (<0.01)	74.48 ± (<0.01)
μ-IBD veto	99.51 ± (<0.01)	99.51 ± (<0.01)	97.63 ± (<0.01)
Light noise	99.99 ± (<0.01)	100.00 ± (<0.01)	100.00 ± (<0.01)
Isolation	97.29 ± (<0.01)	96.20 ± (<0.01)	96.86 ± (<0.01)
IV veto	99.94 ± 0.01	99.95 ± 0.01	99.92 ± 0.01
OV veto	99.94 ± (<0.01)	99.94 ± (<0.01)	99.99 ± (<0.01)
Li+He veto	99.48 ± (<0.01)	99.47 ± (<0.01)	99.88 ± (<0.01)
SM veto	99.83 ± 0.02	99.68 ± 0.04	99.88 ± 0.01
Total	90.86 ± 0.02	89.71 ± 0.04	70.24 ± 0.01

6.7.3 Boundary effect

In the case of the TnC analysis, where the neutron can be captured either by a Gd nucleus or by a H nucleus, the spill-in and the spill-out currents, involving the neutron exchange between NT and GC, of the Gd-only analysis described in section A.3 do not apply. However, even though the Buffer is filled with non-scintillating mineral oil, an event produced outside the Gamma Catcher but close enough to it can be detected if part of its energy is deposited in the scintillator of the GC. These events are known as external spill events $\Phi^{\text{ext}}_{\text{det}}$ and corresponds to any current that involves the Gamma Catcher vessel or the Buffer.

These currents are simulated via two MCs: a MC Geant4 simulation including the patch called NeutronTH, the nominal one used in the collaboration, and a MC generated using the Tripoli4 simulation software dedicated to particle transport through matter.

Since the NeutronTH code describes well enough the neutron thermalization, no correction factor was considered necessary, but the discrepancy between both sim-

ulations is taken as the correction factor uncertainty induced by the external spill effect:

$$R_{\epsilon_{\text{bound}}} = 1.0000 \pm 0.0020 \tag{6.16}$$

This spill is fully correlated between FD and ND, so is irrelevant across ND/FD ratio.

6.7.4 Oscillation fit inputs

In the θ_{13} data to MC fit, the detection efficiency correction factor $R_{\epsilon_{\text{det}}}$(data:MC) will modify the predicted neutrino flux in each energy bin i via:

$$N^{corr}_{\text{pred},i} = N_{\text{pred},i} \cdot R_{\epsilon_{\text{det}}}(\text{data:MC}) \tag{6.17}$$

Then the detection efficiency correction factor enters in the fit as a nuisance parameter (one for each detector) with central value equal to zero, since the factor is already applied in the MC, with an uncertainty, called for simplicity σ_{det} coming from the relative uncertainty of the MC efficiency correction factor:

$$\sigma_{\text{det}} = \frac{\sigma_{\text{tot}}\left(R_{\epsilon_{\text{det}}}(\text{data:MC})\right)}{R_{\epsilon_{\text{det}}}(\text{data:MC})} \tag{6.18}$$

This way these pull terms represents the deviations from the central value.

This total detection efficiency correction factor $R_{\epsilon_{\text{det}}}$ comes from the product of the correction factors from the four contributions (ϵ_{sel}, ϵ_{BG}, $\epsilon_{\text{p\#}}$ and ϵ_{bound}), that are resumed for each detector in table 6.13.

Table 6.13: Compilation of the data to MC correction factors and their uncertainties due to detection efficiency for the TnC analysis.

	FD-I data:MC	FD-II data:MC	ND data:MC
Vetoes Efficiency (%)	90.86 ± 0.02	89.71 ± 0.04	70.24 ± 0.01
IBD Efficiency (%)	100.01 ± 0.33	100.09 ± 0.33	99.92 ± 0.12
Boundary Effect (%)	100.00 ± 0.20	100.00 ± 0.20	100.00 ± 0.20
Proton Number (%)	99.58 ± 0.65	99.61 ± 0.65	99.88 ± 0.66

The final value $R_{\epsilon_{\text{det}}} \pm \sigma R_{\epsilon_{\text{det}}}$(data:MC) for each detector is listed in table 6.14. The uncorrelated part of this uncertainty, calculated following equation 6.19 is also included.

$$\sigma^2_{\text{tot}} = \sigma^2_{\text{unc}} + \sigma^2_{\text{cor}} \tag{6.19}$$

Table 6.14: Total detection efficiency correction factor, total uncertainty and uncorrelated uncertainty for FD-I, FD-II and ND.

	$R_{\epsilon_{\text{det}}}$(data:MC)	σ_{tot}	σ_{unc}
FD-I (%)	90.76	0.69	0.38 (FD-I:ND)
FD-II (%)	89.44	0.68	0.38 (FD-II:ND)
ND (%)	70.10	0.49	0.22 (ND:FD)

In the total detection efficiency correction factor for the FD-I an extra factor of 1.003 is added in the product to correct a reactor tool bug on the fission fractions in the MC. This effect was corrected in FD-II and ND MCs.

The procedure to obtain the uncorrelated part of table 6.14 is detailed next. The uncertainty due to the vetoes efficiency is fully uncorrelated between detectors, i.e., FD-I:FD-II, FD-I:ND and FD-II:ND. The uncertainty of the selection efficiency is composed of a statistical component which is inherently uncorrelated. However the boundary effect is fully correlated between detectors. In the case of the proton number, FD-I:FD-II error is fully correlated but 0.26 is estimated to be the uncorrelated error of the FD with respect to the ND while 0.29 is the uncorrelated error of the ND with respect to the FD. This last calculation is explained in the Appendix C. As example, the calculation of the FD-II to ND uncorrelated error is shown:

FD-II to ND: $0.8944 \cdot \sqrt{0.0004^2 \cdot \frac{1}{0.8971^2} + 0.0033^2 \cdot \frac{1}{1.0009^2} + 0.0026^2 \cdot \frac{1}{0.9961^2}} = 0.0038 = 0.38$

The correlation coefficients are obtained following equation 6.20 and listed in table 6.15.

$$\rho_{\mathrm{xy}} = \frac{\sigma_{\mathrm{x,cor}}\sigma_{\mathrm{y,cor}}}{\sigma_{\mathrm{x,tot}}\sigma_{\mathrm{y,tot}}} \tag{6.20}$$

Table 6.15: Correlation coefficients for the total detection efficiency correction factors of FD-I, FD-II and ND.

$\rho_{\mathrm{FDI,FDII}}$	$\rho_{\mathrm{FDI,ND}}$	$\rho_{\mathrm{FDII,ND}}$
0.809	0.743	0.742

So the correlation between FD-I and FD-II is 81% while the correlation between both FDs and ND is 74%. These correlations are used to build the covariance matrix between the detection efficiency nuisance parameters, that is described in more detail in section 7.3.1.1.

Finally, following equation 6.18, the inputs related to detection systematic (represented as the deviations from the central value) to be used in the fit are:

Table 6.16: Detection systematics inputs for the R+S data to MC fit for FD-I, FD-II and ND.

	FD-I	FD-II	ND
Det.syst.$\pm\ \sigma_{\mathrm{det}}$ (%)	0.00 ± 0.76	0.00 ± 0.77	0.00 ± 0.70

On the other hand, for the Reactor Rate Modulation analysis, the detection efficiency correction factor FD data to ND data is also relevant. Table 6.17, analogously to table 6.13, lists the correction factors data to data for each source of uncertainty.

Table 6.17: Compilation of the data to data correction factors and their uncertainties due to detection efficiency for the TnC analysis.

	FD-I:ND	FD-II:ND
Vetoes Efficiency (%)	129.36 ± 0.03	127.72 ± 0.06
IBD Efficiency (%)	101.28 ± 0.35	101.83 ± 0.36
Boundary Effect (%)	100.00 ± 0.00	100.00 ± 0.00
Proton Number (%)	99.57 ± 0.39	99.57 ± 0.39

All the errors shown in the table are considered as purely uncorrelated between detectors. The total detection efficiency correction factor data to data is shown in table 6.18.

Table 6.18: Final detection efficiency correction factor data to data used as input for the RRM fit.

	FD-I:ND	FD-II:ND
$R_{\epsilon_{det}}$ (data:data)	130.45 ± 0.47	129.50 ± 0.48

Chapter 7

θ_{13} Oscillation Analyses

7.1 Introduction

The $\bar{\nu}_e$ inverse beta decay interactions observed with the Double Chooz detectors are used to measure the electron antineutrino disappearance. The deficit in the rate observed in the far detector relative to that of the near detector is consistent with $\bar{\nu}_e$ conversion to other flavours driven by the θ_{13} oscillation mixing angle.

To measure the value of θ_{13} from the $\bar{\nu}_e$ disappearance probability, DC uses a frequentist strategy, minimizing a χ^2 function that compares the data rate and shape, collected with the two detectors, with the MC signal and background model. The uncertainties entering to the fit are the ones of the neutrino flux prediction (section 3.2.4), energy reconstruction (4.6), detection (6.7), background rates and shape and the data statistics (5.10), in form of covariance matrices or pull parameters.

In order to extract a precise measurement of the oscillation angle, this deficit is studied as a function of the number of operating reactor cores and their thermal power (referred as *Reactor Rate Modulation* analysis, section 7.2) or as a function of the observed energy spectrum in which both the rate of IBD candidates and the spectral shape information are used to fit θ_{13} (*Rate + Shape* analysis, section 7.3).

7.2 Reactor Rate Modulation Analysis

Double Chooz is the unique experiment looking for θ_{13} to be exposed to only two reactors. The total antineutrino flux changes significantly during reactor maintenance periods when one or the two reactors are not functioning.

In the Reactor Rate Modulation (RRM) analysis [141], the observed rate of $\bar{\nu}_e$ candidates in data R^{obs} is compared with the expected one R^{exp} from MC simulations for different thermal power conditions (P_{th}) of the two reactor cores (B1 and B2). Three reactor scenarios are considered:

- B1 and B2 core are on (2-On reactor data)

- B1 or B2 is off (1-Off reactor data)
- B1 and B2 are off (2-Off reactor data)

As the reactor cores are not always operating at exactly the same thermal power (P_{th}), the first two configurations can be subdivided according to different expected averaged rates (see figure 3.1). In the current analysis, all available runs have been grouped into days of data taking, which in turn have been grouped in four different averaged rate bins (for ND and FD-II) and in 7 bins in FDI including one bin of 2-Off reactor data. The observed versus expected neutrino candidate rate (IBD data and MC candidates passing the TnC selection, table 5.9) for each detector can be seen in Fig. 7.1.

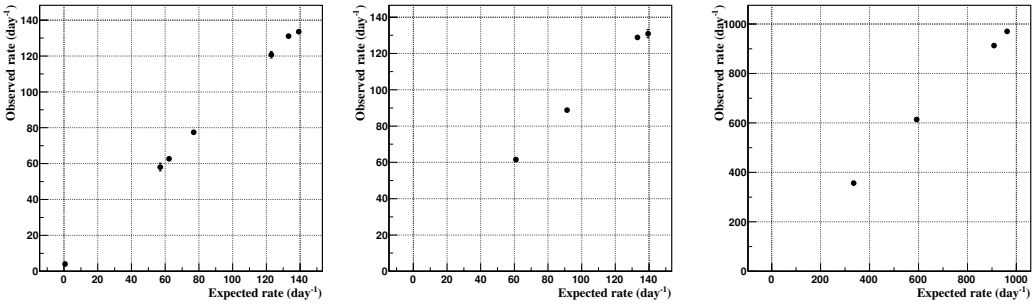

(a) FD-I (b) FD-II (c) ND

Figure 7.1: Observed versus expected neutrino candidate rate, for different reactor power conditions.

This way the value of θ_{13} and the total background rate BG can be derived following equation 7.1:

$$R^{\text{obs}} = \text{BG} + R^{\text{exp-osc}} = \text{BG} + (1 - \sin^2(2\theta_{13})\eta_{\text{osc}})R^{\text{exp}} \tag{7.1}$$

where R^{exp} is the expected rate of $\bar{\nu}_e$ in absence of oscillation. As the accidental background in the observed rate is well determined by means of the off-time coincidence method (section 5.9.1.1), the RRM analysis is performed with accidental-subtracted candidate samples. Therefore, hereafter the total background BG accounts for all background sources except the accidental one. η_{osc} is the average disappearance coefficient over the energies and baselines of the antineutrinos emitted by the reactor cores (eq. 7.2):

$$\eta_{\text{osc}} = \left\langle \sin^2\left(\frac{1.27\Delta m^2_{ee}[\text{eV}^2]L[\text{m}]}{E[\text{MeV}]}\right)\right\rangle \tag{7.2}$$

This coefficient is computed by means of simulations for each one of the data points shown in fig.7.1 as the integration of the normalized antineutrino energy spectrum (E) multiplied by the oscillation effect driven by $\Delta m^2_{ee} = (2.484 \pm 0.036)\cdot 10^{-3}$ eV^2 (taken from [175], [176]) and the distance L between the reactor cores and the detector (see figure 7.2). The complete definition of Δm^2_{ee} is described in section 7.3.2.5.

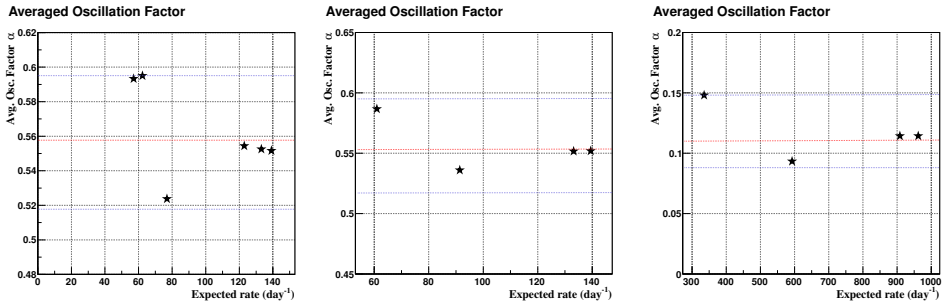

(a) FD-I (b) FD-II (c) ND

Figure 7.2: Average disappearance coefficient η for FD-I, FD-II and ND. Blue horizontal lines corresponds to the disappearance coefficient for each reactor B1 or B2, while the red line is the average of both blue lines.

7.2.1 Direct Measurement of Background using Reactor Off-Off Data

During 7.53 days the two reactors of the Chooz nuclear plant were off. At that time only the FD was taking data. After the shutdown of a given reactor, β-decays continue to occur in the reactor core generating residual neutrinos, as shown in figure 7.3. The majority of the fission products have short lifetime of around some minutes but there are two long life isotopes (^{144}Ce and ^{106}Ru, with halflife comparable to the reactor cyclelength) that represent the major contribution to the neutrino rate. One day after the shutdown, these two isotopes generate the 71% of the residual neutrino rate and the 94% after a week. Thereby, for the 2-Off reactor period, the expected number of residual neutrinos $R^{r-\nu}$ in the detector needs to be estimated. In order to evaluate it, a dedicated simulation has been performed with the FISPACT [177] code, predicting the isotope inventory in the reactor cores. The neutrino spectrum is then computed using the BESTIOLE [178] database. The resulting total number of expected neutrino interactions during the reactor off-off period when corrected for the live time (vetoes) and the detection efficiency computed in Chapter 6, yields 4.18±1.25 detected residual antineutrinos for a period of 7.16 days.

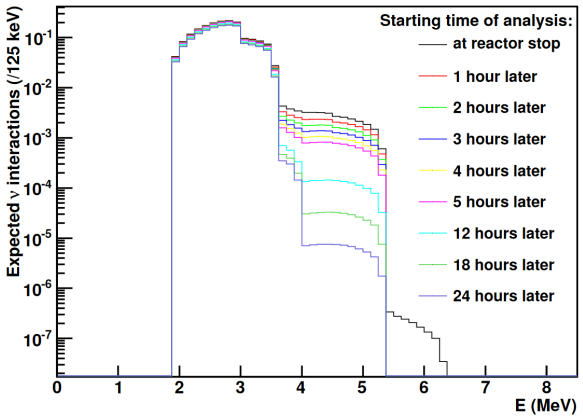

Figure 7.3: Residual $\bar{\nu}_e$ energy spectrum according to the elapsed time passed since the reactor shutdown.

Thanks to this 2-Off period, a direct measurement of the backgrounds in DC oscillation analyses could be performed. The sum of the predicted residual neutrinos and the background estimation provides the number of events that should be observed by the detector. This total prediction gives a rate of 10.06 ± 0.63 events per day, compatible within 1σ with the rate of collected candidates, 9.5 ± 1.2 events per day, demonstrating that there is no additional contributions to be considered in the background model. The total information used is listed in table 7.1 and 7.2.

Table 7.1: Live time, expected residual neutrino rate and expected background rate for FD-I 2-Off period.

	FD-I
Candidates	68
Live Time [day]	7.16
Res. $\bar{\nu}_e$	4.18 ± 1.25
Acc. Prediction	28.139 ± 0.072
^{9}Li Prediction	21.5 ± 4.3
FN Prediction	18.19 ± 0.50
Total Prediction	72.0 ± 4.5

Table 7.2: Expected and observed background rate for the FD-I 2-Off period.

	FD-I [day^{-1}]
BG model	9.5 ± 0.6
Off-Off	8.9 ± 1.2

In 2017 DC counts with a new period of 480 hours of 2-Off reactor data. Thus the background model for the FD-II and ND has been also crosschecked with these 17 days of data, not used in the θ_{13} fit, as well as the good performance of the background vetoes, shown in figure 7.4. The direct measurement is in agreement within 1σ with the prediction (table 7.3).

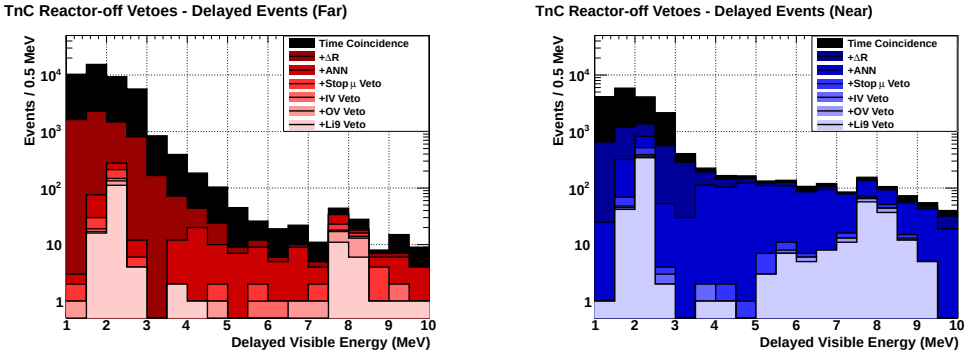

Figure 7.4: E_{del} spectrum of the remaining BG after several vetoes for FD and ND 2-Off period.

Table 7.3: Expected and observed BG rate for the FD-II and ND 2-Off period.

	FD-II [day^{-1}]	ND [day^{-1}]
BG model	9.6 ± 0.6	36.3 ± 2.0
Off-Off	9.8 ± 0.9	39.6 ± 2.5

7.2.2 Systematic Uncertainties

There are three sources of systematics to be accounted for in the RRM analysis: 1) detection efficiency (σ_d), 2) reactor $\bar{\nu}_e$ flux prediction (σ_r), and 3) reactor-off residual $\bar{\nu}_e$ prediction (σ_ν), described in following sections.

7.2.2.1 Detection Systematic Uncertainty

In order to match detection efficiency in both MC and data samples, the Double Chooz MC is corrected by the detection efficiency correction factor reported in table 6.14. This factor accounts for the efficiency of the background vetoes, the efficiency of the selection cuts in the TnC analysis, the boundary effect and the number of protons in NT and GC volumes. For simplicity the uncertainty of this factor is denoted in this chapter as σ_d. In the case of the combined fit (including the three detectors) the uncorrelated error FD to ND, 0.49% of table 6.17 is also included.

7.2.2.2 Reactor Flux Prediction Uncertainty

Concerning the reactor $\bar{\nu}_e$ flux prediction, there are two main contributions that depend on the thermal power, i.e. the uncertainty of the thermal power itself and also the fission fraction of the isotopes present in the reactor fuel.

Total flux-related uncertainty on the expected rate of neutrinos and its breakdown are listed in table 3.6. In the Double Chooz experiment the flux uncertainty treatment differs between single-detector and multi-detector analyses due to different correlation assumptions. In both configurations σ_{IBD} x $\mathrm{S}_k(\mathrm{E})$, $\langle \mathrm{E} \rangle$ and $\sigma_f^{\mathrm{Bugey}}$ are assumed to be fully correlated between reactors and detectors. However correlations of $\mathrm{P_{th}}$ and α_k are treated as fully correlated if the single-detector case (SD) is considered, but fully uncorrelated in the multi-detector case (MD).

The error associated to the thermal power $\mathrm{P_{th}}$ is 0.47% when the two reactors are running at full power, extracted from a detailed study of the EDF [118]-[120]. This is a very good approximation when one integrates over all the data sample (and consequently all reactor operation conditions), but in the RRM fit, since it relies on the data taken at different reactor powers, it is necessary to estimate a $\sigma_{r,i}$, being i each reactor power condition.

In order to compute $\sigma_{\mathrm{P_{th}}}$, four different thermal powers below the nominal one have been used, given by [120]. These points are fitted (eq. 7.3) assuming that the error comes from some constant systematic shift in the power (p1), plus a small contribution which is linear in the power (p0), considering that the errors between each core are fully correlated:

$$\sigma_{\mathrm{P_{th}}} = p0 + \frac{p1}{\mathrm{P_{th}}} \tag{7.3}$$

The fit can be seen in figure 7.5.

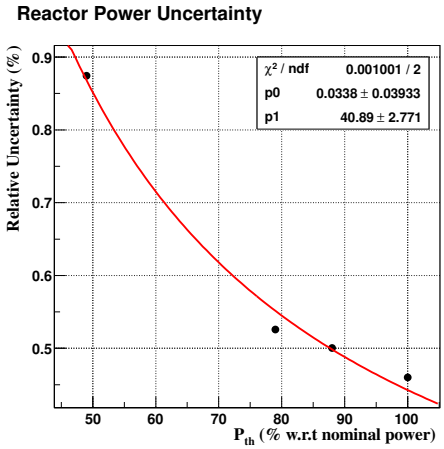

Figure 7.5: Relative thermal power uncertainty $\delta P_{th}/P_{th}(\%)$ as a function of the thermal power (% w.r.t nominal power). Red line corresponds to the error extrapolation.

This error model is used to estimate an averaged reactor uncertainty per day of data taking. Once this averaged error per day is obtained, one can compute the final uncertainty for each one of the 4 averaged rate bins (in ND and FD-II cases) and for the 6 bins in FDI (the off-off reactor point is not included) defined in section 7.2, as it is shown in figure 7.6a. In the case of the SD, all the other sources of reactor systematics (table 3.6), are added quadratically to $\sigma_{P_{th}}$ (figure 7.6b). The total error $\sigma_{r,i}$ (where i stand for each data point) ranges from 1.72% to 1.80% for FD-I, [1.71, 1.82]% for FD-II and [1.71, 1.96]% for ND. The smallest error corresponds to the configuration in which either the two reactors are operating at full power, or one at full power while the other one is off. The largest error corresponds to the configuration in which one reactor is operating at low power while the other is off.

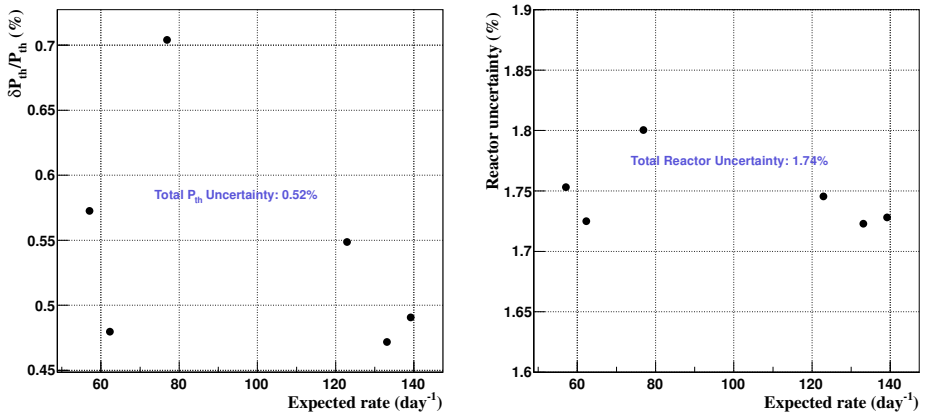

(a) (b)

Figure 7.6: (a) Relative uncertainty on the thermal power for FD-I. (b) Total uncertainty in the $\bar{\nu}_e$ expected rate due to reactor flux prediction for FD-I.

In the case of the MD analysis, where the only factors taken into account are the uncorrelated ones between detectors, only the fraction fission rates uncertainties are added to the thermal power uncertainty, giving an error of $\sigma_r(\text{MD}) = 0.0091$.

7.2.2.3 Residual Neutrinos Uncertainty

As explained above, the number of signal MC events for the off-off period is obtained from the number of expected residual neutrinos from the reactors. This number is estimated as the number of IBD interactions (calculated using the FISPACT rector core simulation) $\times$ selection efficiency estimated with signal MC.

The uncertainty in the number of interactions comes from the comparison between tuned and crude calculations. The dominant error on the residual neutrino rate comes from the uncertainty related to ^{106}Ru and ^{144}Ce, as they are not in equilibrium in the core and their concentration depends on the time of reactors irradiation and shutdown. In other words, their rate of production depends on the ratio of the fissions between ^{235}U and ^{239}Pu. Then the residual neutrinos uncertainty is estimated as the difference in the residual neutrino rate obtained with a crude calculation (without including the real evolution of the reactor cycle) and with a precise one. The number of events in the crude scenario is 30% higher than in the tuned one. Thus a conservative error σ_ν of $\sim$30% is assigned to the residual neutrino number.

7.2.3 Oscillation results

The RRM fit is comparable to a linear fit, where the θ_{13} mixing angle is given by the slope and the total background rate by the intercept, i.e, where none IBD candidate is expected. Therefore this method is independent of any spectral shape information but can constrain the background rate in the fit.

The fit of equation 7.1 is based on a standard χ^2 minimization. The χ^2 is defined as the sum of the different contributions of the single detector 2-On or 1-Off reactor data, the 2-Off FD-I data, background models, systematic uncertainties and global normalization:

$$\chi^2 = \sum_i^N \chi_i^2 + \chi^2_{\text{FDI-off}} + \chi^2_{\text{BG}} + \chi^2_{\text{pen}} + \chi^2_{\text{norm}} \tag{7.4}$$

where χ_i^2 is the term corresponding to the data taken with at least one reactor on for each of the detectors FD-I (eq. 7.6), FD-II (eq. 7.7) and ND (eq. 7.8):

$$\chi_i^2 = \chi^2_{\text{FDI}} + \chi^2_{\text{FDII}} + \chi^2_{\text{ND}} \tag{7.5}$$

$$\chi^2_{\text{FDI}} = \left(\frac{1}{\sigma^{\text{FDI}}_{\text{stat}}}\right)^2 \left(R^{\text{FDI}}_{\text{obs}} - R^{\text{FDI}}_{\text{exp}}(1 + \eta_{\text{osc}} + \textstyle\sum_{r=B1,B2}\left(w_r^{\text{FDI}}\alpha_r^{\text{FDI}}\right) + \epsilon^{\text{FDI}}) - \text{BG}_{\text{FDI}}\right)^2 \tag{7.6}$$

$$\chi^2_{\text{FDII}} = \left(\frac{1}{\sigma^{\text{FDII}}_{\text{stat}}}\right)^2 \left(R^{\text{FDII}}_{\text{obs}} - R^{\text{FDII}}_{\text{exp}}(1 + \eta_{\text{osc}} + \textstyle\sum_{r=B1,B2}\left(w_r^{\text{FDII}}\alpha_r\right) + \epsilon^{\text{FDII}}) - \text{BG}_{\text{FDII}}\right)^2 \tag{7.7}$$

$$\chi^2_{\text{ND}} = \left(\frac{1}{\sigma^{\text{ND}}_{\text{stat}}}\right)^2 \left(R^{\text{ND}}_{\text{obs}} - R^{\text{ND}}_{\text{exp}}(1 + \eta_{\text{osc}} + \textstyle\sum_{r=B1,B2}\left(w_r^{\text{ND}}\alpha_r\right) + \epsilon^{\text{ND}}) - \text{BG}_{\text{ND}}\right)^2 \tag{7.8}$$

being σ_{stat} the statistical uncertainty of R_{obs}, w_r^d the weights that account for the contribution of the reactor r to the detector d, α_r and ϵ_d stand for the pulls associated to the reactor flux prediction systematics and the detection systematics respectively and BG represent the BG rate.

For the 2-Off period, due to the low number of expected residual neutrinos, a Poisson statistic is assumed. In particular, the so called extended Poisson likelihood L, which follows a χ^2 distribution, is convenient:

$$L = \chi^2 = 2\sum_{i=1}^{N}(n_i \ln \frac{n_i}{\nu_i(\tau)} + \nu_i(\tau) - n_i) \tag{7.9}$$

where n is the number of observed events and $\nu(\tau)$ is a model depending on a parameter τ. This likelihood can be adapted to the data with the two reactors off as:

$$\chi^2_{\text{FDI-off}} = 2\Big(N^{\text{obs}} \ln \frac{N^{\text{obs}}}{\text{BG}_{\text{FDI}} + N^{\text{exp}}[1+\epsilon^{\text{FDI}}+\alpha^{\nu}]} + \text{BG}_{\text{FDI}} + N^{\text{exp}}[1+\epsilon^{\text{FDI}}+\alpha^{\nu}] - N^{\text{obs}}\Big) \tag{7.10}$$

where α_ν is the pull for the number of residual neutrinos.

A constraint to the total background rate is given by χ^2_{BG}:

$$\chi^2_{\text{BG}} = \left(\frac{\text{BG}_{\text{FDI}} - \text{BG}^{\text{exp}}_{\text{FDI}}}{\sigma^{\text{exp}}_{\text{BG}_{\text{FDI}}}}\right)^2 + \left(\frac{\text{BG}_{\text{FDII}} - \text{BG}^{\text{exp}}_{\text{FDII}}}{\sigma^{\text{exp}}_{\text{BG}_{\text{FDII}}}}\right)^2 + \left(\frac{\text{BG}_{\text{ND}} - \text{BG}^{\text{exp}}_{\text{ND}}}{\sigma^{\text{exp}}_{\text{BG}_{\text{ND}}}}\right)^2 \tag{7.11}$$

where BG^{exp} is the total background rate estimation arising from the individual estimations using the IBD data (table 5.9) (taking into account that the accidental coincidences are subtracted, so the fitted background is the sum of the Li+He and FN+SM contributions) and σ_B^{exp}, its uncertainty. This constraint on the total BG rate can be removed, treating BG as a free parameter. This is one of the most remarkable features of the RRM fit since it is capable of measuring the total background rate providing a crosscheck of the background model and a background-independent measurement of θ_{13}.

As was explained in section 7.2.2, there are three sources of systematics (σ_{det}, σ_r and σ_ν) to be accounted for in the RRM analysis that are included in the penalty terms:

$$\chi^2_{pen} = \sum_{\substack{d=\text{FDI},\\ \text{FDII,ND}}} \sum_{r=B1,B2} \left(\frac{\alpha_r^d}{\sigma_r^d}\right)^2 + \left(\frac{\alpha^\nu}{\sigma_\nu}\right)^2 + \sum_{\substack{d=\text{FDI},\\ \text{FDII,ND}}} \left(\frac{\epsilon^d}{\sigma^d_{det}}\right)^2 \tag{7.12}$$

Finally the last term in eq. 7.4 corresponds to the correlated normalization error, accounting for the correlated detection and flux systematics. The parameter η_{norm} provides the global normalization:

$$\chi^2_{norm} = \left(\frac{\eta_{norm}}{\sigma_{norm}}\right)^2 \tag{7.13}$$

The detection correlated error between FD and ND is calculated using the values from table 6.14 and the correlation coefficient $\rho_{\text{FD,ND}} = 0.74$ of table 6.15 as:

$$\sigma^{\text{cor}}_{\text{det}} = 0.74 \cdot 0.69 \cdot 0.49 = 0.25\% \tag{7.14}$$

But this error is almost negligible versus the flux correlated error that can be extracted from table 3.6 $\sigma_R^{\text{cor}} = 1.4$. So finally $\sigma_{norm} = \sqrt{0.003^2 + 0.014^2} = 0.014$

7.2.3.1 RRM-II oscillation fit results

Previous analysis of θ_{13} like [141], [131] or [102] shown that the RRM results on θ_{13} are not affected significantly by the selection cuts (or specifically, by the visible energy range considered) as the BG is fitted at the same time. However, the 0.5-20 MeV energy window considered for the IBD selection is not meaningful for a rate-only fit, since in the region from 8.5 to 20 MeV no neutrinos are expected and this region does not add any useful information (according to MC the number of neutrinos with prompt energies larger than 8.5 MeV is only about a 0.024% of the total interactions).

Therefore a new RRM analysis, called RRM-II, has been performed using a reduced prompt energy window, improving the signal to noise ratio (although there is no huge impact on θ_{13} precision). Thus the background rates need to be estimated up to 8.5 MeV (instead of 20 MeV), and the candidates in the [8.5-12] MeV window are used for Li/He estimation, while the candidates between [12-20] MeV could be used for the FN estimation (see figure 7.7 and table 7.4), applying the same selection cuts explained in section 5.7.

Table 7.4: Summary of the background rates and errors used in RRM-II analysis. Accidentals are subtracted in the fit.

	Accidentals [day^{-1}]	FN [day^{-1}]	Li+He [day^{-1}]
FD-I	3.930 ± 0.010	1.09 ± 0.03	2.36 ± 0.28
FD-II	4.320 ± 0.020	1.09 ± 0.03	2.36 ± 0.28
ND	3.110 ± 0.004	8.89 ± 0.18	15.47 ± 1.47

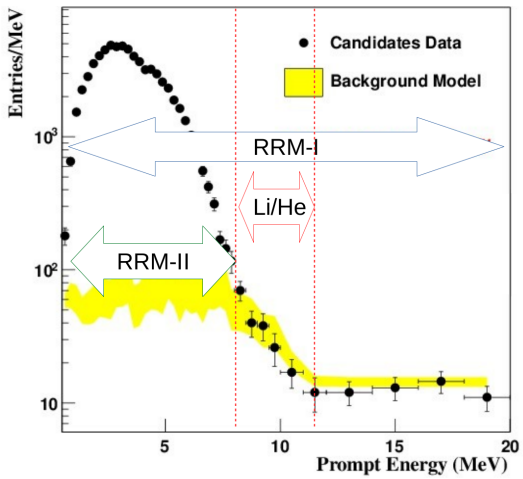

Figure 7.7: Prompt energy neutrino spectra used in the RRM-I analysis [1-20] MeV and in the RRM-II analysis [1-8.5] MeV. Accidental BG subtracted.

Fit Outcome with Background constraint

A χ^2 scan is performed over the possible values of $\sin^2(2\theta_{13})$, minimizing the χ^2 with respect to the three nuisance parameters and the background rate (eq. 7.4). The θ_{13}

measurement of the single detector fit for FD-I, FD-II and ND can be seen in figure 7.8.

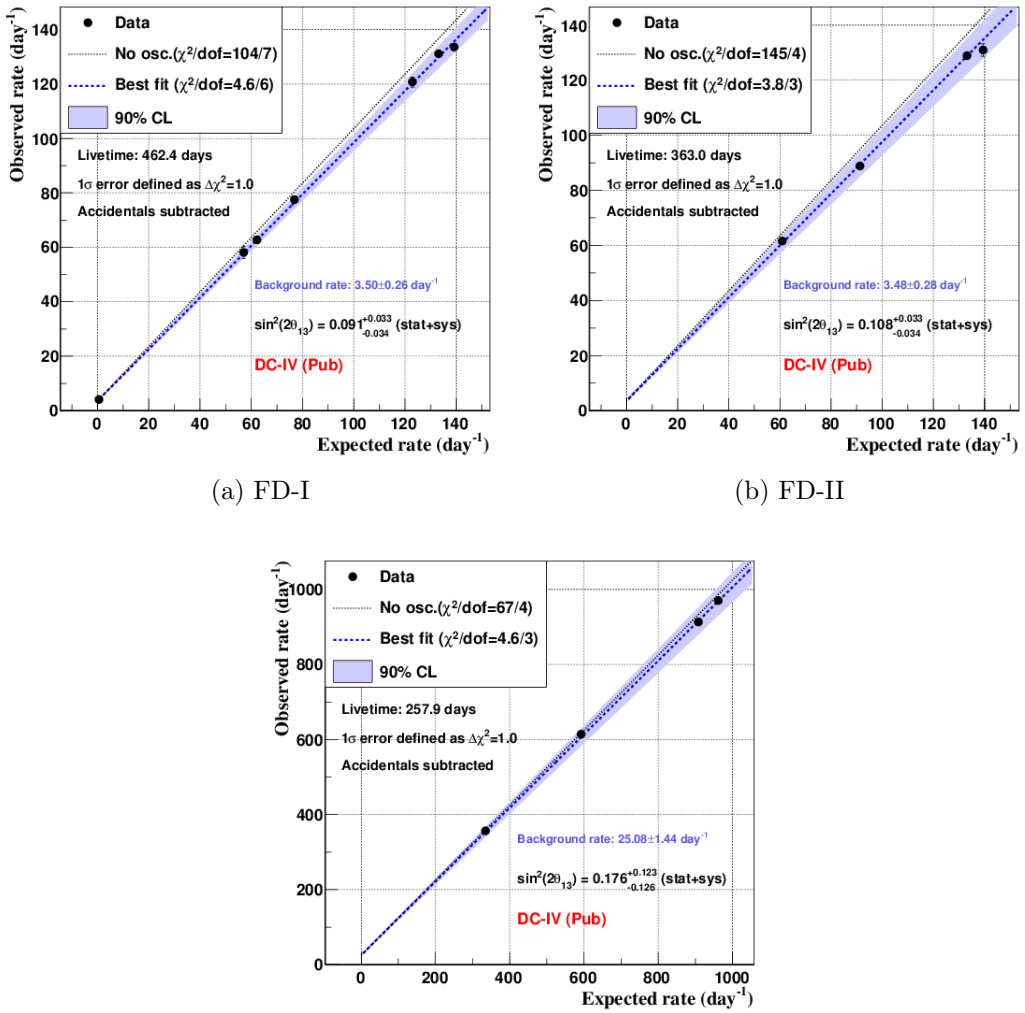

(a) FD-I

(b) FD-II

(c) ND

Figure 7.8: FD-I, FD-II and ND TnC RRM-II fit with background constraint and including the 7 days of reactor-off data for FD-I. The χ^2 minimization accounts for one free parameter (θ_{13}), one constrained parameter (BG), and the three nuisance parameters describing the systematic uncertainties (reactor flux, detection efficiency, residual neutrino rate). The (θ_{13}, BG) best fit is superimposed to the null oscillation hypothesis assuming the background estimated in TnC. The blue region shows the 90% C.L. of the best fit.

Including the three detectors in the χ^2, a global fit combining FD-I, FD-II and ND data can be done. The minimum χ^2, $\chi^2_{\text{min}}/d.o.f. = 12/14$, is found at $\sin^2(2\theta_{13})$ $= 0.095 \pm 0.016$ and $\text{BG}_{\text{FD}} = 3.5 \pm 0.3$ and $\text{BG}_{\text{ND}} = 24.9 \pm 1.4$ events per day (see figure 7.9).

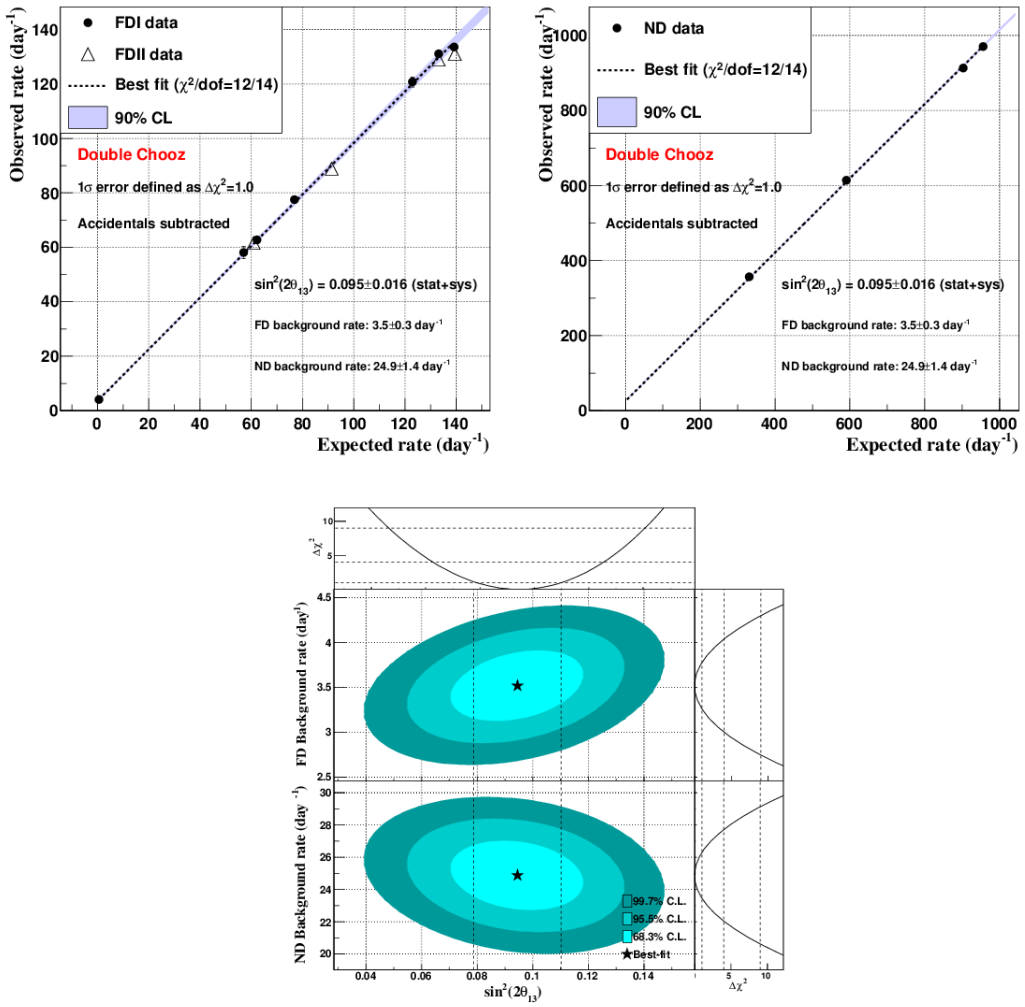

Figure 7.9: Observed versus expected candidates rate for the combined FD-I,FD-II,ND TnC RRM-II fit with background constraint. Upper left: FD-I and FD-II data. Upper right: ND data. Bottom: 1, 2 and 3 σ ($\sin^2(2\theta_{13})$, BG) contour plot.

From this fit it can be extracted that the reactor flux normalization (σ_{norm} is dominated by the reactor flux error) is consistent with expectation: $\eta_{norm} = -0.1 \pm 0.7\%$, so the RRM-II fit is compatible with flux reactor model and furthermore σ_{norm} is reduced from 1.4% to 0.7% thanks to relative comparison FD to ND.

Another configuration of the fit can be carried out by letting the global normalization parameter η free in the χ^2 definition (eq. 7.4), obtaining a compatible result of $\sin^2(2\theta_{13}) = 0.094 \pm 0.017$, as can be seen in figure 7.10. The result for the normalization is in this case η_{norm} = -0.2 ± 0.9%.

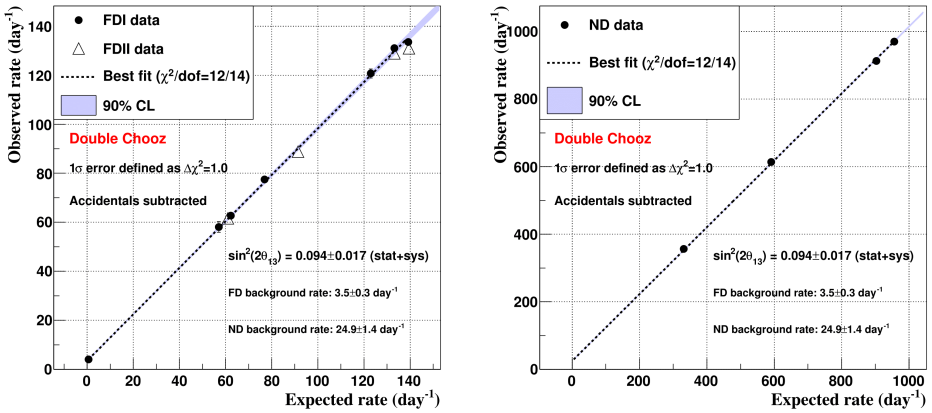

Figure 7.10: FDI,FDII,ND combined RRM-II fit with background constraints and free normalization η. Left: FD-I and FD-II data. Right: ND data.

Fit Outcome without Background constraint

In order to obtain a measurement of θ_{13} independent of the background model, the constraint on the total background rate χ^2_{BG} is removed, treating BG as a free parameter in the fit. Again, a global scan is carried out on the ($\sin^2(2\theta_{13})$, BG) grid minimizing χ^2 at each point w.r.t. the three systematic uncertainty parameters. The best fit is found at $\sin^2(2\theta_{13}) = 0.090 \pm 0.023$ and $\mathrm{BG_{FD}} = 4.0 \pm 0.7$ and $\mathrm{BG_{ND}} = 30.7 \pm 5.0$ events per day, where $\chi^2_{\mathrm{min}}/d.o.f. = 10/12$. The value of $\sin^2(2\theta_{13})$ is consistent with the RRM-II fit with background constraint, and the background rate for FD and ND results in agreement with the expectation: $\mathrm{B^{FD}_{exp}} = 3.45 \pm 0.28$ day^{-1} within 0.7σ and $\mathrm{B^{ND}_{exp}} = 24.36 \pm 1.48$ day^{-1} within 1.2σ. This agreement between the estimation and the BG value extracted from the RRM-II fit can be appreciated in more detail in figure 7.11.

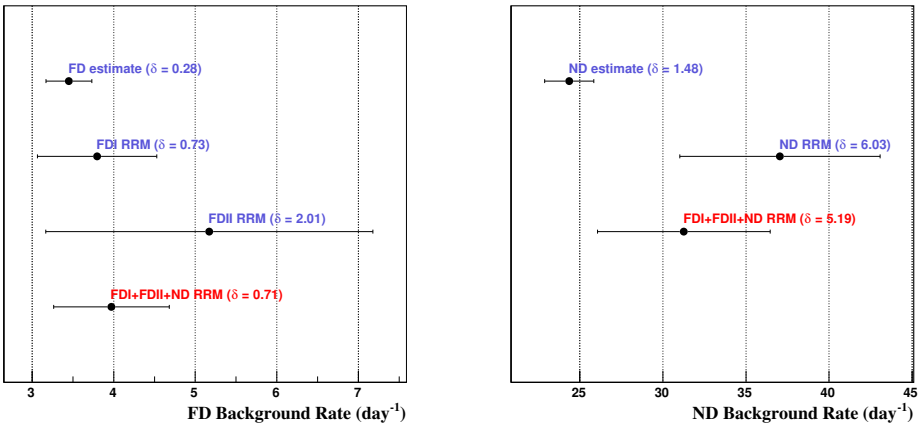

Figure 7.11: Summary of TnC RRM-II background-unconstrained fits. Left: BG FD results. Right: BG ND results.

Impact of the 2-Off data sample

There is also the possibility to include the reactor Off-Off data in the FD-II and also to eliminate this point in the FD-I fit (figure 7.12). This configuration tests the impact of the reactor off-off data in the precision of θ_{13} measurement. In tables 7.5 and 7.6, the results for the RRM-II SD fit with and without BG constraint including the two above mentioned configurations for FD-I and FD-II are listed.

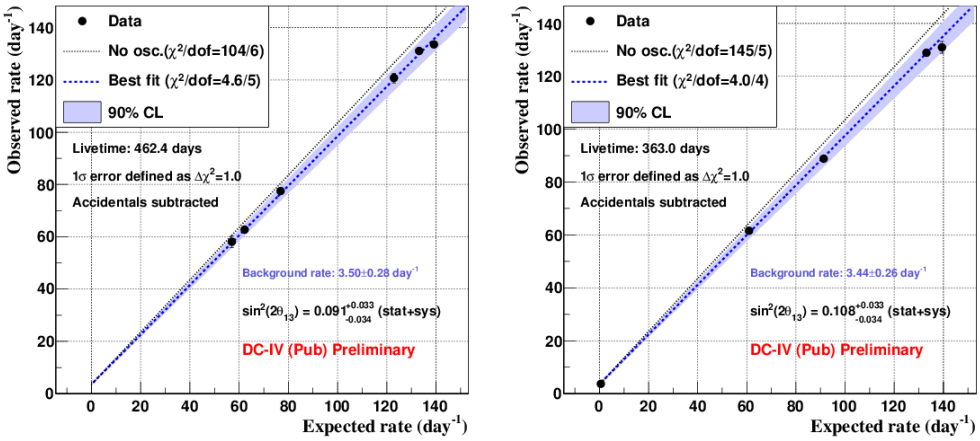

(a) FD-I (b) FD-II

Figure 7.12: Left: FD-I TnC RRM-II fit with background constraint and without including the reactor-off data. Right: FD-II TnC RRM-II fit with no background constraint and including the reactor off data.

Table 7.5: Summary of the FD-I and FD-II $\sin^2(2\theta_{13})$ and background rate fit results with and without the reactor 2-Off data point including the background constraint in the fit.

	$\sin^2(2\theta_{13})$	BG rate [day^{-1}]
FD-I with 2-Off data	$0.091^{+0.033}_{-0.034}$	3.50 ± 0.26
FD-I without 2-Off data	$0.091^{+0.033}_{-0.034}$	3.50 ± 0.28
FD-II with 2-Off data	$0.108^{+0.033}_{-0.034}$	3.44 ± 0.26
FD-II without 2-Off data	$0.108^{+0.033}_{-0.034}$	3.48 ± 0.28

Table 7.6: Summary of the FD-I and FD-II $\sin^2(2\theta_{13})$ and background rate fit results with and without the reactor 2-Off data point with no background constraint in the fit.

	$\sin^2(2\theta_{13})$	BG rate [day^{-1}]
FD-I with 2-Off data	$0.097^{+0.035}_{-0.036}$	3.78 ± 0.73
FD-I without 2-Off data	$0.116^{+0.043}_{-0.044}$	4.91 ± 1.57
FD-II with 2-Off data	$0.107^{+0.035}_{-0.036}$	3.37 ± 0.73
FD-II without 2-Off data	$0.135^{+0.045}_{-0.046}$	5.17 ± 2.01

The following conclusions can be extracted:

- In the BG constraint scenario, the 2-Off reactor data do not affect θ_{13} nor the

background rate due to the fact that the background error is around 0.28% versus the residual neutrinos uncertainty (section 7.2.2.3) of 0.30%.

- Without BG constraint, the value of FD-II $\sin^2(2\theta_{13})$ decreases with the 2-Off point, approaching itself to the FD-I θ_{13} value, and the same behavior is followed by the background rate. In this case the FD-II sample has less statistics and the tension between the background model and the period with Off-Off becomes important.
- In both detectors once the period with Off-Off data is included, the result of θ_{13} remains almost constant between the scenario with and without background constraint within less than 0.12σ for FD-I and 0.02σ for FD-II.
- The constraint on the total background rate given by the 2-Off point improves significantly the precision of $\sin^2(2\theta_{13})$.

BG stability

To ensure that the RRM-II fit has no accidentally bias effects in θ_{13} due to some minor BG instabilities, the BG stability has been motorized [180]-[182]. The results are illustrated in figure 7.13 for accidental background, in figure 7.14 for fast neutrons background and in figure 7.15 for the ^{9}Li contamination.

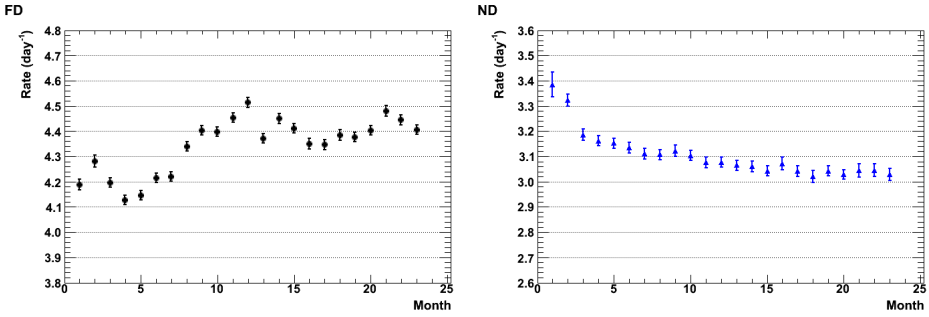

Figure 7.13: Evolution of the accidental background on a monthly basis. Left: FDII data. Right: ND data.

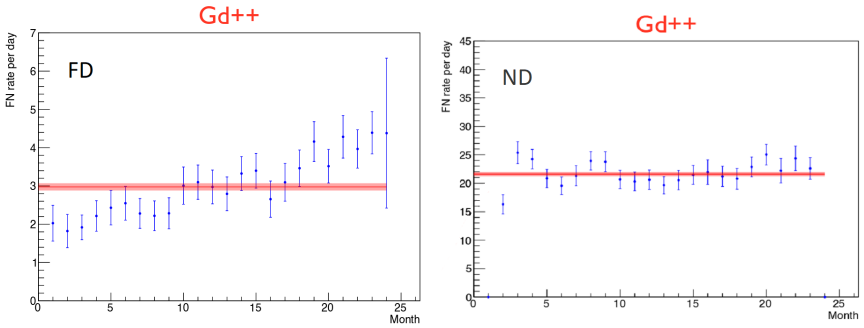

Figure 7.14: Evolution of the fast neutrons on a monthly basis. Left: FDII data. Right: ND data.

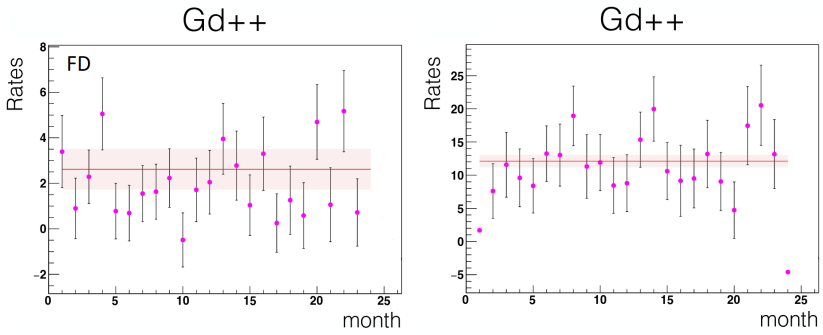

Figure 7.15: Evolution of the ^{9}Li on a monthly basis. Left: FDII data. Right: ND data.

In the case of the accidental background, for both the FD and the ND, the variations are well below 10%, which are further reduced when binning according to the reactor power for the RRM fit. This variation is negligible in the total background rate, given larger contributions of the ^{9}Li and FN. The accidental variation is also much smaller than the total background error. The same reasoning can be followed with the cosmogenic background. However concerning the FN background, there is a trend with FN increasing with time in the FD. To check that this behavior does not have any impact on the fit results, the error of the FN background has been increased by a factor of 2 in the FD-I and FD-II detectors (from 0.03 to 0.06 day^{-1}), working as an effective account for the FN instability. The results are listed in the second column of table 7.7. There is only a small increase in the $\sin^2(2\theta_{13})$ error for the FD-II fit, while no effect in the FD-I is appreciated due to the use of the reactor off-off data. Also there is no impact in the θ_{13} combined fit. In the third column, the error of FN rate in the ND has been also modified from 0.18 to 0.36 day^{-1}. Even increasing this, there is only a minimum change in the θ_{13} value and in the BG rate for the ND but there is no change in the value of θ_{13} from the combined fit.

Table 7.7: Summary of θ_{13} SD and MD fit results and BG rates for the RRM-II fit while the FN error in the FD and ND is increased by a factor of 2.

	$\sigma_{\text{FN}}(\text{FD}) = 0.03$ day^{-1} $\sigma_{\text{FN}}(\text{ND}) = 0.18$ day^{-1}	$\sigma_{\text{FN}}(\text{FD}) = 0.06$ day^{-1} $\sigma_{\text{FN}}(\text{ND}) = 0.18$ day^{-1}	$\sigma_{\text{FN}}(\text{FD}) = 0.06$ day^{-1} $\sigma_{\text{FN}}(\text{ND}) = 0.36$ day^{-1}
FD-I $\sin^2(2\theta_{13})$	$0.091^{+0.033}_{-0.034}$	$0.091^{+0.033}_{-0.034}$	$0.091^{+0.033}_{-0.034}$
FD-I BG rate	3.50 ± 0.26	3.50 ± 0.26	3.50 ± 0.26
FD-II $\sin^2(2\theta_{13})$	$0.108^{+0.033}_{-0.034}$	$0.108^{+0.034}_{-0.035}$	$0.108^{+0.034}_{-0.035}$
FD-II BG rate	3.48 ± 0.28	3.48 ± 0.28	3.48 ± 0.28
ND $\sin^2(2\theta_{13})$	$0.176^{+0.123}_{-0.126}$	$0.176^{+0.123}_{-0.126}$	$0.177^{+0.123}_{-0.126}$
ND BG rate	25.08 ± 1.44	25.08 ± 1.44	25.11 ± 1.47
Combined fit $\sin^2(2\theta_{13})$	0.095 ± 0.016	0.095 ± 0.016	0.095 ± 0.016
Combined fit BG rate	FD: 3.5 ± 0.3 ND: 24.9 ± 1.4	FD: 3.5 ± 0.3 ND: 24.9 ± 1.4	FD: 3.5 ± 0.3 ND: 24.9 ± 1.5

7.2.3.2 RRM-I oscillation fit results

The aim of this section is to obtain a suitable θ_{13} value that could be comparable with the one extracted from the Rate+Shape analysis of section 7.3. For this purpose, a

RRM-I fit following the minimization of the χ^2 described in 7.2.3 is performed, but the prompt energy constraint (explained in 7.2.3.1) is extended from [1-8.5]MeV to [1-20]MeV, as has been done in [141]. In such a way, all the inputs from RRM-II analysis are used with the exception of the background rates, that are exactly the one shown in table 5.9. The outcome results with and without background constraint for $\sin^2(2\theta_{13})$ are displayed in tables 7.8 and 7.9 respectively.

Table 7.8: Summary of θ_{13} and BG rates fit results for the RRM-I including BG constraint.

	$\sin^2(2\theta_{13})$	BG rate [day^{-1}]
FD-I	$0.096^{+0.033}_{-0.034}$	5.49 ± 0.49
FD-II	$0.117^{+0.034}_{-0.035}$	5.64 ± 0.58
ND	$0.107^{+0.126}_{-0.000}$	34.96 ± 1.95
Combined fit	0.110 ± 0.018	FD: 5.5 ± 0.5
		ND: 34.8 ± 1.9

Table 7.9: Summary of θ_{13} and BG rates fit results for the RRM-I without BG constraint.

	$\sin^2(2\theta_{13})$	BG rate [day^{-1}]
FD-I	$0.094^{+0.035}_{-0.037}$	5.39 ± 0.83
FD-II	$0.133^{+0.045}_{-0.046}$	6.66 ± 2.03
ND	$0.310^{+0.143}_{-0.146}$	51.50 ± 6.12
Combined fit	0.089 ± 0.024	FD: 5.6 ± 0.8
		ND: 44.8 ± 5.0

In particular, the result of θ_{13} with BG constraint allows a direct comparison with respect to the one extracted from a Rate-Only (RO) fit where $\sin^2(2\theta_{13}) = 0.1189 \pm 0.0192$ [183]. The two results differs in 0.3σ, but the same value is not expected since the RRM constrains the BG according to the differences in the reactor power. The error in the RRM-I is slightly smaller because with this approach one have more information in the fit: 1-Off reactor data vs 2-Off reactor data.

Comparing $\sin^2(2\theta_{13})$ (RRM-II) = 0.095 ± 0.016 and $\sin^2(2\theta_{13})$ (RRM-I) = 0.110 ± 0.018, fit with background constraint, it can be extracted that both results are fully consistent but the RRM-II is most precise due to a better constraint of the background rates.

7.2.4 Summary and Conclusion for the RRM oscillation analysis

This analysis presents some unique features with respect to the RO or the Rate+Shape fit that will be described in the following sections:

- The RRM oscillation analysis is able to provide oscillation results without relying on a background model.
- It is a simple rate-only analysis yielding almost the same precision as the Rate+Shape official analysis.
- It takes into account variable reactor power.

- When no Off-Off data is included, the fit provides an independent estimation of the total background rate, to be compared with the Off-Off measurements and the background estimates.

7.3 Rate+Shape Oscillation Analysis

The observed deficit between the IBD candidates and the sum of the predicted un-oscillated reactor neutrino signal and the estimated background contamination in each detector can be interpreted as the result of the neutrino oscillation.

The Rate+Shape (R+S) analysis exploits the energy dependence of the neutrino oscillation deficit. The comparison of the measured IBD candidate rate to the predicted rate is hence done within different energy regions of the prompt visible energy. IBD dominates the [1.0-8.0] MeV region, while Li dominates the [8.0-10.0] MeV region and FN dominates the [10.0-20.0] MeV region. The R+S fit takes advantage of these regions to constrain the backgrounds.

In fact, for the TnC analysis the R+S fit uses a prompt energy spectra in the range of [1.0-20.0 MeV] and this is binned in 38 bins of variable width to optimize the event statistics measured at different energies:

- for $(1.0 \leq E_{prompt} < 8.0)$ MeV: 28 bins of 0.25 MeV
- for $(8.0 \leq E_{prompt} < 10.0)$ MeV: 4 bins of 0.5 MeV
- for $(10.0 \leq E_{prompt} < 12.0)$ MeV: 2 bins of 1.0 MeV
- for $(12.0 \leq E_{prompt} < 20.0)$ MeV: 4 bins of 2.0 MeV

The above binning is applied to the 3 observed sets of selected candidates and the 3 non-oscillated MC predictions (FD-I, FD-II and ND) and to the background predictions for accidental, cosmogenic and fast neutron events, although for the plots, FD-I and FD-II have been combined as FD (see figure 7.16 and rates from table 5.9).

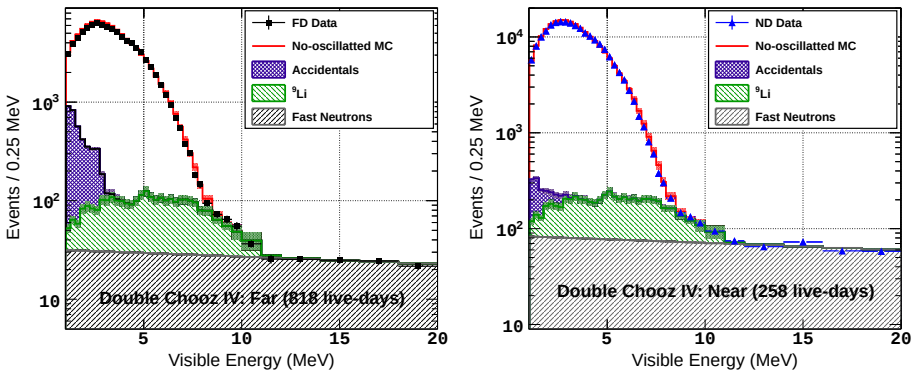

Figure 7.16: Observed IBD candidate visible energy spectrum for FD (black points) and ND (blue triangles) superimposed to the non-oscillation prediction (red line) with the remaining background added: fast neutrons (gray area), ^{9}Li and ^{8}He (green) and accidental coincidences (purple area).

7.3.1 Oscillation analyses with two detectors

In Double Chooz there are two general ways to extract $\sin^2(2\theta_{13})$ information in the fit. The first one constitutes the standard analysis framework for the four DC publications on θ_{13} and it is called the Data-MC (D2MC) fit. Before the completion of the ND, Double Chooz made the oscillation analysis comparing the non-oscillated MC spectrum with the FD-I data. Following the same procedure, the D2MC fit compares simultaneously FD and ND data to MC and background estimations.

A novel oscillation fit in DC has been developed, constructing a predicted spectrum from ND data, including background estimations, and comparing it against FD data. This way the dependence of the fit with the prediction model is overcome without compromising the accuracy and precision of the θ_{13} measurement. This is called the Data-Data fit (D2D). These two strategies are discussed separately in the following sections.

7.3.1.1 Data-MC fit

In the data-MC fit, the three data samples (FD-I, FD-II and ND) are simultaneously compared to the non-oscillated prediction (MC and background estimation), taking into account the correlations existing between systematic uncertainties through covariance matrices. Since there is a distinction between the two periods of FD data taking (FD-I working without the ND and FD-II for the period with 2 detectors), it is worth considering not only the correlations between FD-II and ND but also the correlations between FD-I and FD-II. The correlations between FDI and ND are a convolution of the above two correlations.

χ^2 definition The χ^2 definition of the D2MC fit is shown in eq. 7.15.

$$
\begin{aligned}
\chi^2 &= \sum_{ij}^{3x38} \left((N^{\rm exp}_{\rm FDI})_i - (N^{\rm obs}_{\rm FDI})_i, (N^{\rm exp}_{\rm FDII})_i - (N^{\rm obs}_{\rm FDII})_i, (N^{\rm exp}_{\rm ND})_i - (N^{\rm obs}_{\rm ND})_i\right) \\
&\times M^{-1}_{ij} \begin{pmatrix} (N^{\rm exp}_{\rm FDI})_j - (N^{\rm obs}_{\rm FDI})_j \\ (N^{\rm exp}_{\rm FDII})_j - (N^{\rm obs}_{\rm FDII})_j \\ (N^{\rm exp}_{\rm ND})_j - (N^{\rm obs}_{\rm ND})_j \end{pmatrix} \\
&+ \sum_k \left(\frac{\alpha_k - \alpha^{\rm CV}_k}{\sigma_k}\right)^2 \\
&+ \sum_{m,n} \left(\alpha_m - \alpha^{\rm CV}_m\right) C^{-1}_{mn} \left(\alpha_n - \alpha^{\rm CV}_n\right)^T \\
&+ 2\left(N^{\rm obs}_{\rm off} \ln\left[\frac{N^{\rm obs}_{\rm off}}{N^{\rm exp}_{\rm off}}\right] + N^{\rm obs}_{\rm off} + N^{\rm exp}_{\rm off}\right)
\end{aligned}
\tag{7.15}
$$

Here i, j run over energy bins for FD-I, FD-II, and ND (3×38 bins in total). $N^{\rm exp}_i$ is the number of predicted events in the i^{th} bin and $N^{\rm obs}_i$ is the number of observed (data) events. M_{ij} is the total covariance matrix that comes from the sum of several matrices corresponding to the following sources of uncertainty: accidental

and cosmogenic BG shape, the reactor flux and the energy, being

$$M_{ij} = M_{ij}^{\text{flux}_0} + M_{ij}^{\text{energy}} + M_{ij}^{\text{acc},^9\text{Li}} \tag{7.16}$$

On the other hand α_k are the nuisance parameters with predicted central values (CV) α_k^{CV}, while C_{mn} is the covariance matrix between nuisance parameters of the three detectors. The nominal D2MC fit uses a nuisance parameter approach for the BG rates, the FN BG shape and the detection efficiency per detector. In the case of the effective squared mass difference Δm^2_{ee} and the Bugey4 normalization, since the uncertainty value is the same for FD and ND, there is no need to use the covariance matrix C_{mn}.

The last addend in eq. 7.15 represents the reactor-off term, that follows a log-likelihood distribution and due to the low expected number of residual neutrino events, it is treated with Poisson statistics. $N_{\text{off}}^{\text{exp}}$ and $N_{\text{off}}^{\text{obs}}$ correspond to the expected and observed events in the 7.16 days of 2-Off period (table 7.1. It is used in the fit to constrain the total background rate win the absence of $\bar{\nu}_e$.

The first and second addends can be rewritten in more detail as:

$$\begin{aligned}
&+ \quad \frac{(\Delta m^2 - \Delta m^2_{ee})^2}{\sigma^2_{\Delta m^2_{ee}}} + \frac{\alpha_{\text{B4}} - 0}{\sigma^2_{\alpha_{\text{B4}}}} \\
&+ \quad (D_{\text{FDI}} - (D_{\text{FDI}})_{\text{CV}}, D_{\text{FDII}} - (D_{\text{FDII}})_{\text{CV}}, D_{\text{ND}} - (D_{\text{ND}})_{\text{CV}}) \\
&\times \quad \begin{pmatrix} \sigma^2_{\text{D}_{\text{FDI}}} & \rho_{\text{D}_{\text{FDI}}\text{D}_{\text{FDII}}}(\sigma_{\text{D}_{\text{FDI}}}\sigma_{\text{D}_{\text{FDII}}}) & \rho_{\text{D}_{\text{FDI}}\text{D}_{\text{ND}}}(\sigma_{\text{D}_{\text{FDI}}}\sigma_{\text{D}_{\text{ND}}}) \\ \rho_{\text{D}_{\text{FDI}}\text{D}_{\text{FDII}}}(\sigma_{\text{D}_{\text{FDI}}}\sigma_{\text{D}_{\text{FDII}}}) & \sigma^2_{\text{D}_{\text{FDII}}} & \rho_{\text{D}_{\text{FDII}}\text{D}_{\text{ND}}}(\sigma_{\text{D}_{\text{FDII}}}\sigma_{\text{D}_{\text{ND}}}) \\ \rho_{\text{D}_{\text{FDI}}\text{D}_{\text{ND}}}(\sigma_{\text{D}_{\text{FDI}}}\sigma_{\text{D}_{\text{ND}}}) & \rho_{\text{D}_{\text{FDII}}\text{D}_{\text{ND}}}(\sigma_{\text{D}_{\text{FDII}}}\sigma_{\text{D}_{\text{ND}}}) & \sigma^2_{\text{D}_{\text{ND}}} \end{pmatrix} \\
&\times \quad \begin{pmatrix} D_{\text{FDI}} - (D_{\text{FDI}})_{\text{CV}} \\ D_{\text{FDII}} - (D_{\text{FDII}})_{\text{CV}} \\ D_{\text{ND}} - (D_{\text{ND}})_{\text{CV}} \end{pmatrix} \\
&+ \quad (FN_{\text{sh0}} - (FN_{\text{sh0}})_{\text{CV}}, FN_{\text{sh1}} - (FN_{\text{sh1}})_{\text{CV}}, FN_{\text{sh2}} - (FN_{\text{sh2}})_{\text{CV}}) \\
&\times \quad \begin{pmatrix} \sigma^2_{\text{FN}_{\text{sh0}}} & \rho_{\text{FN}_{\text{sh0}}\text{FN}_{\text{sh1}}}(\sigma_{\text{FN}_{\text{sh0}}}\sigma_{\text{FN}_{\text{sh2}}}) & \rho_{\text{FN}_{\text{sh0}}\text{FN}_{\text{sh2}}}(\sigma_{\text{FN}_{\text{sh0}}}\sigma_{\text{FN}_{\text{sh2}}}) \\ \rho_{\text{FN}_{\text{sh0}}\text{FN}_{\text{sh1}}}(\sigma_{\text{FN}_{\text{sh0}}}\sigma_{\text{FN}_{\text{sh1}}}) & \sigma^2_{\text{FN}_{\text{sh1}}} & \rho_{\text{FN}_{\text{sh1}}\text{FN}_{\text{sh2}}}(\sigma_{\text{FN}_{\text{sh1}}}\sigma_{\text{FN}_{\text{sh2}}}) \\ \rho_{\text{FN}_{\text{sh0}}\text{FN}_{\text{sh2}}}(\sigma_{\text{FN}_{\text{sh0}}}\sigma_{\text{FN}_{\text{sh2}}}) & \rho_{\text{FN}_{\text{sh1}}\text{FN}_{\text{sh2}}}(\sigma_{\text{FN}_{\text{sh1}}}\sigma_{\text{FN}_{\text{sh2}}}) & \sigma^2_{\text{FN}_{\text{sh2}}} \end{pmatrix} \\
&\times \quad \begin{pmatrix} FN_{\text{sh0}} - (FN_{\text{sh0}})_{\text{CV}} \\ FN_{\text{sh1}} - (FN_{\text{sh1}})_{\text{CV}} \\ FN_{\text{sh2}} - (FN_{\text{sh2}})_{\text{CV}} \end{pmatrix} \\
&+ \quad (BG_{\text{FDI}} - (BG_{\text{FDI}})_{\text{CV}}, BG_{\text{FDII}} - (BG_{\text{FDII}})_{\text{CV}}, BG_{\text{ND}} - (BG_{\text{ND}})_{\text{CV}}) \\
&\times \quad \begin{pmatrix} \sigma^2_{B_{\text{FDI}}} & \rho_{B_{\text{FDI}}B_{\text{FDII}}}(\sigma_{B_{\text{FDI}}}\sigma_{B_{\text{FDII}}}) & \rho_{B_{\text{FDI}}B_{\text{ND}}}(\sigma_{B_{\text{FDI}}}\sigma_{B_{\text{ND}}}) \\ \rho_{B_{\text{FDI}}B_{\text{FDII}}}(\sigma_{B_{\text{FDI}}}\sigma_{B_{\text{FDII}}}) & \sigma^2_{B_{\text{FDII}}} & \rho_{B_{\text{FDII}}B_{\text{ND}}}(\sigma_{B_{\text{FDII}}}\sigma_{B_{\text{ND}}}) \\ \rho_{B_{\text{FDI}}B_{\text{ND}}}(\sigma_{B_{\text{FDI}}}\sigma_{B_{\text{ND}}}) & \rho_{B_{\text{FDII}}B_{\text{ND}}}(\sigma_{B_{\text{FDII}}}\sigma_{B_{\text{ND}}}) & \sigma^2_{B_{\text{ND}}} \end{pmatrix} \\
&\times \quad \begin{pmatrix} BG_{\text{FDI}} - (BG_{\text{FDI}})_{\text{CV}} \\ BG_{\text{FDII}} - (BG_{\text{FDII}})_{\text{CV}} \\ BG_{\text{ND}} - (BG_{\text{ND}})_{\text{CV}} \end{pmatrix} \\
&+ \quad \frac{(\nu_{\text{res}} - (\nu_{\text{res}})_{\text{CV}})^2}{(\sigma_{\nu_{\text{res}}})^2}
\end{aligned} \tag{7.17}$$

In equation 7.17 the first two addends corresponds to the penalty terms given by the nuisances parameters of Δm^2 and B4 normalization, while the next three sets of addends are the penalties of the detection efficiency D, FN BG shape $FN_{\rm sh}$ and BG rates BG (including accidentals, FN and ^{9}Li).

Therefore such a χ^2 definition has 112 degrees of freedom: 38 energy bins x 3 detectors + Reactor-off term - 3 free parameters ($\sin^2(2\theta_{13})$ and ND and FD cosmogenic BG rates). The ^{9}Li background rates are unconstrained in the fit. All input parameters agree with their output within less that 1σ, except for the cosmogenic rates when they are constrained, so they are treated as free parameters in the fit. The Minimization code is based on the MINUIT [184] package.

7.3.1.2 Data-Data fit

The D2D fit was developed in order to take advantage of the ND as a monitor of the reactor flux and to avoid any MC dependence of the fit. However, since this fit uses the comparison between FD and ND data, which has finite statistics, this method is expected to lead a worse sensitivity to $\sin^2(2\theta_{13})$ than the Data-MC fit.

In the D2D, the fit follows the next procedure:

- The ND data (in visible energy) is unfolded. This unfolding consists of:
  - Removing the backgrounds.
  - Converting the visible energy to $\bar{\nu}_e$ energy.
  - Correcting the ND neutrino data with the ND efficiency.

  The obtained spectrum is expected to be the IBD reactor $\bar{\nu}_e$ spectrum passing through the ND: no background, in neutrino energy, without θ_{13} correction and normalized as a perfect detector.

- The neutrino energy dependence due to θ_{13} oscillation (in true energy) is applied to the unfolded ND data. The aim is to obtain the expected reactor spectrum passing through the FD with θ_{13}. For this step, it is required to know the proportion of flux received by each detector and the distance to the reactors in order to build a correct energy distortion induced by θ_{13}. The unfolded ND spectrum is also corrected with the FD data efficiency.

- This expected reactor spectrum passing through the FD (in neutrino energy) is then folded with the FD response (in order to have it in visible energy). At this point, the expected detected spectrum in the FD has been obtained assuming that the FD gets the same reactor spectrum and flux than the ND.

- However this is not totally true since DC is not a perfect isoflux experiment due to the relative position of the detectors with respect to the reactors. In the case of FD-I, since the period of data taking is not synchronous with the ND, the thermal power fluctuation and the fuel evolution are not the same for both detectors and need to be corrected.

- A rate and shape correction factor is thus used to consider all these effects. This factor consists of a ratio of the flux expected in the ND vs the expected in the FD, and it will be denoted in the fit as w_i(E).

Thus, the energy bin-dependent normalization factor is defined as:

$$w_i = \frac{N_p^{\mathrm{FD}}}{N_p^{\mathrm{ND}}} \times \frac{T_{\mathrm{live}}^{\mathrm{FDI+FDII}}}{T_{\mathrm{live}}^{ND}} \times \frac{\epsilon_{\mathrm{det}}^{\mathrm{FD}}}{\epsilon_{\mathrm{det}}^{\mathrm{ND}}} \times \frac{\sum_R \phi_R^{\mathrm{FDI+FDII}}(1/L_R^{\mathrm{FD}})^2}{\sum_R \phi_R^{\mathrm{ND}}(1/L_R^{\mathrm{N}})^2} \times \frac{P_{\mathrm{osc}}^{\mathrm{FD}}(i)}{P_{\mathrm{osc}}^{\mathrm{ND}}(i)} \tag{7.18}$$

This way the differences in proton number N_p, livetime $\mathrm{T_{live}}$, detection efficiency ϵ_{det}, flux ϕ_R and distance to reactors L_R are taking into account in the fit. The last term is the oscillation probability $P_{\mathrm{osc}}(E_\nu)$ and describes the difference in oscillation magnitude between FD and ND, being a function of the mixing angle θ_{13} and the effective mass squared difference $\Delta \mathrm{m}^2_{ee}$.

The procedure followed to obtain w_i value lies on the calculation of the ratio between data and MC events for the each detector, after all corrections have been applied. In this way, every effect is already included (flux, baseline, efficiencies, proton numbers). Then, in the data to data fit only the probability ratio $\frac{P_{\mathrm{osc}}^{\mathrm{FD}}(i)}{P_{\mathrm{osc}}^{\mathrm{ND}}(i)}$ is calculated per bin.

χ^2 definition The χ^2 definition for the D2D fit is similar to eq. 7.15 and is defined as:

$$\begin{aligned}
\chi^2 &= \sum_{ij}^{38} \left(N_i^{\mathrm{FDI*}} + N_i^{\mathrm{FDII}} - w_i N_i^{\mathrm{ND}}\right) M_{ij}^{-1} \left(N_j^{\mathrm{FDI*}} + N_j^{\mathrm{FDII}} - w_j N_j^{\mathrm{ND}}\right)^T \\
&+ \sum_k \left(\frac{\alpha_k - \alpha_k^{\mathrm{CV}}}{\sigma_k}\right)^2 \\
&+ \sum_{m,n} \left(\alpha_m - \alpha_m^{\mathrm{CV}}\right) C_{mn}^{-1} \left(\alpha_n - \alpha_n^{\mathrm{CV}}\right)^T
\end{aligned} \tag{7.19}$$

FDI* is the corrected FD-I spectrum, since it was running at a different period than FD-II and ND. The correction is given by the ratio between the $\bar{\nu}_e$ spectra of FD-I and FD-II ([185]). The penalty terms are given by the nuisance parameters as for the D2MC case but in this case the D2D fit uses only the BG rates and $\Delta \mathrm{m}^2_{ee}$ as nuisance terms and the rest of uncertainties are treated as covariance matrices.

In equation 7.19, M_{ij} represents the total covariance matrix:

$$M_{ij} = M_{ij}^{\mathrm{flux}} + M_{ij}^{\mathrm{energy}} + M_{ij}^{\mathrm{det}} + M_{ij}^{\mathrm{acc,^9Li,FN}} \tag{7.20}$$

To build these matrices, the D2D fit uses the inputs from D2MC fit, but in a different fashion, since the D2D has only 38 energy bins. The matrix elements are defined as:

$$\begin{aligned}
\sigma^2(\mathrm{FDI*} + \mathrm{FDII} - w\mathrm{ND}) \rightarrow \quad & (\sigma^2_{\mathrm{FDI}} + \sigma^2_{\mathrm{FDII}} + w^2\sigma^2_{\mathrm{ND}} \\
& - 2w\rho_{\mathrm{FDII:ND}}\sigma_{\mathrm{FDII}}\sigma_{\mathrm{ND}} \\
& - 2w\rho_{\mathrm{FDI:ND}}\sigma_{\mathrm{FDI}}\sigma_{\mathrm{ND}} \\
& - 2\rho_{\mathrm{FDI:FDII}}\sigma_{\mathrm{FDI}}\sigma_{\mathrm{FDII}})
\end{aligned}$$

where σ_d corresponds to the same value used in equation 7.17. The correlation parameters $\rho_d d$ are taken from the off-diagonal terms of the D2MC input matrices. Along these lines the error cancellation between FD and ND data sets is ensured, since the χ^2 compares the FD to its prediction (scaled ND).

7.3.2 Systematic Uncertainties

In the Rate+Shape fit, the uncertainties are taken into account via two methods: covariance matrices and penalty terms. A covariance matrix can represent both statistical and systematic uncertainties and it is useful to handle complicated uncertainties including bin-to-bin correlations, however it can only handle symmetric errors. On the other hand, the advantage of the use of nuisance parameters is the possibility to check the after fit parameter, related to an uncertainty source, in order to validate its agreement or not with the input information, but it has the disadvantage of being very CPU-time consuming, since each parameter has to be tested to minimize the χ^2.

The systematic uncertainties present in the Rate+Shape fit are described in the following subsections.

7.3.2.1 Energy Uncertainty

As was explained in section 4.4, the R+S fit needs to take into account the remaining differences between data and MC model in terms of energy, that is, the light non-linearity, the uniformity, the stability and the charge non-linearity corrections. These corrections are simplified into three parameters per detector (a', b', c', equation 4.12) that produce the energy correction function range showed in figure 7.17, with 1σ, 2σ and 3σ error bars indicated.

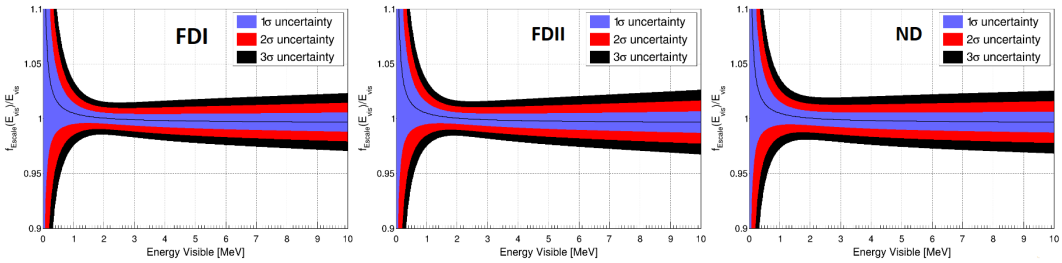

Figure 7.17: Energy scale correction functions for FDI, FDII and ND.

In the Rate+Shape fit a covariance matrix can be built from these parameters. The difference per energy bin between these nominal values and the values obtained after 10^5 randomizations defines the elements of the covariance matrix that are introduced in the oscillation fit. The covariance matrix M_{ij}^{energy} is shown in figure 4.18.

7.3.2.2 Reactor flux Uncertainty

The reactor flux uncertainty is also treated as a covariance matrix. It combines the uncertainties from the parameters used to predict the ν_e flux observed during the detectors data taking periods, listed in table 3.6. The final reactor matrix is a 114×114 matrix, taking into account the reactor-to-reactor and reactor-to-detector correlations [130]. The final covariance matrix M_{ij}^{flux} is shown in figure 3.11. A special parameter is the Bugey-4 anchor point, that is a common input for the three data-sets, and it is used as a nuisance parameter in the data to MC fit, so the M_{ij}^{flux} is generated with Bugey-4 $\langle\sigma_f\rangle^{B4}$ error equal to zero. In the D2D fit, the anchor point is removed because the normalization is given directly by the ND.

7.3.2.3 Detection systematics Uncertainty

In the case of the detection efficiency uncertainty, it can be treated by either covariance matrix (D2D fit) or nuisance parameters (D2MC fit). In both cases the values shown in table 6.16 are introduced as the σ_d values of equations 7.17 and 7.21. The correlation coefficients of table 6.15 are used as the inputs of the covariance matrices for the pull terms in the D2MC fit and in the calculation of the elements for the covariance matrix M_{ij}^{det} in the D2D fit.

7.3.2.4 Background rates and shapes Uncertainty

The background rates (accidental, fast neutrons and cosmogenic backgrounds) of table 5.9 are included in both fits as penalty terms. Since FD-I and FD-II FN and cosmogenic rates have the same value for both detectors, they are considered as a common input FD in the fit.

Concerning the background shapes, it is needed to distinguish between both R+S fits. In the D2MC fit, the FN background shape is provided as a parametrized function, fitted with three parameters that are used as nuisance parameters in the data to MC fit:

$$\alpha_{\text{FN shape1}} \times e^{-\alpha_{\text{FN shape2}} \cdot x} + \alpha_{\text{FN shape3}} \cdot x \tag{7.21}$$

These parameters have the same values for the three detectors, and are included in the fit calculation only once (fourth addend in equation 7.17). In the D2D fit, the FN shape is introduced as a covariance matrix.

For the accidental and cosmogenic cases, a covariance matrix is used both in D2MC and D2D fit.

Both shapes of FN and cosmogenic backgrounds are treated as fully correlated between the three data sets, while the accidentals are uncorrelated.

7.3.2.5 Δm^2_{ee} Uncertainty

Δm^2_{ee} is the effective mass square difference:

$$\Delta m^2_{ee} = \cos^2\theta_{12}\Delta m^2_{31} + \sin^2\theta_{12}\Delta m^2_{32} \tag{7.22}$$

Δm^2_{ee} provides the minimum position in the ratio plot of the prompt spectrum to the expected non-oscillated spectrum. However, given the ∼1.0 km baseline of the FD, this point is at the lowest energy part of the positron spectra. Thus, Double Chooz is not able to measure simultaneously Δm^2 and $\sin^2(2\theta_{13})$, and the measured value of $\Delta m^2 = (2.484 \pm 0.036) \cdot 10^{-3}$ eV^2 is used as a nuisance parameter. This value is calculated ranging over the N.H. and I.H. assumptions based on the NuFit 3.0 values [175], [176].

7.3.3 Oscillation fit results

7.3.3.1 D2MC fit results

Best-fit outputs of the minimization parameters and their errors are compared to the fit input values in table 7.10. The D2MC fit with the above configuration yields $\sin^2(2\theta_{13}) = 0.105 \pm 0.014$ with $\chi^2/\text{NDF} = 182/112$ and a precision of 13.3%.

Table 7.10: Best-fit values of χ^2 minimization parameters for the D2MC fit. Input and output values of the nuisance parameters are shown for comparison. The third column indicates if the input values are constrained in the fit.

Parameter	Inputs	Const.	Output
$\sin^2(2\theta_{13})$	-	n	0.1049 ± 0.0139
Minimum χ^2	-	-	182.1
NDF	-	-	112
$\Delta m^2(x10^{-3})eV^2$	2.484 ± 0.036	y	2.484 ± 0.036
FD-I Detection (%)	0.00 ± 0.763	y	0.188 ± 0.714
FD-II Detection (%)	0.00 ± 0.771	y	-0.033 ± 0.722
ND Detection (%)	0.00 ± 0.699	y	0.085 ± 0.634
Bugey-4 normalization (%)	0.000 ± 1.400	y	0.363 ± 0.826
FD-I acc. rate [day^{-1}]	3.930 ± 0.010	y	3.930 ± 0.010
FD-II acc. rate [day^{-1}]	4.320 ± 0.020	y	4.319 ± 0.020
ND acc. rate [day^{-1}]	3.110 ± 0.004	y	3.110 ± 0.004
FD FN rate [day^{-1}]	2.540 ± 0.070	y	2.503 ± 0.054
ND FN rate [day^{-1}]	20.770 ± 0.430	y	20.849 ± 0.308
FD ^{9}Li rate [day^{-1}]	3.010 ± 0.600	n	2.623 ± 0.273
ND ^{9}Li rate [day^{-1}]	12.320 ± 2.010	n	14.516 ± 1.478
FN shape [0]	180.720 ± 3.920	y	181.225 ± 3.865
FN shape [1]	0.015 ± 0.001	y	0.015 ± 0.001
FN shape [2]	-0.296 ± 0.041	y	-0.290 ± 0.041
Residual $\bar{\nu}_e$ [day^{-1}]	4.180 ± 1.250	y	4.167 ± 1.239

Pull terms shown in this table give access to physical observables like the BG rates or detection efficiency, demonstrating that there is good agreement between input and fit output values, within 1σ. Several other fit configurations, such as constraining ^{9}Li rate or letting B4 normalization as a free parameter, have been performed, obtaining compatible results of θ_{13}

The ratio of the observed spectra to the non-oscillated predictions for FD and ND are displayed in figure 7.18 (FD-I and FD-II are combined in FD with the proper error propagation for simplicity). In the plots the best fit solution contrasts with the non-oscillation hypothesis. Both detectors ratios shown a deficit at low energy (higher in the FD) induced by the θ_{13} oscillation. Also a common excess can be appreciated around the 5 MeV region, leading to a large χ^2/NDF due to the distortions between data and MC prediction are not cover by the systematics uncertainties. This excess is explained in more detail in section 7.4. It can be also appreciated the cancellation of correlated uncertainties from the single detector (SD) configuration (showed as green region in the figure) to the multidetector (MD) configuration (red region).

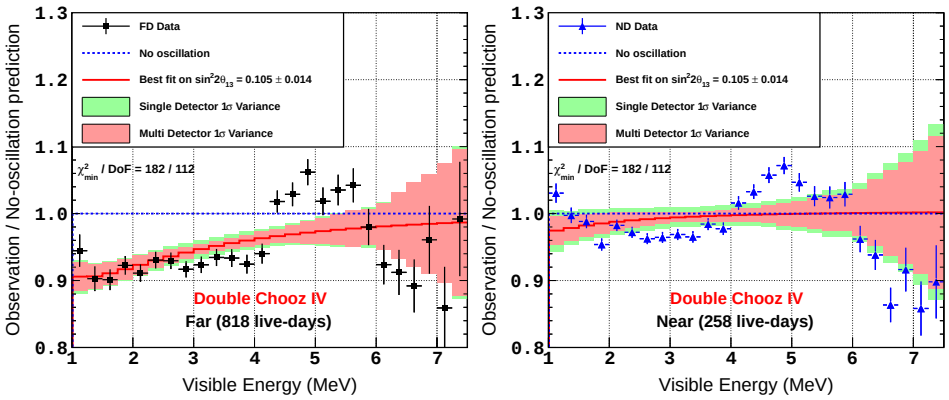

Figure 7.18: FD (left) and ND(right) observed to predicted spectrum ratios (black dots and blue triangles). Best-fit/no-oscillation MC shown in red solid line. Red and green bands represent SD and MD systematic uncertainties.

Table 7.11 summarises the contributions of each systematic uncertainty to the final θ_{13} value. The statistical precision of $\sin^2(2\theta_{13})$ is 0.005, so systematics dominate the measurement. The largest contribution comes from the reactor flux prediction uncertainty, due to the large contribution of the FD-I data, not fully correlated with ND due to the different period of data taking. Detection systematics also dominate due to the lack of knowledge on the numbers of protons in the GC. The impact of energy, background and Δm^2_{ee} is negligible. It is needed to clarify that there are effective correlations among systematics, causing the total uncertainty to be larger than the sum of the individual squared uncertainties. The difference corresponds to a 0.0065 (6.1%) term.

Table 7.11: Systematics contributions to the total uncertainty of $\sin^2(2\theta_{13})$.

Parameter	Uncertainty	Fractional
Reactor flux	0.0081	7.6%
Detection	0.0073	6.8%
Energy	0.0018	1.7%
Background	0.0018	1.7%
Δm^2_{ee}	0.0018	1.7%
Statistics	0.0054	5.0%
Total	0.0141	13.3%

7.3.3.2 D2D fit results

As seen in figure 7.18, the MC is not fully representative of the DC data. Therefore, the D2D fit has been carried out in order to validate that these deviations between the data and the MC do not affect the result of $\sin^2(2\theta_{13})$.

Best-fit outputs of the minimization parameters and their errors are compared to the fit input values in table 7.12. The D2D fit with the above configuration yields $\sin^2(2\theta_{13}) = 0.103 \pm 0.017$ with $\chi^2/\text{NDF} = 28/37$ and a precision of 16.5%. The ratio of the BG subtracted FD data to ND data (scaled) is shown in figure 7.19.

Table 7.12: Best-fit values of χ^2 minimization parameters for the D2D fit. Input and output values of the nuisance parameters are shown for comparison. The third column shows if the input values are constrained in the fit

Parameter	Inputs	Const.	Output
$\sin^2(2\theta_{13})$	-	n	0.1034 ± 0.0170
Minimum χ^2	-	-	28.1
NDF	-	-	37
Δm^2(x10^{-3}eV^2	2.484 ± 0.036	y	2.482 ± 0.036
FD-I acc. rate [day^{-1}]	3.930 ± 0.010	y	3.930 ± 0.010
FD-II acc. rate [day^{-1}]	4.319 ± 0.020	y	4.320 ± 0.020
ND acc. rate [day^{-1}]	3.110 ± 0.004	y	3.110 ± 0.004
FD corr. rate [day^{-1}]	2.540 ± 0.070	y	2.500 ± 0.058
ND corr. rate [day^{-1}]	20.770 ± 0.430	y	20.783 ± 0.429
FD ^{9}Li rate [day^{-1}]	3.010 ± 0.600	y	2.612 ± 0.347
ND ^{9}Li rate [day^{-1}]	12.320 ± 2.010	y	12.558 ± 1.909

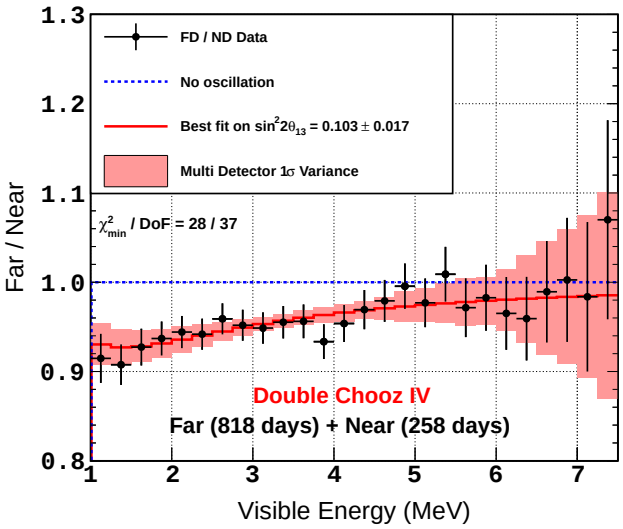

Figure 7.19: Ratio of the observed energy spectrum from FD to that from the ND data after the correction for the different baselines. The red line shows the best-fit value. Systematics uncertainties (red region) comes from the square root of the covariance matrix diagonal terms.

7.3.3.3 D2MC fit vs D2D fit

Table 7.13 shows the $\sin^2(2\theta_{13})$ values for the Data-to-MC and the Data-to-Data fit, as well as the χ^2/NDF. The nominal result of $\sin^2(2\theta_{13})$ is the D2MC, but the independent crosscheck with the D2D proves the agreement between both results and the robustness of the D2MC configuration. Looking at the results, it is clear that the D2MC fit has better sensitivity in $\sin^2(2\theta_{13})$ than the D2D. On the contrary, it has worse χ^2/NDF due to the fact that there is a large tension between data and MC in the region of (4,6) MeV (see figure 7.18). This distortion is not observed in the FD

data over ND data ratio, shown in figure 7.19, suggesting that it is correlated among the two datasets and comes from the MC prediction.

Table 7.13: Best-fit values of $\sin^2(2\theta_{13})$ and χ^2/NDF for the D2MC and the D2D fit.

	Data to MC	Data to Data
$\sin^2(2\theta_{13})$	0.1049 ± 0.0139	0.1034 ± 0.0170
Min χ^2/NDF	182.1/112	28.1/37

7.3.3.4 Impact of reactor model prediction on θ_{13}

The impact of the spectral distortion of the 5 MeV region in the θ_{13} measurement is scrutinized using Asimov data, considering a similar distortion as found in the data. The behaviour of the θ_{13} measurement as a function of the reactor flux model uncertainty increase factor is shown in figure 7.20. In the case of the single detector fit (detector data to its MC), the θ_{13} value shows a clear dependence with the reactor model uncertainty, since the Asimov value matches the input θ_{13} only when the flux uncertainty is increase up to 4σ. This extra uncertainty accommodates the 5 MeV excess.

On the contrary, the multi-detector measurement provides a robust θ_{13} measurement, since it is found to vary within 1% with the increase of the reactor model uncertainty. It can be also appreciated that the larger χ^2 is reduced from 182 to 93, alleviating the χ^2 tension due to the model uncertainty underestimation, with almost no impact on the θ_{13} value.

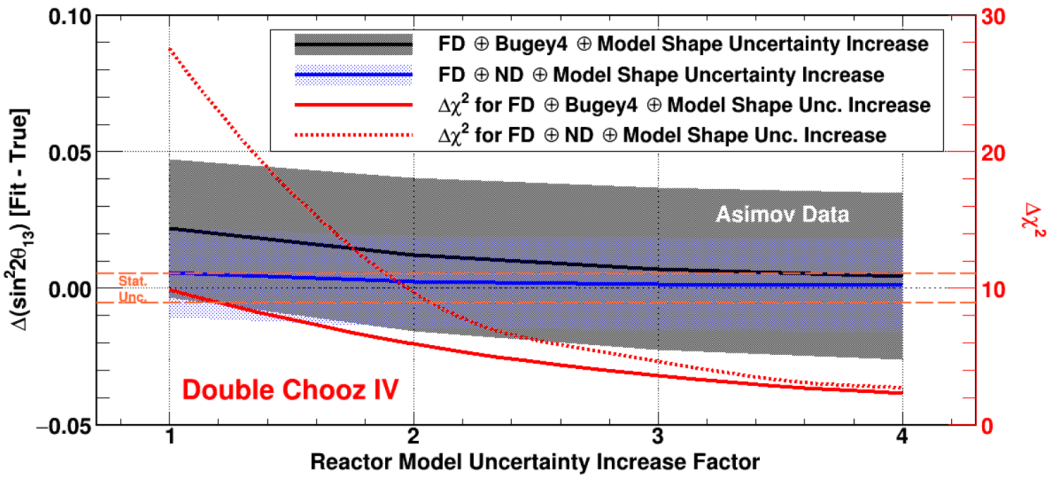

Figure 7.20: Illustration of the spectral distortion impact on θ_{13} using Asimov data. The SD case, strongly dependence with the reactor flux uncertainty, is shown as a black line. The MD case, blue line, shows a robust θ_{13} measurement since no impact is found when the flux uncertainty is increased to match the 5 MeV spectral excess. Figure from [140].

7.4 Neutrino energy spectral distortion

Since the reevaluation of the reactor neutrino flux prediction [126], [127], two discrepancies between prediction and measurement have been observed. On the one hand, there is a ∼6% total measured flux deficit, known as the reactor antineutrino anomaly [88]. On the other hand, there is an observed excess over prediction for neutrino energies between 5−7 MeV. The distortion present in the spectral shape when comparing the data to the prediction was first reported by Double Chooz in 2014 [186] and then confirmed by the other two reactor antineutrino experiments, Daya Bay [187] and RENO [188]. In figure 7.21, a comparison between the data and the prediction as a function of the visible energy is demonstrated for the three reactor experiments. Every experiment observes the same behaviour with a deficit around 3 MeV and a 10% excess around 5MeV with respect to the non-oscillation case. All curves use the same normalization, i.e. the ratios were normalized in order to have the same number of events on the prediction and on the data.

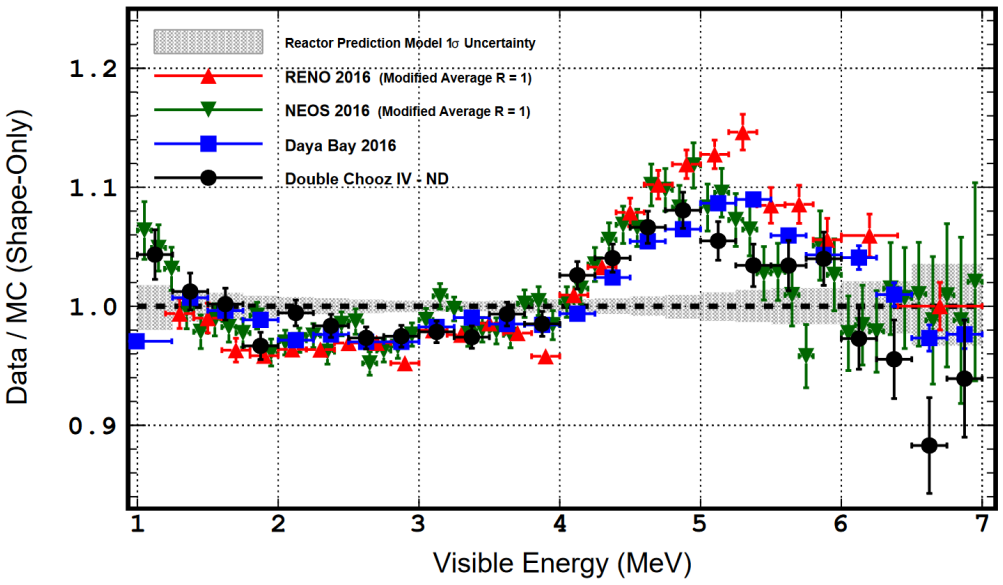

Figure 7.21: Comparison of the spectral distortion between the three current reactor neutrino experiments and NEOS from the ratio of the ND data to prediction. Figure from [140].

Regarding the figure 7.21, since the ratios appear as a function of the visible energy, there are some differences between the three reactor experiment results:

- There could be small discrepancies induced by the detector response, which is not the same in the three experiments. However since the three experiments use the same type of detectors, this effect is expected to be small.

- It should be mentioned that Double Chooz does not use the same antineutrinos spectra reference for the prediction than Daya Bay and RENO. The three experiments use the antineutrino spectra reference from Patrick Huber for the ^{235}U, ^{239}Pu and ^{241}Pu ([126]), which are derived from the integral of the beta

measurement performed in the 80's at the ILL reactor by Schrekenbach. The conversion from the beta spectrum to the antineutrino spectrum is done using the "conversion" method [189]. In Daya Bay and RENO, the spectra from Thomas Mueller for the ^{238}U is used and it is derived from a summation calculation [127]. Double Chooz on its behalf, uses the spectra derived from a measurement at the FRM-II reactor that was released in 2014 and done by N. Haag [128]. The fact that Double Chooz is not using the same spectra for the ^{238}U could be responsible for a small difference on the ratio plot compared to the other experiments but this difference will be lower than 2% in the [1,7] MeV range.

- The three reactor are using Pressurized Water reactor (PWR). Despite of not having exactly the same fission fraction, they have a consistent shape of the distortion. However right now, it is not possible to conclude on the potential effect of the fuel composition on the distortion using only Daya Bay, RENO and Double Chooz experiments, due to the flux uncertainties are still too large and the fission fraction too close among experiments. But by adding the recent measurement of Neos, it seems that the bump is likely induced by the plutonium isotopes rather than the uranium ones [190].

Moreover Double Chooz has developed some other analyses to study the possible sources of this energy structure, in particular the existence of an accounted background source or a missing contributions to the reactor models. Concerning the background model, the 2-Off reactor data taken in Double Chooz allows for an independent and inclusive background measurement, thus accounting even for possible unknown sources [191]. It was seen that the sum of the individual background sources accounted for in the background model (accidental coincidences, fast-neutrons/stopping-muons and cosmogenic isotopes) was bigger than the total background measured with the 2 reactors off within the uncertainty, disfavouring the hypothesis of an unaccounted background contribution.

Taking into account the second possible source of the spectral distortion, if the excess around 5 MeV is due to an unaccounted reactor contribution, it must be correlated to the reactor power. As the Double Chooz RRM analysis utilizes the correlation between the observed rate and the reactor thermal power to derive both the mixing angle θ_{13} and the total background rate, it can be used to test the hypothesis of a bias in the flux prediction.

In [131], the IBD data is divided into four independent subsamples and the RRM fits have been carried out for different energy regions ([1-3] MeV, [3-4.25] MeV,[4.25-6] MeV,[6-8] MeV), constraining $\sin^2(2\theta_{13})=0.090^{+0.009}_{-0.008}$ from Daya Bay measurement [192] while leaving as free parameters both the total background rate and a flux normalization term with respect to the central value of the flux model α_r in equation 7.7. The best fit value of the background rate agrees with both the background model and the reactor off measurement, while the best fit values for the flux normalization deviates by 2σ from the prediction in the 4.25-6.00 MeV window, as shown in figure 7.22.

Therefore it is concluded that this result is consistent with the reported correlation between the energy distortion and the thermal power, thus reinforcing the case for a flux model bias and disfavouring again the background model as the source of the

energy distortion. Moreover if the total background rate is constraint to the background model, the discrepancy between the flux model and the RRM best fit value in the 4.25-6.00 bin is increased to 3σ. Furthermore, also in [131], a strong correlation between the rate of excess and the number of operating reactors is confirmed.

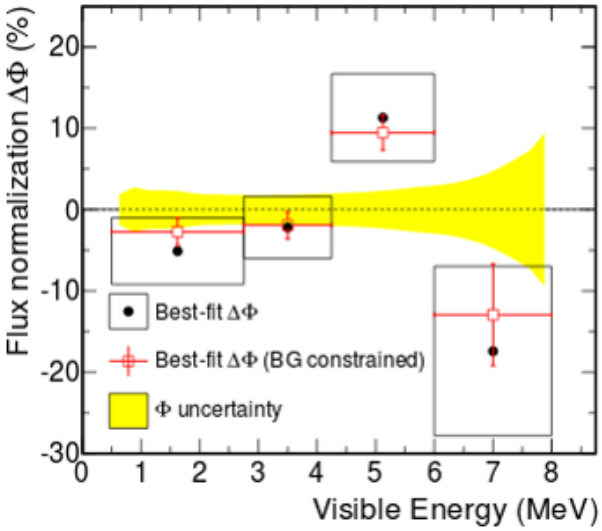

Figure 7.22: RRM best fit values of the reactor flux normalization w.r.t the central value prediction (black circles with error boxes) and also including the background constraint to the estimation (red empty squares with error bars). Uncertainty in the flux prediction is shown as a yellow area.

Given the correlation of the excess with the reactor power, the most likely explanation is a bias in the reactor flux models, as interpretation of DC and other experimental data. In fact, Daya Bay has observed correlations between the reactor core fuel evolution and changes in the reactor antineutrino flux and energy spectrum [193], indicating as well that the ∼6% discrepancy between the measured reactor neutrino rate and the prediction is likely due to reactor model. Changes in the IBD yield and spectrum per fission are represented as a function of the effective fission fraction of ^{239}Pu, which increases with the reactors fuel cycles. These yield measurements are used to calculate the cross sections per fission of ^{239}Pu and ^{235}U, showing a discrepancy of 0.7σ and 2.5σ from the theoretical values when they are combined with the reactor antineutrino rates of [194]. This last discrepancy suggests that ^{235}U may be the primary contributor to the reactor antineutrino anomaly. New physics, like the presence of sterile neutrinos, seems to be unlikely the cause of the discrepancy with the prediction since, in this case, the deficit should be constant independent to fuel composition.

One way to reinforce this conclusion is explained in [195]. The authors propose the combination of a experiment using reactors which are highly enriched in ^{235}U (HEU) with another one using commercial reactors with typically lower enrichment (LEU). Along this line, the comparison of the antineutrino spectra measured at reactors fuelled with LEU or HEU could clarify if the shoulder at 5 MeV is created (1) with similar strength by all the actinides, i.e, ^{235}U, ^{239}Pu, ^{238}U and ^{241}Pu (2) entirely by

^{235}U or (3) by any actinide except ^{235}U. This comparison could be performed using the ND data from Double Chooz (LEU) and Stereo experiments (HEU) with a $\bar{\nu}_e$ spectrum emitted by ^{235}U solely, based on the reference antineutrino spectra from Huber–Haag as shown in figure 7.23.

Thus the measurements from new reactor experiments as Stereo [196], Prospect [197] or Solid [198], in preparation for the search of short-baseline neutrino oscillation with high enriched ^{235}U research reactors could be capable to strongly constraint the shape of the ^{235}U.

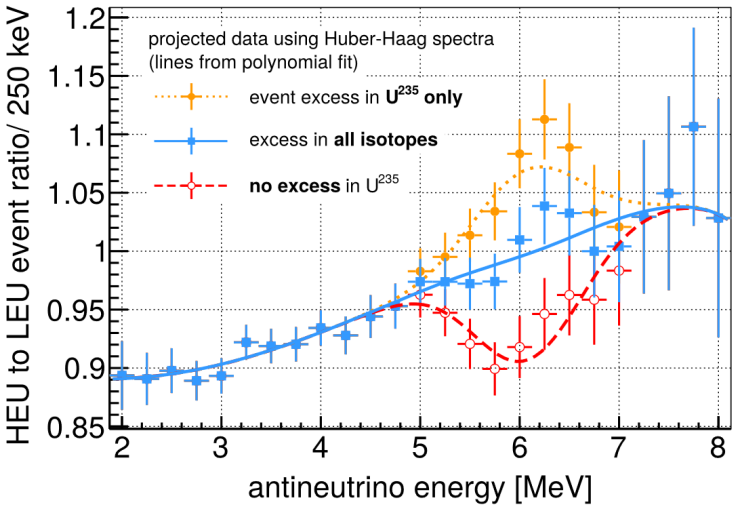

Figure 7.23: Event ratio of HEU to LEU antineutrino spectra for three hypotheses explained in the text. Data points show the ratio of the projected data for Stereo (HEU) and Double Chooz ND (LEU) using the Huber–Haag spectra for two years of data taking. The errors are statistical and include the model uncertainty of the Huber–Haag spectra considering correlation among fission isotopes. From [195].

In conclusion there are certain suggestions on the possible nuclear physics origins of this distortion which favours a flaw in the ^{235}U reactor antineutrino flux prediction, but this problem is not completely solved yet.

7.5 Summary of the Double Chooz oscillation fit results

From the beginning of the Double Chooz experiment, in April 2011, several analyses to determine θ_{13} have been carried out. In the one-detector phase FD-I, 489.51 days of run-time have been collected and the disappearance of the $\bar{\nu}_e$ has been studied, measuring the $\sin^2(2\theta_{13})$ using the Gd-channel and H-channel as a function of the visible energy (R+S) and the reactor power (RRM). The best results obtained using only the FD are written in table 7.14.

Table 7.14: Best-fit values of $\sin^2(2\theta_{13})$ achieved in the DC one-detector phase.

Analysis	$\sin^2(2\theta_{13})$
R+S Gd [131]	$0.090^{+0.032}_{-0.029}$
R+S H [102]	$0.124^{+0.030}_{-0.039}$
RRM-I Gd [131]	$0.090^{+0.034}_{-0.035}$
RRM-I H [102]	$0.095^{+0.038}_{-0.039}$
RRM-I Gd+H [102]	$0.088^{+0.033}_{-0.033}$

The last measurement in the table, RRM-I Gd+H, is obtained when the RRM fit is applied simultaneously to 2 sets of data: the hydrogen capture candidates presented in [102] and the gadolinium capture candidates of [131], including background estimates as a constraint in the fit. The uncertainties of the two different data sets are considered as fully correlated for the reactor flux and residual neutrino rate uncertainties and fully uncorrelated for the background uncertainties and the detection systematics.

The precision of these results was limited by the low statistics. A sensitivity study concluded that, even after three years running with the two detectors configuration, the Double Chooz measurements would be still dominated by statistics. Fortunately the statistical power of the experiment has been highly improved, almost by a factor of three with respect to Gd-only analysis, by including simultaneously neutron captures on G and H in the neutrino selection.

The latest results of $\sin^2(2\theta_{13})$ achieved with the multi-detector configuration (FD+ND), using the TnC technique that have been described along this chapter are listed in table 7.15. The results obtained using only the rate information (Rate-Only) or the shape information (Shape-Only) are added for completeness. The Rate-Only fit is performed by summing up all the energy bins from the χ^2 of equation 7.15 in a single bin, that is, the rate for each detector since the shape information is not present any more. On the other hand, by renormalizing the prediction histograms to the data one, at each fit step the total rate information is lost and a Shape-Only fit is performed.

Table 7.15: Best-fit values of $\sin^2(2\theta_{13})$ achieved in the DC multi-detector phase.

Analysis	$\sin^2(2\theta_{13})$
R+S D2MC [140]	0.105 ± 0.014
R+S D2D [140]	0.103 ± 0.017
RRM-II w/BG const. [140]	0.095 ± 0.016
RRM-II wo BG const. [199]	0.090 ± 0.022
RRM-I w/BG const. [199]	0.110 ± 0.018
RRM-I wo BG const. [199]	0.089 ± 0.024
Rate-Only [183]	0.119 ± 0.019
Shape-Only [183]	0.086 ± 0.037

Furthermore to the statistics improvement, recent $\sin^2(2\theta_{13})$ DC measurements has also achieved a major reduction of the systematic uncertainties, listed in table 7.11, being the most limiting the reactor flux uncertainty, since the FD-I still represents a

large fraction of the data, and the detection systematics due to the lack of precision in the proton number of the GC.

Comparing both tables 7.14 and 7.15, it can be extracted that all the θ_{13} results shown for the single and the multi-detector cases are compatible within errors. Finally, the most recent results of $\sin^2(2\theta_{13})$ using RRM and R+S fits described in this chapter together with the best results achieved with only FD-I are summarized in figure 7.24.

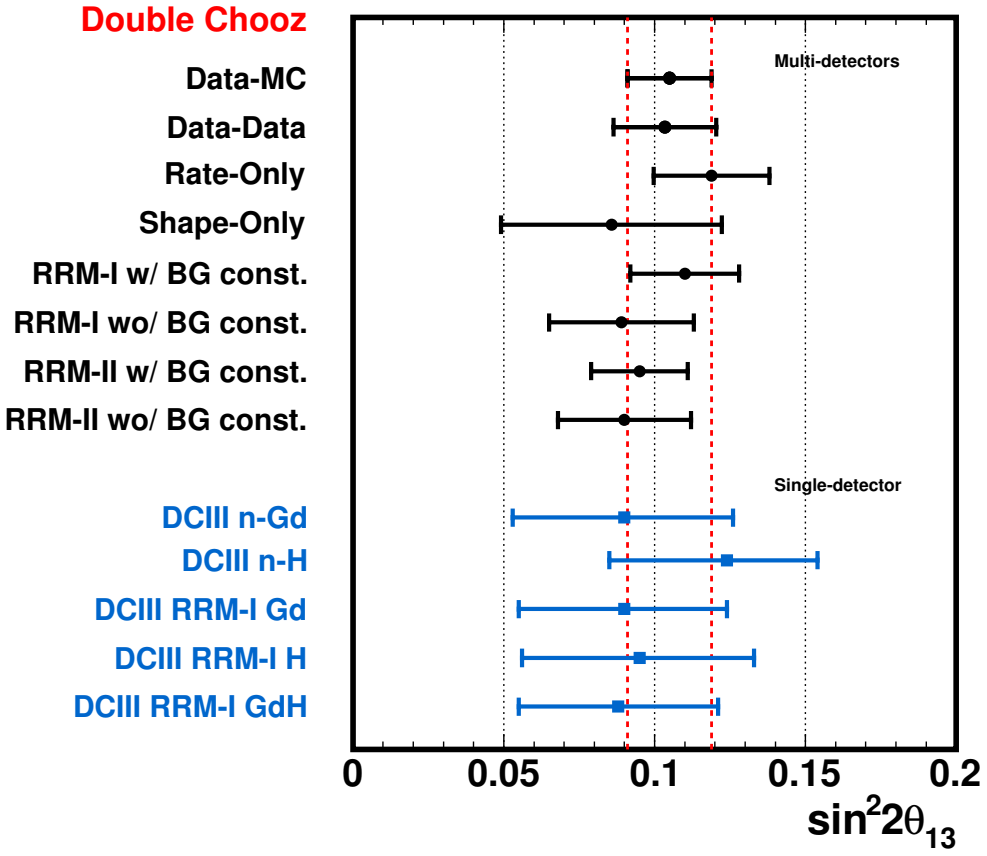

Figure 7.24: Summary of most the recent results of $\sin^2(2\theta_{13})$ obtained with the TnC multi-detector analysis using the R+S (D2MC and D2D) and RRM fits (black dots) and the most precise measurements achieved using only FD-I Gd-only and H-only selections (blue squares). Good agreement among all results is observed.

7.6 Future prospects

The Double Chooz $\sin^2(2\theta_{13})$ best fit result is compared with the current measurements from several experiments in figure 7.25. A central value of DC $\sin^2(2\theta_{13}) = 0.105 \pm 0.014$ is compatible within 1.4σ ompared to today's best knowledge, domi-

nated by the Daya Bay experiment latest measurement $\sin^2(2\theta_{13}) = 0.086 \pm 0.003$ [200]. As seen in table 7.11, systematic uncertainties dominate the result, so statistical fluctuations are disfavoured. The deviation to the latest RENO result [201] lowers to 1.1σ due to the fact that this experiment has lower precision than Daya Bay ($\sin^2(2\theta_{13}) = 0.090 \pm 0.006$). T2K [56] and NOvA [202] measurements has larger uncertainties due to their marginalisation over the unknown δ_{CP} and the θ_{23} octant, but accelerator measurements are compatible with reactor results.

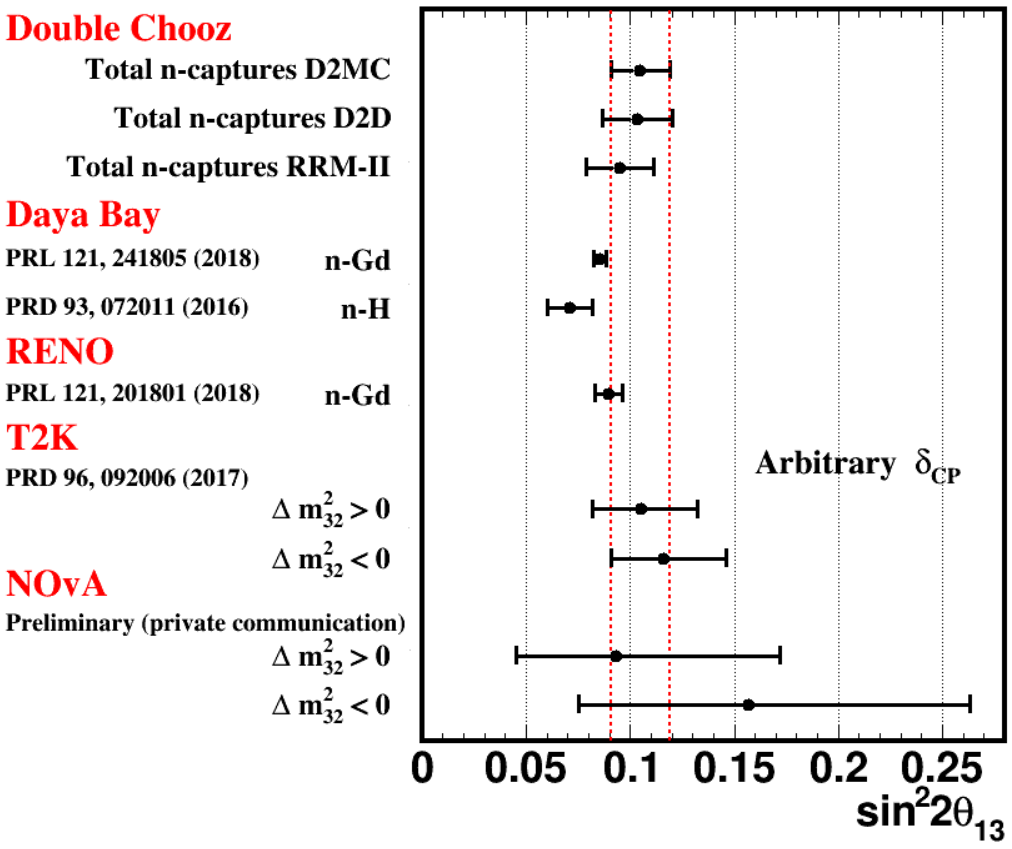

Figure 7.25: Comparison of the measured $\sin^2(2\theta_{13})$ by reactor and accelerator neutrino experiments.

The improvement that DC could achieve in θ_{13} by accumulating more statistics is displayed in figure 7.26. In the TnC analysis, 15 months of MD data have been used but there are still 21 months to be analysed that will slightly improve θ_{13} statistical uncertainty (10%). However the projection plot indicates that the experiment has reached a statistical plateau after the 3 years of data taking. Therefore Double Chooz has stopped the data taking in 2018 and the detectors are in process of being dismantled.

In the current analysis, the detection systematics uncertainty drives the final sensitivity, falling on the proton number uncertainty in the GC. After the decommissioning of the detector, DC expects to improve the lack of knowledge from an uncertainty of 0.65% to 0.20%, by performing new weight measurements of the GC liquid. Consid-

ering this improvement and also analysing some FD-I data stored between 2013-2015 that were taken during the commissioning of the FD-II (∼268 days), DC will achieve an uncertainty in the θ_{13} measurement of around 0.010, an improvement larger that taking data during more than six years in the current configuration (figure 7.27).

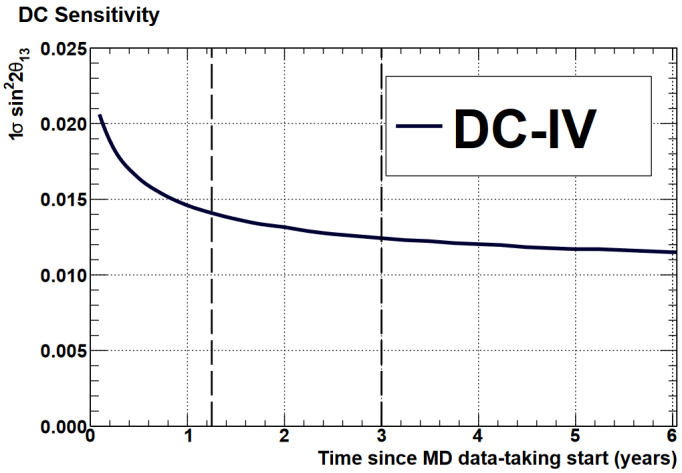

Figure 7.26: 1σ uncertainty of $\sin^2(2\theta_{13})$ for the D2MC fit in the current analysis. The first vertical line indicates the current sensitivity (15 months of data with multi-detector configuration) and the second line shows the sensitivity with 3 years of MD data, that is, with the analysis of the total data acquired by Double Chooz.

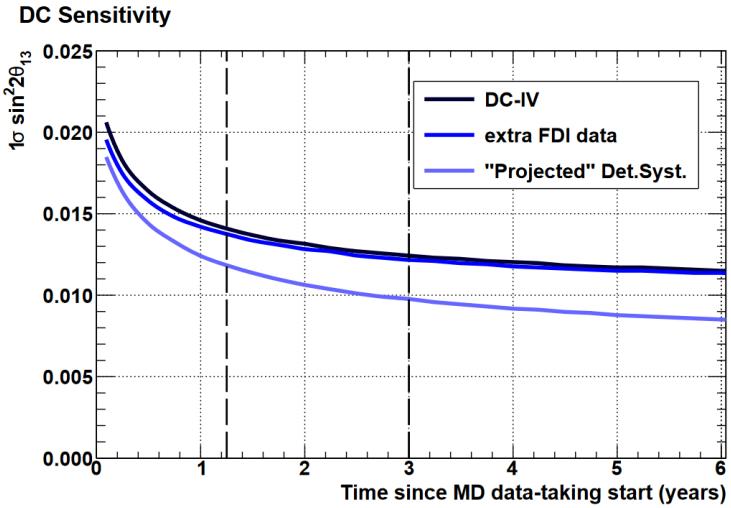

Figure 7.27: 1σ uncertainty of $\sin^2(2\theta_{13})$ for the D2MC fit in the projected configuration (improvement of the proton number uncertainty and extra available FD-I data). The first vertical line indicates the current sensitivity (15 months of data with multi-detector configuration) and the second line the sensitivity with the analysis of the total DC data.

Chapter 8

Summary and Conclusions

The high precision θ_{13} value measured by reactor experiments is a critical input not only to improve current knowledge on neutrino oscillation phenomena but also to ongoing and future experiments in search of the neutrino mass ordering and the leptonic CP violation.

In 2011 Double Chooz showed the first indication of a non-zero θ_{13} value, with the evaluation of the reactors data compiled only by the Far Detector at a baseline of $\sim$1 km. Since then, the measurement of the θ_{13} mixing angle has been improved, culminating with the result shown in this thesis, in which the two detectors configuration, near and far, has been exploited for the first time.

Reactor neutrino experiments are unique to provide an unambiguous and precise determination of θ_{13}, not affected by degeneracies or correlations between oscillation parameters. They look for the survival probability of the electron antineutrinos $\bar{\nu}_e$ coming from nuclear reactors:

$$P_{\bar{\nu}_e \to \bar{\nu}_e} = 1 - \sin^2(2\theta_{13}) \sin^2 \left(\frac{1.27 \Delta m^2_{13}\ L[m]}{E_{\bar{\nu}_e}[MeV]} \right)$$

Thus the flux and spectrum of the antineutrinos arriving to the far and near detectors need to be measured. These particles interact with the protons of the detectors liquid scintillator and are detected via the inverse beta decay, producing a correlated pair of signals. The prompt signal corresponds to the annihilation of the e^+ and the delayed signal to the neutron capture.

The new generation of reactor experiments, Double Chooz, Daya Bay and RENO, has achieved its best results analysing the neutron captures on Gadolinium, due to the fact that the energy released after the capture, 8 MeV, is well above the energy region of natural radioactivity. An independent analysis to the data sample using only captures on Hydrogen, with an energy of 2.2 MeV, has been also performed. This analysis suffers from high contamination of non-correlated backgrounds.

With 490 days of data collected only with the FD, Double Chooz measured θ_{13} with two different oscillation analyses, one comparing the observed $\bar{\nu}_e$ rate to the predicted one at different power regimes, called Reactor Rate Modulation (RRM) and another one studying the $\bar{\nu}_e$ disappearance as a function of the visible energy, called

Rate+Shape (R+S). The measurements of the mixing angle with these methods are:

$$\begin{aligned} \sin^2(2\theta_{13}) &= 0.088^{+0.033}_{-0.023} \quad \text{RRM (Gd,H)} \\ \sin^2(2\theta_{13}) &= 0.090^{+0.032}_{-0.029} \quad \text{R+S (Gd)} \\ \sin^2(2\theta_{13}) &= 0.124^{+0.030}_{-0.039} \quad \text{R+S (H)} \end{aligned}$$

These results are based either on the Gd selection, neutron captures on Gd, or on the H selection, n-captures on H.

The work presented in this thesis is based on the analysis of 865 days of exposure collected, for the first time, with the multi-detector configuration (FD+ND), improving this way the systematic uncertainty on the reactor precision thanks to the nearly iso-flux geometry, whereby both the FD and the ND are exposed to the same fraction of $\bar{\nu}_e$ from both reactors. Furthermore Double Chooz has developed a new IBD detection method based on the Total neutron Capture (TnC) technique, which considers neutron captures over all possible isotopes in the full detector volume. This new method not only increases the statistics by almost a factor of 3 (the neutrino rate in the near (far) detector is increasing to about 900 (140) events/day), but also causes a significant reduction of the detection systematics, since there is no need to consider any distinction among neutron captures on Gd or H and the complex neutron spill in/out currents among the detector volumes.

This thesis describes step by step the procedure to achieve best the fit value for the θ_{13} oscillation angle. First of all the reactor flux uncertainties on the signal normalization are detailed. This translates into an almost total rate+shape flux error cancellation thanks to the iso-flux configuration (uncorrelated error between ND and FD-II is $\sim$0.1%). Despite the ND, the reactor flux prediction is still important in the analysis, due to the use of 481 days of data extracted from the single detector operation of the FD-I (uncorrelated error between ND and FD-I 0.66%).

The oscillation analysis also needs an input related to the energy scale systematics, including uniformity, stability and non-linearities to account the remaining differences between data and MC model. An energy resolution of 8%/MeV is achieved after corrections.

The next step falls on the selection of the antineutrino signals. First, a preselection requires that the trigger must be totally efficient (E_{vis}>0.4 MeV), eliminates the tagged muons and the subsequent events using the detector vetoes information and rejects also the light noise signals produced by the light emission of the PMTs bases. From the preselected sample, $\bar{\nu}_e$s are identified as pairs of signals close in time and space. The energy range of the selected e^+ signal takes into account the energy spectrum of the incident neutrino, which is expected to finish at 8.5 MeV but this window is extended up to 20 MeV to constrain background events of cosmogenic isotopes, fast neutrons and stopping muons. The energy range of the delayed signal is maximally open to accept both H and Gd neutron captures (1.3<E_{del}<10 MeV) simultaneously. However due to the extension up to 1.3 MeV, accidental coincidences are the dominant background contribution. To reduce this background, DC makes use of a multivariable analysis based on an artificial neural network (ANN) that uses the spatial and temporal coincidence of the prompt and delayed signals and the neutron capture energy as input parameters, since they exhibit different pattern between neutrino candidates and random coincidences.

In addition to these requirements, several vetoes and techniques have been developed to reject fast neutrons background and cosmogenic isotopes contamination. The signal to noise ratio in both detectors is still well above 10 with this new TnC selection and the background subtraction has negligible impact on the θ_{13} oscillation fit. To validate the background model, Double Chooz relies on one of its unique features, i.e, the measurement of the background when the two reactors of the nuclear plant are off, obtaining compatible results between the prediction and the direct measurement.

This thesis is focused on the detection systematic uncertainties associated to the neutrino signal detection, one of the dominant contributions to the θ_{13} precision. With the TnC method, the IBD detection efficiency is factorized into four components: the inefficiency of the background vetoes, the uncertainty of the number of protons in the scintillator volume, the boundary term that allows to consider the spill events involving either the buffer or the gamma-catcher acrylic tank volumes and the efficiency of the IBD candidates selection. Both vetoes and boundary efficiencies uncertainty play a negligible role in the θ_{13} measurement. In contrast, the θ_{13} measurement is dominated by the imprecise measurement on the GC proton number, since this volume was originally not considered as a target for IBD interactions.

Concerning the fourth component, refereed as selection efficiency, it is defined as the ratio of the IBD antineutrino candidates passing the TnC selection over an open selection with a loose ANN cut (to reduce accidental background) that integrates over $\sim$98% of the detectable IBD's. This analysis is carried out with the neutrons coming directly from the IBD reaction, since they are homogeneously distributed inside the whole detector volume allowing volume-wide studies of the detector performance. The selection efficiency for the FD data is 86.78 $\pm$ 0.21% (MC: 86.75 $\pm$ 0.01%) and 85.47 $\pm$ 0.08% for the ND data (MC: 85.54 $\pm$ 0.02%). The discrepancy between the FD and ND selection efficiency comes from the slightly different ANN cut chosen for each detector (ANN$>$0.86 for the FD and ANN$>$0.85 for the ND), with the purpose of achieving identical prompt energy selection efficiency across detectors. On the other hand the efficiency of the MC matches the one of the data within 0.1%.

During the development of the thesis, a small concentration of Gd in the ND GC was found. To confirm that the TnC is leak insensitive by construction, the selection efficiency of four ND MCs with different concentration of Gd in GC (no Gd in GC, 1.1 μg/cm^3, 1.55 μg/cm^3 and 2.4 μg/cm^3 of Gd) has been compared with ND and FD selection efficiency data. The MC selection efficiency is compatible within errors with the data efficiency for ND and FD detectors, being the biggest discrepancy (less that 2σ) found when the ND data is compared to the MC with 2.4 μg/cm^3. When the ND data is compared with the baseline MC (with 1.1 μg/cm^3), the difference is less than 0.9σ in the full detector volume. This way it has been demonstrated that any change on the Gd concentration in the GC has no impact in the selection efficiency. In addition, the stability of the selection efficiency for 23 months of FD-II+ND data has been tested, concluding that the efficiency of both detectors are stable in time.

Finally Double Chooz has observed a deficit with respect to the predictions that is interpreted as an oscillation. Thus the θ_{13} mixing angle is obtained using the RRM and the R+S fit. In the case of the R+S fit, two independent oscillation analyses have been carried out: the first one, and the nominal measurement, performs a comparison of the data to the prediction (data to MC fit) and the second one compares directly

FD data to ND data (data to data fit). The results of θ_{13} are:

$$\begin{aligned} \sin^2(2\theta_{13}) &= 0.095 \pm 0.016 \quad \text{RRM} \\ \sin^2(2\theta_{13}) &= 0.105 \pm 0.014 \quad \text{R+S (data to MC)} \\ \sin^2(2\theta_{13}) &= 0.103 \pm 0.017 \quad \text{R+S (data to data)} \end{aligned}$$

All the results are compatible within errors, being the R+S data to MC the most precise result since it uses both the shape and rate information. In all cases these results are dominated by the systematics uncertainties. The largest contributions come from the reactor uncertainty, since the FD-I data set represents a large fraction of the total data, and from the detection systematics, dominated by the GC proton number uncertainty. With the analysis of the full data set as well as with the measurement of the GC proton number after the detector dismantling, Double Chooz expects a total uncertainty on $\sin^2(2\theta_{13})$ below 0.01.

Comparing the DC θ_{13} measurement, with the average θ_{13} value extracted from the PDG, it can be appreciated that there is a discrepancy of 1.5σ in the central value. Since the statistical uncertainties in reactor experiments are small, a statistical fluctuation is unlike to be the only cause of this difference.

A combined "reactor-θ_{13}" measurement is expected to remain as the world reference, relying on systematic uncertainties in the per mille level. Thus, the redundancy of multiple experiments is critical to ensure accuracy and precision.

Appendix A

Gd-only Detection Efficiency

The estimation of the expected neutrino events in the detectors is carried out taking into account the inverse beta decay detection efficiency, as was described in equation 3.1. This detection efficiency is factorized as in the case of the TnC following the equation 6.1:

$$\epsilon_{\text{det}}^{\text{IBD,Gd}} \equiv \epsilon_{\text{sel}}^{\text{Gd}} \cdot \epsilon_{\text{BG}}^{\text{Gd}} \cdot \epsilon_{\text{p\#}}^{\text{Gd}} \cdot \epsilon_{\text{bound}}^{\text{Gd}} \tag{A.1}$$

However in the case of the Gd only analysis, where only the gadolinium captures are considered, the term relative to the selection efficiency, ϵ_{sel}, is divided into three terms:

$$\epsilon_{\text{sel}}^{\text{Gd}} = \epsilon_{\text{sel}}^{\text{Gd}} \cdot f_{\text{Gd}} \cdot \epsilon_{\text{spill}} \tag{A.2}$$

where

- $\epsilon_{\text{sel}}^{\text{Gd}}$ evaluates the efficiency of the IBD selection cuts (energy of the prompt and delayed events of the IBD signal and the time and spatial coincidence between the prompt and the delayed signals).
- f_{Gd} estimates the fraction of neutron captures in Gd and studies the relative abundance of neutron captures on the Gd-nuclei vs the H captures.
- ϵ_{spill} computes the neutron currents among the different volumes of the detector (ν-target $\leftrightarrow$ GC and GC $\leftrightarrow$ buffer).

In the TnC analysis, only the first term ϵ_{sel} is relevant, as explained in section 6.3. These detection efficiency terms are studied using different neutron sources or simulations. For the $\epsilon_{\text{n-capture}}$ the ^{252}Cf neutron events in the detector center are used. The $\epsilon_{\text{sel}}^{\text{Gd}}$ is studied using IBD neutrons distributed in the entire detector. As a cross-check for this efficiency, fast neutrons coming from spallation muons are used. For ϵ_{spill} MC simulations are implemented in order to evaluate this term.

Each of these terms and the different neutron sources used to study them are explained in the following sections. Moreover the efficiency correction factors data to MC and data to data are calculated in the same way as in TnC analysis (see section 6.3, equations 6.7 and6.8).

A.1 Gd-only selection efficiency

The Gd-only selection efficiency $\epsilon_{\text{sel}}^{\text{Gd}}$ corresponds to the efficiency of the selection cuts used to define the IBD candidates, that is, the energy of delayed signal E_{del}, the time correlation ΔT and the distance between the vertex positions of the prompt and delayed signals ΔR. As in the TnC analysis, the performance of the selection efficiency analysis is carried out with the neutrons coming directly from the IBD reaction. The selection efficiency is defined as:

$$\epsilon_{\text{sel}}^{\text{Gd,m}} = \frac{N(\text{IBD} \cap \text{Gd BG vetoes})}{N(\text{IBD*} \cap \text{Gd BG vetoes})} \tag{A.3}$$

where:
IBD = $(0.5 < \text{E}_{\text{prompt}} < 8.5)$ MeV $\cap$ $(0.5 < \Delta\text{T} < 150)$ μs $\cap$ $(4 < \text{E}_{\text{del}} < 10)$ MeV $\cap$ $\Delta\text{R} < 1000$ mm
IBD* = $(0.5 < \text{E}_{\text{prompt}} < 8.5)$ MeV $\cap$ $(0.5 < \Delta\text{T} < 800)$ μs $\cap$ $(3.5 < \text{E}_{\text{del}} < 10)$ MeV $\cap$ $\Delta\text{R} < 1200$ mm,
being N the number of events passing the cuts shown in parentheses and m stands for either data or MC. The background vetoes for the Gd-only analysis are similar to the ones for the TnC analysis. As happening in the TnC analysis, the extension of the prompt energy window up to 20 MeV to accumulate background is not useful for this analysis, so the prompt energy window is restricted to 0.5 MeV $< \text{E}_{prompt} <$ 8.5 MeV. In the denominator of eq. A.3 one can find the cuts as open as possible to select neutrons getting a compromise between signal and accidental background. This way the lower limit of the delayed energy has been increased up to 3.5 to select possible Gd captures without including the ones in Hydrogen. The higher ΔT limit has been opened up to 800 μs to include the Gd captures in the GC. ΔR can be relaxed only to 1200 mm because wider spatial coincidences implies the selection of more accidental events.

Once the background vetoes are applied to reduce stopping muons, fast neutrons and cosmogenic isotopes, the most important background contribution falls on accidental coincidences. As happening in TnC analysis, it is needed to subtract this background to the data, so the same selection cuts of equation A.3 are applied to the accidental sample except the time coincidence which is obtained from the off-time method. Again there are some cuts that do not affect in the same way to the on-time (antineutrino candidates) and the off-time (accidental coincidences) selection, so the off-time sample is corrected using the accidental correction factors. For the Gd-only selection the correction factors used are displayed in tables A.1, A.2, A.3 and A.4.

Table A.1: Global accidental correction factors for ND in the Gd-only analysis.

	Numerator	Denominator
f_{run}	1.00053	1.00053
f_{μ}	1.325	1.228
f_{iso}	1.023	1.021
f_{Li9}	0.98 $\pm$ 0.03	0.99 $\pm$ 0.03
Total	1.33 $\pm$ 0.03	1.24 $\pm$ 0.03

Table A.2: Global accidental correction factors for FD-I in the Gd-only analysis.

	Numerator	Denominator
f_{run}	1.00044	1.00044
f_{μ}	1.055	1.039
f_{iso}	1.026	1.025
f_{Li9}	0.86 ± 0.02	0.93 ± 0.02
Total	0.93 ± 0.02	0.99 ± 0.02

Table A.3: Global accidental correction factors for FD-II in the Gd-only analysis.

	Numerator	Denominator
f_{run}	1.00042	1.00042
f_{μ}	1.054	1.039
f_{iso}	1.036	1.036
f_{Li9}	0.93 ± 0.05	0.95 ± 0.05
Total	1.02 ± 0.05	1.03 ± 0.05

Table A.4: Global accidental correction factors for FD-I+FD-II combination in the Gd-only analysis.

	Numerator	Denominator
Total	0.98 ± 0.03	1.01 ± 0.03

Once the antineutrino data and the accidental samples that satisfy the selection and the open selection cuts of eq. A.3 and the accidental correction factors have been computed, the selection efficiency value for the data of each detector is obtained again with the formula 6.10.

Gd-only selection efficiencies for every detector for data and MC sample are summarized in table A.5 (only statistical errors, calculated as in the TnC selection efficiency, are shown).

Table A.5: Gd-only selection efficiency data and MC in the full detector volume.

	FD-I	FD-II	FD	ND
$\epsilon_{\mathrm{Gd}}^{\mathrm{data}}(\%)$	96.772 ± 0.187	96.845 ± 0.293	96.794 ± 0.170	95.162 ± 0.084
$\epsilon_{\mathrm{Gd}}^{\mathrm{MC}}(\%)$	96.765 ± 0.013	96.760 ± 0.013	96.763 ± 0.009	95.393 ± 0.020

In comparison to the TnC selection efficiency results, the values for the Gd-only analysis are higher and have lower statistical errors. This is due to the high S/B ratio (∼26 in FD, ∼ and ∼34 in ND) and the smaller number of accidental coincidences (0.067 day $^{-1}$ in the FD-I, 0.118 in the FD-II day $^{-1}$ and 1.62 day $^{-1}$), since the accidentals are confined in the H region, not included in the Gd-only analysis, making easier the subtraction.

Finally the selection efficiency correction factors are listed in table A.6 (only statistical errors are shown).

Table A.6: Selection efficiency correction factors data to MC, data to data and MC to MC for the Gd-only analysis. Only statistical errors considered.

$R^{Gd}_{\epsilon_{sel}}$(Data:MC)	FD-I:FD-I	FD-II:FD-II	FD:FD	ND:ND
	1.0001 ± 0.0019	1.0009 ± 0.0030	1.0003 ± 0.0018	0.9976 ± 0.0009
$R^{Gd}_{\epsilon_{sel}}$(Data:Data)	FD-I:ND	FD-II:ND	FD:ND	
	1.0169 ± 0.022	1.0177 ± 0.0032	1.0171 ± 0.0020	
$R^{Gd}_{\epsilon_{sel}}$(MC:MC)	FD-I:ND	FD-II:ND	FD:ND	
	1.0144 ± 0.0002	1.0143 ± 0.0002	1.0144 ± 0.0002	

In the Gd-only selection efficiency, it can be distinguished two sources of systematics. The first one, analogously to the TnC analysis, comes directly from the difference between MC with 1.55 and 1.1 $\mu g/cm^3$ Gd concentration in GC calculated with Gd-only efficiency eq.A.3:

Table A.7: ND MC selection efficiency for the MCs with 1.1 and 1.55 $\mu g/cm^3$ of Gd concentration in the GC in Gd-only.

	MC ND (1.1 $\mu g/cm^3$)	MC ND (1.55 $\mu g/cm^3$)
$\epsilon^{MC,\ Gd}_{sel}$(%)	95.393 ± 0.020	94.924 ± 0.022

$R^{Gd}_{\epsilon_{sel}}(MC_{1.1}ND : MC_{1.55}ND) = 1.0049 \pm 0.0003 \rightarrow$ Systematic error = 0.0049

This first source of systematic is applied to any ratio involving ND data or MC. Now this is applied on data as well since it should take into account not only a possible MC bias, but also possible variations in time as well as inhomogeneities in the GC volume due to the leak.

Differences between FD and ND is due to the Gd leak in the ND GC that it is not present in the FD. A graphical explanation is present in figure A.1. On the left part of the figure is represented the ND selected IBD candidates passing the IBD selection, i.e, the numerator of the selection efficiency definition in the upper part and the candidates passing the denominator in the bottom part. The same pattern is plotted on the right part of the figure for the FD, where there is no component concerning Gd in the GC. Making the ratios of the numerator to the denominator, it can be seen that since there are more entries in the denominator of the ND due to the captures in the GC, the resulting efficiency is going to be lower in the ND than in the FD.

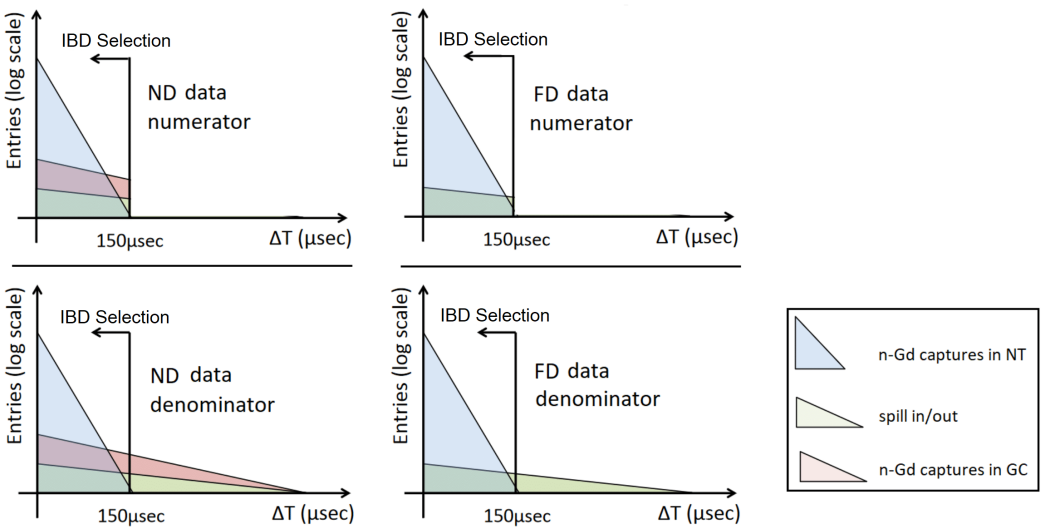

Figure A.1: Schematic explanation for the difference in the selection efficiency between FD data and ND data. There is an extra contribution present in the ND due to the Gd in the GC and the captures taking place in this volume have larger ΔT than 150 μs due to the competitiveness between Gd and H captures in the GC. From [155].

To account for this discrepancy between FD and ND, a second source of systematic error has to be included in the efficiency correction factors of table A.6. To quantified this difference, a new efficiency definition has been developed, call "extended efficiency", which follows the following equation:

$$\epsilon^{m}_{\text{ext}} = \frac{N(\text{IBD Gd} \cap \text{all vetoes Gd})}{N(\text{IBD TnC} \cap \text{all vetoes TnC})} \tag{A.4}$$

where
IBD Gd = $(1.0 < \text{E}_{\text{prompt}} < 8.5)$ MeV $\cap$ $(0.5 < \Delta\text{T} < 150)$ μs $\cap$ $(4 < \text{E}_{\text{del}} < 10)$ MeV $\cap$ $\Delta\text{R} < 1000$ mm
IBD TnC = $(1.0 < \text{E}_{\text{prompt}} < 8.5)$ MeV $\cap$ $(0.5 < \Delta\text{T} < 800)$ μs $\cap$ $(1.3 < \text{E}_{\text{del}} < 10)$ MeV $\cap$ $\Delta\text{R} < 1200$ mm,
being N the number of events passing the cuts shown in parentheses and m stands for either data or MC.

With this definition, the systematic uncertainty has been determined as the difference between the efficiency ratio of the MC without leak in GC and the MC with 1.1 μg/cm^3 Gd concentration in GC calculated with Gd-only efficiency eq.A.3 and Gd-extended efficiency eq.A.4:

- Gd-only efficiency ratio:

$$\begin{aligned} \text{R}^{\text{Gd}}_{\text{sel}}(\text{MC:MC}) &= \frac{\epsilon^{\text{Gd}}_{\text{sel}}[\text{ND MC(no Gd in GC)}]}{\epsilon^{\text{Gd}}_{\text{sel}}[\text{ND MC}(1.1\mu\text{g/cm}^3)]} = \frac{96.732 \pm 0.017}{95.393 \pm 0.019} \\ &= 1.0140 \pm 0.0003\% \end{aligned} \tag{A.5}$$

- Gd-extended efficiency ratio:

$$\begin{aligned} R_{ext}(\text{MC:MC}) &= \frac{\epsilon_{ext}[\text{ND MC}(1.1\mu g/cm^3)]}{\epsilon_{ext}[\text{ND MC(no Gd in GC)}]} = \frac{32.382 \pm 0.025}{31.977 \pm 0.025} \\ &= 101.27 \pm 0.11\% \end{aligned} \tag{A.6}$$

Being then the bias between the Gd-only selection efficiency and the extended efficiency:

$$\Delta^{bias} = 101.40 - 101.27 = 0.13\%$$

This bias is considered as the second source of systematics in the efficiency correction factor results. This protects the efficiency determination from the uncertainty on the proton number, the non-linearity in concentration, the non-homogeneous position and the spill effect between the GC boundary and the Buffer. This systematic is applied to any ratio including ND data or MC when comparing to the FD.

As in the TnC section 6.3.2, the final selection efficiency correction factors, including statistical and systematics errors, for the FD and ND are listed in table A.8.

Table A.8: Selection efficiency correction factors for Gd-only analysis including statistical and systematics errors.

$R_{\epsilon_{sel}}$(Data:MC)	FD:FD	ND:ND
	1.0003 ± 0.0018	0.9976 ± 0.0050
$R_{\epsilon_{sel}}$(Data:Data)	FD:ND	
	1.0171 ± 0.0055	
$R_{\epsilon_{sel}}$(MC:MC)	FD:ND	
	1.0144 ± 0.0051	

A.1.1 Extra systematic studies

The stability of the correction factor against perturbations in the efficiency definition was checked by loosening the E_{del} cut in the denominator of equation A.3:

- Original
  $(0.5 < \Delta t < 800)\mu s \cap (3.5 < E_{del} < 10)\text{MeV} \cap (0 < \Delta R < 1200)\text{mm}$

- $E_{del} > 3.0$ MeV
  $(0.5 < \Delta t < 800)\mu s \cap (3.0 < E_{del} < 10)\text{MeV} \cap (0 < \Delta R < 1200)\text{mm}$

No significant deviation was observed from the original value obtained with eq. A.3 as it can be seen in figure A.2 and A.3.

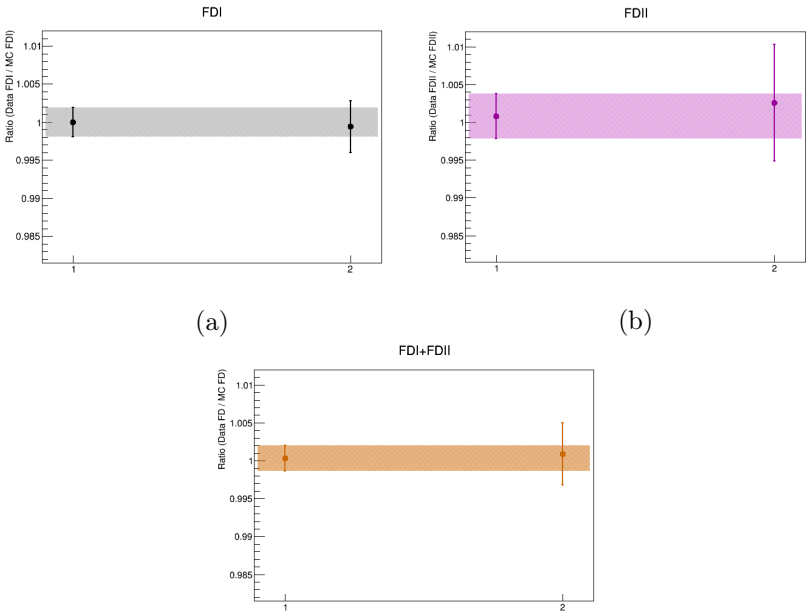

Figure A.2: Selection efficiency correction factor between data and MC for (a) FD-I, (b) FD-II and (c) FD, being the x axis the 2 variations of the denominator cuts explained in the text (original and $E_{del} > 3.0$ MeV). The results are compatible within 1 sigma indicated as colour bands.

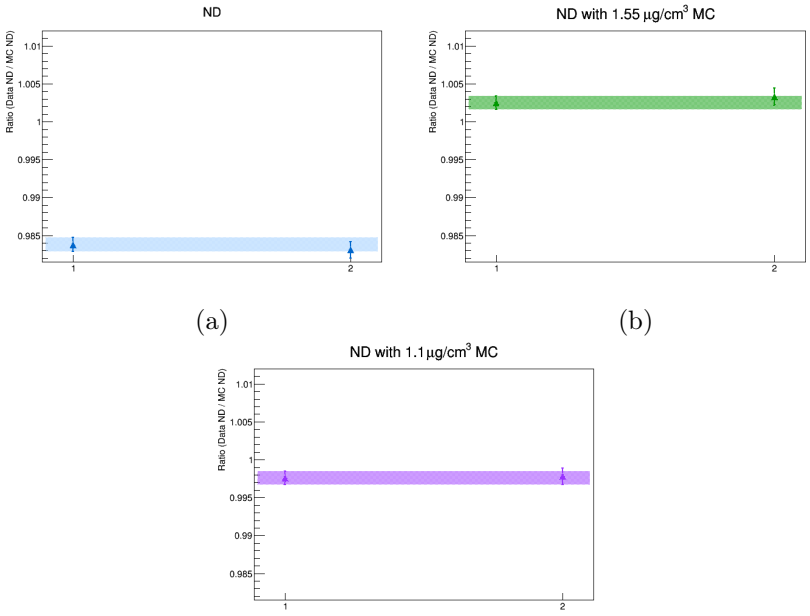

Figure A.3: Selection efficiency correction factor between ND data and ND MC with (a) no Gd in GC, (b) 1.55 μg/cm^3 in GC and (c) 1.1 μg/cm^3 in GC. The pattern is the same as figure A.2.

A.1.2 Crosscheck of the Gd-only efficiency with fast neutrons

To verify the results shown in section A.1, an alternative analysis with fast neutrons (FN) has been carried out [156]. However, IBD neutrons and FN cannot be compared directly with the same selection cuts due to after-μ inefficiencies of the detectors. Therefore the efficiency definition has been chosen to match the FN selection:

$$\epsilon_{\mathrm{FN}} = \frac{N(\mathrm{IBD}_{\mathrm{FN}} \cap \text{all vetoes Gd-only})}{N(\mathrm{IBD}^*_{\mathrm{FN}} \cap \text{all vetoes Gd-only})} \tag{A.7}$$

where:

$\mathbf{IBD_{FN}}$ = $(0.5 < \mathrm{E_{prompt}} < 8.5)$ MeV $\cap$ $(21 < \Delta\mathrm{T} < 150)$ μs $\cap$ $(5 < \mathrm{E_{del}} < 10)$ MeV $\cap$ $\Delta\mathrm{R} < 1000$ mm
$\mathbf{IBD^*_{FN}}$ = $(0.5 < \mathrm{E_{prompt}} < 8.5)$ MeV $\cap$ $(21 < \Delta\mathrm{T} < 800)$ μs $\cap$ $(4.5 < \mathrm{E_{del}} < 10)$ MeV $\cap$ $\Delta\mathrm{R} < 1200$ mm

As can be seen the differences between this definition and the previous Gd-only definition (eq.A.3) fall to the lower cut on ΔT equals to 21 μs (instead of 0.5) and lower $\mathrm{E_{del}}$ cut equals to 5 (4.5) MeV on the numerator (denominator).

From the FN analysis, without subtracting the off-time sample, the following results have been achieved:

ϵ_{FN} (Data ND) = 89.00 $\pm$ 0.10 %
ϵ_{FN} (Data FD-II) = 91.49 $\pm$ 0.23%

$\mathbf{R_{\epsilon_{FN}}(Data\ FD\text{-}II : Data\ ND) = 1.0280 \pm 0.0028}$

With IBD-neutrons and using the equation A.7:

ϵ_{FN} (Data ND) = 91.92 $\pm$ 0.13%
ϵ_{FN} (Data FD-II) = 94.24$\pm$ 0.33%

$\mathbf{R_{\epsilon_{FN}}(FDII{:}ND) = 1.0252 \pm 0.0039}$

There is only a discrepancy of 0.6 σ. So the agreement between the results of the ratios with FN and IBD neutrons verify the Gd-only efficiency results with IBD neutrons.

A.2 Gadolinium fraction

The neutron capture is a competitive process between the different isotopes in the detector liquid scintillator. It depends on the neutron capture cross-section and the abundance of the isotopes present in the medium. The Gd fraction $\mathrm{f_{Gd}}$ or GdF represents the proportion of radioactive neutron captures that occur on Gd. Considering

the energy spectra for data and simulations (see figure A.4), it is possible to see that the Gd-capture events are mainly distributed with energies between 3.5 and 10 MeV (Gd-capture peak and its tail). The H-captures are distributed with visible energies in the range [1.3, 3.5] MeV.

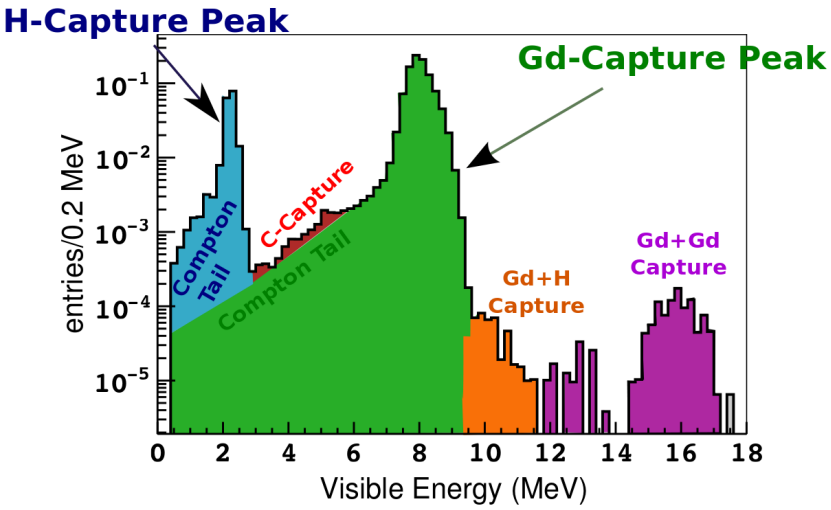

Figure A.4: Delayed energy spectra for Californium source data after background subtraction. Colored areas represent the observed energies for different captures in the liquid scintillator. Figure from [159].

The measurement of the Gd fraction (GdF) in data and in MC is done using the neutrons from the ^{252}Cf source and also the neutrons coming from the IBD reaction. Following the same reasoning than in the neutron selection efficiency, one need to compute the following correction factors:

$$\mathrm{R}_{f_{\mathrm{Gd}}}(\text{Data : MC}) \equiv \frac{f_{\mathrm{Gd}}(\text{Data XD})}{f_{\mathrm{Gd}}(\text{MC XD}} \qquad \text{XD} = \text{FD, ND} \tag{A.8}$$

$$\mathrm{R}_{f_{\mathrm{Gd}}}(\text{Data FD : Data ND}) \equiv \frac{f_{\mathrm{Gd}}(\text{Data FD})}{f_{\mathrm{Gd}}(\text{data ND})} \tag{A.9}$$

A.2.1 Californium-252 measurement

The ^{252}Cf calibration source was introduced in section 2.8. This isotope of the Cf is the most stable among the others with a life-time of $\tau = 3.816$ yr. This element in 97% of the times decays through alpha decay, whereas the 3% of the times it decays via spontaneous fission. In these last case, gamma-radiation and neutrons are emitted. In fact this source is used as a prolific neutron emitter, yielding ≥ 12.9 neutrons per second.

As in the case of the antineutrinos for the neutron selection efficiency analysis, the valid trigger selection follows the one from section 5.6.1. Then the first event observed in the detector are the fission fragments gammas, causing the prompt trigger. Then only the events succeeding the prompt trigger in a defined time window will be tagged

as delayed events which consist on the neutron captures after the fission neutrons have thermalized. Considering all of this, the events are selected in the next steps:

- **Prompt event** (fission gammas):
  - $(4 < E_{vis} < 30)$ MeV
  - at least after 1.5 ms with reference to the last trigger event. This works as an isolation cut to avoid selecting neutrons from a previous event as the prompt signal.
- **Delayed events** (neutron captures):
  More than 1 event can occur (multiplicity > 1) with the next properties (^{252}Cf tipically emits 3.757 neutrons per fission [158]):
  - $0.5 < E_{vis} < 25$ MeV
  - $0.5 < \Delta t < 1000$ μs

The fission gammas with energies lower than 4 MeV are neglected because they could be contaminated with correlated and accidental backgrounds. This accidental background is measured and subtracted as in equation 6.10 using an off-time window method simpler than the one for antineutrinos. In this method, when a real fission event happens (on-time event) virtual prompts are simulated after 4·N ms, where N are the number of windows from 1 to 6 to enhance statistics. In their corresponding delayed window, single candidates are searched, considering the Californium selection criteria. If a single event is observed in this window, it is considered as a background event, named off-time events. The accidental rate is corrected using an accidental correction factor that takes into account the amplitude and the number of windows.

The fraction of neutron captures on Gd nuclei is defined as

$$f_{Gd} = \frac{N(3.5 \text{ MeV} < E_{delayed} < 10 \text{ MeV})}{N(1.3 \text{ MeV} < E_{delayed} < 10 \text{ MeV})} \tag{A.10}$$

With this definition, valid for data and MC, the energy spectrum is divided in events due to H- or Gd-captures. It should be noted that the small amount of carbon captures happening around 5 MeV is included in the Gd-capture region. The double captures due to Gd+H at $\sim$ 10.2 MeV and Gd+Gd at $\sim$ 16 MeV are neglected in this analysis.

Using the high statistics Cf data located at the detector center (x,y,z) = (0,0,12) mm, where the leakage of neutrons out of the ν-target is negligible, the Gd fraction results are the one in table A.9. Statistical errors are calculated following a binomial distribution equivalent to the one in equation 6.12.

Table A.9: Data and MC Gd fraction using the ^{252}Cf source in the center of the detector. Only statistical errors shown.

	FD-II	ND
f_{Gd}^{data}(%)	85.62 ± 0.04	85.41 ± 0.03
f_{Gd}^{MC}(%)	87.66 ± 0.04	87.61 ± 0.04

With these numbers the data to data and data to MC GdF ratios are listed in table A.10, where only the statistical uncertainties are considered.

Table A.10: Gadolinium fraction ratios for the ^{252}Cf source.

$R_{f_{Gd}}$(Data:MC)	FD:FD	ND:ND
	0.9767 ± 0.0006	0.9748 ± 0.0005
$R_{f_{Gd}}$(Data:Data)	FD:ND	
	1.0025 ± 0.0006	

Concerning the systematic uncertainty of the data to data ratio, it is extracted from variations of the cuts in equation A.10. Varying the low energy cut, the maximum discrepancy of the ratio is 0.03%. In addition the correlation time cut was also varied and a discrepancy of 0.04% is observed using a minimum time cut between Δt_{min} = 0.5 μs and 15 μs. The combination of these numbers yields 0.05% and is considered the total systematic uncertainty on $R_{f_{Gd}}$(Data FD : Data ND) due to low energy and correlation time background events.

Even with this systematic, the difference between FD and ND is not covered. Considering these results, the $\sim$ 0.25% discrepancy between the two detectors is significant. The difference might be related to the leak in the ND GC (lower Gd fraction in ND by dilution of the target with GC liquid).

Concerning the ratio of the GdF data and MC, the delayed energy spectra used for the measurement are shown in figure A.5. There is a discrepancy between data and MC for energies below the H peak, which is attributed to a source related background (e.g. radioactive decays of fission fragments not accounted in the simulation) [159].

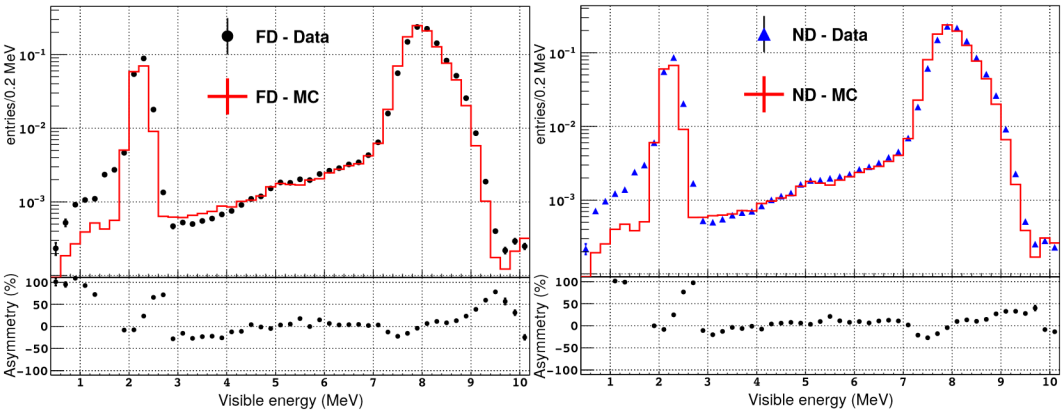

Figure A.5: Delayed energy spectra for far (left) and near (right) detectors data and MC simulations at the target center. Asymmetry plots corresponds to $2\frac{A-B}{A+B}$ where A, B are FD, ND or MC number of events depending on the plot.

The ND MC used here does not have the Gd leak simulated in the GC. However from figure A.6, it can be appreciated that in the center of the detector, where the

Gd concentration is around 1 g/l, it is needed a huge change in the Gd concentration to observe a variation in the Gd capture fraction. The smallest Gd concentration in the volume, a change in the concentration implies bigger variation in the Gd fraction. In fact in the GC, where the Gd concentration is small, an increase of Gd means a strong variation in the Gd fraction.

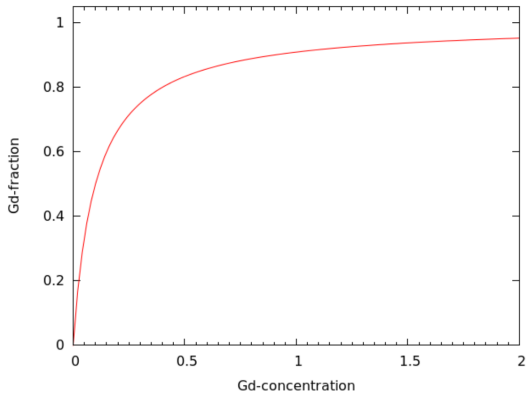

Figure A.6: Fraction of neutrons captured on Gd vs Gd concentration in g/l.

The systematic uncertainty for the data to MC correction factors are estimated from the difference between FD and ND correction factor results. The 0.19% discrepancy also covers the discrepancies between energy and time correlation variation results.

The final results for the GdF ratios, including systematics errors, are summarized in table A.11.

Table A.11: Gadolinium fraction ratios for the ^{252}Cf source including statistical and systematic errors.

$R_{f_{Gd}}$(Data:MC)	FD:FD	ND:ND
	0.9767 ± 0.0020	0.9748 ± 0.0020
$R_{f_{Gd}}$(Data:Data)	FD:ND	
	1.0025 ± 0.0008	

The total uncertainties are estimated in order to be dominated by the systematic bias produced by the discrepancy between detectors. In that way, the proposed results for GdF ratios data to MC are in agreement between them considering the total uncertainty.

A.2.2 Crosscheck with IBD antineutrinos

As a crosscheck of the results shown in section A.2.1, a similar analysis of the Gd fraction has been carried out using the neutrons from the IBD reaction. However the Gd-fraction definition (eq. A.10) needs to be optimized in terms of signal to background ratio, since there are differences in the signal selection cuts depending

on the chosen sample. The Gd fraction definition for the IBD events are:

$$f_{Gd}^{IBD} = \frac{N(3.5\ MeV < E_{delayed} < 10MeV \cap 0.5\ \mu s < \Delta T < 150\ \mu s \cap \Delta R < 1\ m)}{N(1.6\ MeV < E_{delayed} < 10\ MeV \cap 0.5\ < \Delta T < 150\ \mu s \cap \Delta R < 1\ m)} \tag{A.11}$$

Moreover a cut in the prompt energy $1 < E_{prompt} < 8.5$ MeV and the TnC vetoes used in the TnC efficiency definition eq.6.4 are also included in this definition. To avoid border effects and to be consistent with the Cf source analysis in which only the data taken at the center of the detector is used, a fiducial volume of 800 cm around the target is required ($\rho < 0.8$ m and $z < 0.8$ m). With this definition, the ratios data to data and data to MC are summarized in table A.12.

Table A.12: Gadolinium fraction ratios for the antineutrino source. Only statistical errors are shown.

$R_{f_{Gd}}$(Data:MC)	FD:FD	ND:ND
	0.9811 ± 0.0034	0.9814 ± 0.0023
$R_{f_{Gd}}$(Data:Data)	FD:ND	
	0.9985 ± 0.0034	

The results for the GdF correction factors obtained with the ^{252}Cf source and the IBD samples are consistent within errors, although it can be easily appreciated that the GdF calculated with the second method suffers from a poor statistics and cannot compete with the high statistics of the radioactive source.

A.3 Spill-in/out

In the Gd-only analysis, the NT volume acts as the fiducial volume for the IBD selection using neutron captures on Gd-nuclei. The energy dependence in the neutron capture cross sections causes that neutrons need to slow down until they can be captured in the detector. When an IBD neutron is captured on a different volume where it was created, the so called spill event appears. It can occur for neutrons produced in the NT and captured in the GC (spill-out), and for IBD processes on the GC where the neutron is captured in the NT (spill-in) as can be seen in figure A.7. These events do not cancel out, and need to be evaluated in the neutron detection efficiency. This term ϵ_{spill} is evaluated with a low energy neutron physics modeling, developed with a Monte Carlo simulation.

The number of detected events in the ν-target that pass the IBD selection in the simulation can be written as:

$$N_{det} = \epsilon_{det}(N^T - N^{SO}) + N_{det}^{SI} + N_{det}^{SO} \tag{A.12}$$

where N^T is the number of IBD interactions in the ν-target, N^{SO} is the number of spill-out events, N_{det}^{SI} is the number of spill-in events passing the Gd selection and N_{det}^{SO} is the number of the IBD interactions in the ν-target in which the neutron was

captured outside it but passes the Gd selection anyway. ϵ_{det} is the detection efficiency of the neutrons produced and captured within the ν-target, and it is defined as the product of the Gd fraction and the selection efficiency obtained with the Geant4 simulation, which are corrected using the factors computed in the previous sections to match the data.

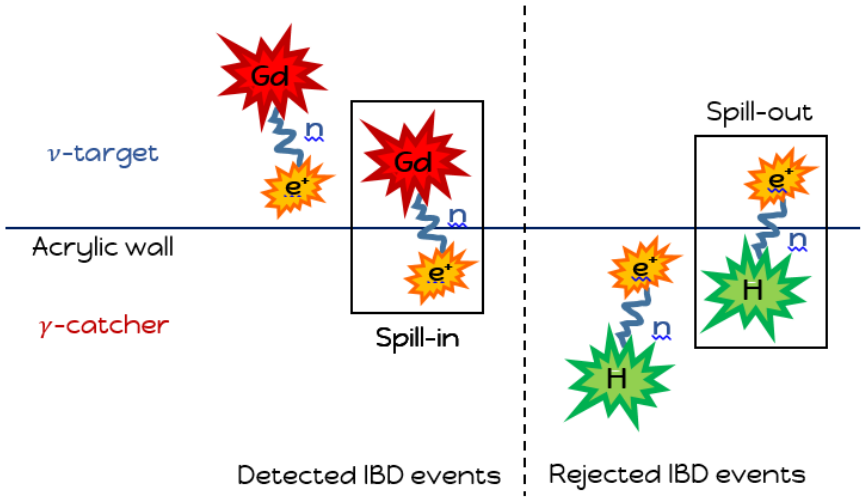

Figure A.7: Illustration of the spill in/out border effect.

Equation A.12 can be rewritten as:

$$N_{\text{det}} = \epsilon_{\text{det}} \cdot N^T (1 + \phi_{\text{det}}^{\text{spill}}) \tag{A.13}$$

where

$$\phi_{\text{det}}^{\text{spill}} \equiv \frac{1}{N^T} \left(\frac{N_{\text{det}}^{SI} + N_{\text{det}}^{SO}}{\epsilon_{\text{det}}} - N^{SO} \right) \tag{A.14}$$

This way there is a correction of the number of the detected events in the target due to the neutron mobility factor. The term $\phi_{\text{det}}^{\text{spill}}$ is equivalent to the factor ϵ_{spill} in section A.1.

To obtain this factor, two MC have been performed. The first one uses the Geant4's NeutronHPElastic code [160, 161] to simulate the neutron resulting of the IBD interaction with a kinetic energy in the range of tens of keV and then the loss of this energy in the elastic scatterings until the neutron approaches to the thermalization range. However if the neutron kinetic energy falls below 4eV, the interaction with H nuclei is substituted by the NeutronTH model which is the Double Chooz custom implementation of the low energy neutron scattering [162, 163]. These MCs are compared again Tripoli4 [164], a code specifically designed for the simulation of the low energy neutron transport.

The detected spill current ϕ^{spill} is found to be 2.08% using the Geant4-NeutronTH simulation and 2.36% using the Tripoli4 simulation. Since the NeutronTH code describes well enough the neutron thermalization, no correction factor was considered necessary, but the discrepancy between both simulations is taken as the normalization uncertainty induced by the spill effect.

$$R_{\epsilon_{\text{spill}}} = 1.0000 \pm 0.0027 \tag{A.15}$$

A.4 Gd-only Detection Efficiency Summary

In a similar way as was done in the last Gd-only publication of the Double Chooz collaboration [131], the final Gd-only detection efficiency correction factors data to MC are shown in table A.13.

Table A.13: Compilation of the MC efficiency correction factors and their uncertainties due to detection efficiency for the Gd-only selection

	FD-I:MC	FD-II:MC	ND:MC
IBD Selection Efficiency (%)	100.01 ± 0.19	100.09 ± 0.30	99.76 ± 0.50
Gd Fraction (%)	97.67 ± 0.20	97.67 ± 0.20	97.48 ± 0.20
Spill in/out (%)	100.00 ± 0.27	100.00 ± 0.27	100.00 ± 0.27

Appendix B

TnC Selection Efficiency maps

B.1 IBD candidates distributions

The delayed energy spectra B.1 and temporal B.2 and spatial coincidence distributions B.3 for data, MC and accidentals are shown on the following figures for the FD-I, FD-II and ND. The events passing the IBD selection, that is, the numerator cuts of equation 6.4 are shown in the left part (ANN>0.85 for FD and ANN>0.86 for ND) while the events passing the open conditions of the denominator are displayed on the right part of each figure. The comparison between the signal, once the accidental sample has been removed, and MC shows a very good agreement, validating that the accidental sample has been well subtracted.

From the plots of the E_{del} distributions (fig. B.1), it can be appreciated that the ANN>0.85 or ANN>0.85 cut makes that all events in the region between ∼2.8-3.5 MeV are rejected due to the low signal-to-background ratio in this interval. This fact is not appreciated in the the plots in the right due to the looser cut in ANN>0.1. In all the distributions it can be seen that the accidental coincidences around the H peak energy are reduced due to the application of the ANN and they are well subtracted from data. Finally it is possible to observe that the accidental energy distribution is highly similar in FD-I and FD-II, validating the combination of both accidental correction factor as is done in table 6.2.

In figure B.2 it can be appreciated what was shown in section 6.3.1, i.e, the accidental distribution, previously to the application of the ANN was flat, but the ANN causes that the accidental background at high ΔT is mostly rejected but at low ΔT they are classified as antineutrino-like event, given to the distribution certain slope.

Finally from the ΔR distributions in figure B.3, the conclusion extracted falls on the fact that the ANN>0.85 or 0.86 rejects the majority of accidental events above 900 mm.

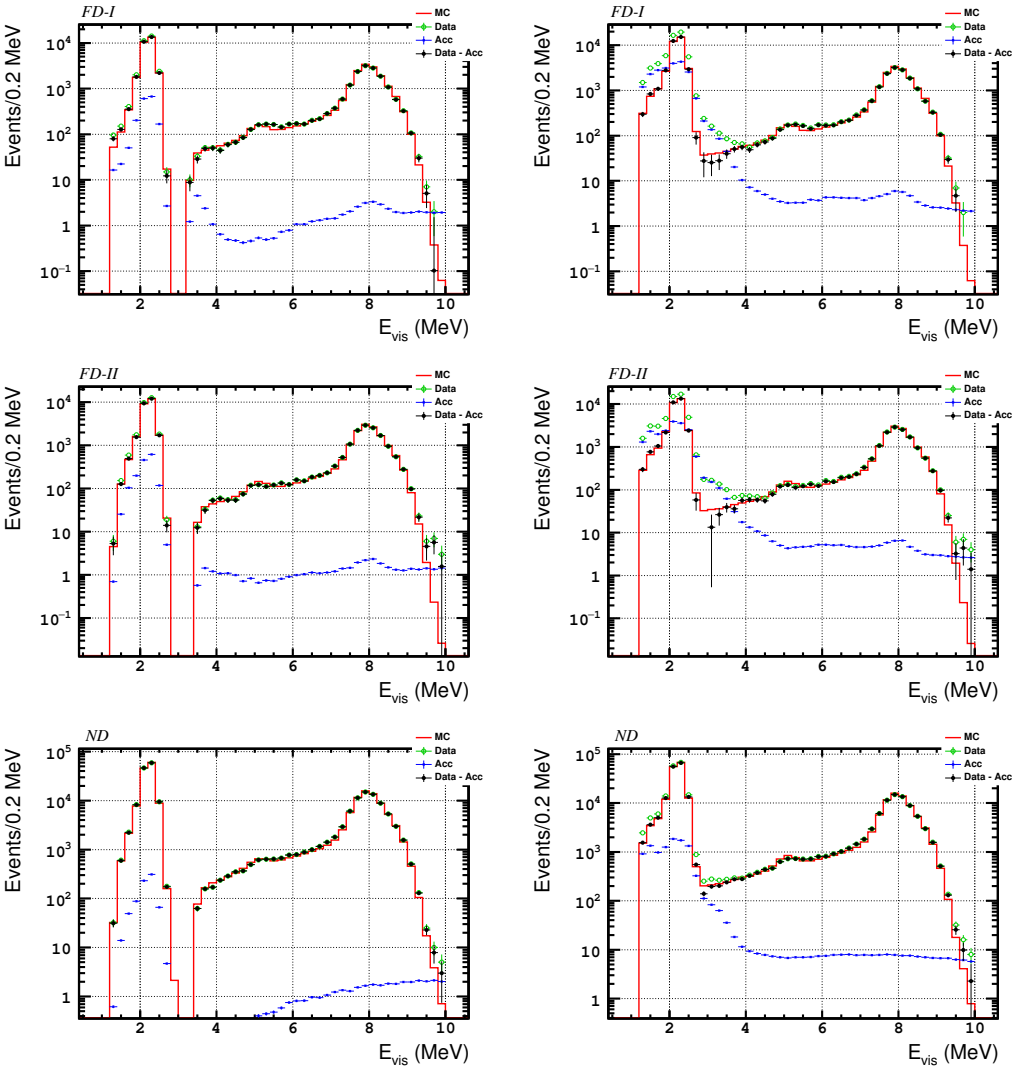

Figure B.1: Delayed energy distributions. The common pattern of the figures is the following: FD-I distributions in the upper row, FD-II in the central row and finally ND distributions in the last row. Left plots show the events passing the numerator of equation 6.4 while right plots represent the events passing the denominator. Neutrino candidates are shown as empty green circles and accidentals as blue squares. Black points represent the final distribution for the IBD signal once the accidentals have been subtracted. The MC distribution is shown as the red histogram and has been normalized to the integral of the final data sample.

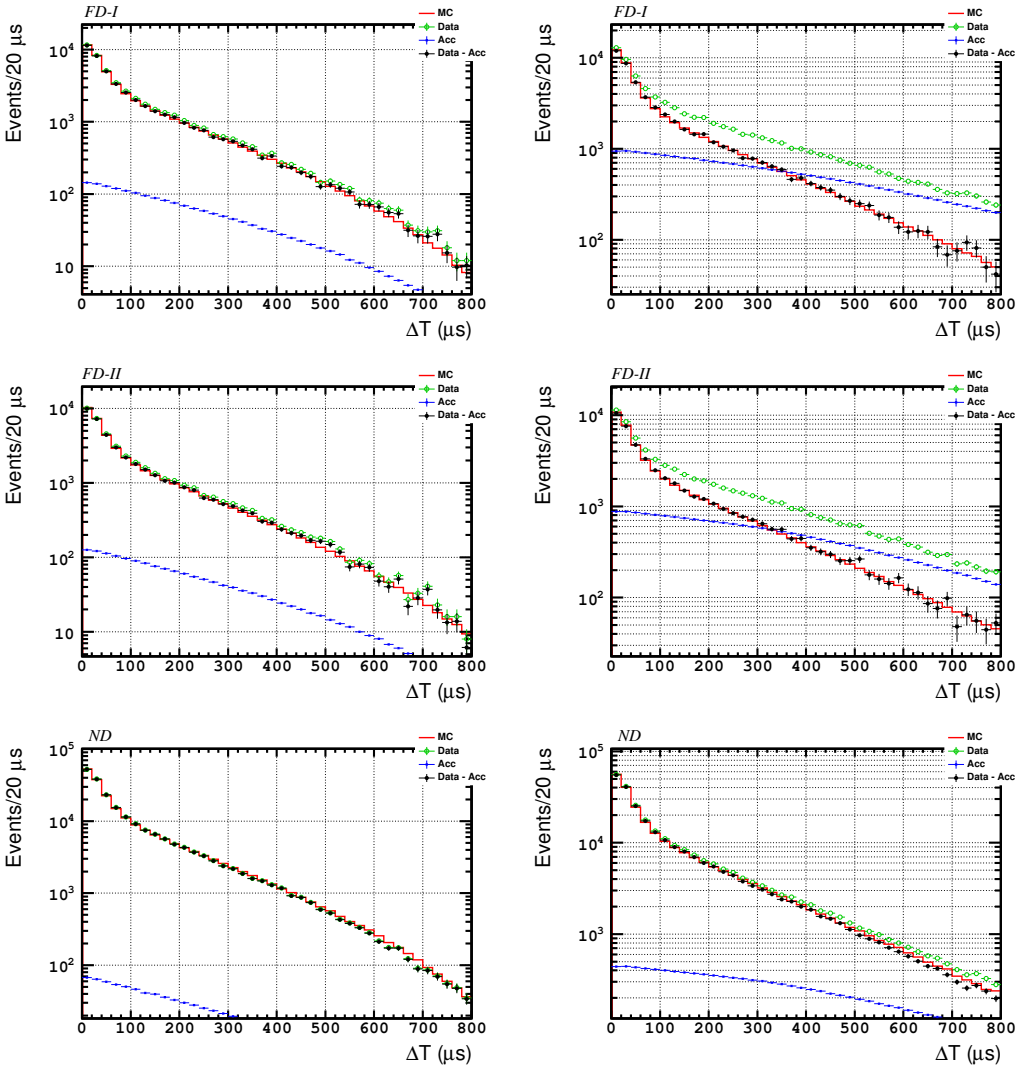

Figure B.2: Distributions of the prompt-delayed trigger time interval. Colours and markers follow the ones of figure B.1

.

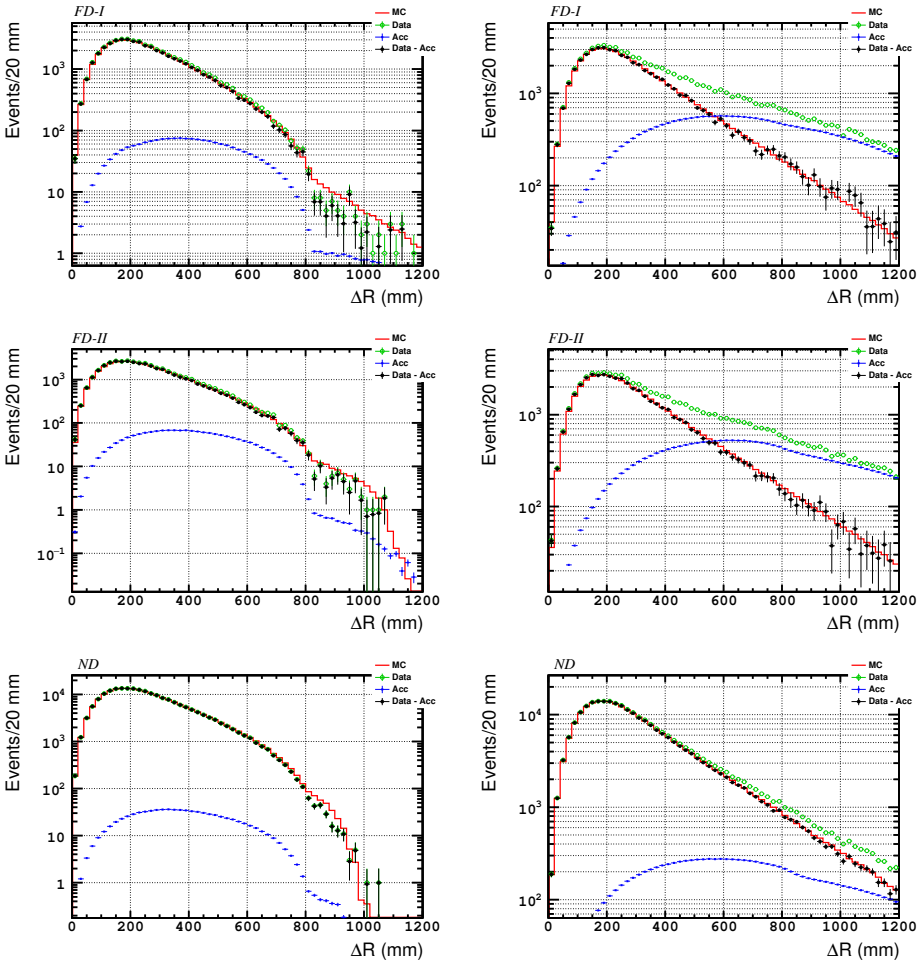

Figure B.3: Distribution of the prompt-delayed reconstructed vertex distance. Colours and markers follow the ones of figure B.1

.

B.2 Selection Efficiency maps

B.2.1 2D maps

The major advantage of these IBD neutrons is that they are produced homogeneously inside the detector, so they are especially well-suited for a direct measurement of the volume-wide detector performance, allowing to study the different response between data and MC. In figures B.4-B.6, the selection efficiency can be seen as a function of the spatial variables ρ and z for all detectors, comparing the data with accidentals subtracted (left plots) to the MC sample (right plots). There is a good agreement between data and MC maps, although it can be noticed that the last ones have 100 times more statistics than data in the case of the FD-I and FD-II, and 10 times more in the case of the ND.

If the integration volume was reduce only to the center of the target, the efficiency would be higher than in the full volume. The explanation falls on the fact that in the GC the H captures predominate, which have larger ΔT and the ANN cuts more events with shorter ΔT. In figure B.7 are shown the accidental background events divided in 3 regions of delayed energy. The first region corresponds to E_{del}<3 MeV (H captures) and can be seen that these events remain up until ΔT $\sim$ 800μs, while events corresponding to Gd captures (E_{del}>6 MeV) are fully rejected above ΔT > 600μs. This behaviour is the same as the one seen in figure 6.5.

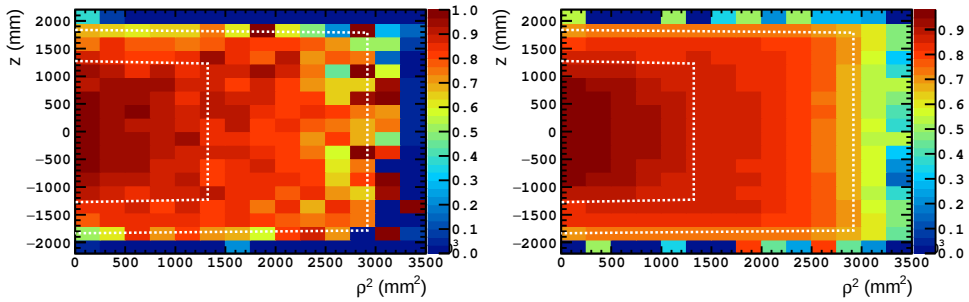

Figure B.4: Selection efficiency maps for FD-I. IBD candidates once the accidental background is subtracted are shown on the left and the antineutrino MC in the right plot. The inner dashed line delimits the Target. The outer dashed line demarcates the Gamma Catcher.

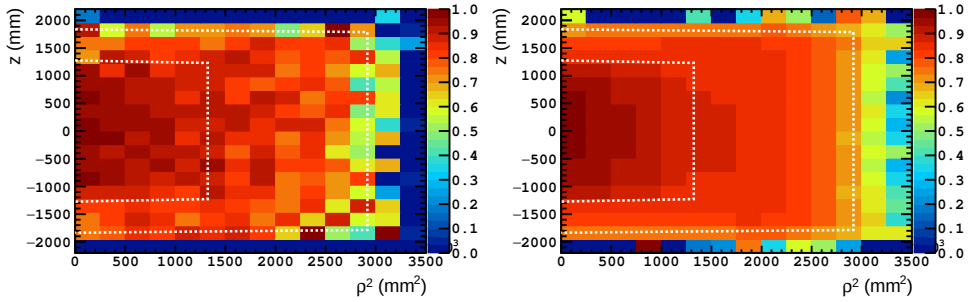

Figure B.5: Selection efficiency maps for FD-II.

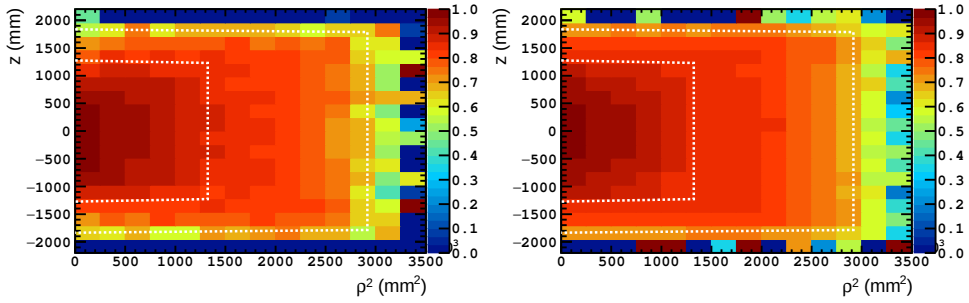

Figure B.6: Selection efficiency maps for ND.

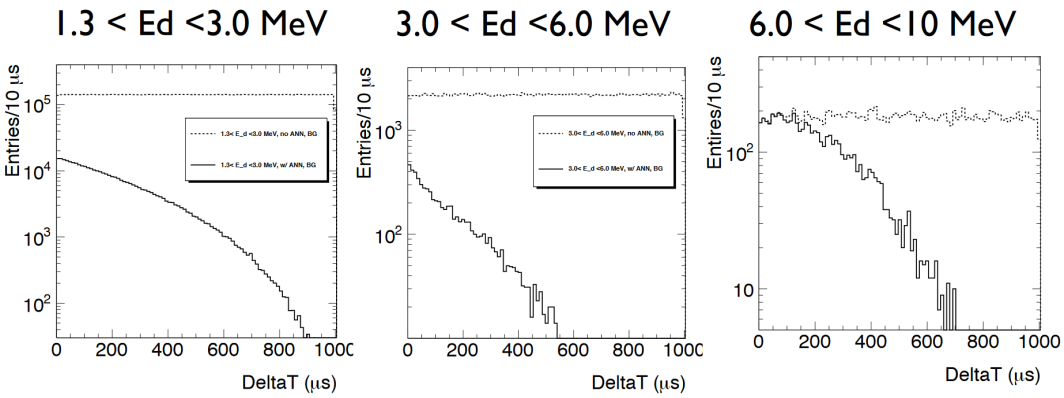

Figure B.7: ΔT distribution for accidental background events in 3 different delayed energy ranges before (dotted line) and after (solid line) applying the ANN cut. From [168]

B.2.2 ρ and z efficiency projections

Further investigations about the agreement between data and MC for each detector (data to MC comparison, figure 6.6) as well as between data for different detectors (data to data comparison, figure 6.8) can be done studying selection efficiency variations along the z dimension or the ρ^2 axis.

B.2.2.1 Data to MC comparison

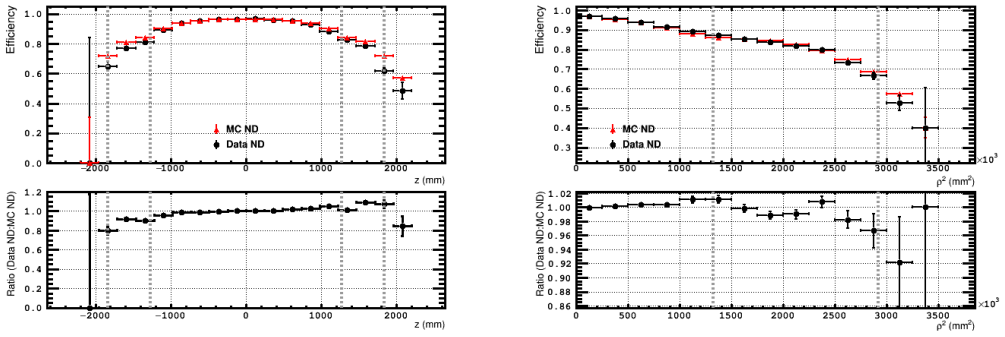

Figure B.8: Selection efficiency projections onto z (left plot) and ρ^2 (right plot) axes for ND data and MC. Data with accidentals subtracted is represented as black circles, MC as red triangles. The inner (outer) pair of dashed lines enclose the Target (GC). The agreement between data and MC can be seen in the bottom plot, where the ratio between both is represented, being close to 1.

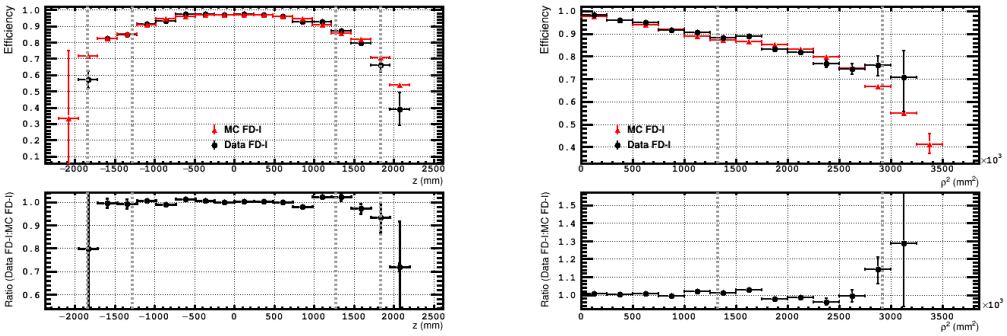

Figure B.9: Selection efficiency projections onto z and ρ^2 axes for FD-I data and MC.

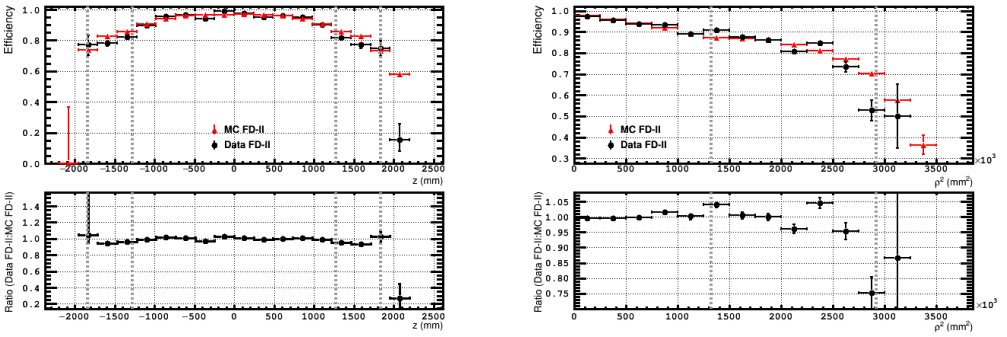

Figure B.10: Selection efficiency projections onto z and ρ^2 axes for FD-II data and MC.

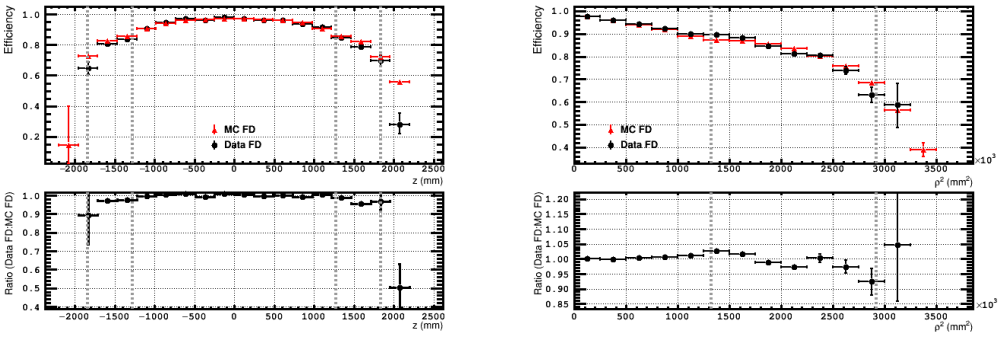

Figure B.11: Efficiency map projections onto z and ρ^2 axes for FD (combination of FD-I and FD-II) data and MC.

B.2.2.2 Data to Data comparison

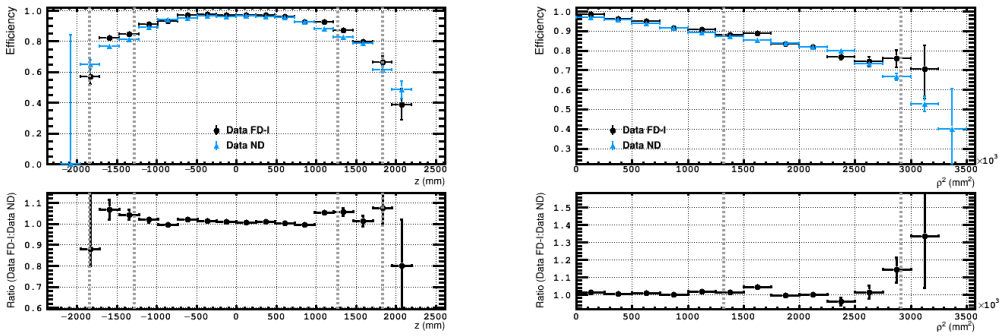

Figure B.12: Selection efficiency projections onto z and ρ^2 axes. FD-I (black circles) and ND (blue triangles) data have accidental background subtracted. The inner (outer) pair of dashed lines enclose the Target (GC).

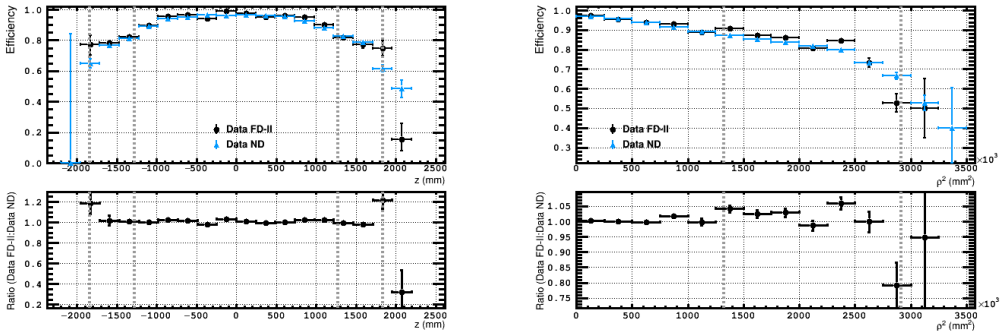

Figure B.13: Selection efficiency projections onto z and ρ^2 axes for FD-II and ND data.

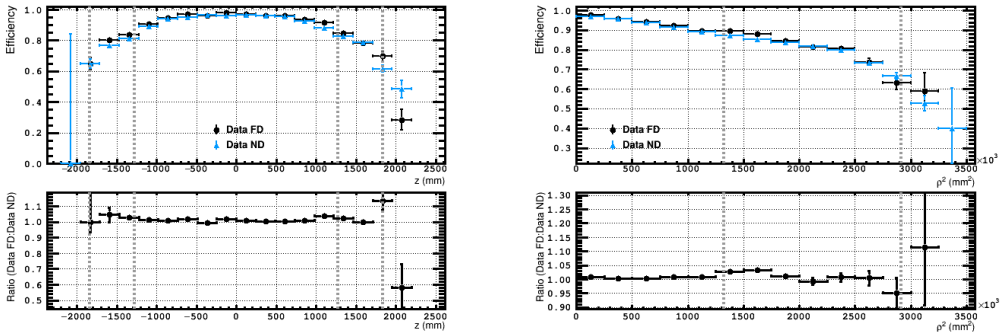

Figure B.14: Selection efficiency projections onto z and ρ^2 axes for FD combined and ND data.

Appendix C

Proton Number Uncertainty

To calculate the uncertainties and correlations of the numbers referring as Proton Number in table 6.13, several steps have been followed.

First of all, it is needed to know the uncertainties of the proton numbers coming from NT and GC weight measurements and the correlations between volumes. The number of protons are calculated as:

$$N_p = \frac{f_H \cdot M_{liquid}}{m_H} \tag{C.1}$$

where n_H is the proton number, f_H is the hydrogen mass fraction, m_H is the hydrogen mass and M_{liquid} is the liquid mass.

In the case of the target, the liquids for FD and ND are coming from the same batch and only one measurement of the f_H was performed, so both the near and the far use the same central value of f_H (f_H(ND)=f_H(FD)) and the same associated uncertainty, being fully correlated. However the liquid mass estimation M_{liquid} is based on the uncorrelated mass measurement between ND and FD. From [169], the next parameters values are obtained:

$$\begin{aligned} f_H(NT) = &= 0.1360 \pm 0.0004 \rightarrow \sigma_{relative} = 0.0004/0.1360 \cdot 100 = 0.29\% \\ M^{ND}_{liquid}(NT) &= (8326.5 \pm 3.8)kg \rightarrow \sigma_{relative} = 0.05\% \\ M^{FD}_{liquid}(NT) &= (8291.5 \pm 7.3)kg \rightarrow \sigma_{relative} = 0.09\% \end{aligned} \tag{C.2}$$

To calculate the correlated and uncorrelated part and the correlation between two variables, the following formulas have been taken into account:

$$(\sigma^{\text{tot}})^2 = (\sigma^{\text{cor}})^2 + (\sigma^{\text{unc}})^2 \tag{C.3}$$

$$\rho_{X:Y} = \frac{\sigma^{\text{cor}}_X \sigma^{\text{cor}}_Y}{\sigma^{\text{tot}}_X \sigma^{\text{tot}}_Y} = \sqrt{\left(1 - \frac{(\sigma^{\text{unc}}_X)^2}{(\sigma^{\text{tot}}_X)^2}\right)\left(1 - \frac{(\sigma^{\text{unc}}_Y)^2}{(\sigma^{\text{tot}}_Y)^2}\right)} \tag{C.4}$$

Taking into account these two equations C.3 and C.4, the uncertainties and correlations for the proton number in the target are shown in table C.1

Table C.1: Proton number uncertainties and correlations in the target.

NT		**ND**				**FD**	
	cor(%)	**uncor(%)**	**tot(%)**	ρ_{NDFD}	**cor(%)**	**uncor(%)**	**tot(%)**
f_H	0.29	0	0.29	1	0.29	0	0.29
M_{liquid}	0	0.05	0.05	0	0	0.09	0.09
Total(%)	0.29	0.05	**0.30**	**0.947**	0.29	0.09	**0.31**

In the case of the γCatcher, the liquids for FD and ND are coming from different batch. For each the near and the far GC, 10 measurements of f_H were performed [170] . These 20 measurements (10 for the near and 10 for the far) were performed with the same experimental setup and by consequence share a common correlated uncertainty. This common correlated uncertainty is of 1% . From [169], the next parameters values are obtained:

$$\begin{aligned} f_H^{ND}(GC) &= 0.14527 \pm 0.001464 \rightarrow \sigma_{relative} = 1.01\% \\ f_H^{FD}(GC) &= 0.14577 \pm 0.001462 \rightarrow \sigma_{relative} = 1.00\% \\ M_{liquid}^{ND}(GC) &= (18200.14 \pm 87.22)kg \rightarrow \sigma_{relative} = 0.48\% \\ M_{liquid}^{FD}(CG) &= (18056.22 \pm 78.99)kg \rightarrow \sigma_{relative} = 0.44\% \end{aligned} \tag{C.5}$$

Table C.2: Proton number uncertainties and correlations in the GC.

GC		**ND**				**FD**	
	cor(%)	**uncor(%)**	**tot(%)**	ρ_{NDFD}	**cor(%)**	**uncor(%)**	**tot(%)**
f_H	1.00	0.12	1.01	0.990	1.00	0.08	1.00
M_{liquid}	0	0.48	0.48	0	0	0.44	0.44
Total(%)	1.00	0.49	**1.12**	**0.819**	1.00	0.44	**1.10**

So finally the relative proton number uncertainty used for this analysis is 0.30% for ND target, 0.31% for FD target, 1.12% for ND γCatcher and 1.10% for FD γCatcher.

C.1 Inputs for the fit

There are two important numbers that are introduced in the fit. In the first place one need to know the total uncertainty induced by the proton number on the IBD measurement in the full detector volume and secondly the correlation between the near and the far IBD signals, which depends on the contribution of each volume to the total number of interactions. As an example, here is detailed the calculation for the FD-II.

The relative uncertainty on the IBD signal associated to the proton number can

be calculated using:

$$\sigma_{tot}(N_p) = \sqrt{\sum_i \left(\frac{\sigma^i_{Np}}{Np^i} w_i\right)^2} \tag{C.6}$$

being w_i the proportion of IBD interactions that occurs in the different volumes of each detector listed in table C.3 [173]:

Table C.3: Proportion of IBD interactions (w_i) in percent in each volume of the detector from the MC.

	ND	FD-I	FD-II
Target	41.014	41.021	40.730
GC	58.258	58.225	58.529
Target tank	0.513	0.533	0.521
GC tank	0.134	0.139	0.138
Buffer	0.080	0.082	0.083

So for FD-II:

$$\sigma_{tot}(N_p) = \sqrt{\left(0.31\frac{40.730}{100}\right)^2 + \left(1.10\frac{58.529}{100}\right)^2} = 0.65\%$$

The uncertainty induced by the NT and γCatcher will be:

$$\sigma_{NT}(N_p) = \sqrt{\left(0.31\frac{40.730}{100}\right)^2} = 0.12\%$$

$$\sigma_{GC}(N_p) = \sqrt{\left(1.10\frac{58.529}{100}\right)^2} = 0.64\%$$

To calculate correlation between volumes and detectors, it is needed to understand the correlated and uncorrelated part of these two uncertainties. For this, the numbers from tables C.1 and C.2 are considered:

$$\sigma^{cor}_{NT}(N_p) = \sqrt{\left(0.29\frac{40.730}{100}\right)^2} = 0.12\% \qquad \sigma^{uncor}_{NT}(N_p) = \sqrt{\left(0.09\frac{40.730}{100}\right)^2} = 0.04\%$$

$$\sigma^{cor}_{GC}(N_p) = \sqrt{\left(1.00\frac{58.529}{100}\right)^2} = 0.59\% \qquad \sigma^{uncor}_{GC}(N_p) = \sqrt{\left(0.44\frac{58.529}{100}\right)^2} = 0.26\%$$

And the correlated and uncorrelated uncertainty in the full volume:

$$\sigma^{cor}_{tot}(N_p) = \sqrt{(\sigma^{cor}_{NT})^2 + (\sigma^{cor}_{GC})^2} = \sqrt{0.12^2 + 0.59^2} = 0.60\%$$

$$\sigma^{uncor}_{tot}(N_p) = \sqrt{(\sigma^{uncor}_{NT})^2 + (\sigma^{uncor}_{GC})^2} = \sqrt{0.04^2 + 0.26^2} = 0.26\%$$

Analogously a similar calculation has been followed to compute ND and FD-I numbers.

Table C.4: Total, correlated and uncorrelated proton number relative uncertainties for FD-II and ND.

	$\sigma_{tot}\%$	$\sigma_{tot}^{cor}\%$	$\sigma_{tot}^{uncor}\%$
FD-II	0.65	0.26	0.60
ND	0.66	0.29	0.59

Table C.5: Total, correlated and uncorrelated proton number relative uncertainties.

	$N_p\%$	$\sigma_{tot}\%$	$\sigma_{tot}^{cor}\%$	$\sigma_{tot}^{uncor}\%$
FD-I	99.58	0.65	0.60	0.26
FD-II	99.61	0.65	0.60	0.26
ND	99.88	0.66	0.29	0.59

To calculate correlation coefficients, the formula C.4 is used. As an example the correlation between ND and FD-II is shown:

$$\rho_{\text{ND:FD-II}} = \frac{0.60 \cdot 0.60}{0.66 \cdot 0.66} = 0.824 \tag{C.7}$$

So finally the inputs for the fit are resume below in table C.5:
More details of these calculations can be found on [174].

Bibliography

[1] J. Chadwick, *Verh. der Deutschen Physikalischen Ges.* **16**, 383 (1914)

[2] W. Pauli. *Phys. Today* **31N9** 27 (1978)

[3] J. Chadwick, *Nature* **129**, 312 (1932)

[4] E. Fermi, *Z. Phys.* **88**, 161 (1934)

[5] H. Bethe and R. Peierls, *Nature* **133**, 532 (1934)

[6] F. Reines and C. L. Cowan, *Phys. Rev.* **92** 830 (1953)

[7] C. L. Cowan, F. Reines, F. B. Harrison, H. W. Kruse and A. D. McGuire, *Science* **124**, 103 (1956)

[8] `https://en.wikipedia.org/wiki/File:Standard_Model_of_Elementary_Particles.svg`

[9] P. Higgs, *Phys. Rev. Lett.* **13**, 508 (1964)

[10] M. Gell-Mann, P. Ramond, and R. Slansky, *Proceedings: Supergravity Workshop Stony Brook*, New York, September 27-28, 1979, pp. 315–321. arXiv:1306.4669 (1979)

[11] T. Yanagida, *Proceedings: Workshop on the Unified Theories and the Baryon Number in the Universe*, Tsukuba, Japan, 13-14 Feb 1979, pp. 95–99, (1979)

[12] G. Kane, *The Dawn of Physics Beyond the Standard Model*, *Scientific American* (2003)

[13] A. Osipowicz *et al.*, (KATRIN Collaboration), arXiv:0109033 (2001)

[14] C. Kraus *et al.*, (Mainz Collaboration), *Eur. Phys. J. C* **40**, 447 (2005)

[15] V. N. Aseev *et al.*, (Troitsk Collaboration), *Phys. Rev. D* **84**, 112003 (2011)

[16] D. Parno, (KATRIN Collaboration), *"KATRIN: Toward a High-Precision Neutrino-Mass Determination with Tritium"*, talk at XXVIII International Conference on Neutrino Physics and Astrophysics, 4-9 June 2018, Heidelberg, Germany, `http://doi.org/10.5281/zenodo.1287933` (2018)

[17] G. Rybka, (Project-8 Collaboration), *"Project 8: Progress Towards using Cyclotron Radiation Emission Spectroscopy on Atomic Tritium for a Neutrino Mass Measurement"*, talk at XXVIII International Conference on Neutrino Physics and Astrophysics, 4-9 June 2018, Heidelberg, Germany, `http://doi.org/10.5281/zenodo.1286954` (2018)

[18] L. Gastaldo, *"Determining the Electron Neutrino Mass with Ho-163"*, talk at XXVIII International Conference on Neutrino Physics and Astrophysics, 4-9 June 2018, Heidelberg, Germany, `http://doi.org/10.5281/zenodo.1286950` (2018)

[19] P. Springer, C. Bennett and P. Baisden, *Phys.Rev. A* **35**, 679 (1987)

[20] E. Majorana, *Nuovo Cim.* **14**, 171 (1937)

[21] W. H. Furry, *Phys. Rev.* **56**, 1184 (1939)

[22] M. Agostini *et al.*, (GERDA Collaboration), *Phys.Rev.Lett.* **120**, 132503 (2018)

[23] O. Azzolini *et al.*, (CUPID-0 Collaboration), *Phys.Rev.Lett.* **120**, 232502 (2018)

[24] C. Alduino *et al.*, (CUORE Collaboration), *Phys.Rev.Lett.* **120**, 132501 (2018)

[25] A. Gando *et al.*, (KamLAND-Zen Collaboration), *Phys.Rev.Lett.* **117**, 082503 (2016)

[26] C. Giunti, *Nucl. Phys. B* **908**, 336 (2016)

[27] N. Aghanim *et al.*, (Planck Collaboration), arXiv:1807.06209 (2018)

[28] B. Pontecorvo, *Zh. Eksp. Teor. Fiz.* **33**, 549 (1957)

[29] Z. Maki, M. Nakagawa, and S. Sakata, *Prog. Theor. Phys.,* **28**, 870880 (1962)

[30] M. Blennow, A. Yu. Smirnov, *Adv. High Energy Phys.* **2013**, 972485 (2013)

[31] D. Davis Jr, D.S. Harmer and K. C. Hoffman, *Phys. Rev.* **20**, 1205 (1968)

[32] J. N. Bahcall, A. M. Serenelli and S. Basu, *Astrophys. J.* **621**, L85 (2005)

[33] P. Anselmann *et al.*, (GALLEX Collaboration), *Phys. Lett. B* **285**, 376 (1992)

[34] A. I. Abrazov *et al.*, (SAGE Collaboration), *Phys. Rev. Lett.* **67**, 3332 (1991)

[35] K. S. Hirata *et al.*, (KAMIOKANDE-II Collaboration), *Phys. Rev. Lett.* **63**, 16 (1989)

[36] S. Fukuda *et al.*, (Super-Kamiokande Collaboration), *Phys. Rev. Lett.* **86**, 5651 (2001)

[37] S. Fukuda *et al.*, *Phys. Lett. B* **539**, 179 (2002)

[38] B. Aharmin *et al.*, (SNO Collaboration), *Phys. Rev. C* **72**, 055502 (2005)

[39] G. Bellini *et al.*, (Borexino Collaboration), *Phys. Rev. Lett.* **108**, 051302 (2012)

[40] G. L. Fogli et al., *Phys. Rev. D***67**, 073002 (2003); M. Maltoni, T. Schwetz, and J.W. Valle, *Phys. Rev. D* **67**, 093003 (2003); A. Bandyopadhyay *et al.*, *Phys. Lett. B* **559**, 121 (2003); J.N. Bahcall, M.C. Gonzalez-Garcia, and C. Pea-Garay, *JHEP* **0302**, 009 (2003); P.C. de Holanda and A.Y. Smirnov, *JCAP* **0302**, 001 (2003)

[41] A. Gando *et al.*, (KamLAND Collaboration), *Phys. Rev. D* **88**, 033001 (2013)

[42] I. Esteban *et al.*, *JHEP* **1701**, 087 (2017)

[43] K. S. Hirata *et al.*, (Kamiokande Collaboration), *Phys. Lett. B* **335**, 237 (1994)

[44] D. Casper *et al.*, (IMB Collaboration), *Phys. Rev. Lett.* **66**, 2561 (1991)

[45] Y. Fukuda *et el.* (Super-Kamiokande Collaboration), *Phys. Rev. Lett.* **81**, 1562 (1998)

[46] M. Tanabashi *et al.*, (Particle Data Group), *Phys. Rev. D* **98**, 030001 (2018)

[47] M. Ambrosio *et al.*, (MACRO Collaboration), *Phys. Lett. B* **434**, 451 (1998)

[48] M. Sanchez *et al.*, (Soudan-2 Collaboration], *Phys. Rev. D* **68**, 113004 (2003)

[49] S. Adrian-Martinez *et al.*, (ANTARES Collaboration), *Phys. Lett. B* **714**, 224 (2012)

[50] M. G. Aartsen *et al.*, (IceCube Collaboration), *Phys. Rev. Lett.* **111**, 081801 (2013)

[51] M. H. Ahn *et al.*, (K2K Collaboration), *Phys. Rev. D* **74**, 072003 (2006)

[52] D. G. Michael *et al.*, (MINOS Collaboration), *Phys. Rev. Lett.* **97**, 191801 (2006)

[53] K. Abe *et al.*, (T2K Collaboration), *Phys. Rev. D* **85**, 031103 (2012)

[54] P. Adamson *et al.*, (NOνA Collaboration), *Phys. Rev. D* **93**, 051104 (2016)

[55] R. B. Patterson (NOνA Collaboration), *Nucl. Phys. (Proc. Supp.) B* **235-236**, 151 (2013)

[56] K. Abe *et al.*, (T2K Collaboration), *Phys. Rev. D* **96**, 092006 (2017)

[57] M. A. Acero *et al.*, (NOνA Collaboration), *Phys. Rev. D* **98**, 032012 (2018)

[58] P. Adamson *et al.*, (MINOS Collaboration), *Phys. Rev. Lett.* **112**, 191801 (2014)

[59] K. Abe *et al.*, (Super-Kamiokande Collaboration), *Phys. Rev. D* **97**, 072001 (2018)

[60] M. G. Aartsen *et al.*, (IceCube Collaboration), *Phys. Rev. Lett.* **120**, 071801 (2018)

[61] K. Abe *et al.*, (T2K Collaboration), *Phys. Rev. Lett.* **107**, 041801 (2011)

[62] P. Adamson *et al.*, (MINOS Collaboration), *Phys. Rev. Lett* **107**, 181802 (2011)

[63] P. Vogel, L. Wen and C. Zhang, *Nature Commun.* **6**, 6935 (2015)

[64] M. Appolinio *et al.*, (CHOOZ Collaboration), *PEur. Phys. J. C* **27**, 331 (2003)

[65] F. Boehm *et al.*, (Palo Verde Collaboration), *Phys. Rev. D* **64**, 112001 (2001)

[66] Y. Abe *et al.*, (Double Chooz Collaboration), *Phys. Rev. Lett.* **108**, 131801 (2012)

[67] F. P. An *et al.*, (Daya Bay Collaboration), *Phys. Rev. Lett.* **108**, 171803 (2012)

[68] J. K. Ahn *et al.*, (RENO Collaboration), *Phys. Rev. Lett.* **108**, 191802 (2012)

[69] A. Cucoanes, P. Novella, A. Cabrera, M. Fallot, A. Onillon, M. Obolensky and F. Yermia, arXiv:1501.00356 (2015)

[70] P.F. de Salas, D.V. Forero, C.A. Ternes, M. Tórtola, J.W.F. Valle, *Physics Letters B* **782**, 633 (2018)

[71] NuFIT 4.0 (2018), `www.nu-fit.org` I. Esteban, M.C. Gonzalez-Garcia, A. Hernandez-Cabezudo, *et al. J. High Energ. Phys.* **2019**, 106 (2019)

[72] Y.-F. Li, *Int. J. Mod. Phys.*: Conf. Ser. **31**, 1460300 (2014)

[73] R. Acciarri *et al.*, (DUNE Collaboration), arXiv:1601.05471 (2016)

[74] M. Freund, *Phys. Rev. D* **64**, 053003 (2001)

[75] Morgan Wascko, *"T2K Status, Results, and Plans"*, talk at XXVIII International Conference on Neutrino Physics and Astrophysics, 4-9 June 2018, Heidelberg, Germany, `http://doi.org/10.5281/zenodo.1286752` (2018)

[76] B. Abi *et al.*, (DUNE Collaboration), arXiv:1807.10334 (2018)

[77] Mayly Sanchez, *"NOvA Results and Prospects"*, talk at XXVIII International Conference on Neutrino Physics and Astrophysics, 4-9 June 2018, Heidelberg, Germany, `http://doi.org/10.5281/zenodo.1286758` (2018)

[78] P. F. De Salas, S. Gariazzo, O. Mena, C. A. Ternes and M. Tórtola, arXiv:1806.11051 (2018)

[79] C. Adams *et al.*, arXiv:1307.7335 (2013)

[80] K. Abe *et al.*, (Hyper-Kamiokande Collaboration), arXiv:1805.04163 (2018)

[81] Adam Aurisano, *"Recent Results from MINOS and MINOS+"*, talk at XXVIII International Conference on Neutrino Physics and Astrophysics, 4-9 June 2018, Heidelberg, Germany, `http://doi.org/10.5281/zenodo.1286760` (2018)

[82] S. Schael *et al.*, (SLD Electroweak Group, DELPHI, ALEPH, SLD, SLD Heavy Flavour Group, OPAL, LEP Electroweak Working Group, L3), *Phys. Rept.* **427**, 257 (2006)

[83] G. Mangano, G. Miele, S. Pastor, T. Pinto, O. Pisanti *et al.*, *Nucl. Phys. B* **729**, 221 (2005)

[84] C. Giunti, M. Laveder, *Phys. Rev. C*, **83**, 065504 (2011)

[85] A. Aguilar *et al.*, (LSND Collaboration), *Phys. Rev. D* **64**, 112007 (2001)

[86] B. Armbruster *et al.*, (KARMEN Collaboration) *Phys. Rev. D* **65**, 112001 (2002)

[87] A. A. Aguilar-Arevalo *et al.*, (MiniBooNE Collaboration), arXiv:1805.12028 (2018)

[88] G. Mention, M. Fechner, T. Lasserre, T. A. Mueller, D. Lhuillier, M. Cribier, A. Letourneau, *Physical Review D* **83**, 073006 (2011)

[89] N. Allemandou *et al.*, (STEREO Collaboration), *JINST* **13**, 07 (2018)

[90] I. Alekseev *et al.*, (DANSS collabortion), arXiv:1804.04046 (2018)

[91] Y. J. Ko *et al.*, (NEOS Collaboration), *Phys. Rev. Lett.* **118**, 121802 (2017)

[92] M. G. Aartsen *et al.*, (IceCube Collaboration), *Phys. Rev. D* **95**, 112002 (2017)

[93] P. Adamson *et al.*, (NOνA Collaboration), *Phys. Rev. D* **96**, 072006 (2017)

[94] F. P. An *et al.*, (Daya Bay Collaboration), *Phys. Rev. Lett.* **113**, 141802 (2014)

[95] M. Dentler *et al.*, *JHEP* **1808**, 010 (2018)

[96] M. Vivier, *Geodetic survey results*, Double Chooz Internal **DC-doc-6286** (2015)

[97] P. Vogel and J. F. Beacom, *Phys. Rev. D* **60**, 053003 (1999)

[98] D. H. Wilkinson, *Nucl. Instrum. Meth. A* **404**, 305 (1998)

[99] A. Pichlmaier, V. Varlamov, K. Schreckenbach and O. Geltenbort, *Phys. Lett. B* **693**, 221 (2010)

[100] C. Aberle, C. Buck, B. Gramlich, F. X. Hartmann, M. Lindner, S. Schönert, U. Schwan, S. Wagner and H. Watanabe, *JINST* **7**, P06008 (2012)

[101] Y. Abe *et al.*, (Double Chooz Collaboration), *Phys. Rev. Lett. B* **723**, 66 (2013)

[102] Y. Abe *et al.*, (Double Chooz Collaboration), *JHEP* **1601**, 163 (2016)

[103] Hamamatsu Photonics KK, Large Photocathode Area Photomultiplier Tubes, `http://www.hamamatsu.com/jp/en/index.html`

[104] C.Bauer *et al.*, *JINST* **6**, P06008 (2011)

[105] T. Matsubara *et al.*, *Nucl. Instrum. Meth. A* **661**, 16 (2012)

[106] E. Calvo *et al.*, *Nucl. Instr. Meth. A* **621**, 222 (2010)

[107] K. Zbiri, arXiv:1104.4045 (2011)

[108] Y. Abe *et al.*, (Double Chooz Collaboration), *Phys. Rev. D* **86**, 052008 (2012)

[109] CAEN Corporation, `http://www.caentechnologies.com`

[110] F. Beissel, A. Cabrera, A. Cucoanes, J. V. Dawson, D.Kryn *et al.*, *JINST* **8**, T01003 (2013)

[111] R. Brun and F. Rademakers, *Nucl. Instrum. Meth A* **389**, 81 (1997)

[112] P. Barrillon *et al.*, *MAROC: Multi-Anode ReadOut Chip*, Technical report, IN2P3, LAL-Orsay (2007)

[113] Altera Corporation, *Cyclone FPGA Family Data Sheet*, Technical report, Cyclone series (2008)

[114] The National Nuclear Data Center (NNDC), Nuclear Physics Database, Brookhaven National Laboratory, `http://www.nndc.bnl.gov/`

[115] I. Ostrovsky, *Guide tube IRR*, Double Chooz Internal **DC-doc-887** (2009)

[116] A. Onillon, PhD Thesis, École des Mines, Nantes (2014)

[117] A. Onillon, *Double Chooz reactor flux calculation and systematics*, Double Chooz Internal **DC-doc-6955** (2016)

[118] E. Tournu *et al.*, EDF TechnicalNote (2001)

[119] Standard AFNOR XP X 07-020 (1996)

[120] Y. Caffari, J.M. Favennec, EDF tech-note H-P1C-2011-02007-F

[121] V. Kopeokin *et al.*, Physics of Atomic Nuclei, **67**, 1892 (2004)

[122] O. Meplan *et al.*, *MURE: MNCP Utility for Reactor Evolution - Description of the methods, first applications and results.* In Nuclear Power for the XXIst Century: From basic research to high-tech industry. ENC 2005: European Nuclear Conference (2005)

[123] J. F. Briesmeister, *MCNP - A General Monte Carlo N-Particle Transport Code*, Los Alamos National Laboratory, LA-12625-M (1997)

[124] G. Marleau, A. Hebert and R. Roy. *A User Guide for dragon.* Technical report, Institut de génie nucléaire, Ecole Polytechnique de Montreal (2000)

[125] F.Von Feilitzsch *et al.*, *Phys.Lett. B* **118**, 162 (1982)

[126] P. Huber, *Phys. Rev. C* **84**, 024617 (2011)

[127] T. Mueller *et al.*, *Phys. Rev. C* **83**, 054615 (2011)

[128] N. Haag *et al.*, *Phys. Rev. Lett.* **112**, 122501 (2014)

[129] Y. Declais *et al.*, *Phys. Lett. B* **338**, 383 (1994)

[130] A. Onillon *Flux prediction covariance matrices for DC-IV* , Double Chooz Internal **DC-doc-7251** (2017)

[131] Y. Abe *et al.*, (Double Chooz Collaboration), *JHEP* **1410**, 86 (2014)

[132] J. Allison, K. Amako, J. Apostolakis, H. Araujo, P. Dubois *et al.*, *IEEE Trans. Nucl. Sci.* **53**, 270 (2006)

[133] C. Aberle, C.Buck, F. Hartmann, S.Schonert and S. Wagner, *JINST* **6**, P11006 (2011)

[134] J.B. Birks, *Proc. Phy. Soc. London Sect. A* **64**, 874 (1951)

[135] I. Stancu *The Ge-68 Calibration Data*, Double Chooz Internal **DC-doc-3397** (2011)

[136] Y.Abe *et al.*, (Double Chooz Collaboration), *Nucl. Instrum. Meth. A* **764**, 330 (2014)

[137] Y. Abe *et al.*, (Double Chooz Collaboration), *JINST* **8**, P08015 (2013)

[138] C. Aberle *et al.*, *Chem. Phys. Lett.* **516**, 257 (2011)

[139] M. Chaveau, *Energy scale*, Double Chooz Internal **DC-doc-6950**(2016)

[140] H. de Kerret *et al.*, (Double Chooz Collaboration), arXiv:1901.09445

[141] Y. Abe *et al.*, (Double Chooz Collaboration), *Phys. Rev. Lett. B* **735**, 51 (2014)

[142] Y. Abe *et al.*, (Double Chooz Collaboration), *JINST* **11**, P08001 (2016)

[143] `https://root.cern.ch/tmva`

[144] R. Sharankova, *ANN for DC-IV*, Double Chooz Internal **DC-doc-6672** (2016)

[145] A.Hourlier, PhD Thesis, APC, Paris (2016)

[146] T. Kawasaki, *Vertex Energy reconstruction in AC Japan*, Double Chooz Internal **DC-doc-1863** (2010)

[147] J.M. López-Castaño, PhD Thesis, Ciemat, Madrid (2017)

[148] H. de Kerret *et al.*, (Double Chooz Collaboration), *JHEP* **1811**, 053 (2018)

[149] J.I. Crespo-Anadón, PhD Thesis, Ciemat, Madrid (2015)

[150] G. Cowan, *Error analysis for efficiency*, RHUL Physics (2008)

[151] D. Navas_Nicolás *et al.*, *IBD efficiencies Gd and Gd++*, ouble Chooz Internal **DC-doc-6823** (2016)

[152] C. J. Clopper and E. S. Pearson, *Biometrica* **26** 404 (1934)

[153] R. Brun and F.Rademakers, *Nucl.Instrum.Meth. A* **389**, 81 (1997)

[154] "TEfficiency Class Reference" `https://root.cern.ch/doc/master/classTEfficiency.html` (2015)

[155] M. Ishitsuka, *DT analysis rationale*, Double Chooz Internal **DC-doc-6815** (2016)

[156] T.J.C. Bezerra, *IBD efficiency cross-check with FN*, Double Chooz Internal **DC-doc-6980** (2016)

[157] T.J.C. Bezerra, *Tuning Gd@GC of ND MC*, Double Chooz Internal **DC-doc-6995** (2016)

[158] Landolt-Bornstein New Book Series, *"Subvolume A1 - Low Energy Neutrons and their Interaction with Nuclei and Matter. Part 1: 9. Nuclear fission, 9.3 Fission neutrons - 9.4 Fission gammas",* Volume: 16A1, ISBN: 978-3-540-60857-8, Springer-Verlag (2000)

[159] H. Almazan, Master Thesis, University of Heidelberg, Heidelberg (2017)

[160] S. Agostinelli et al., (Geant4 Collaboration), *Nucl. Instrum. Meth. A* **506** 250 (2003)

[161] J. Allison, K. Amako, J. Apostolakis, H. Araujo, P.A. Dubois, et al., *IEEE Trans. Nucl. Sci.* **53** 270 (2006)

[162] A. Etenko, *Slow neutrons modelling*, Double Chooz Internal **DC-doc-1264** (2009)

[163] A. Etenko, *Slow neutrons modelling II*, Double Chooz Internal **DC-doc-1430** (2010)

[164] TRIPOLI-4 version 8.1, 3D general purpose continuous energy Monte Carlo Transport code, "NEA-1716/07" `http://www.oecd-nea.org/tools/abstract/detail/nea-1716` (2013)

[165] `https://www.basf.com/global/en.html`

[166] C. Buck, *Number of protons in Target and GC*, Double Chooz Internal **DC-doc-3236** (2011).

[167] V.Sibille et al., *Weights measurements in the Double Chooz experiments*, Double Chooz Internal **DC-doc-6683** (2016)

[168] R. Sharankova, *Application of ANN to Gd++*, Double Chooz Internal **DC-doc-6334** (2015)

[169] M. Vivier, C.Buck, *Proton number in NT and GC using geometric volumes calculations*, Double Chooz Internal **DC-doc-6786** (2017)

[170] C. Buck, *Proton number. New results from TUM measurements*, DC-doc-7103 (2017)

[171] C. Buck, *Analysis of Buffer X-TOS sample* Double Chooz Internal **DC-doc-5580** (2014)

[172] A. J. Franke, PhD thesis, Columbia University, New York (2012)

[173] A. Onillon, *Final proton number correction DC-IV*, Double Chooz Internal **DC-doc-7228** (2017).

[174] A. Onillon, *Proton number uncertainty review*, Double Chooz Internal **DC-doc-7290** (2017)

[175] Esteban, I., Gonzalez-Garcia, M.C., Maltoni, M. et al., *JHEP01* **087** (2017).

[176] NuFIT 3.1 (2017), www.nu-fit.org.

[177] R. A. Forrest, *FISPACT-2007: user manual*, **UKAEA-FUS-534** (2007), http://www.ccfe.ac.uk/assets/Documents/ukaea-fus-534.pdf.

[178] T. A. Mueller, D. Lhuillier, M. Fallot, A. Letourneau, S. Cormon, M. Fechner, L. Giot and T. Lasserre, *Phys. Rev. C* **83**, 054615 (2011).

[179] J. Felde, *Rate Only Analysis Including a Variable Reactor Power Error*, Double Chooz Internal **DC-doc-3583** (2012)

[180] C. Palomares, *Accidental BG Stability and Impact to RRM*, Double Chooz Internal **DC-doc-7274** (2017)

[181] C. Jollet, *Li evolution in Time*, Double Chooz Internal **DC-doc-7255** (2017)

[182] A. Meregaglia, *FN evolution in Time*, Double Chooz Internal **DC-doc-7254** (2017)

[183] T. J. C. Bezerra, χ^2 *Fit Results*, Double Chooz Internal **DC-doc-7323** (2017)

[184] F. James, M. Roos, *Computer Physics Communication* **10**, 343 (1975)

[185] T.J.C. Bezerra, *Proposal of Data-Data Fit Including FD-I*, Double Chooz Internal **DC-doc-7196** (2017)

[186] H. de Kerret, proceedings of Neutrino 2014, http://neutrino2014.bu.edu.

[187] Liang Zhan, proceedings of NuTEL 2015, arXiv:1506.01149

[188] Seo-Hee Seo, proceedings of Neutrino 2014, arXiv:1410.7987

[189] K. Schereckenbach *et al.*, *Phys. Lett. B* **160**, 325 (1985)

[190] P. Huber, *Phys. Rev. Lett.* **118**, 042502 (2017)

[191] Y. Abe *et al.* (Double Chooz Collaboration), *Phys. Rev. D* **87**, 011102 (2013)

[192] F. P. An *et al.* (Daya Bay Collaboration), *Phys. Rev. Lett.* **112**, 061801 (2014)

[193] F. P. An *et al.* (Daya Bay Collaboration), *Phys. Rev. Lett.* **118** 251801 (2017)

[194] C. Giunti, *Phys. Rev. D* **96**, 033005 (2017)

[195] C. Buck *et al. Phys. Lett. B* **765**, 159 (2017)

[196] H. Almazan *et al.* (Stereo Collaboration), *Phys. Rev. Lett.* **121**, 161801 (2018)

[197] J. Ashenfelter *et al.* (PROSPECT Collaboration), arXiv:1812.10877 (2018)

[198] N. Ryder *et al.* (Solid Collaboration), arXiv:1510.07835 (2015)

[199] D. Navas-Nicolás, P. Novella, *DC-IV RRM Fit technote*, Double Chooz Internal **DC-doc-7126** (2017)

[200] D. Adey *et al.* (Daya Bay Collaboration), *Phys. Rev. lett* **121**, 241805 (2018)

[201] G. Bak *et al.* (RENO Collaboration), *Phys. Rev. Lett.* **121**, 201801 (2018)

[202] P. Adamson et al. (NOvA collaboration), (unpublished).